

PROCEEDINGS OF THE KECK GEOLOGY CONSORTIUM

Volume 32
2019
2018-2019 Projects

Dr. Cameron Davidson and Dr. Karl Wirth, Editors
Co-Directors, Keck Geology Consortium

Marga Miller
Keck Geology Consortium Administrative Assistant
Macalester College

*Keck Geology Consortium
Macalester College
1600 Grand Ave, St. Paul, MN 55105
(651) 696-6108, Info@KeckGeology.org*

ISSN# 1528-7491

Funding Provided by:
Keck Geology Consortium Member Institutions
The National Science Foundation Grant NSF-REU 1659322

PROCEEDINGS OF THE KECK GEOLOGY CONSORTIUM
ISSN# 1528-7491

2018-2019 Projects

Cameron Davidson Editor and Co-Director Carleton College	Keck Geology Consortium Macalester College 1600 Grand Ave. St Paul, MN 55105	Karl Wirth Editor and Co-Director Macalester College
--	---	--

Keck Geology Consortium Member Institutions:

Amherst College, Beloit College, Carleton College, Colgate University, The College of Wooster, The Colorado College, Franklin & Marshall College, Macalester College, Mt Holyoke College, Oberlin College, Pomona College, Smith College, Trinity University, Union College, Washington & Lee University, Wesleyan University, Whitman College

2018-2019 GATEWAY PROJECTS

LANDSCAPE AND ENVIRONMENTAL CHANGE IN GLACIER NATIONAL PARK, MONTANA, U.S.A.

Faculty: KELLY MACGREGOR, Macalester College and AMY MYRBO, LacCore/CSDCO, University of Minnesota

Students: ELIZAVETA ATALIG, Wesleyan University; ETIENNE CHENEVERT, Macalester College; ELIZABETH MOORE, Washington and Lee University; BONNIE PAGE, Franklin and Marshall College; ANNA PEARSON, Smith College; JOSHUA STEPHENSON, Macalester College; JACOB WATTS, Colgate University

USING GARNETS TO EXPLORE THE BEGINNING OF SUBDUCTION ON SANTA CATALINA ISLAND, CALIFORNIA

Faculty: ZEB PAGE, Oberlin College and JADE-STAR LACKEY, Pomona College

Students: BLAIZE ADLER-IVANBROOK, Colorado College; NATHANIEL BESS, Franklin and Marshall College; AMANI CANADA, Trinity University; JUAN ESPARZA, Tarrant County College; SARAH HAMPTON, Oberlin College; ERIC HASEGAWA, Amherst College; JAMES KARROUM, Rice University; LORENA PARAS, Smith College; PAIGE VOSS, Pomona College

2018-2019 ADVANCED PROJECTS

STRUCTURAL EVOLUTION OF A SEGMENTED NORMAL FAULT TRANSFER ZONE, SEVIER FAULT, SOUTHERN UTAH

Faculty: BEN SURPLESS, Trinity University

Students: CHARLEY HANKLA, College of Wooster; CAROLINE MCKEIGHAN, Trinity University; CURTIS SEGARRA, Trinity University; MADISON WOODLEY, Mt Holyoke College

PALEOENVIRONMENTAL ANALYSIS OF ANCIENT (PETRO)CALCIC SOIL HORIZONS: DISENTANGLING CLIMATIC, GEOMORPHIC, AND BIOLOGICAL RECORDS IN THE MOJAVE DESERT

Faculty: COLIN R. ROBINS, Claremont McKenna, Pitzer, and Scripps Colleges

Students: ETHAN CONLEY, Beloit College; KURT CRANDALL, Pitzer College; INDIA FUTTERMAN, Vassar University; PENELOPE VORSTER, Mt Holyoke College

2018-2019 ADVANCED PROJECTS – Continued

GEOLOGY OF THE CHUGACH-PRINCE WILLIAM TERRANE IN NORTHERN PRINCE WILLIAM SOUND, ALASKA

Faculty: JOHN GARVER, Union College and CAM DAVIDSON, Carleton College

Students: WILL FISHER, Union College; VICTOR GARCIA, University of Texas-Austin; NICHOLAS GROSS ALMONTE, Carleton College; ALYSALA MALIK, Carleton College; CAITLIN NOSEWORTHY, College of St Norbert; MOLLIE POPE, Union College

ASSESSING VEGETATION AND FLUVIAL RESPONSES TO THE PALEOCENE-EOCENE THERMAL MAXIMUM IN THE HANNA BASIN (WYOMING, U.S.A.)

Faculty: BRADY Z. FOREMAN, Western Washington University and ELLEN CURRANO, University of Wyoming

Students: JAMES CHISHOLM, California State University, San Bernardino; KEIFER NACE, Whitman College; XAVIER NOGUEIRA, Temple University; JAKE POLSAK, Western Washington University; ANTHONY SEMERARO, Western Washington University; CHRISTINE SHONNARD, Beloit College

Short Contributions and Posters – Montana Gateway Project

LANDSCAPE AND ENVIRONMENTAL CHANGE IN GLACIER NATIONAL PARK, MONTANA, U.S.A.
KELLY MACGREGOR, Macalester College and AMY MYRBO, LacCore/CSDCO, University of Minnesota

SEDIMENT TRANSPORT AND DEPOSITION IN FISHERCAP LAKE AND THE SWIFTCURRENT VALLEY, GLACIER NATIONAL PARK, MONTANA, USA

MACGREGOR, Kelly¹, MYRBO, Amy², ABOUD, Diala¹, ATALIG, Elizaveta³, CHENEVERT, Etienne¹, MOORE, Elizabeth⁴, PAGE, Bonnie⁵, PEARSON, Anna⁶, STEPHENSON, Joshua¹ and WATTS, Jacob⁷, (1)Geology, Macalester College, 1600 Grand Avenue, St. Paul, MN 55105, (2)LacCore/CSDCO, Department of Earth Sciences, University of Minnesota, 500 Pillsbury Dr. SE, Minneapolis, MN 55455, (3)Wesleyan University, Middletown, CT 06459, (4)Washington and Lee University, Lexington, VA 24450, (5)Franklin and Marshall College, Lancaster, PA 17603, (6)Smith College, Northampton, MA 01063, (7)Colgate University, Hamilton, NY 13346

USING LAKE CORES TO ANALYZE SEDIMENT TRANSPORT AND ENVIRONMENTAL CHANGE IN SWIFTCURRENT LAKE, GLACIER NATIONAL PARK, MONTANA, USA

MYRBO, Amy¹, MACGREGOR, Kelly², ABOUD, Diala², ATALIG, Elizaveta³, CHENEVERT, Etienne², MOORE, Elizabeth⁴, PAGE, Bonnie⁵, PEARSON, Anna⁶, STEPHENSON, Joshua² and WATTS, Jacob⁷, (1)LacCore/CSDCO, Department of Earth Sciences, University of Minnesota, 500 Pillsbury Dr. SE, Minneapolis, MN 55455, (2)Geology, Macalester College, 1600 Grand Avenue, St. Paul, MN 55105, (3)Wesleyan University, Middletown, CT 06459, (4)Washington and Lee University, Lexington, VA 24450, (5)Franklin and Marshall College, Lancaster, PA 17603, (6)Smith College, Northampton, MA 01063, (7)Colgate University, Hamilton, NY 13346

Short Contributions and Posters – California Gateway Project

USING GARNETS TO EXPLORE THE BEGINNING OF SUBDUCTION ON SANTA CATALINA ISLAND, CALIFORNIA

ZEB PAGE, Oberlin College and JADE-STAR LACKEY, Pomona College

AN INVESTIGATION OF THE CATALINA GARNET-BLUESCHIST: MAJOR AND TRACE ELEMENT COMPOSITION AND ZONING IN GARNET AND LAWSONITE FROM A MULTIPLY SUBDUCTED BLOCK

ADLER-IVANBROOK, B.; HAMPTON, S. K.; ESPARZA LIMON, J. P.; LACKEY, J. S.; PAGE, F. Z.
AA(Colorado College, Colorado Springs, CO, United States b_adlerivanbrook@coloradocollege.edu), AB(Geology, Oberlin College, Oberlin, OH, United States shampton@oberlin.edu), AC(Life and Physical Sciences, Tarrant County College, Hurst, United States juan.esparza580@my.tccd.edu), AD(Pomona College, Claremont, CA, United States JadeStar.Lackey@pomona.edu), AE(Oberlin College, Oberlin, OH, United States zeb.page@oberlin.edu)

MAJOR AND TRACE ELEMENT ZONING IN GARNETS OF UNUSUAL SIZE FROM BLOCKS HOSTED BY ULTRAMAFIC MÉLANGE, SANTA CATALINA ISLAND, CALIFORNIA

CANADA, A. L.; KARROUM, J. G., II; PARAS, L.; LACKEY, J. S.; PAGE, F. Z.
AA(Trinity University, San Antonio, TX, United States amanilcanada@gmail.com), AB(Rice University, Houston, TX, United States jameskarroumii@gmail.com), AC(Smith College, Northampton, United States lparas@smith.edu), AD(Pomona College, Claremont, CA, United States JadeStar.Lackey@pomona.edu), AE(Oberlin College, Oberlin, OH, United States zeb.page@oberlin.edu)

MAJOR AND TRACE ELEMENT ANALYSIS OF GARNET CRYSTALS FROM A HORNBLENDEITE BLOCK AND RIND ON SANTA CATALINA ISLAND, CA: INSIGHTS INTO METASOMATIC PROCESSES IN SUBDUCTION MÉLANGE

BESS, N. T.; HASEGAWA, E. M.; VOSS, P. R.; LACKEY, J. S.; PAGE, F. Z.
AA(Franklin and Marshall College, Lancaster, PA, United States nbess@fandm.edu), AB(Geology, Amherst College, Amherst, MA, United States ehasegawa20@amherst.edu), AC(Geology, Pomona College, Claremont, United States prva2017@mymail.pomona.edu), AD(Pomona College, Claremont, CA, United States JadeStar.Lackey@pomona.edu), AE(Oberlin College, Oberlin, OH, United States zeb.page@oberlin.edu)

Short Contributions – Utah Advanced Project

STRUCTURAL EVOLUTION OF A SEGMENTED NORMAL FAULT TRANSFER ZONE, SEVIER FAULT, SOUTHERN UTAH

BEN SURPLESS, Trinity University

AN ANALYSIS OF FRACTURES AROUND THE SEVIER FAULT ZONE IN RED HOLLOW CANYON NEAR ORDERVILLE, UTAH

CHARLEY H. HANKLA, The College of Wooster

Research Advisor: Shelley Judge

ANALYZING DEFORMATION WITHIN A NORMAL FAULT TRANSFER ZONE USING SFM 3D MODELING

CAROLINE MCKEIGHAN, Trinity University

Research Advisor: Benjamin Surpless

GEOMECHANICAL ANALYSIS OF SEDIMENTARY LAYERING AS A STRUCTURAL CONTROL ON FAULT PROPAGATION

CURTIS SEGARRA, Trinity University

Research Advisor: Benjamin Surpless

GIS ANALYSIS OF SUBSIDIARY STRUCTURES WITHIN A MAJOR NORMAL FAULT TRANSFER ZONE

MADISON WOODLEY, Mount Holyoke College

Research Advisor: Michelle Markley

Short Contributions – Nevada Advanced Project

PALEOENVIRONMENTAL ANALYSIS OF (PETRO)CALCIC SOIL HORIZONS IN THE MOJAVE DESERT

COLIN R. ROBINS, Claremont McKenna, Pitzer, and Scripps Colleges (The Claremont Colleges Consortium)

MORPHOLOGY AND GENESIS OF PEDOGENIC OIDS IN CALCIC AND PETROCALCIC SOIL HORIZONS

ETHAN W. CONLEY, Beloit College

Research Advisor: Jim Rougvie

WHAT CAN PETROCALCIC LAMINAE TELL US ABOUT SOIL PROCESSES AND PALEOENVIRONMENTS?

KURT CRANDALL, Pitzer College

Research Advisor: Colin Robins

INTERPRETING POTENTIAL BARIUM SOURCES AT MORMON MESA, NV USING GEOCHEMICAL AND GEOMORPHOLOGICAL DATA

INDIA FUTTERMAN, Vassar College

Research Advisor: Kirsten Menking

$\delta^{13}\text{C}$ AND $\delta^{18}\text{O}$ GEOCHEMISTRY OF PEDOGENIC CARBONATES OF MORMON MESA, SOUTHEASTERN NEVADA, USA

PENELOPE VORSTER, Mount Holyoke College

Research Advisor: Steve Dunn

Short Contributions – Alaska Advanced Project

GEOLOGY OF THE CHUGACH-PRINCE WILLIAM TERRANE IN NORTHERN PRINCE WILLIAM SOUND, ALASKA

JOHN I. GARVER, Union College and CAMERON DAVIDSON, Carleton College

ZIRCON FACIES IN THE PALEOCENE-EOCENE ORCA GROUP INDICATE A PROVENANCE LINK TO THE CHUGACH TERRANE, PRINCE WILLIAM SOUND, ALASKA

WILL SPARKHAWK FISHER, Union College

Research Advisor: John Garver

CRYSTALLIZATION AGES AND GEOCHEMISTRY OF THE MINERS BAY AND CEDAR BAY PLUTONS, PRINCE WILLIAM SOUND, ALASKA

VICTOR R. GARCIA JR., The University of Texas at Austin

Research Advisor: Daniel F. Stockli

AGE AND PROVENANCE OF THE UPPER CRETACEOUS TO PALEOCENE VALDEZ GROUP OF THE CHUGACH TERRANE FROM THE RICHARDSON HIGHWAY AND NORTHERN PRINCE WILLIAM SOUND, ALASKA

NICHOLAS GROSS ALMONTE, Carleton College

Research Advisor: Cameron Davidson

U-PB DATING OF DETRITAL ZIRCON FROM TURBIDITES OF THE CHUGACH AND PRINCE WILLIAM TERRANES, ALASKA: SIGNIFICANCE OF THE CONTACT FAULT SYSTEM AS A TERRANE BOUNDARY

ALYSALA MALIK, Carleton College

Research Advisor: Cameron Davidson

AGE AND TECTONIC SETTING OF THE PALEOCENE GLACIER ISLAND VOLCANIC SEQUENCE OF THE ORCA GROUP IN PRINCE WILLIAM SOUND, ALASKA

CAITLIN NOSEWORTHY, Saint Norbert College

Research Advisor: Tim Flood

PROVENANCE OF SANDSTONE CLASTS FROM CONGLOMERATE OF THE PALEOCENE-EOCENE ORCA GROUP IN PRINCE WILLIAM SOUND, ALASKA

MOLLIE D. POPE, Union College

Research Advisor: John Garver

Short Contributions – Wyoming Advanced Project

ASSESSING VEGETATION AND FLUVIAL RESPONSES TO THE PALEOCENE-EOCENE THERMAL MAXIMUM IN THE HANNA BASIN (WYOMING, U.S.A.)

ELLEN D. CURRANO, University of Wyoming and BRADY Z. FOREMAN, Western Washington University

EVALUATION OF BULK ORGANIC CARBON ISOTOPE RECORDS FROM EARLY PALEOGENE STRATA IN THE HANNA BASIN (WYOMING, U.S.A.) SPANNING THE PALEOCENE-EOCENE THERMAL MAXIMUM

JAMES CHISHOLM, Department of Geological Sciences, California State University, San Bernardino

Research Advisor: Joan E. Fryxell

VEGETATION STRUCTURE AND LITHOLOGY RESPONSE TO THE PALEOCENE-EOCENE THERMAL MAXIMUM IN THE HANNA BASIN, WYOMING

KEIFER NACE, Whitman College

Research Advisor: Pat Spencer

PROVENANCE OF FLUVIAL AND DELTAIC SANDSTONES ACROSS THE PALEOCENE-EOCENE BOUNDARY, HANNA BASIN, WYOMING

XAVIER ROJAS NOGUEIRA, Temple University

Research Advisor: Jesse Thornburg

VARIABILITY IN VEGETATION DENSITY ACROSS LATERALLY COEVAL STRATIGRAPHIC SECTIONS WITHIN THE HANNA BASIN, WYOMING, USA

JAKE POLSAK, Western Washington University

Research Advisor: Brady Z. Foreman

PALEOCURRENT VARIABILITY IN MEANDERING AND BRAIDED RIVER SYSTEMS: MODERN CALIBRATION AND STRATIGRAPHIC CASE STUDIES SPANNING THE PALEOCENE-EOCENE THERMAL MAXIMUM

ANTHONY SEMERARO, Western Washington University

Research Advisor: Brady Z. Foreman

EARLY PALEOGENE OVERBANK DEPOSITIONAL PATTERNS IN THE HANNA BASIN AND COMPARISON WITH COEVAL STRATA IN THE BIGHORN BASIN (WYOMING, U.S.A.)

CHRISTINE SHONNARD, Beloit College

Research Advisor: Jay Zambito

LANDSCAPE AND ENVIRONMENTAL CHANGE IN GLACIER NATIONAL PARK, MONTANA, U.S.A.

KELLY MACGREGOR, Macalester College
AMY MYRBO, LacCore/CSDCO, University of Minnesota

INTRODUCTION

Glacier National Park (GNP), Montana is sensitive to climate change as observed through glacial retreat (e.g., Key et al., 2002) and ecosystem adjustments (e.g., Klasner and Fagre, 2002), and there is widespread interest in the effects of future climate change in this unique and public space. Our research project was aimed at understanding environmental and climate change variability in near-pristine alpine basins in North America, with the goal of collecting data that is relevant to the debate about landscape response to climate change in the northern Rockies since the last glaciation. The research project has relevance to the research communities in geomorphology, Quaternary geology, glaciology, and paleoclimatology, as well as to the general public interested in climate change since the retreat of Ice Age glaciers.

The choice of lakes on which to focus during the project was based on a substantial body of past work in the Many Glacier Region of eastern GNP. In 2005, 2010, and 2014, we collected lake cores in Swiftcurrent Lake, Lake Josephine, and lower Grinnell Lake, all of which are located downstream of Grinnell Glacier (Figures 1 & 2). Work done on these cores by previous students (many of them as part of Keck projects) has provided additional constraints on climate and environmental history in the basin since the end of the Last Glacial Maximum (e.g., MacGregor et al., 2011; Schachtman et al., 2015). The overarching goal of the project this year was to understand sediment transport and deposition in the lower end of Swiftcurrent and Grinnell valleys, and how those processes document

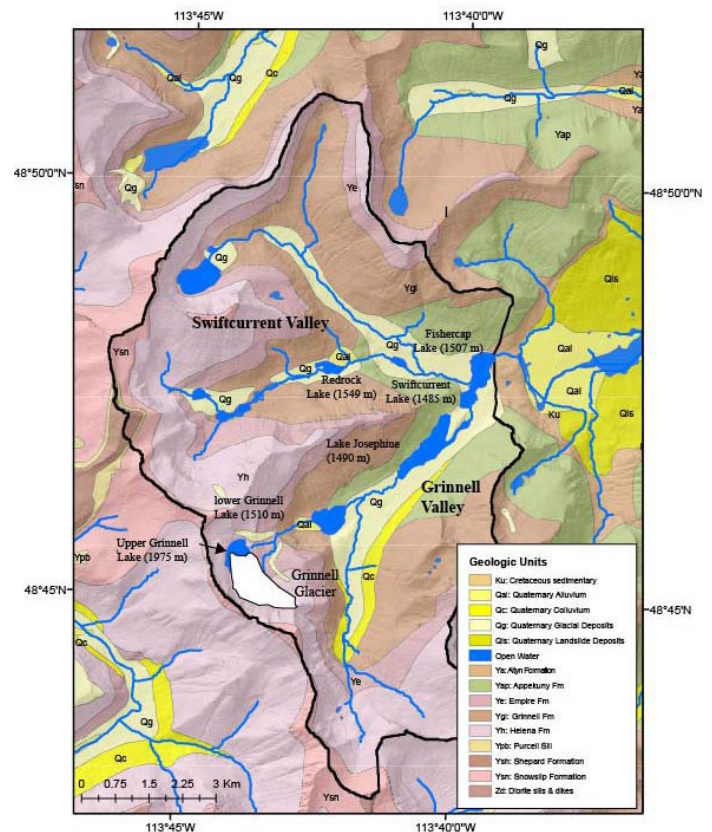


Figure 1. Geologic setting of the Many Glacier area of Glacier National Park, MT. Geologic units are generally either Precambrian meta-sedimentary formations or Quaternary surficial deposits. The southern valley (Grinnell Glacier Valley) has Grinnell Glacier in its headwaters, and serves as the source of water, sediment, and water-borne debris for most of the lake cores. The northern valley (Swiftcurrent Valley) contributes water to the northern subbasin of Swiftcurrent Lake. Map after MacGregor et al., 2011, from Whipple, 1992; courtesy of C. Riihimaki, Princeton University.

changes in environment and climate over centuries to millennia. Our field work included the collection of lake sediment cores from two lakes (Fishercap and Swiftcurrent), measuring water discharge and sediment concentrations in lakes and streams to

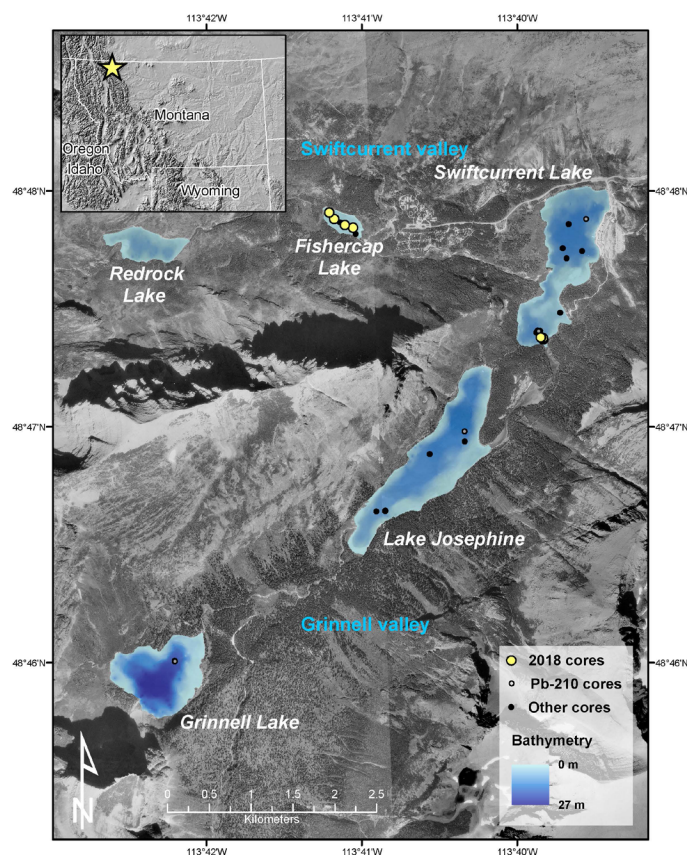


Figure 2. Map of Swiftcurrent and Grinnell Valleys, Glacier National Park, MT. Coring sites from 2018 shown as yellow dots, with coring sites from previous years as black dots. Blue shading represents lake bathymetry collected between 2010-2018.

investigate the sediment budget in the valley systems, measurements of lake bathymetry (depth) for lakebed morphology and sediment trapping efficiency, and reconnaissance of two lakes (one in Swiftcurrent valley, another on the Park's West Side) for future coring.

In summer 2018, eight students (including one near-peer mentor) participated in the Glacier National Park Gateway Keck Geology Consortium project (Figure 3). Students arrived in Minnesota and spent



Figure 3. Field photo of the group on a sunny day hiking on the Continental Divide, Glacier National Park, MT.

five days at Macalester College for classroom and laboratory 'crash courses' to prepare for the project. This included mini-lectures, hands-on activities, training at LacCore, grocery shopping, meal planning, and gear organization. Most students had taken no more than one geology course, so we spent some of the early meetings talking about major earth science concepts and the nature of scientific inquiry in geology. This included the geologic evolution of GNP (sedimentary rock formation, igneous intrusions, mountain-building), global climate change (Pleistocene, Holocene, and recent), and surface processes (weathering and hillslopes, glacial erosion, fluvial transport). After packing the vans to the brim, we spent two days driving to Many Glacier (camping in Makoshika State Park, MT on the way out). Upon arrival to Many Glacier, we learned the National Park Service (NPS) campground was closed to tent camping due to grizzly bear activity and were relocated for two nights to the Rising Sun campground in St. Mary's, about an hour drive south. The campground was beautiful and we enjoyed getting to know Sue (the camp host), but were happy to move closer to our field area when the bear threat was reduced. We spent 10 more amazing days camping, cooking, and working in the Many Glacier campground.

The first several days in the field were spent getting to know the geology, biology, and history of the Park, talking with Park Rangers/Interpreters, getting our boats inspected for invasive species control, and carrying all of our equipment to the first lake we cored (Fishercap). Most days we divided into two teams, with Team A on the coring craft and Team B collecting bathymetric data, water and sediment discharge samples, and talking with curious Park visitors who were hiking past where we were working. Students rotated regularly among these groups to learn and practice different methodologies. We collected a total of 2.6 meters of core from Fishercap Lake and 14.2 meters of core from Swiftcurrent Lake. We did several group hikes, including a Ranger-led hike to Iceberg Lake, a group hike to Grinnell Glacier, and a hike up to Logan Pass along the continental divide (mountain goats and marmots included!). We also drove to West Glacier and hiked through part of the area burned during the 2017 fires near Lake McDonald Lodge;



Figure 4. Photo of group with Many Glacier Park Rangers after research presentation (Bear Ranger Bob featured).

this included a reconnaissance trip to Fish Lake for future coring. Our daily conversations with the public (on the trail, from sampling sites, in the campground, at the evening Ranger talks) were highlights, as was the talk we gave to the Many Glacier NPS staff about our research (Figure 4). The constant public contact helped the students to develop their “elevator pitches” for talking about their research, which served them well when they presented their posters at GSA.

After returning to the Twin Cities, students spent two weeks analyzing the cores and other data we collected in the field. Measurements of the sediments’ geophysical properties (density, magnetic susceptibility) were collected on the whole core (0.5 cm resolution) using the Geotek Multi-Sensor Core Logger. Cores then were split lengthwise, cleaned, and imaged at 20 pixels per mm on the Geotek CIS linescan digital camera. Initial core description (ICD) was done following the nomenclature found in Schnurrenberger and others (2003). Smear slides were taken in horizons of interest to look at the clastic, authigenic, and biogenic components of the sediment. Split core sections were then logged on the Geotek XYZ at 0.5 cm resolution for high-resolution magnetic susceptibility and color reflectance. Students ran loss-on-ignition (LOI) on every centimeter of the cores, made and described smear slides, helped with correlation of overlapping cores, dried and weighed filters, and made calculations of water discharge and suspended sediment concentrations. Finally, students divided into two groups and wrote and submitted abstracts for GSA (MacGregor et al., 2019; Myrbo et al., 2019).

The entire group reconvened in Indianapolis, Indiana

for GSA in November 2018 to present the results of their research in a Limnogeology poster session (Figure 5). The two posters, “Sediment transport and deposition in Fishercap Lake and the Swiftcurrent Valley, Glacier National Park, Montana, USA” and “Using lake cores to analyze sediment transport and environmental change in Swiftcurrent Lake, Glacier National Park, Montana, USA” were busy with visitors; both can be found on the Keck Geology website. Below is a summary of the research motivation and findings of the GNP Gateway students.

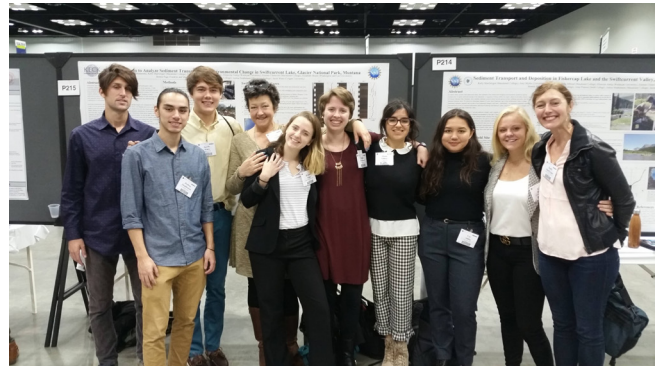


Figure 5. Photo of group during presentations at GSA in Indianapolis, IN, 2019.

FIELD SETTING

The Many Glacier region of Glacier National Park, Montana is located to the east of the Continental Divide and includes several small cirque glaciers and glacially carved lakes (Figure 1). Swiftcurrent Lake, the most accessible of the formerly glaciated lakes, receives water and sediment from two valleys: the southern subbasin of the lake has a 36-km² drainage basin that includes Grinnell Glacier (~2000 m elevation), Upper and lower Grinnell lakes, and Lake Josephine, while the northern portion of the lake has a drainage area of 44 km² that includes Swiftcurrent Glacier, Iceberg Lake, Bullhead Lake, Redrock Lake, Fishercap Lake, Swiftcurrent Creek and its tributaries. The Many Glacier Hotel, completed by 1918, sits near the Swiftcurrent Lake outlet.

The entire drainage basin is underlain by the Middle Proterozoic Belt Supergroup, which is comprised primarily of siltstones, shales, and sandstones (Figure 1; Horodyski, 1983). Grinnell Glacier is currently eroding the stromatolitic Siyeh Limestone of the Helena Formation, which consists of dolomitic

limestone and calcitic argillite (Whipple, 1992). The only bedrock source of dolomite in the valley is at the highest elevations of the basins, and is the rock on which Grinnell and Swiftcurrent glaciers currently reside. Lake Josephine and Swiftcurrent Lake are underlain by late Pleistocene tills on order of 1-3 m thick (Earhart et al., 1989; Carrara, 1990; Whipple, 1992). Recent work by Schachtman and others (2015) shows that Grinnell Glacier was likely at or near the southern end of Swiftcurrent Lake at ~17 ka based on the presence of varved sediments in the lake.

KEY FINDINGS

Swiftcurrent Valley

Our goal was to provide some initial morphometric data on the lakes, and to characterize the transport and deposition of material in transport from Swiftcurrent Valley into the northern basin of Swiftcurrent Lake. We measured bathymetry of Fishercap and Redrock lakes, the two lakes furthest downvalley in a chain of paternoster lakes in the Swiftcurrent Valley, which joins the Grinnell Valley at Swiftcurrent Lake. Our bathymetric measurements and coring demonstrated that Fishercap Lake is relatively shallow (~0.8 m; Figure 2) and uniform in depth, with a slightly deeper upvalley region. Redrock Lake had a maximum water depth of ~6.5 m, with the deepest water on the southern edge of the lake, which may be structurally controlled. We also collected a downlake transect of cores from Fishercap Lake, the final lake in the chain. Fine sediment accumulation in Fishercap Lake is generally massive, with organic content ranging from 5-40% with an average of 15%. The most upvalley core contained laminated sediments in contrast to the other three cores in the transect. We observed frequent moose grazing in the lake, suggesting macrobioturbation of lake sediments. There was a dense gravel layer below the sediment-water interface that appears to be uniform across the basin, potentially suggesting past desiccation of the lake. The fine-grained sediment above the gravel is thickest at the upvalley end of the lake (85 cm) and grades to 40 cm at the downvalley end of the lake.

To constrain the timing of possible lake desiccation, we collected basal charcoal radiocarbon samples

at the bottom of all four Fishercap Lake cores, and collected an additional sample from the most upvalley core that contained laminations. Ages for cores 1-3 are somewhat difficult to interpret based on their young age (during a period when the radiocarbon calibration curve is complicated), but are within the past ~500 years. The most upvalley laminated core was significantly older with a basal age of ~4400 radiocarbon years. This suggests a portion of the lake may not have fully dried, or that the gravel layer represents an older desiccation event with a hiatus in deposition in the majority of the lake basin. Notably, Fishercap is significantly more shallow than any lake in the Grinnell Valley, and is therefore unlikely to be an important sediment trap for material moving down Swiftcurrent Valley (MacGregor et al, 2019).

Grinnell Valley

We collected a transect of three composite cores along the inlet delta region of Swiftcurrent Lake where the stream enters from Lake Josephine. Bathymetric data showed increasing water depths with distance from the inlet stream (Figure 2). Core sediments contained laminations but were not varved, and were generally silt and clay-rich with minor sandy contributions. Diatoms were pervasive in the top several meters of sediments, and clastic units are comprised of several clay minerals, quartz, feldspars, and dolomite. In all three Swiftcurrent Lake cores we collected the Mazama ash (7.7 ka; Zdanowicz et al., 1999), and the longest core contained the Glacier Peak G ash (13.55 ka; Kuehn et al., 2009; Foit et al., 1993; Mehringer et al., 1984) and Mount St. Helens J ash (13.87 ka; see Schachtman et al, 2015 for references). The Mazama ash occurs at different depths in each core in the transect, and shows that sedimentation rates are variable across the inlet despite similar water depths. Hiatuses are also likely in these sequences. We calculated average sedimentation rates from the top of the Mazama tephra (7630 BP) to the present. From proximal to distal from the inlet (sites 1-3, respectively), those rates were 0.19, 0.41, and 0.52 mm/yr. The average sedimentation rate for the Schachtman et al (2015) core, farther from the inlet, is 0.59 mm/year. Sedimentation rates increase with distance from the inlet, which was surprising: we originally hypothesized that more transported

sediments would be deposited closer to where the stream enters the lake. This finding, suggests that the inlet stream is eroding as well as depositing sediment, and that some transported sediment may bypass the delta entirely, especially during high water discharge periods. Smear slides show an increase in grain size from clays dominating sediments older than the Glacier Peak G/Mt. St. Helens J ashes to coarser sediment in the upper ~2 m of the cores (Myrbo et al., 2019).

Suspended sediment and water discharge data

We measured suspended sediment concentrations at inlets and outlets of Redrock, Fishercap, and Swiftcurrent lakes to provide preliminary insights into sediment sources and sinks within the valleys. Preliminary total suspended solids (TSS) data show TSS is higher at the outlets than at the inlets of Redrock and Fishercap lakes, suggesting that the lakes are not currently efficient sediment traps and may be sources of material for Swiftcurrent Lake. Comparison of sediment concentrations from Swiftcurrent and Grinnell Valleys suggests that Swiftcurrent Valley transports more sediment than Grinnell Valley into Swiftcurrent Lake. Preliminary estimates of water discharge coming from Lake Josephine show more water enters Swiftcurrent Lake from Grinnell Valley than that from Swiftcurrent Valley, but TSS concentrations are lower in the Grinnell Valley discharge. This has implications for our interpretations of climate and environmental change from cores that receive sediment and water from both valleys (MacGregor et al., 2019; Myrbo et al., 2019).

ACKNOWLEDGEMENTS

This material is based upon work supported by the Keck Geology Consortium and the National Science Foundation under Grant No. 1659322. We extend special thanks to the National Park Service (permit GLAC-2014-SCI-0010), the Many Glacier Rangers and Park Service staff, and our campground hosts for their support. We thank LLNL for their rapid turnaround on our radiocarbon dates, and LacCore staff for their encouragement and patience during our residence.

REFERENCES

- Carrara, P.E., 1990, Surficial geologic map of Glacier National Park, Montana. 1:100,000.
- Earhart, R.L., Raup, O.B., Whipple, J.W., Isom, A.L., and Davis, G.A., 1989, Geologic maps, cross section, and photographs of the central part of Glacier National Park, Montana.
- Foit, J. F. F., Mehringer, J. P. J., & Sheppard, J. C., 1993. Age, distribution, and stratigraphy of Glacier Peak tephra in eastern Washington and western Montana, United States. *Canadian Journal of Earth Sciences* 30, 535-552.
- Horodyski, R.J., 1983, Sedimentary geology and stromatolites of the Mesoproterozoic belt Supergroup, Glacier National Park, Montana: *Precambrian Research*, v. 20.
- Kuehn, S. C., Froese, D. G., Carrara, P. E., Foit, F. F., Pearce, N. J. G., & Rotheisler, P., 2009. Major- and trace-element characterization, expanded distribution, and a new chronology for the latest Pleistocene Glacier Peak tephras in western North America. *Quaternary Research* 71, 201-216.
- Key, C.H., Fagre, D.B., and Menicke, R.K., 2002, Glacier retreat in Glacier National Park, Montana, in Williams, R.S. and Ferrigno, J.G., eds., *Satellite image atlas of glaciers of the world: North America: U.S. Geological Survey Professional Paper 1386-J*, U.S. Government Printing Office, Washington D.C. p 365-381.
- Klasner, F.L. and Fagre, D.B., 2002, A half century of change in alpine treeline patterns at Glacier National Park, Montana, U.S.A.: *Arctic, Antarctic, and Alpine Research*, v. 34, p. 53-61.
- MacGregor, K.R., Riihimaki, C.A., Myrbo, A., Shapley, M.D., and Jankowski, K., 2011, Geomorphic and climatic change over the past 12,900 years at Swiftcurrent Lake, Glacier National Park, Montana: *Quaternary Research*, v. 75, doi:10.1016/j.yqres.2010.08.005.

- MacGregor, K., Myrbo, A., Abboud, D., Atalig, E., Chenevert, E., Moore, E., Page, B., Pearson, A., Stephenson, J., Watts, J. (2018) Sediment transport and deposition in Fishercap Lake and the Swiftcurrent Valley, Glacier National Park, Montana, USA. Geological Society of America Abstracts with Programs. Vol. 50, No. 6. doi: 10.1130/abs/2018AM-321580
- Mehring Jr, P.J., Sheppard, J.C., and Foit Jr., F.F., 1984, The age of Glacier Peak tephra in west-central Montana: Quaternary Research, v. 21, p. 36-41.
- Myrbo, A., MacGregor, K., Abboud, D., Atalig, E., Chenevert, E., Moore, E., Page, B., Pearson, A., Stephenson, J., Watts, J. (2018) Using lake cores to analyze sediment transport and environmental change in Swiftcurrent Lake, Glacier National Park, Montana, USA. Geological Society of America Abstracts with Programs. Vol. 50, No. 6. doi: 10.1130/abs/2018AM-321678
- Schachtman, N., MacGregor, K.R., Myrbo, A., Hencir, N.R., Riihimaki, C.A., Thole, J., Bradtmiller, L. (2015). Lake core record of Grinnell Glacier dynamics during the Late Pleistocene and Younger Dryas, Glacier National Park, Montana, U.S.A. Quaternary Research, v. 84, no. 1, p. 1-11, doi:10.1016/j.yqres.2015.05.004
- Schnurrenberger, D., Russell, J., Kelts, K., 2003. Classification of lacustrine sediments based on sedimentary components. Journal of Paleolimnology, v. 29, p. 141-154.
- Whipple, J.W., 1992, Geologic map of Glacier National Park, Montana. 1:100,000.
- Zdanowicz, C.M., Zielinski, G.A., Germani, M.S., 1999. Mount Mazama eruption; calendrical age verified and atmospheric impact assessed. Geology 27, 621-624.

SUBDUCTION INITIATION OF GEOSCIENTISTS: KECK CATALINA II

ZEB PAGE, Oberlin College

JADE STAR LACKEY, Pomona College

NICOLLETTE MITCHELL, Project Mentor, Oberlin College

CLARAMARGARET FLOOD, Peer Mentor, Oberlin College

Students: **BLAIZE ADLER-IVANBROOK**, Colorado College; **NATHANIEL BESS**, Franklin & Marshall College; **AMANI CANADA**, Trinity University; **JUAN PABLO ESPARZA**, Tarrant County College; **ERIC HASEGAWA**, Amherst College; **SARAH HAMPTON**, Oberlin College; **JAMES KARROUM II**, Rice University; **LORENA PARAS**, Smith College; **PAIGE VOSS**, Pomona College

INTRODUCTION

Franciscan-like subduction-related metamorphic rocks (blocks of garnet-bearing blueschist and amphibolite) were recognized on Santa Catalina Island by the first half of the twentieth century (Woodford, 1924; Bailey, 1941). However, the modern era of Catalina geology began with detailed mapping and a tectonic model by Platt (1975). The metamorphic rocks of Catalina (sometimes referred to as the Catalina Schist) consist of mappable units of metasedimentary and ultramafic mélange that range from lawsonite-blueschist to amphibolite facies, with increasing grade correlated with structural height (Platt, 1975). Platt's initial subdivision of the island into blueschist, greenschist, amphibolite, and ultramafic units bounded by shallow dipping thrust faults (Fig. 1) has been refined, with the "greenschist" unit now defined as epidote amphibolite and epidote blueschist overprinted with greenschist-facies assemblages (Grove and Bebout, 1995).

The highest-grade amphibolite unit from Catalina records peak conditions of 7-12 kbar and 650-750 °C based on cation thermometry and fluid inclusion barometry (Platt, 1975; Sorensen and Barton, 1987). The unusually high temperatures and Barrovian-like assemblages of the highest-grade rocks became the basis for the interpretation that the Catalina Schist was formed in a nascent subduction zone. In this model, the amphibolite-facies rocks were

formed at the initiation of subduction and recorded high temperatures due to proximity with the hot mantle wedge; the inverted metamorphic gradient of underthrust lower-grade units recorded the subsequent cooling of the trench (Platt, 1975; Cloos, 1985; Peacock, 1987). More recent analysis of detrital zircon ages from Catalina metasedimentary rocks has revealed that accretion of the Catalina Schist occurred over at least a 20 My period, with the lowest-grade units containing detrital zircons younger than the 115 Ma metamorphic age yielded by the high-grade rocks (Grove et al., 2008). Furthermore, a single garnet blueschist block (Fig. 1) found in the blueschist-facies mélange yielded high-error Rb-Sr and Ar-Ar ages of ~150 Ma suggesting that a pre-Catalina subduction zone existed in the region. The age of the garnet blueschist block was firmly established by a 155 ± 8 U-Pb sphene age collected during the 2012 Keck project (Awalt et al., 2013). However, the P-T history of this key sample remains unconstrained, possibly due to multiple episodes of subduction as the Catalina trench become superimposed on the remnants of a thermally mature subduction zone through subduction erosion (Grove et al., 2008).

Santa Catalina Island has long been used as a field laboratory to investigate devolatilization and fluid flow in subduction zones. Petrologic, geochemical, and chronological constraints on Santa Catalina Island have been used to document extensive fluid flow and

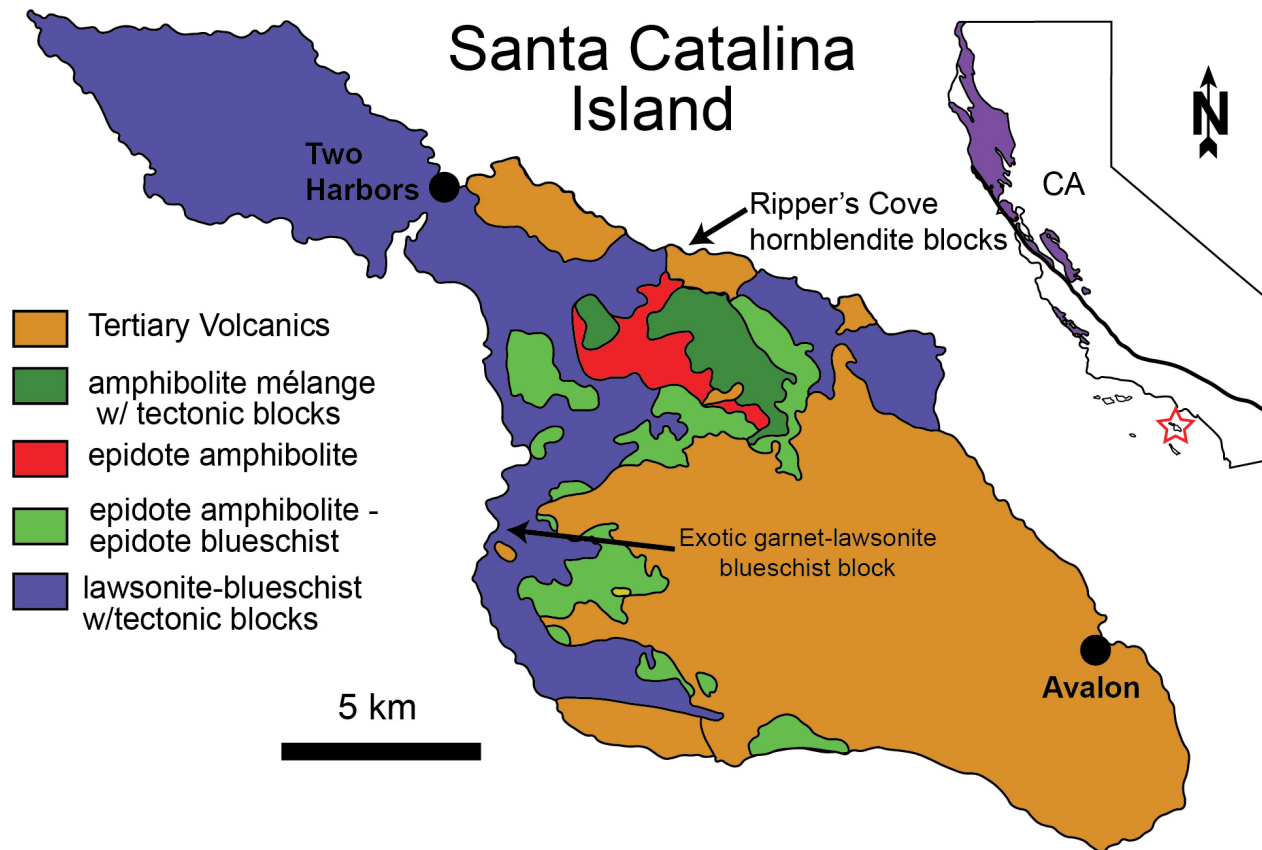


Figure 1: Geologic sketch map of Santa Catalina Island, California, modified from Platt (1975) and Grove and Barton (1995). The location of Catalina Island is shown in the red star on the inset map; the Franciscan Complex is shown in purple. The proposed study areas are shown in black rectangles.

metasomatism due to devolatilization of sediments during subduction (e.g., Sorensen and Grossman, 1989; Bebout, 1991; 2007; King et al., 2006, 2007). Many blocks in the amphibolite/ultramafic mélange have talc or tremolite metasomatic selvages or reaction rinds similar to those found in the Franciscan Complex. Unlike in the Franciscan, some of these selvages contain garnet that is compositionally different from that found in the blocks (Penniston-Dorland et al., 2013). In situ analysis of oxygen isotopes based on samples collected during the 2012 Keck Project has demonstrated that selvages contain garnet that grew both before and after rind formation (Leung et al., 2016). These garnets likely contain further information on the P-T history of rind formation and on the trace element composition of rind forming fluids.

In the summer of 2018, we undertook a nine-student Keck Gateway project using the geology of Santa Catalina Island, California as an introduction to the

study of metamorphic rocks and metasomatism both in the laboratory and in the field. Students worked collectively on three projects using in situ analysis of major and trace elements in garnet to address questions of tectonics (timing of garnet vs. lawsonite growth in garnet blueschist, trace element zoning in amphibolite garnets with and without plagioclase) and metasomatism (major and trace elements in rind garnets). The project began with students joining Page, Buckle, and Flood on the Oberlin campus for two weeks. During this time, we had several local field trips and team-building exercises but had a primary focus on analyzing garnets from previously-prepared thick sections by SEM/EDS. By the end of the two weeks, major-element traverses of garnets from four different tectonic blocks from Catalina were completed, and targets were selected for trace-element analysis. At this point, the team flew to Los Angeles, joining Lackey for a week in the field that involved investigating field relations of the tectonic blocks already under study, limited new sample collection,

and a digital mapping exercise on blocks in mélangé. The final two weeks of the project were spent on the campus of Pomona College measuring trace-element compositions of garnet and lawsonite by laser ablation inductively-coupled mass spectrometry (LA-ICP-MS), measuring bulk-rock compositions by X-ray Fluorescence Spectrometry, analyzing data, drafting abstracts and posters.

STUDENT PROJECTS

An investigation of the Catalina garnet-blueschist: Major and trace element composition and zoning in garnet and lawsonite from multiply subducted block

Blaize Adler-Ivanbrooke, Juan Esparza, Sarah Hampton

As described above, a large garnet-lawsonite blueschist block with an anomalously old age is a key sample in understanding the tectonic history of Catalina. Preliminary attempts at thermodynamic modeling in order to reconstruct the pressure-temperature evolution of the rock did not succeed in reproducing the observed metamorphic assemblage. One possibility is that the garnet and dated sphene formed in an early metamorphism at 155Ma, and the lawsonite and glaucophane recrystallized in a second lawsonite-blueschist metamorphism after 115Ma. This is consistent with color zonation in glaucophane (Awalt et al., 2013). Detailed petrography by electron microscope revealed that lawsonite is texturally late, and, in particular, exists as veins that crosscut resorbed garnet adding further credence to a multiple-subduction origin (Adler-Ivanbrooke et al. (2018). Elevated Heavy Rare Earth Element (HREE) content in both late lawsonite and early garnet suggest that lawsonite grew at the expense of garnet or with a metasomatic source of HREE (e.g., Mulcahy et al., 2014). Garnet exists only in a m-thick band through the block, and whole rock geochemistry of multiple samples across the block show that this is not because of compositional differences and is likely due to preservation of garnet only within the core of the block.

Major and Trace Element Zoning in Garnets of Unusual Size from Blocks Hosted by Ultramafic Mélange, Santa Catalina Island, California

Amani Canada, James Karroum II, Lorena Paras

Most Catalina garnet-hornblende rocks contain no plagioclase, however, the presence of plagioclase and granitic veins in some blocks led Sorensen and Barton (1987) to conclude that all garnet-hornblende rocks are residuum from the partial melting of a basaltic precursor during subduction initiation. Canada et al. (2018) compared the major and trace-element zoning patterns in three garnet-hornblende blocks: two (one plagioclase-bearing) with typical garnet sizes for the island (<5mm diameter), and a third unusual plagioclase-bearing sample containing ~3cm diameter garnets collected during the 2012 Keck project.

Garnets from all three samples were found to have similar major and trace-element zoning patterns, suggesting a similar bulk composition and P-T evolution for mafic blocks with or without plagioclase, supporting the notion of the absence of plagioclase being due to melt extraction. Unlike the single existing published analysis of trace elements in Catalina (Sorensen and Grossman, 1989), HREE were not found to increase in the rims of garnets, however, Cr did increase in some garnet rims, perhaps due to metasomatism from a mantle-source.

Major and trace element analysis of garnet crystals from a hornblendeite block and rind on Santa Catalina Island, CA: Insights into metasomatic processes in subduction mélangé

Nathaniel Bess, Eric Hasegawa, Paige Voss

Leung et al. (2016) documented three different generations of garnets in a single rind sample from one block on Catalina, first described by Penniston-Dorland et al., (2013). Three students worked collaboratively to describe the mineralogy of a block and two samples of garnet-bearing rind (Fig. 2). Bess et al. (2018) showed that, similar to the oxygen isotope record, different populations of garnets in block and rind show different trace-element patterns. Metasomatic rinds have two different generations of garnet, mm-scale crystals that have core major and trace-element compositions similar to the block garnet. Rims on large rind garnets differ from the rims of block garnets, but are similar in major and trace elements to a second generation of 100µm-scale



Figure 2: Students draw and photograph a tectonic block of garnet hornblendite with actonite-chlorite rind at Ripper's Cove, Santa Catalina Island, California.

garnets found in quartz veins that cut the rind.

Collectively, the three groups were able to provide the community important new trace-element data on garnets to the study of metamorphism and metasomatism on Santa Catalina Island. These data help shed new light on slab-melting within nascent subduction zones, and help add more evidence for the idea of multiple episodes of subduction within the subduction mélange channel. In undertaking this research students gained valuable field and laboratory skills as well as participating in many discussions on the different careers available to geologists and the importance of and challenges inherent in increasing diversity in the geosciences.

REFERENCES

Awalt, M.B., Page, F.Z., Walsh, E.O., Kylander-Clark, A.R.C., and Wirth, K.R., 2013, New evidence for old subduction in the Catalina Schist, Santa Catalina Island, CA: Geological Society of

America Abstracts with Programs, v. 45, p. 798.

Adler-Ivanbrook B, Hampton SK, Esparza Limon JP, Lackey JS, and Page FZ (2018) An investigation of the Catalina garnet-blueschist: Major and trace element composition and zoning in garnet and lawsonite from a multiply subducted block, Abstract T21F-0290 presented at 2018 AGU Fall Meeting, Washington, DC 10-14 Dec.

Bailey, E.H., 1941, Mineralogy, petrology, and geology of Catalina Island, California: Ph.D. Thesis, Stanford University.

Bebout, G.E., 1991, Field-based evidence for devolatilization in subduction zones; implications for arc magmatism: *Science*, v. 251, p. 413–416.

Bebout, G.E., 2007, Metamorphic chemical geodynamics of subduction zones: *Earth and Planetary Science Letters*, v. 260, no. 3-4, p. 373–393.

- Bess NT, Hasegawa EM, Voss PR, Lackey JS, and Page FZ (2018) Major and trace element analysis of garnet crystals from a hornblendeite block and rind on Santa Catalina Island, CA: Insights into metasomatic processes in subduction mélange, Abstract T21F-0292 presented at 2018 AGU Fall Meeting, Washington, DC 10-14 Dec.
- Canada AL, Karroum JG, Paras L, Lackey JS, and Page FZ (2018) Major and Trace Element Zoning in Garnets of Unusual Size from Blocks Hosted by Ultramafic Mélange, Santa Catalina Island, California, Abstract T21F-0291 presented at 2018 AGU Fall Meeting, Washington, DC 10-14 Dec.
- Cloos, M., 1985, Thermal Evolution of Convergent Plate Margins - Thermal Modeling and Reevaluation of Isotopic Ar-Ages for Blueschists in the Franciscan Complex of California: *Tectonics*, v. 4, p. 421–433.
- Grove, M., and Bebout, G., 1995, Cretaceous tectonic evolution of coastal southern California: Insights from the Catalina Schist: *Tectonics*, v. 14, p. 1290–1308.
- Grove, M., Bebout, G.E., Jacobson, C., Barth, A., Kimbrough, D., King, R.L., Zou, H., Lovera, O., Mahoney, B., and Gehrels, G.E., 2008, The Catalina Schist: Evidence for middle Cretaceous subduction erosion of southwestern North America, in *Formation and Applications of the Sedimentary Record in Arc Collision Zones*: Geological Society of America Special Paper 436, p. 335–361.
- King, R.L., Bebout, G.E., Moriguti, T., and Nakamura, E., 2006, Elemental mixing systematics and Sr-Nd isotope geochemistry of melange formation: Obstacles to identification of fluid sources to arc volcanics: *Earth and Planetary Science Letters*, v. 246, p. 288–304.
- King, R.L., Bebout, G.E., Grove, M., Moriguti, T., and Nakamura, E., 2007, Boron and lead isotope signatures of subduction-zone melange formation: Hybridization and fractionation along the slab-mantle interface beneath volcanic arcs: *Chemical Geology*, v. 239, p. 305–322.
- Leung, M.C., Page, F.Z., Penniston-Dorland, S.C., Kitajima, K., and Valley, J.W., 2016, Constraints on garnet-bearing metasomatic rind growth in subduction mélange through SIMS analysis of oxygen isotopes, in *Geological Society of America*, p. 281880–1.
- Mulcahy, S.R., Vervoort, J., and Renne, P.R., 2014, Dating subduction-zone metamorphism with combined garnet and lawsonite Lu-Hf geochronology: *Journal of Metamorphic Geology*, v. 32, no. 5, p. 515–533, doi: 10.1111/jmg.12092.
- Peacock, S., 1987, Creation and Preservation of Subduction-Related Inverted Metamorphic Gradients: *Journal of Geophysical Research-Solid Earth and Planets*, v. 92, p. 12763–12781.
- Penniston-Dorland, S.C., Gorman, J.K., Bebout, G.E., Piccoli, P.M., and Walker, R.J., 2014, Reaction rind formation in the Catalina Schist: Deciphering a history of mechanical mixing and metasomatic alteration: *Chemical Geology*, v. 384, no. C, p. 47–61, doi: 10.1016/j.chemgeo.2014.06.024.
- Platt, J.P., 1975, Metamorphic and deformational processes in the Franciscan Complex, California: some insights from the Catalina Schist terrane: *Bulletin of the Geological Society of America*, v. 86, p. 1337–1347.
- Sorensen, S.S., 1986, Petrologic and geochemical comparison of the blueschist and greenschist units of the Catalina Schist Terrane, southern California, in Evans, B.W. and Brown, E.H. eds. *Blueschists and Eclogites*: Geological Society of America Memoir 164, Geological Society of America, p. 59–75.
- Sorensen, S.S., and Grossman, J., 1989, Enrichment of trace elements in garnet amphibolites from a paleo-subduction zone: Catalina Schist, Southern California: *Geochimica et Cosmochimica Acta*, v. 53, p. 3155–3177.
- Sorensen, S.S., and Barton, M., 1987, Metasomatism and Partial Melting in a Subduction Complex - Catalina Schist, Southern California: *Geology*, v.

15, p. 115–118.

Woodford, A.O., 1924, The Catalina metamorphic facies of the Franciscan Series: University of California Publications in Geological Sciences, v. 15, p. 49–68.

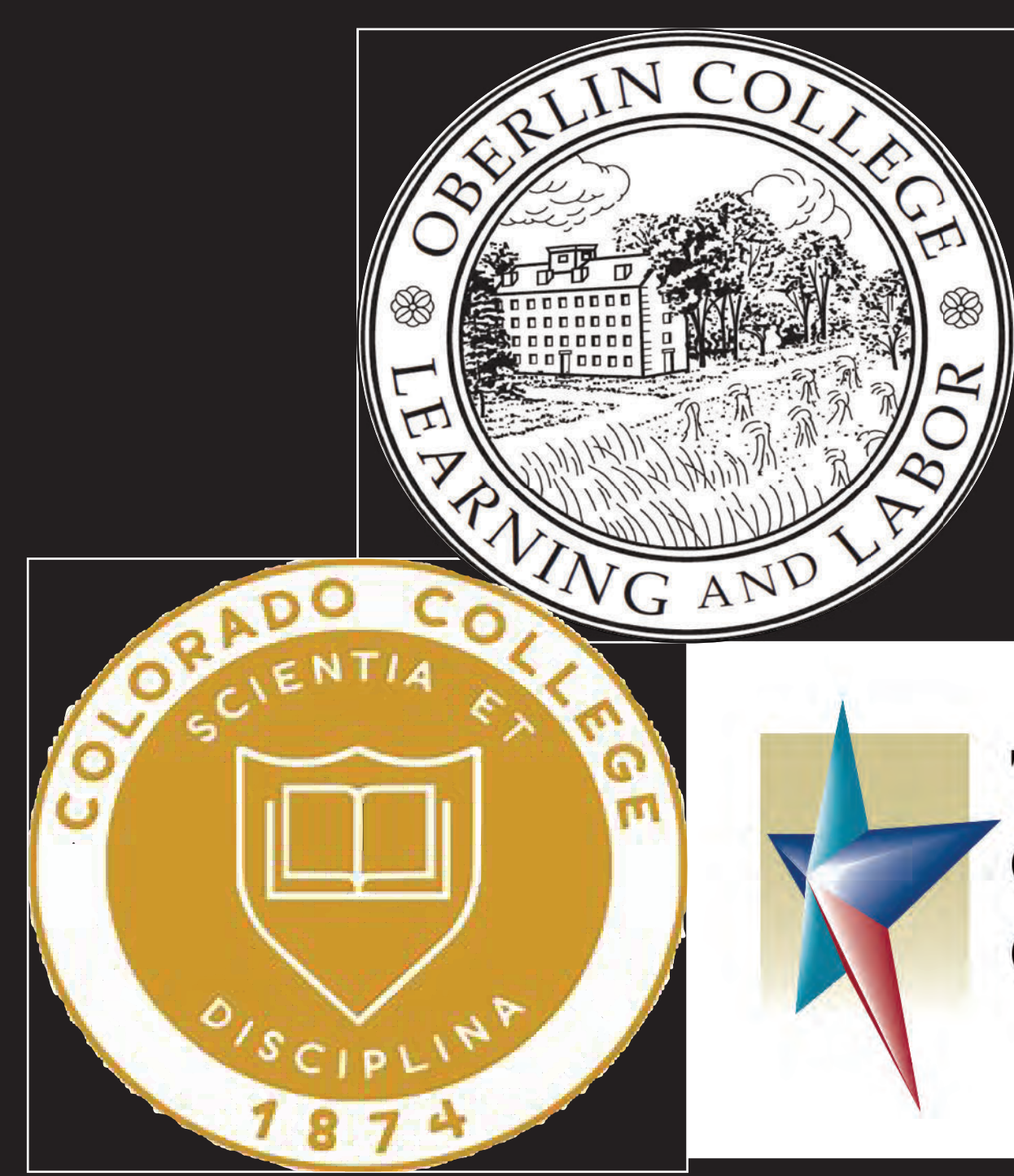
An investigation of the Catalina garnet-blueschist: Major and trace element composition and zoning in garnet and lawsonite from multiply subducted block

Blaize Adler-Ivanbrook¹, Juan P. Esparza², Sarah Hampton³, Jade Star Lackey⁴, F. Zeb Page³

¹Department of Geology, Colorado College, 14 East Cache La Poudre St. Colorado Springs, CO, 80903,

²Department of Life and Physical Sciences, Tarrant County College District, Northeast Campus 828 W. Hardwood Road, Hurst, TX, 76054-3299,

³Department of Geology, Oberlin College, 52 West Lorain Street, Oberlin, OH, 44704, ⁴Department of Geology, Pomona College, 333 N. College Way Claremont, CA, 91711



Introduction

Within the blueschist unit of Santa Catalina Island, blocks of garnet bearing lawsonite-blueschist were identified and sampled for further exploration. This specific block, found along the west coast, is approx. 155 Ma, which is older than other garnet-bearing Catalina blocks of approx. 115 Ma (Grove et al, 2008; Awalt et al, 2013). Based on existing hypotheses about this block, we investigated the possibility of the blueschist undergoing multiple subduction events.

The mineralogy of the garnet-blueschist includes (in order of abundance) glaucophane, phengite, lawsonite, garnet, and sphe, along with trace amounts of apatite, albite, rutile, quartz, zircon and barite. Additionally, the garnet end-member composition overall is 50-60mol% Almandine, 20-30mol% Grossular, 8-12mol% Pyrope, 10-15mol% Spessartine, many garnets are strongly fractured.

Major Element Analysis of Garnets

By using SEM, 8 garnets ranging from 326 μm to 1200 μm were transversed from rim to rim.

- The majority of Garnets across the three samples displayed at least minor zoning, exhibited by significant decreases in Mn/spessartine and an increase in Fe/almandine from core to rim. Minor increases in pyrope and grossular were also observed from core to rim (Fig. 5).
- During exploration, we found further evidence of changing metamorphic conditions such as zoned glaucophane, and rutile with a sphe reaction rim.
- Textural features include clearly fractured garnets, often with quartz, phengite and lawsonite growth within the cracks.
- Quartz, mica, and feldspar veins and inclusions are frequent throughout the garnets. Typically, lawsonite could be found adjacent to the garnet.

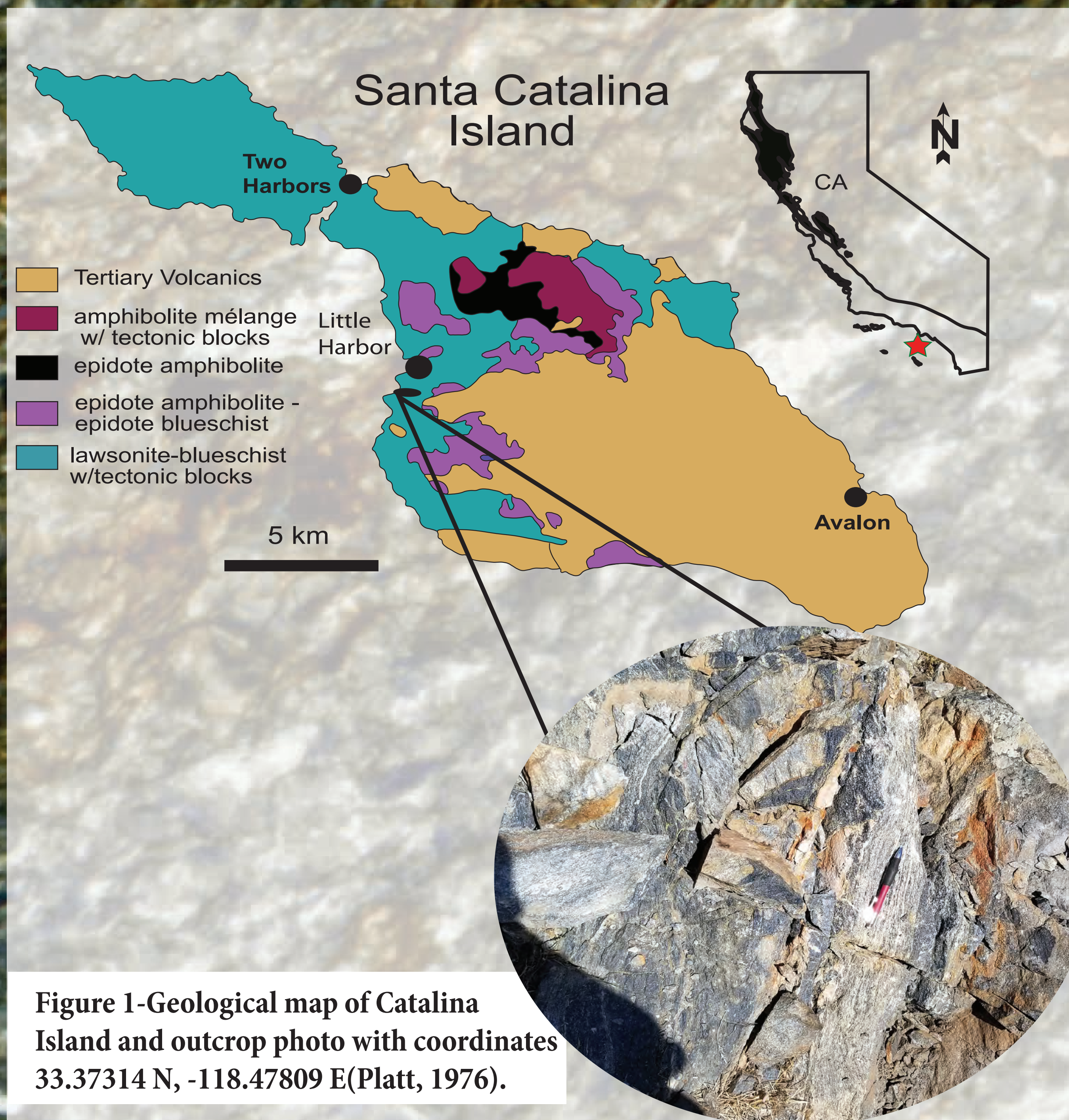
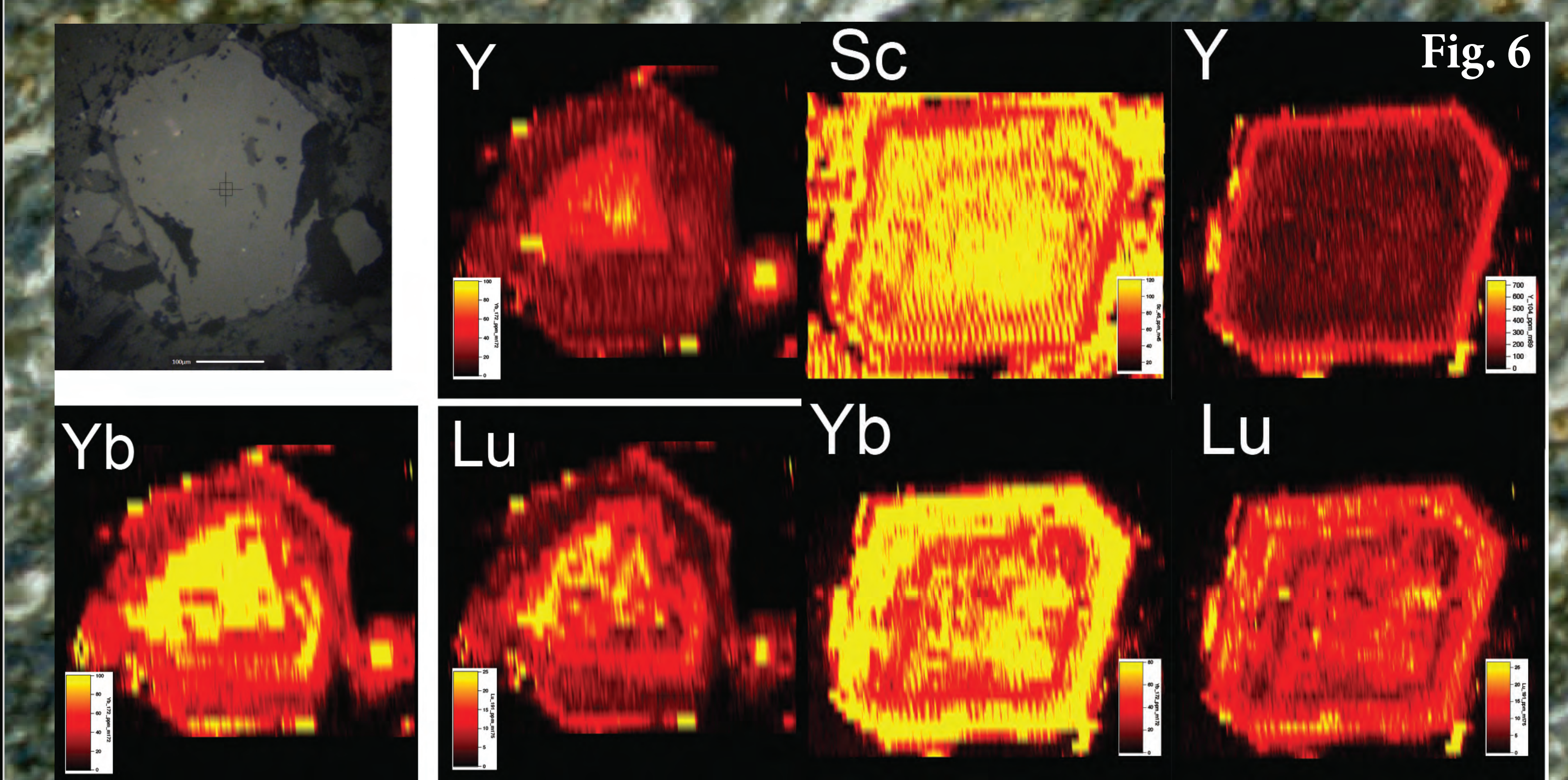
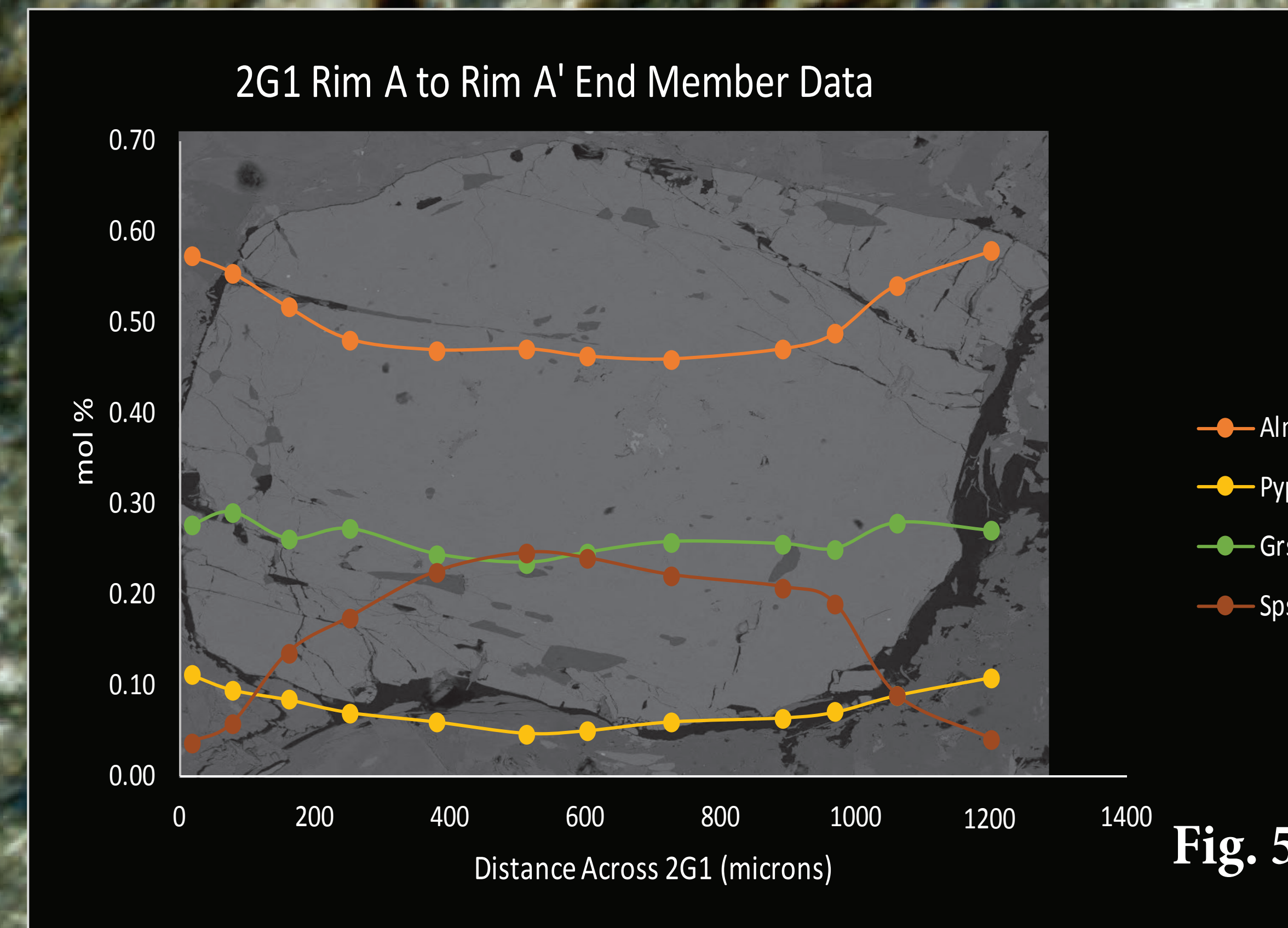


Figure 1-Geological map of Catalina Island and outcrop photo with coordinates 33.37314 N, -118.47809 E(Platt, 1976).

Methods

- Major elements were analyzed at Oberlin College with a Tescan Vega 3 Scanning Electron Microscope with an Oxford Instruments Energy Dispersive Spectrometer.

- Trace elements were analyzed in the David W. and Claire B. Oxtoby Environmental Isotope Lab, at Pomona. Samples are ablated with and ESI NWR193 ArF laser and isotopes are analyzed with an Agilent 8900 triple quadrupole ICP-MS operated in a NH₃-O₂ gas cell mode to minimize interferences among rare earth elements. Glasses NIST-612 and BCR-2 were used for standardization of trace and major elements, respectively using Al from SEM analyses as an internal standard.

- X-ray Fluorescence (XRF) was used to compare bulk chemical composition between non-garnet-bearing lawsonite blueschist and garnet bearing lawsonite-blueschist samples.

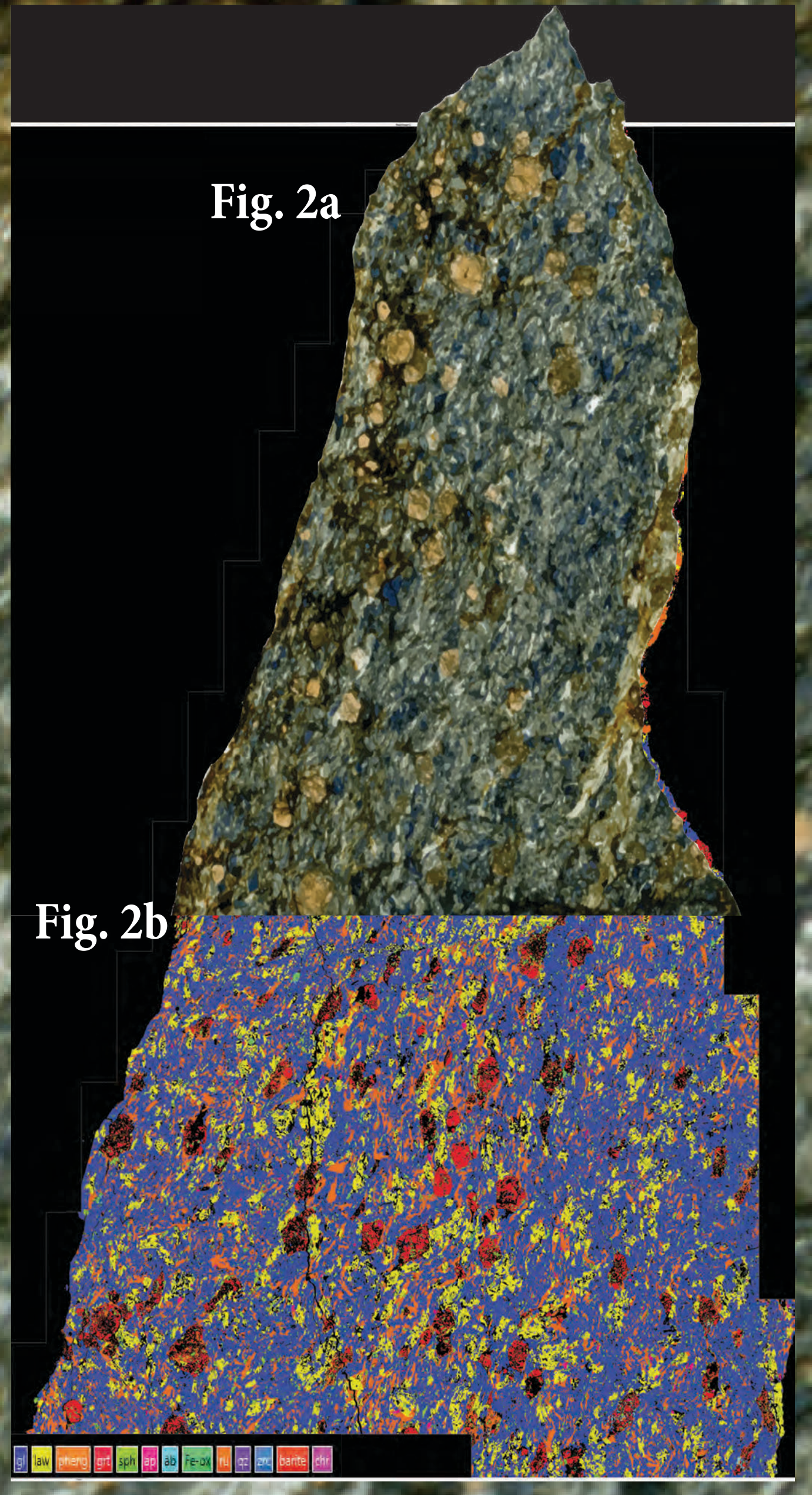


Figure 2a) Photo of thick section sample. b) Mineral identification-map of thick section sample. Figure 3a) Back-scattered electron image of fractured garnet with lawsonite and phengite crystal growth within the cracks. b) detail of same image

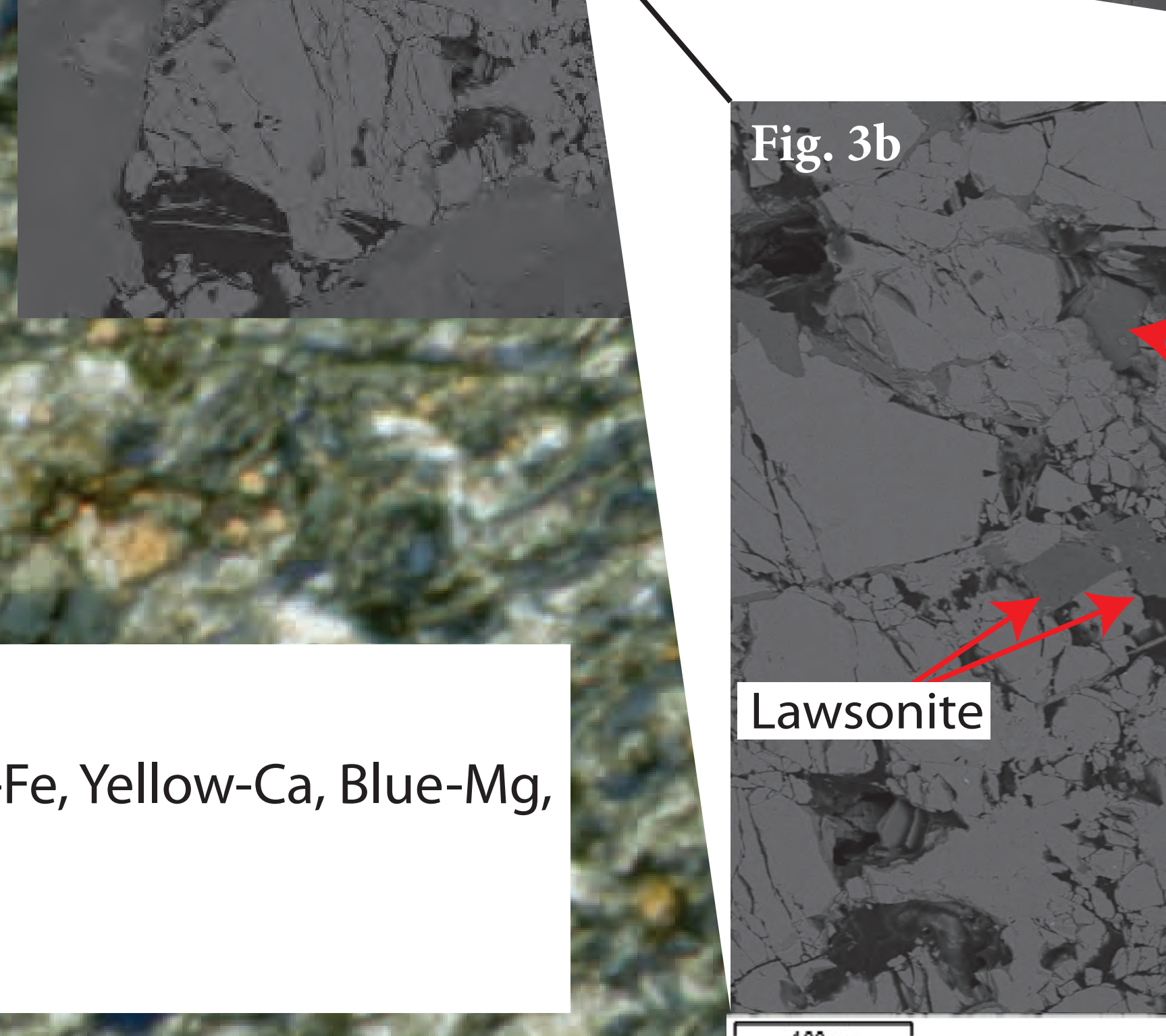
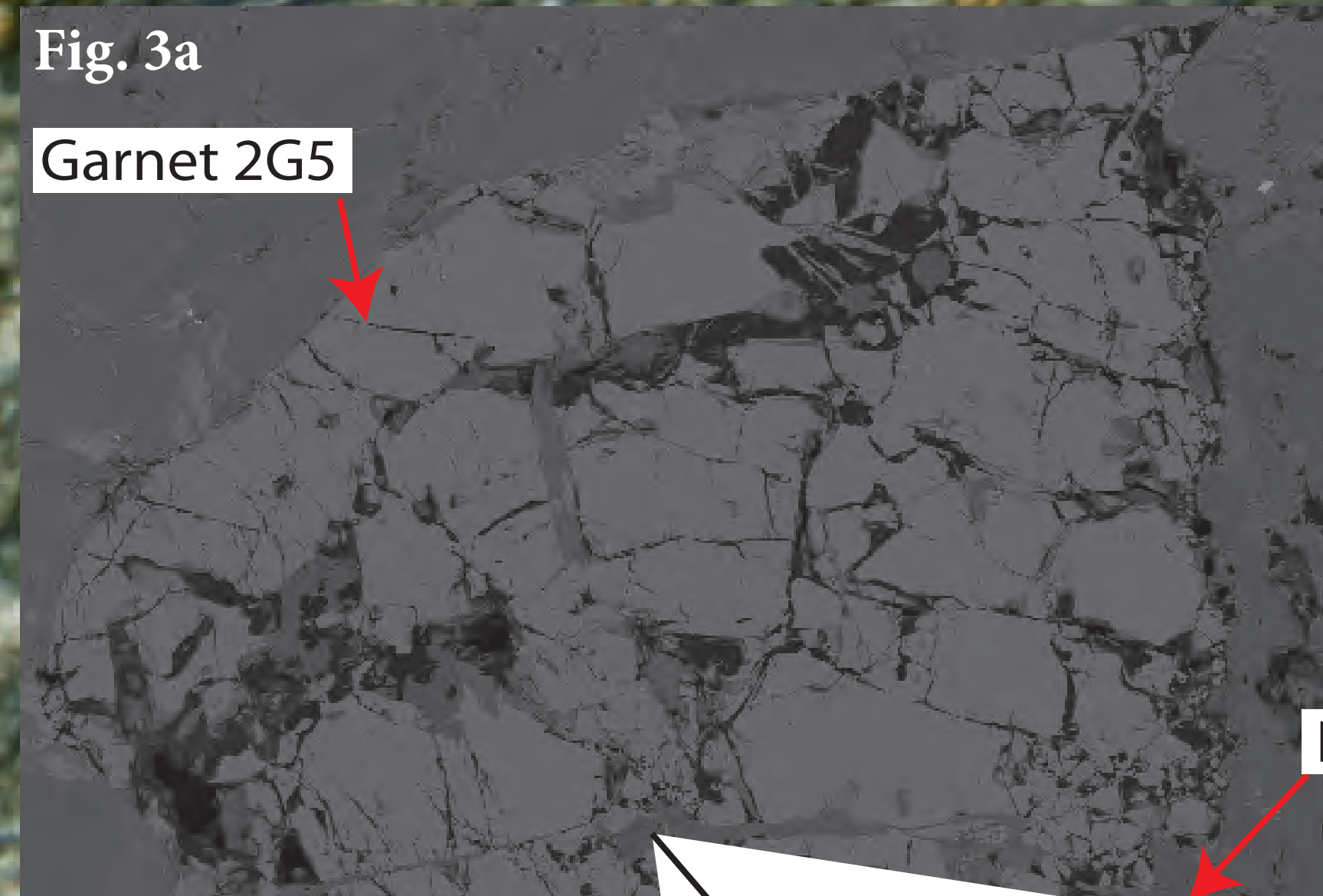
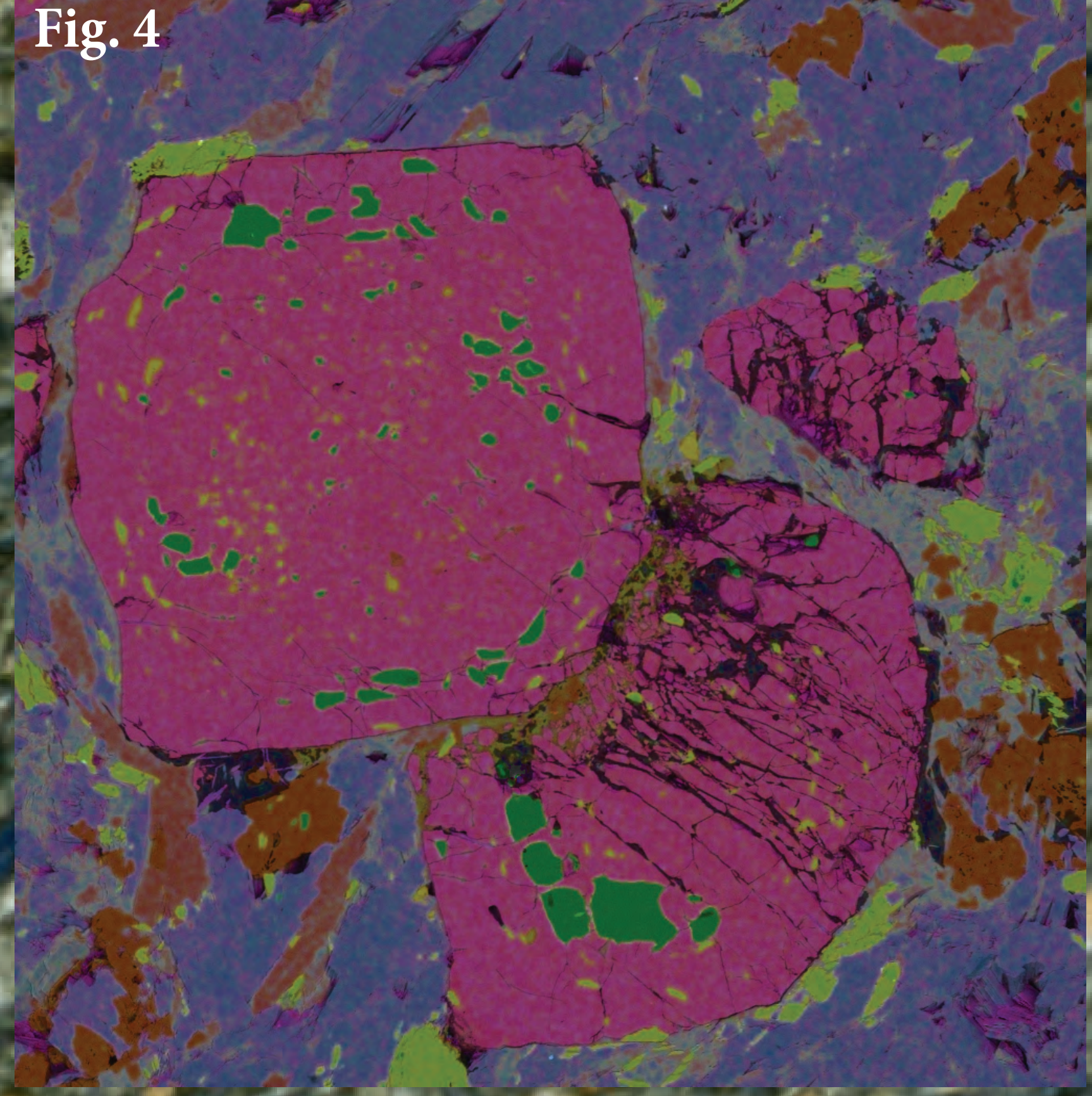


Figure 4- Elemental map of 2G6-7s. Legend: Dark Green-Si, Red-Al, Pink-Fe, Yellow-Ca, Blue-Mg, Light Green-Mn

Bulk Composition

-Overall, there are no trends or significant differences in the bulk composition of garnet-bearing and non-garnet bearing blueschist, contrary to thoughts after field observation (Fig 8, below). Thus the chemical variability across the block is unlikely the control on garnet growth.

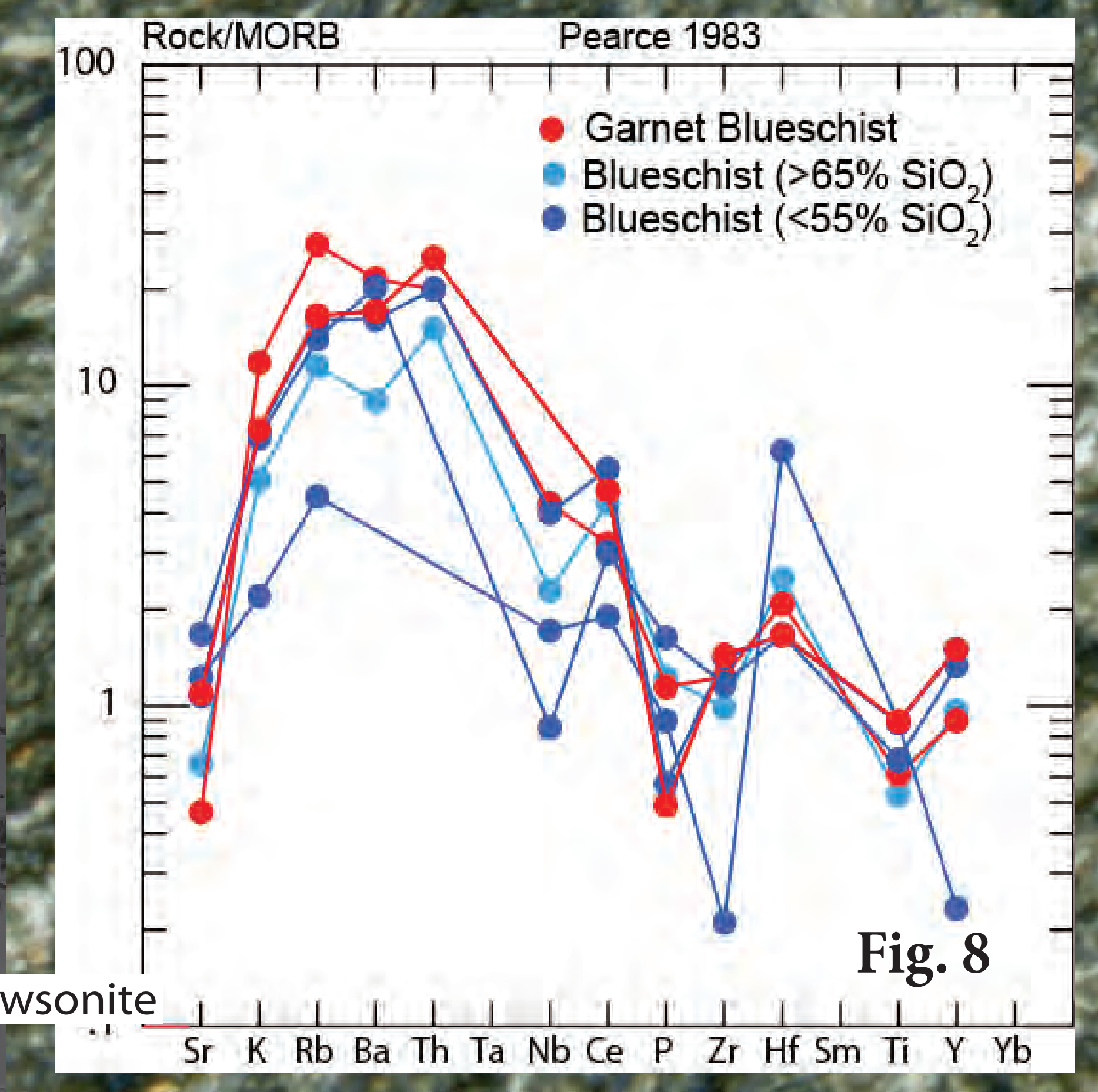


Figure 8- Using mid oceanic ridge basalt (MORB) to compare the bulk composition of garnet bearing lawsonite blueschist with non-bearing lawsonite blueschist.

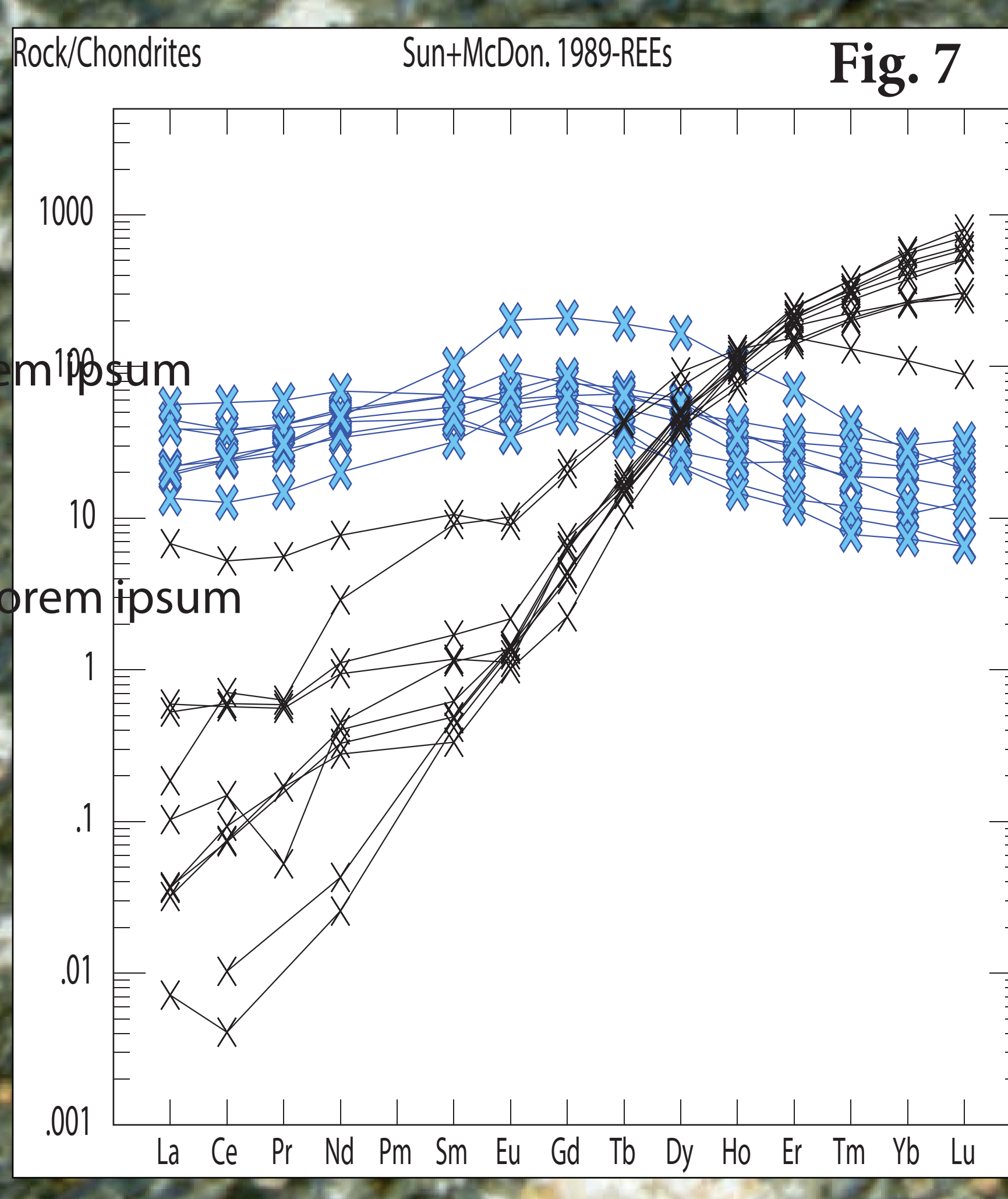


Figure 7- Comparing REE between lawsonite (blue) and garnet (black) with LA-ICP-MS system.

Figure 5- Garnet (2G1) endmember zoning measured with data obtained from EDS transverse.

Figure 6- Trace element maps displaying variation of heavy rare earth element concentration in two garnets.

Trace Element Analysis

-Major element zoning data collected with the LAICP-MS supported the SEM data obtained by traverses on the SEM.

-Lu levels -- which have previously been used in the relative growth dating of lawsonite and garnets (Mulachy, et. al, 2014) -- were similar in both garnet and lawsonite. Also, mapping displays irregular zonation rings of some trace elements (Fig. 6)

-In general, the heavy rare earth elements are more abundant in garnet than lawsonite in the blueschist (fig. 7).

Discussion and Conclusion

Evidence for multiple subduction events includes textural differences of garnets within the same sample; fragmented garnets are seen only a couple hundred microns away from untattered garnets. Lawsonite growth within cracks of garnets suggests infiltration occurred after the garnets fractured, thus placement took place during a possible second subduction event. Additionally, irregular zoning of trace elements in the garnets indicates an interruption during the garnet's growth, likely caused by a second subduction event. During the second subduction event, surrounding minerals break down releasing a new influx of heavy rare earth metals to the garnets. The lack of an overall trend in the bulk composition of garnet-bearing versus non-garnet-bearing blueschist, indicated composition of the blueschist does not affect the placement of garnet growth.

References

- Awalt, et al., 2013, New evidence for old subduction in the Catalina Schist, Santa Catalina, CA. Geological Society of America Abstracts with Programs. Vol. 45, No. 7, p. 798

- Grove, et al., 2008, The Catalina Schist: Evidence for middle Cretaceous subduction erosion of southwestern North America. Geological Society of America Special Paper 436, p. 335-361.

- Platt, J.P., 1975. Metamorphic and deformational processes in the Franciscan Complex, California: some insights from the Catalina Schist terrance. Geol. Soc. Am. Bull. 86, 1337-1347.

- Mulachy, et. al, 2014, Dating subduction-zone metamorphism with combined garnet and lawsonite Lu-Hf geochronology. Journal of Metamorphic Geology. Vol 32, p. 515-533

Acknowledgements

This study was funded by the Keck Geology Consortium and the National Science Foundation (REU1659322). The Oxtoby Isotope Lab was funded by a grant from the Moore Foundation (GBMF5417). The SEM at Oberlin College was funded by a grant from the National Science Foundation (MRI162627). Special thanks to Clara Margaret Flood, Nicollette Mitchell, Nigel McMillion, and Kyle McCarty for their help and guidance throughout the project.

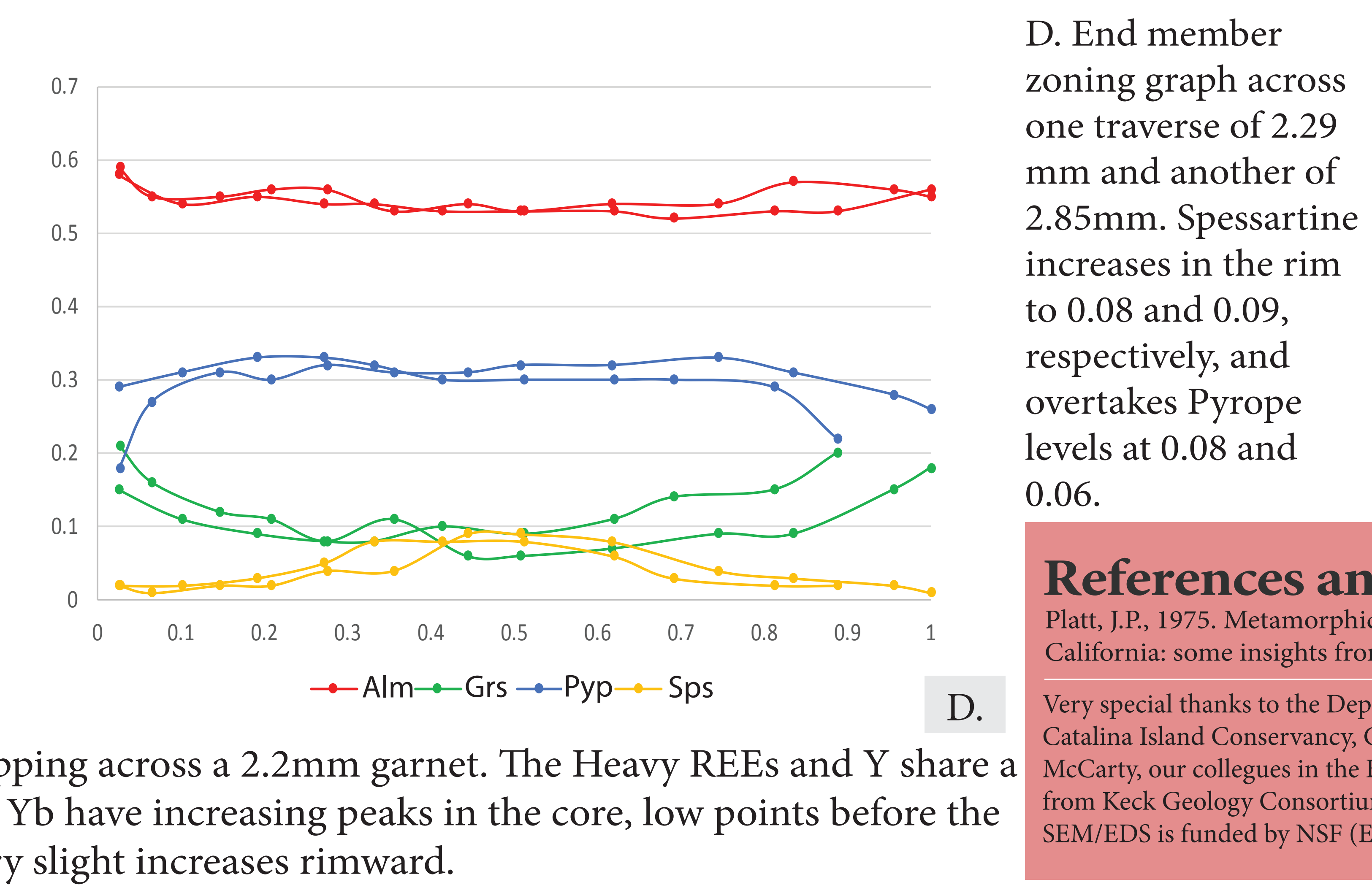
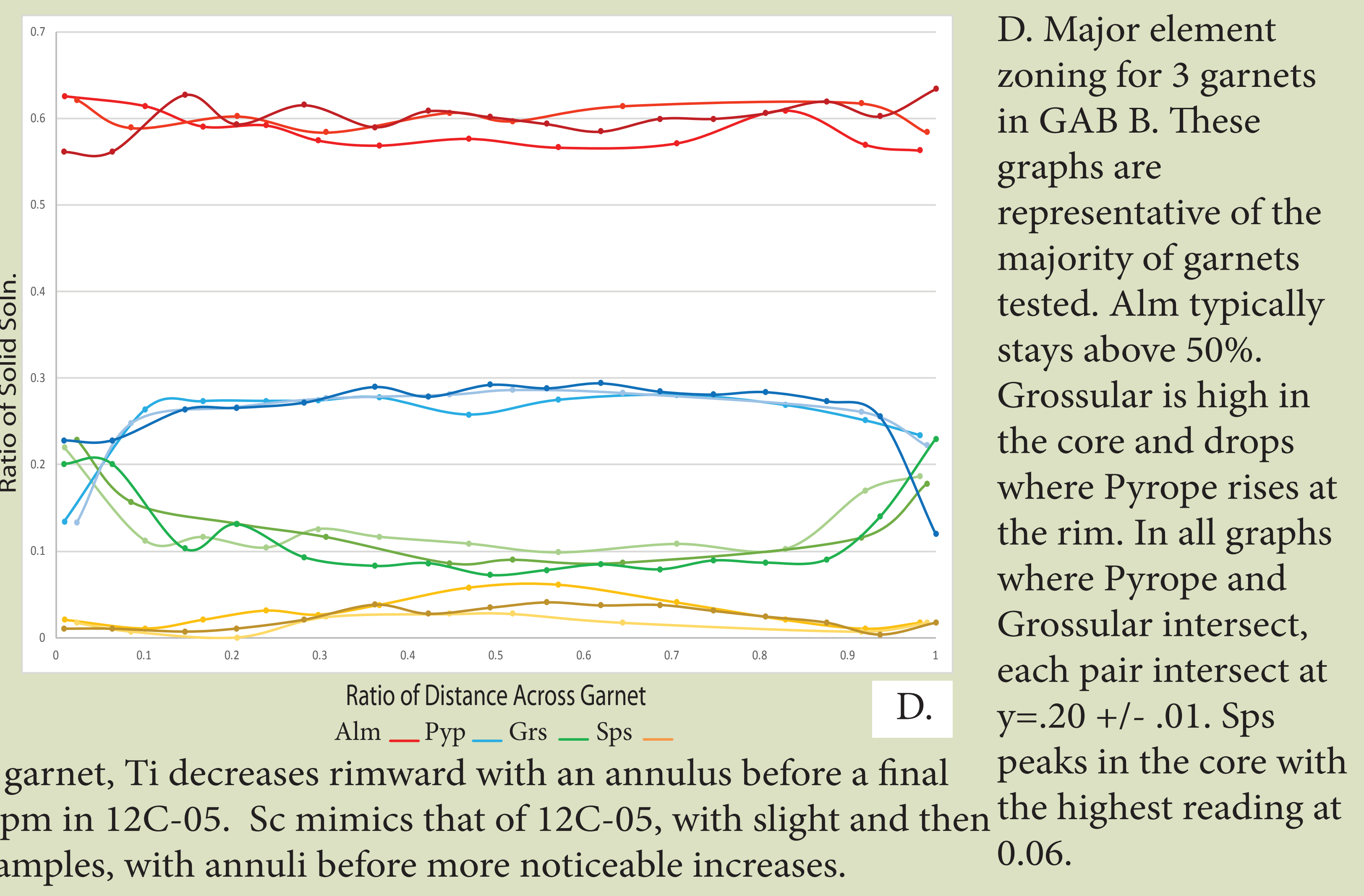
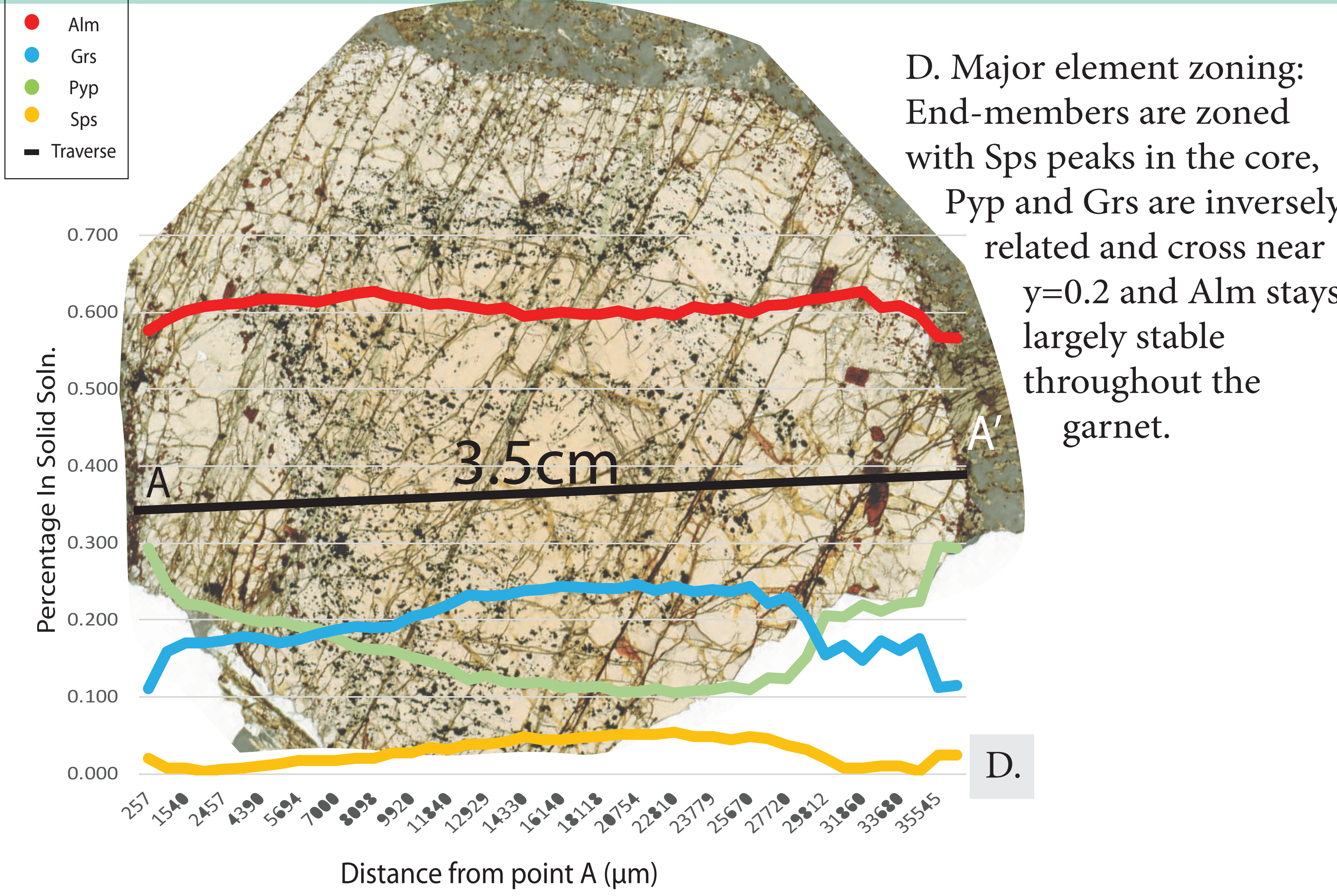
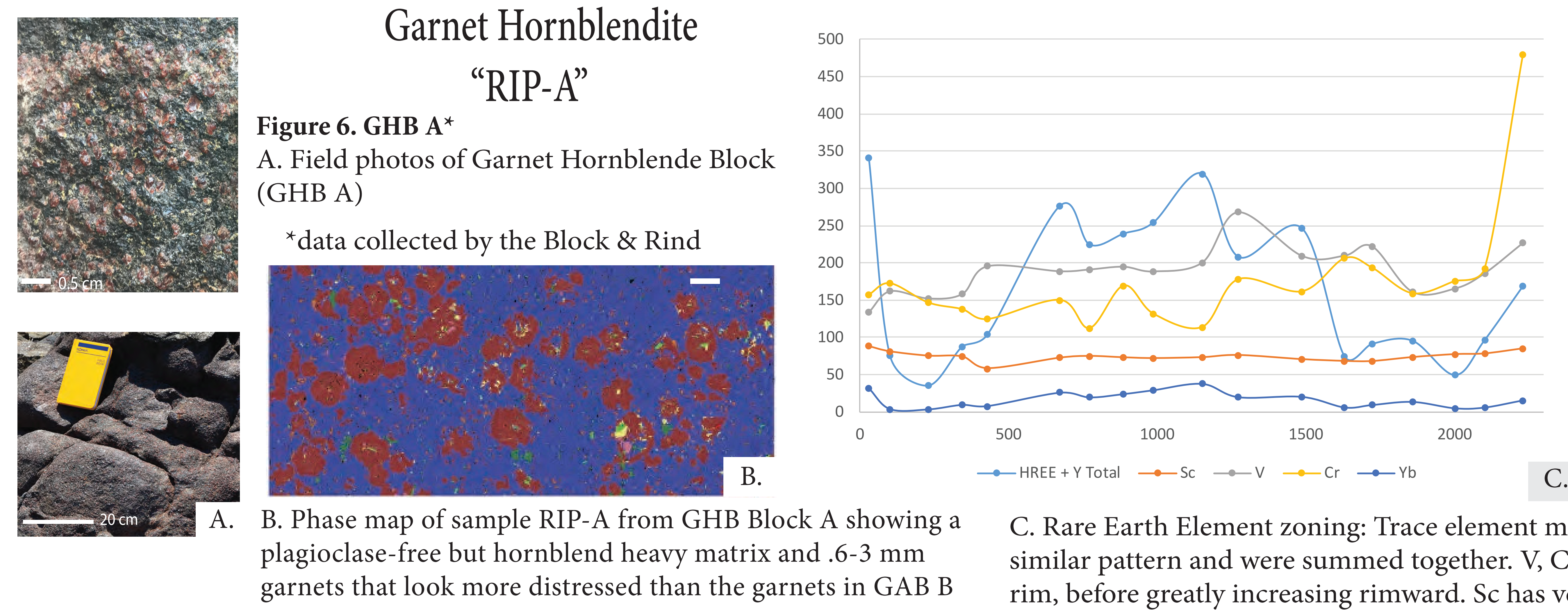
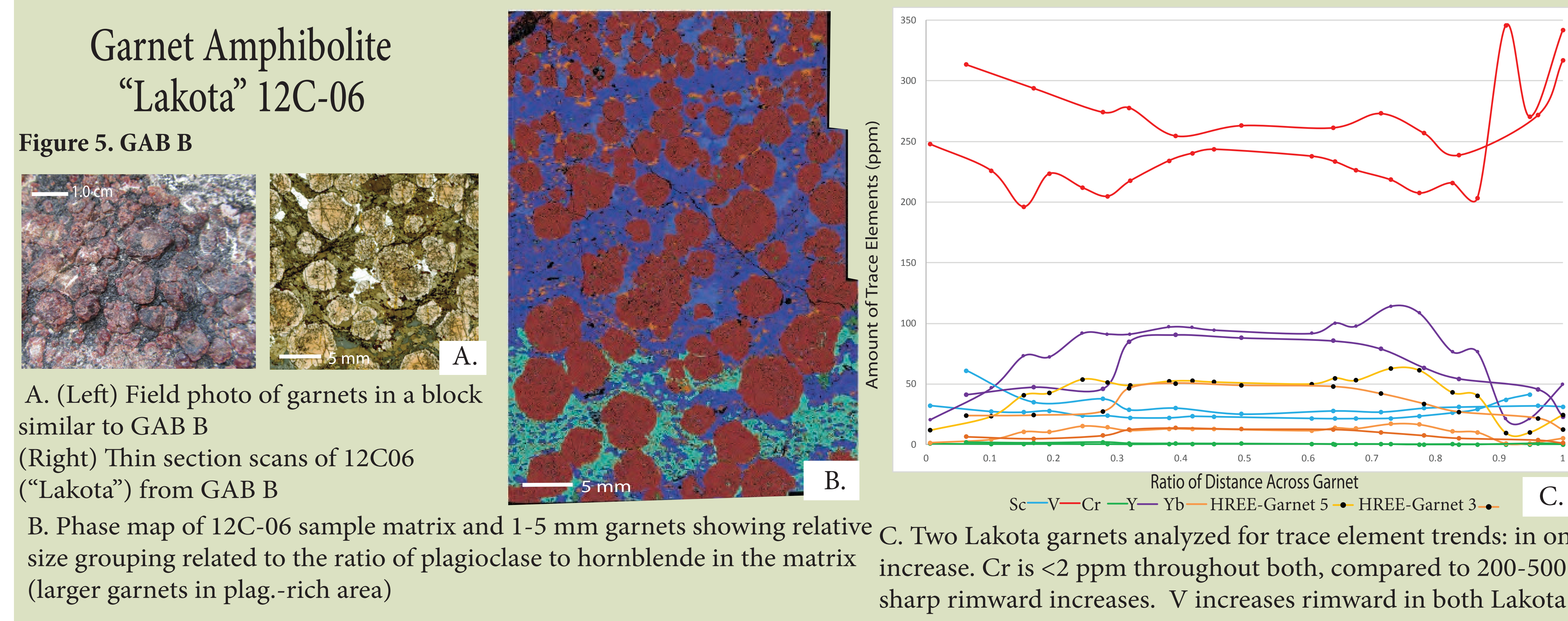
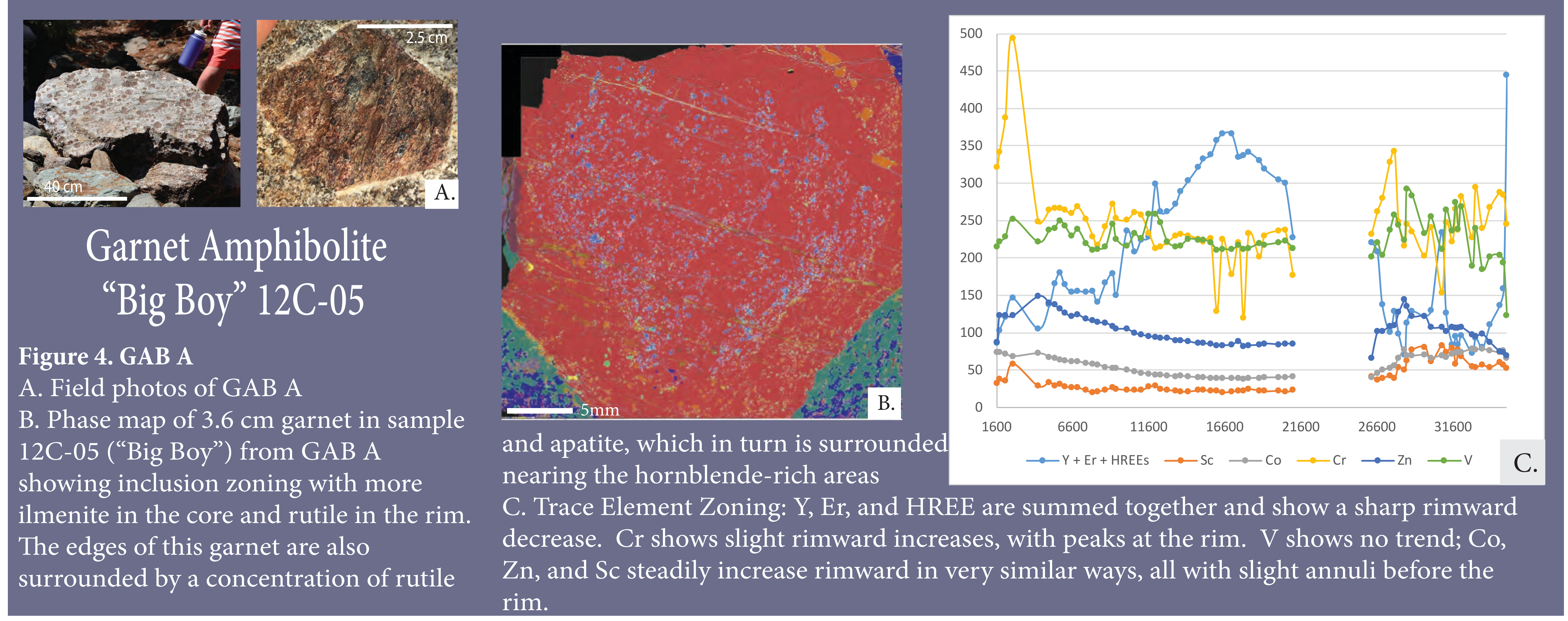
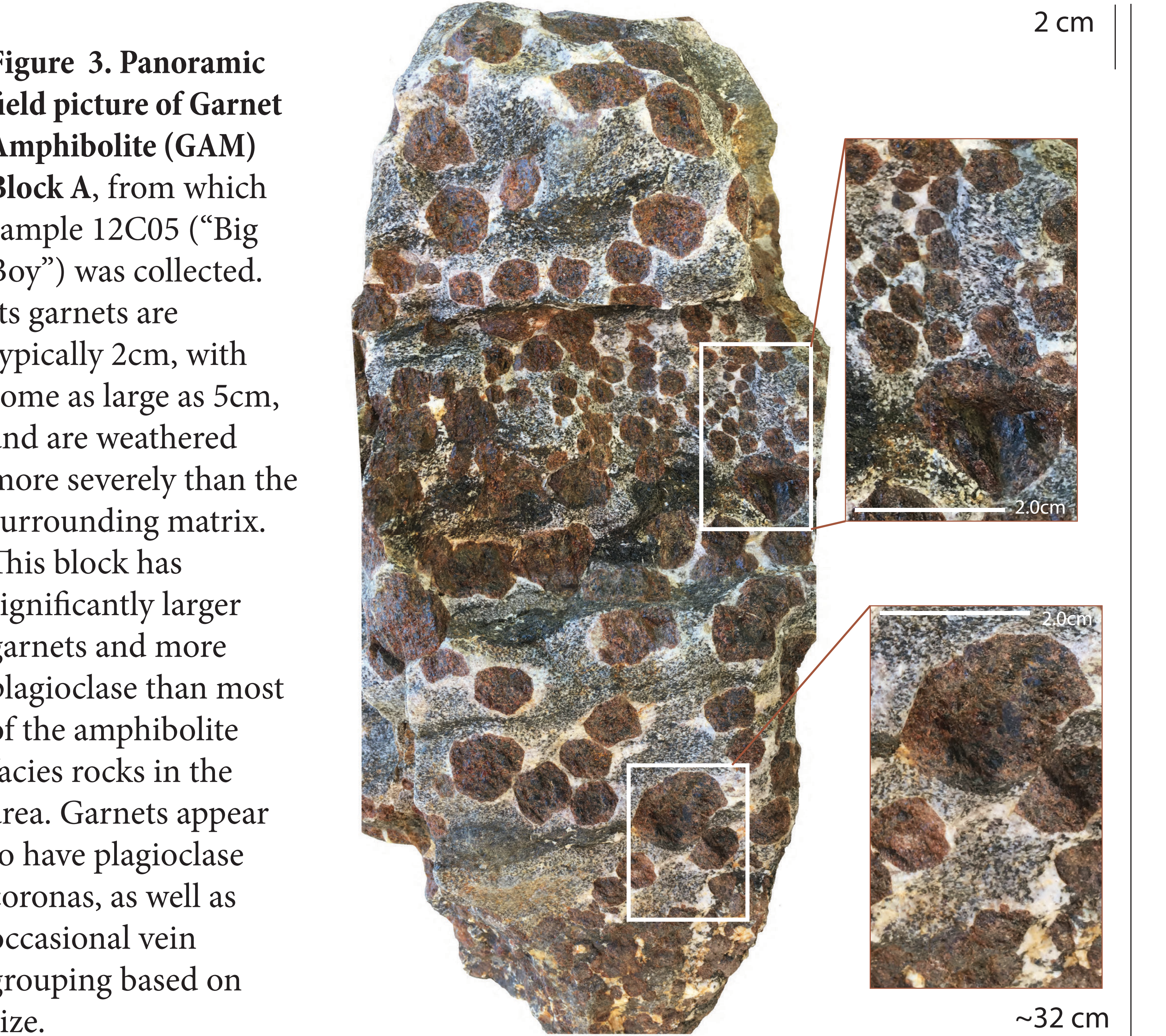
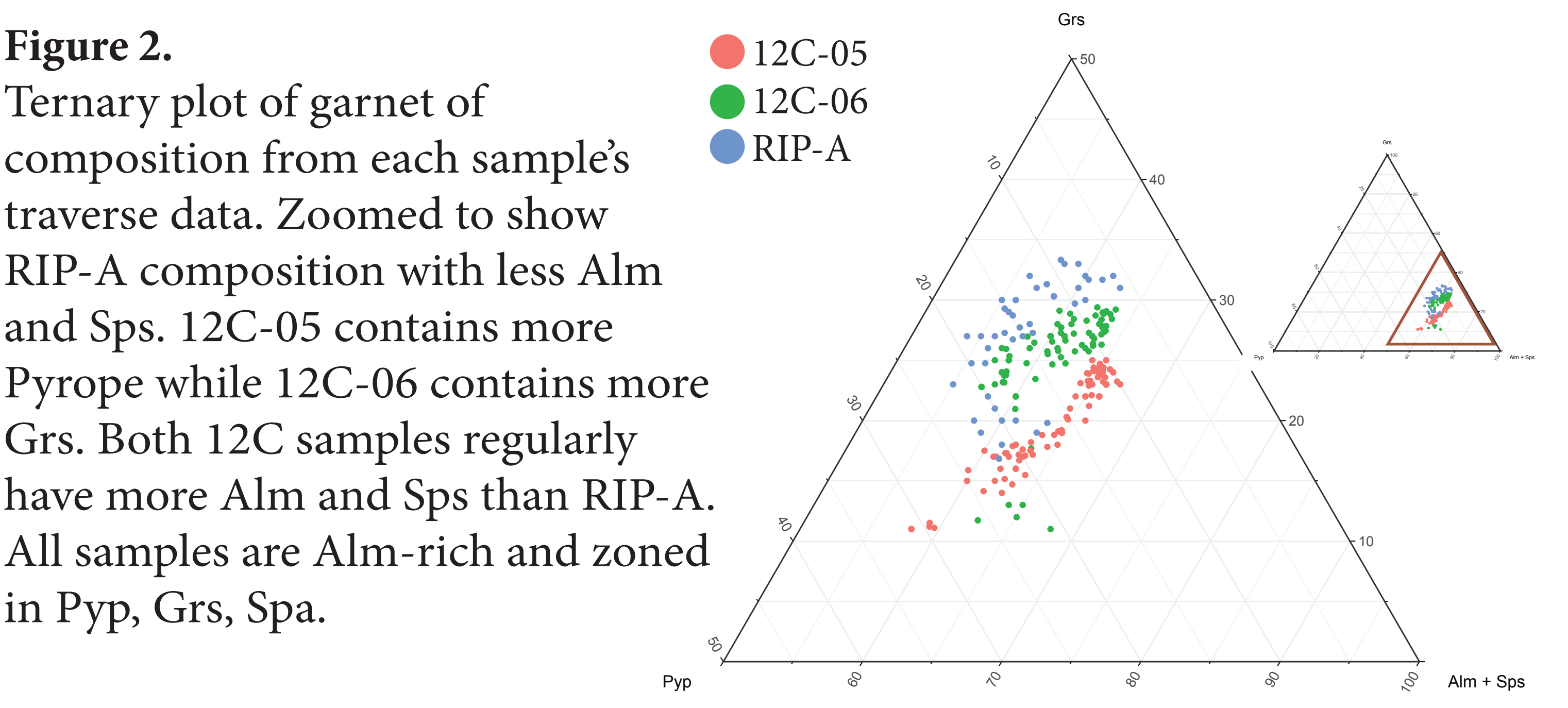
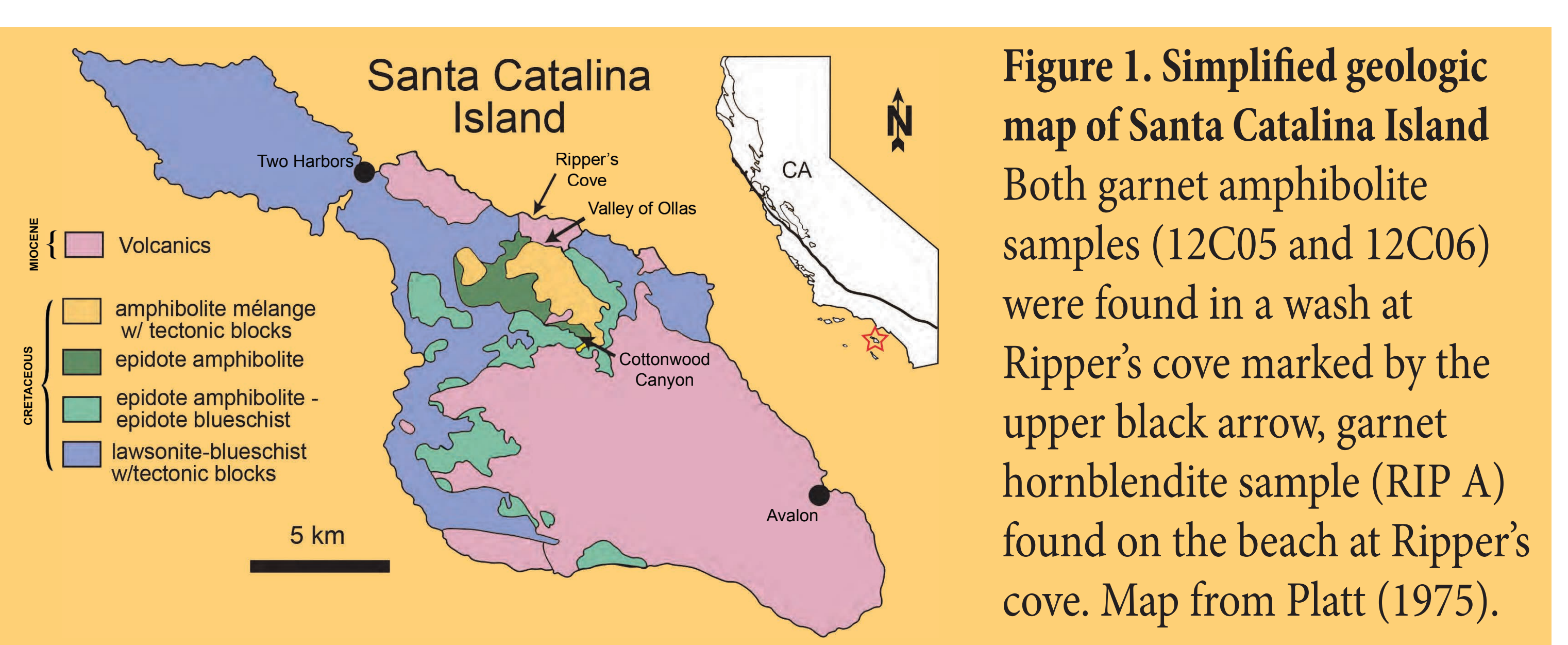
Major and Trace Element Zoning in Garnets of Unusual Size from Blocks Hosted by Ultramafic Mélange, Santa Catalina Island, California

Amani L. Canada¹, James G. Karroum II,² Lorena Paras,³ F. Zeb Page,⁴ Jade Star Lackey⁵

1. Department of Geoscience, Trinity University, One Trinity Place, San Antonio, Tx, 7212
 2. Department of Earth, Environmental, and Planetary Sciences, Rice University, 6100 Main St, Houston, Tx, 77095
 3. Department of Geology, Smith College, 1 Chapin Way, Northampton, Ma, 01063
 4. Department of Geology, Oberlin College, 173 W Lorain St, Oberlin, OH 44074
 5. Geology Department, Pomona College, 333 N College Way, Claremont, CA 91711

Introduction

Santa Catalina Island is known for the study of metamorphic mélangé in the context of subduction, and especially the role of metasomatism in creating garnet-bearing rocks. Mafic blocks in mélangé were found to have differing textures and mineral assemblages. Three samples found weathered from the amphibolite facies ultramafic mélangé in Ripper's Cove were studied: garnet-hornblende and two textures of garnet-amphibolite.



Overview

The garnet hornblende sample has 1-2 mm garnets within hornblende, rutile, and sphene, in a block and rind from Ripper's Cove. The two other samples are from plagioclase-bearing garnet-amphibolite blocks, one with mm-scale garnets, the other with garnets as large as 5 cm. SEM and BSE were used to create analyses of garnet end-members with traverses of up to forty points. LAICP-MS was used to generate trace element analyses using traverses of up to seventy points and up to twenty-eight elements. Garnets from the garnet-hornblende block have zoning from cores (Alm₅₀Pyp₃₀Grs₁₀Sps₁₀) to rims (Alm₅₅Pyp₂₀Grs₂₀Sps₅). Trace element analysis of a garnet shows Y + HREE; Cr; Zn; Co; and Sc decreasing towards annuli and then increasing rimward. A sample from a Ripper's Cove garnet amphibolite grades from larger garnets in a plagioclase matrix to smaller garnets in hornblende. Major element traverses of 3-5 mm garnets yield Alm₅₉Pyp₈Grs₂₈Sps₅ in cores, Alm₆Pyp₁₂Grs₂₆Sps₁ in annuli, and Alm₆₀Pyp₂Grs₁₀Sps₂ in rims. Garnet inclusions include ilmenite, sphene, rutile, and apatite. Rimward decreases in Grs and increases in Pyp may be from consumption of nearby Ca early in formation, causing Mg to be used next. Rimward Sps increases may indicate resorption of Mn late in formation. The core of a 3.6 cm garnet from ultramafic mélangé (Alm₆₀Pyp₁₁Grs₂₄Sps₅) contains many ilmenite inclusions. Its annulus is Alm₆₁Pyp₂₁Grs₁₇Sps₁, and rim is Alm₅₇Pyp₂₉Grs₁₂Sps₂ with many rutile inclusions. Many late chlorite veins run through it. HREE decrease rimward, usually by over 50% and with sharp contrast between core and rim; MREE follow the same pattern, in lower ppm. Y notably is 275 ppm at core and ~75 at rim. Sc, Co, and Zn slightly increase rimward. Similar major and trace element zoning patterns across different textures and lithologies of Catalina mafic rocks suggest similar histories and conditions of formation.

References and Acknowledgements
 Platt, J.P., 1975. Metamorphic and deformational processes in the Franciscan Complex, California: some insights from the Catalina Schist terrane. Geol. Soc. Am. Bull. 86, 1337-1347.
 Very special thanks to the Departments and Facilities at Pomona College and Oberlin College, the Catalina Island Conservancy, Clara Margaret Flood and Nicolette Mitchell, Nigel McMillon, Kyle McCarty, our colleagues in the Block & Rind group, the Oxtoby Isotope Lab at Pomona, and funding from Keck Geology Consortium (National Science Foundation grant: 1659322). The Oberlin SEM/EDS is funded by NSF (EAR 1626271)

Major and trace element analysis of garnet crystals from a hornblende block and rind on Santa Catalina Island, CA: Insights into metasomatic processes in subduction mélangé

Nathaniel Bess¹, Eric Hasegawa², Paige Voss³, Jade Star Lackey³, and F. Zeb Page⁴

¹Department of Earth and Environment, Franklin and Marshall College, Lancaster, PA 17604-3003, ²Department of Geology, Amherst College, 11 Barrett Hill Dr, Amherst, MA 01002-5000
³Department of Geology, Pomona College, 185 E. 6th St, Claremont, CA 91711, and ⁴Department of Geology, Oberlin College, 52 West Lorain Street, Oberlin, OH 44074

Overview

Santa Catalina Island off of the coast of southern California is iconic for demonstrating subduction and metasomatic processes. The subject of this study is a tectonic block from the amphibolite facies mélangé which is located in Ripper's Cove on the island. This block and its rind are unusual due to the amount of the rind which remains visible and the existence of garnets within this rind. As a result, it has been the subject of previous studies including major element analysis (Penniston-Dorland et al., 2014, Chem.Geo.) and oxygen isotope analysis (Leung et al., 2016, GSA Abstr). Here analysis of garnet zoning patterns, inclusions, and trace elements are used to further understand these metasomatic processes.



Figure 3. A. Garnet hornblende block (yellow star) with garnet-bearing actinolite-rich rind (red star). Field notebook is 19cm long. B. Detail of garnet-rich block (bottom of image) to garnet-poor rind transition. Coin is ~2.5cm in diameter.

Major Element Zoning

Analysis of major element concentration was completed using Tescan Vega 3 SEM Oxford EDS system.

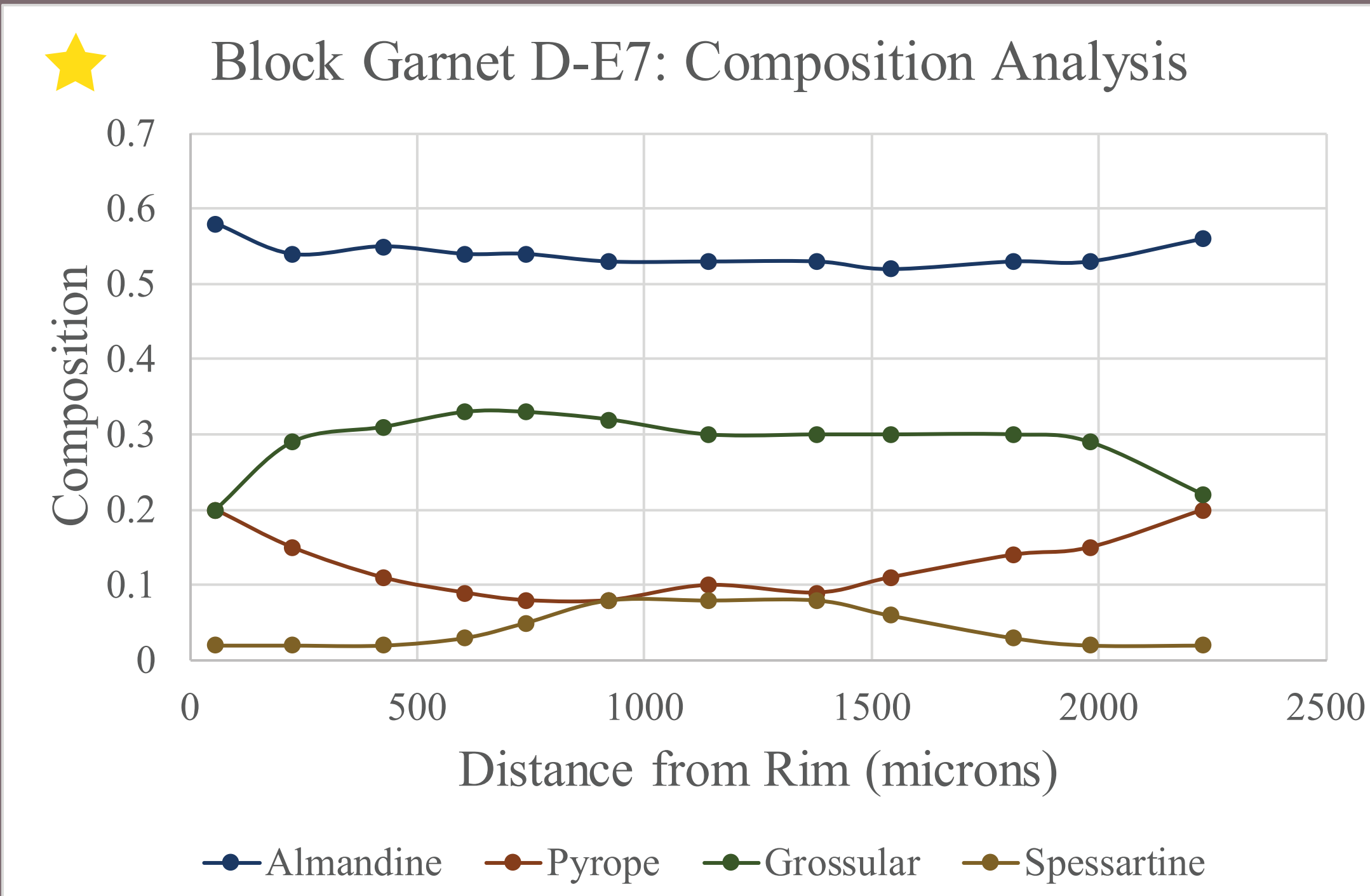


Figure 5. Prograde major element zoning found in block garnet crystals.

Trace Element Zoning

Analysis of trace element concentrations was completed using laser ablation ICP-MS on an Agilent 8900 in ammonia-oxygen gas blend mode.

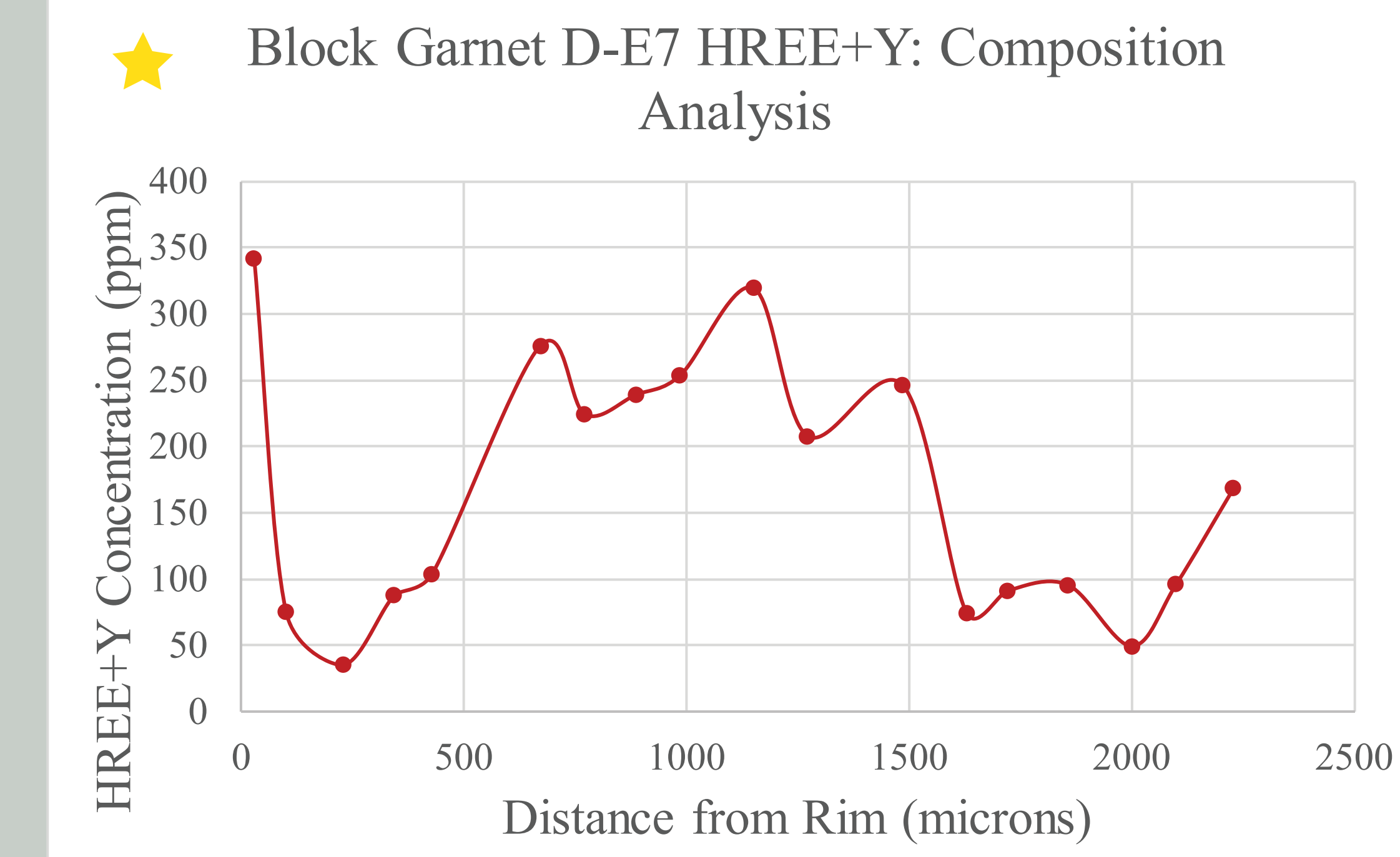


Figure 8. HREE+Y is elevated in block garnet cores and rims, occasionally with intermediate annuli.

Discussion and Conclusion

The different scales of the trace element data for the block and large rind garnet crystals are likely a product of heterogeneous distribution of HREE throughout the entire block. The major and trace element findings indicate that this block and rind experienced three metamorphic events. The first formed garnet crystals in a mafic rock (presumably during subduction), the second formed a reaction rind that traps some of the garnet crystals from the first metamorphism, and the third formed new garnet crystals (and rims on relict garnet crystals) in the rind. The composition of this block is very similar to another block with unusually large garnet crystals that a fellow group in this Keck project researched, indicating a common mafic origin. Overall, this analysis provides a platform for further understanding not only the history of Santa Catalina Island, but also the geochemical interactions of blocks in subduction zone mélanges.

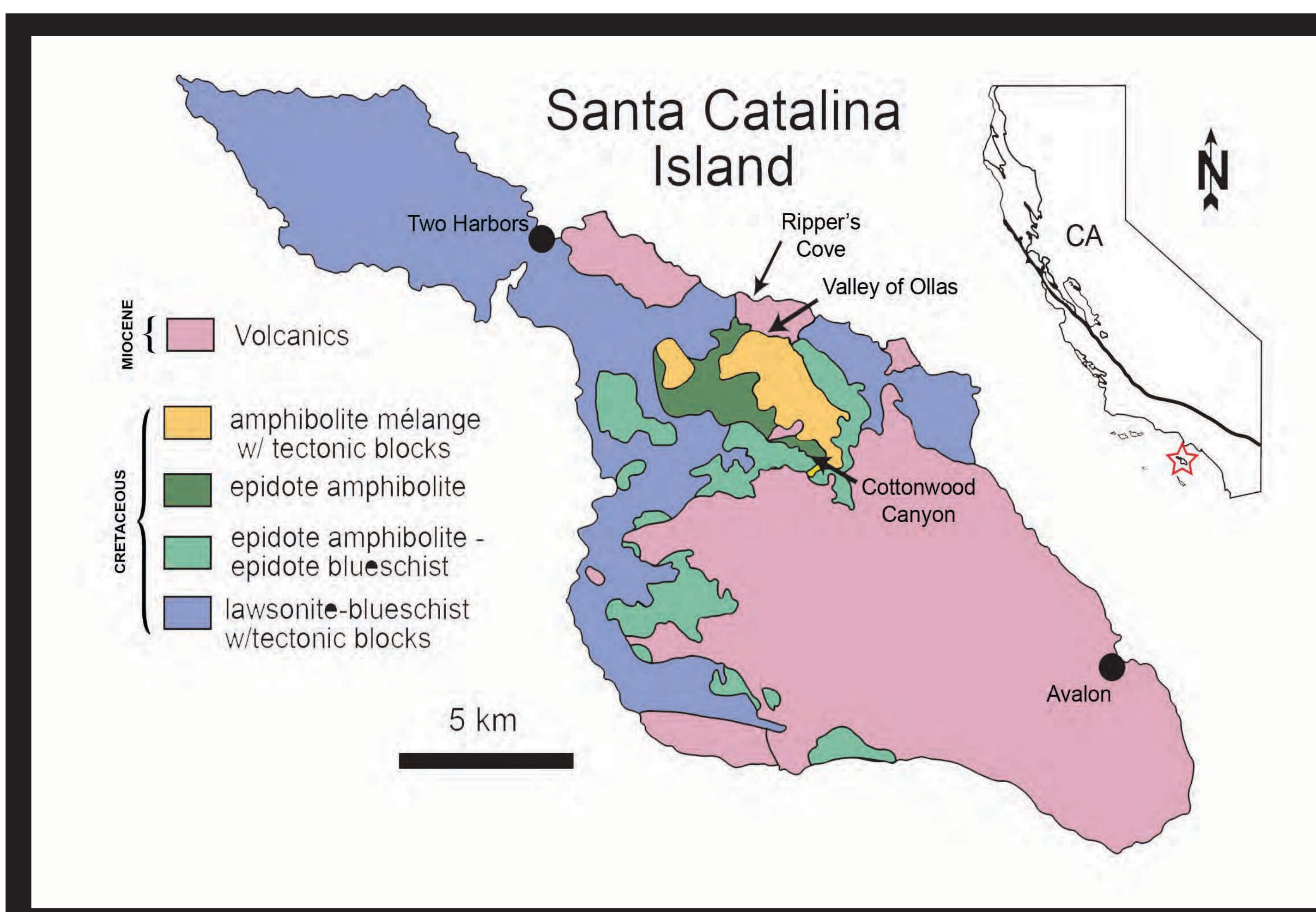


Figure 1. Map of Catalina Island, located off the coast of Los Angeles, California (after Platt, 1975). The block and rind we studied was found as float on the beach at Ripper's Cove.

Figure 4. Ternary diagram of garnet crystal major elements in block and rind. The rind contains abundant ~200mm-scale small garnet crystals and rare ~2mm-scale larger garnet crystals.

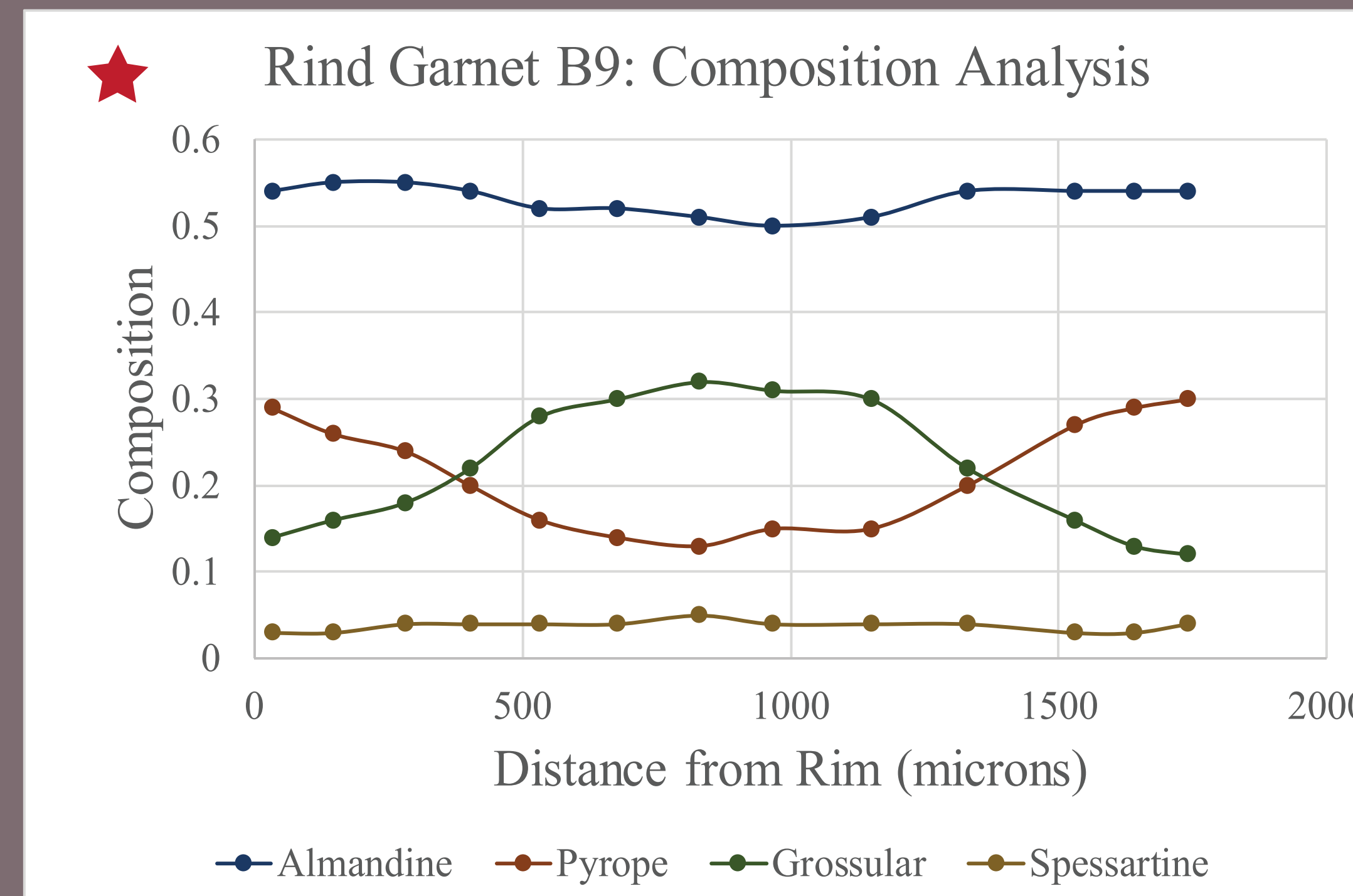
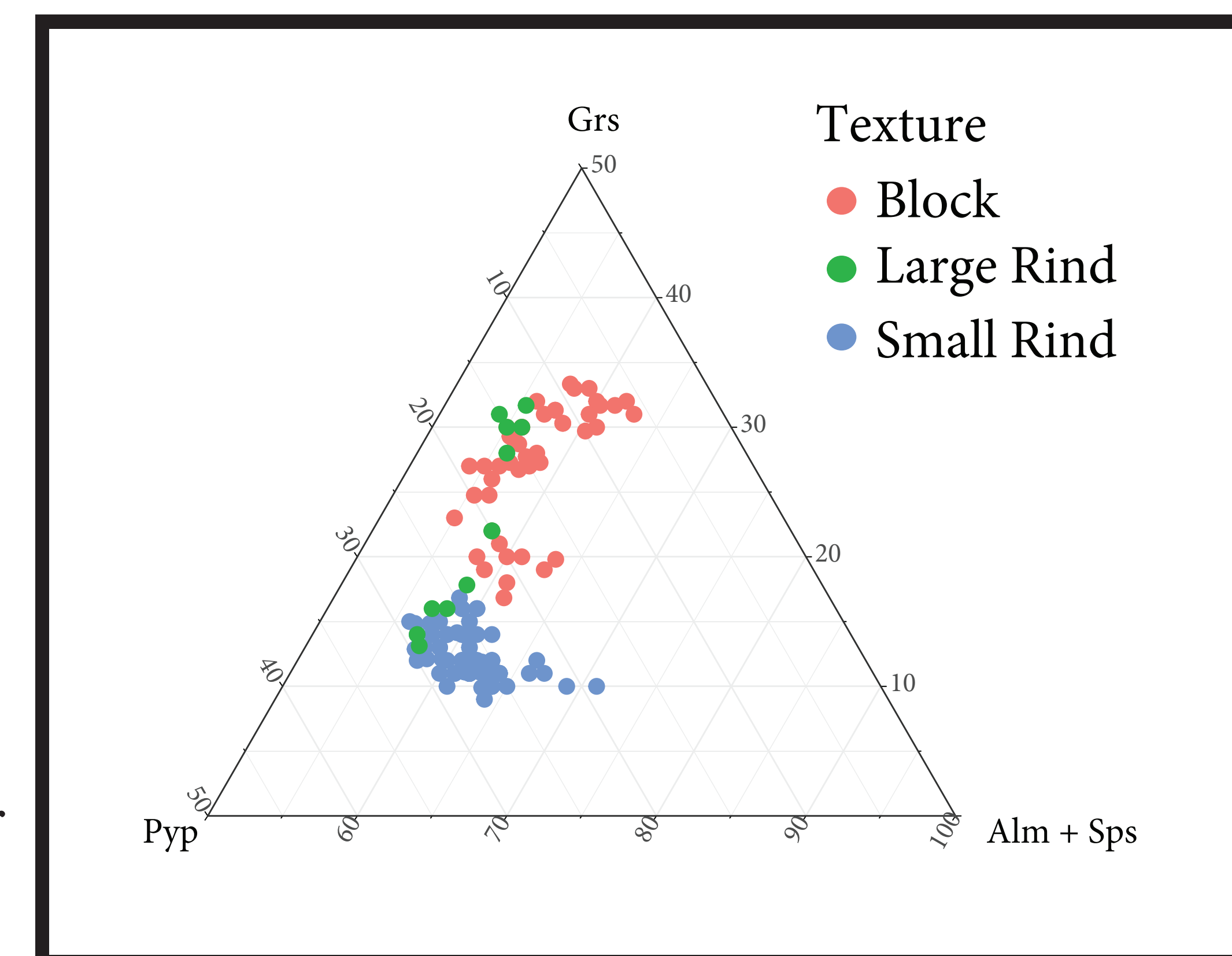


Figure 6. Large rind garnet cores resemble block garnet cores, but zoning in rims is extended to lower Ca and higher Mg compositions.

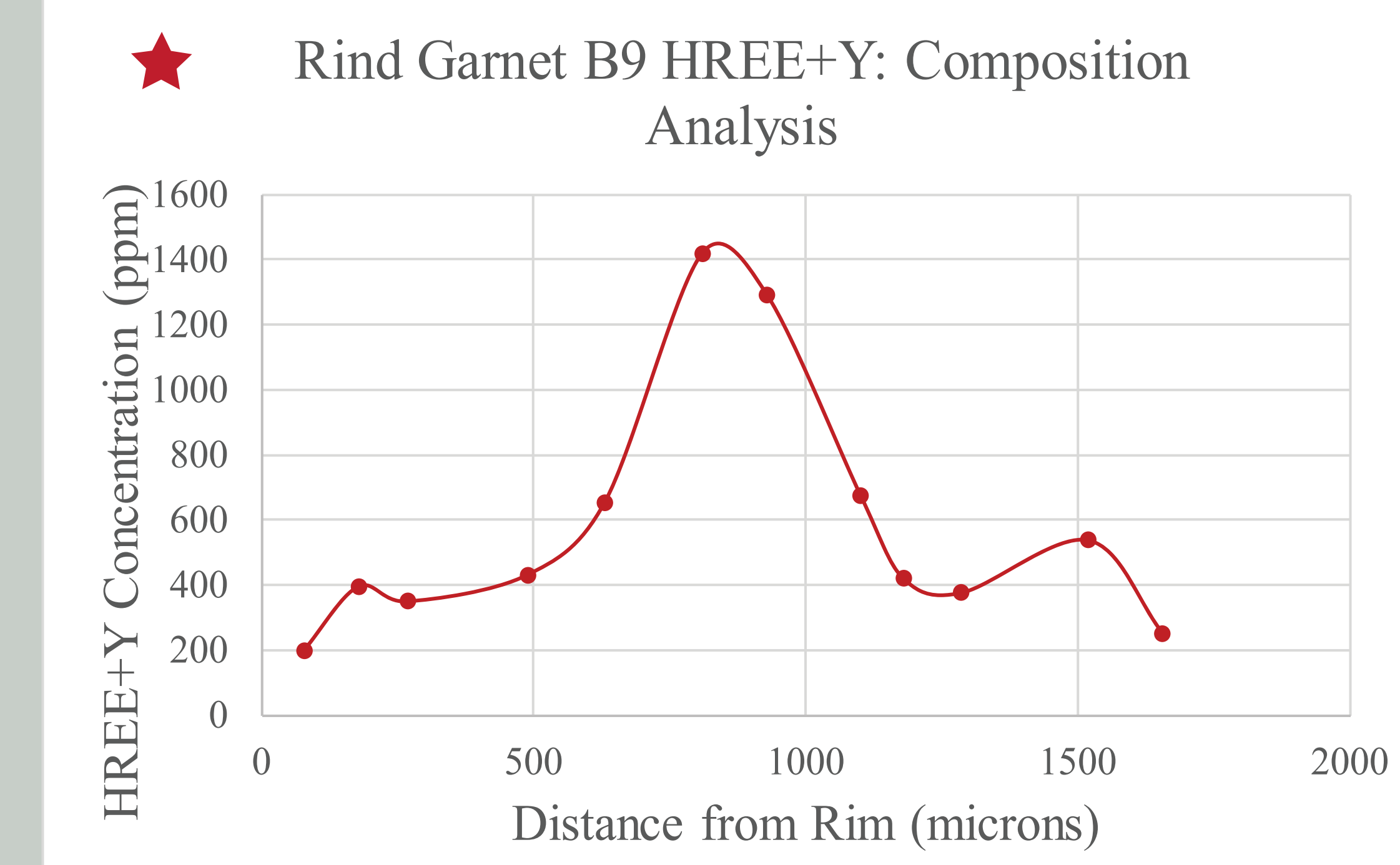


Figure 9. Large rind garnet crystal has similar HREE+Y peak in its core, but with greater concentrations, and an annulus near the rim.

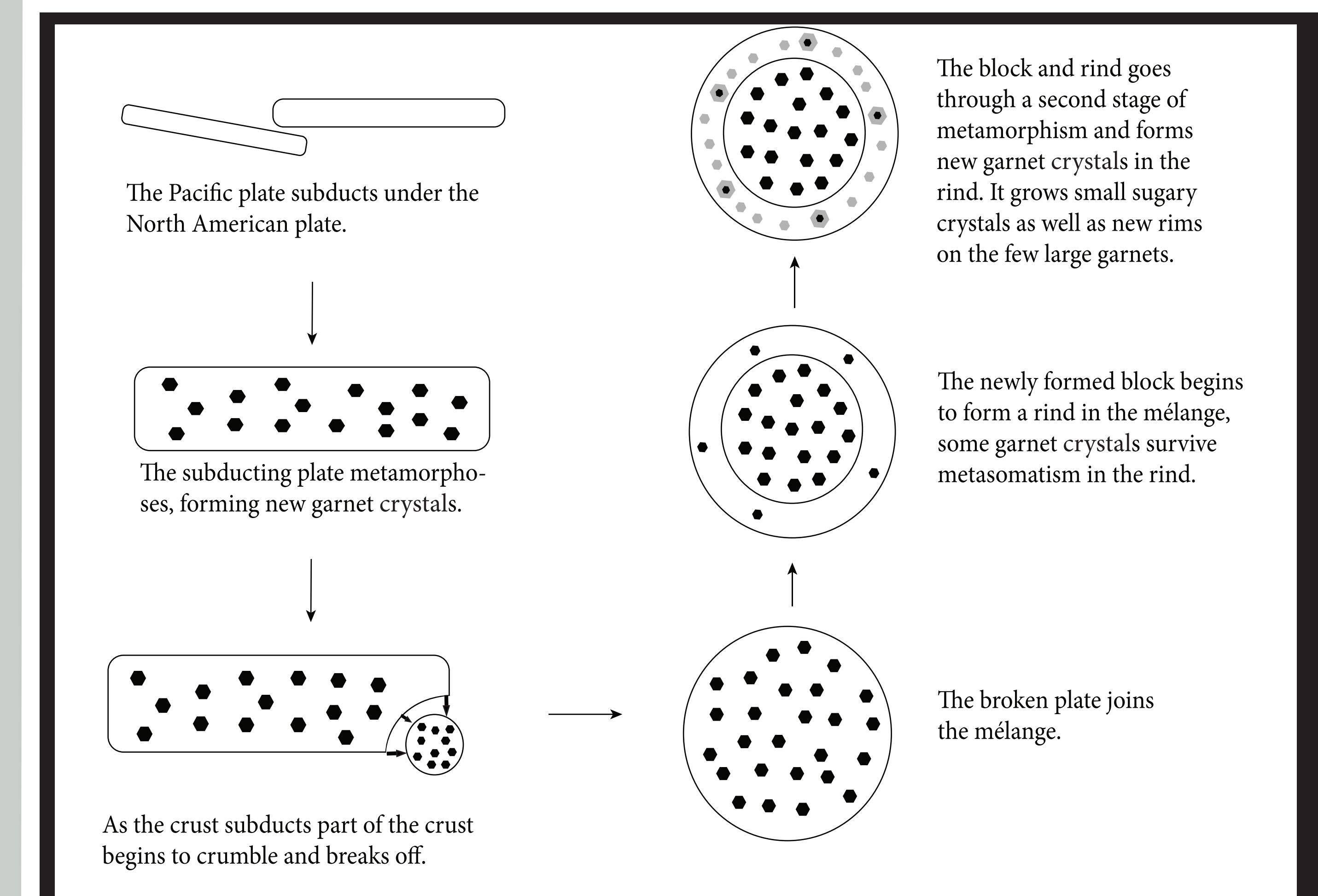


Figure 11. Schematic diagram illustrating the path of the block through the mélangé.



Figure 2. A. Backscattered electron mosaic of the rind sample RIPC. The samples has clearly defined sugary garnet crystal veins, indicated by an orange box. Garnet crystal RIPC-B9 is indicated by a green box. B. SEM zoning map of calcium in garnet crystal RIPC-B9. Calcium is concentrated in the center. C. SEM zoning map of magnesium in the same garnet crystal on sample RIPC.

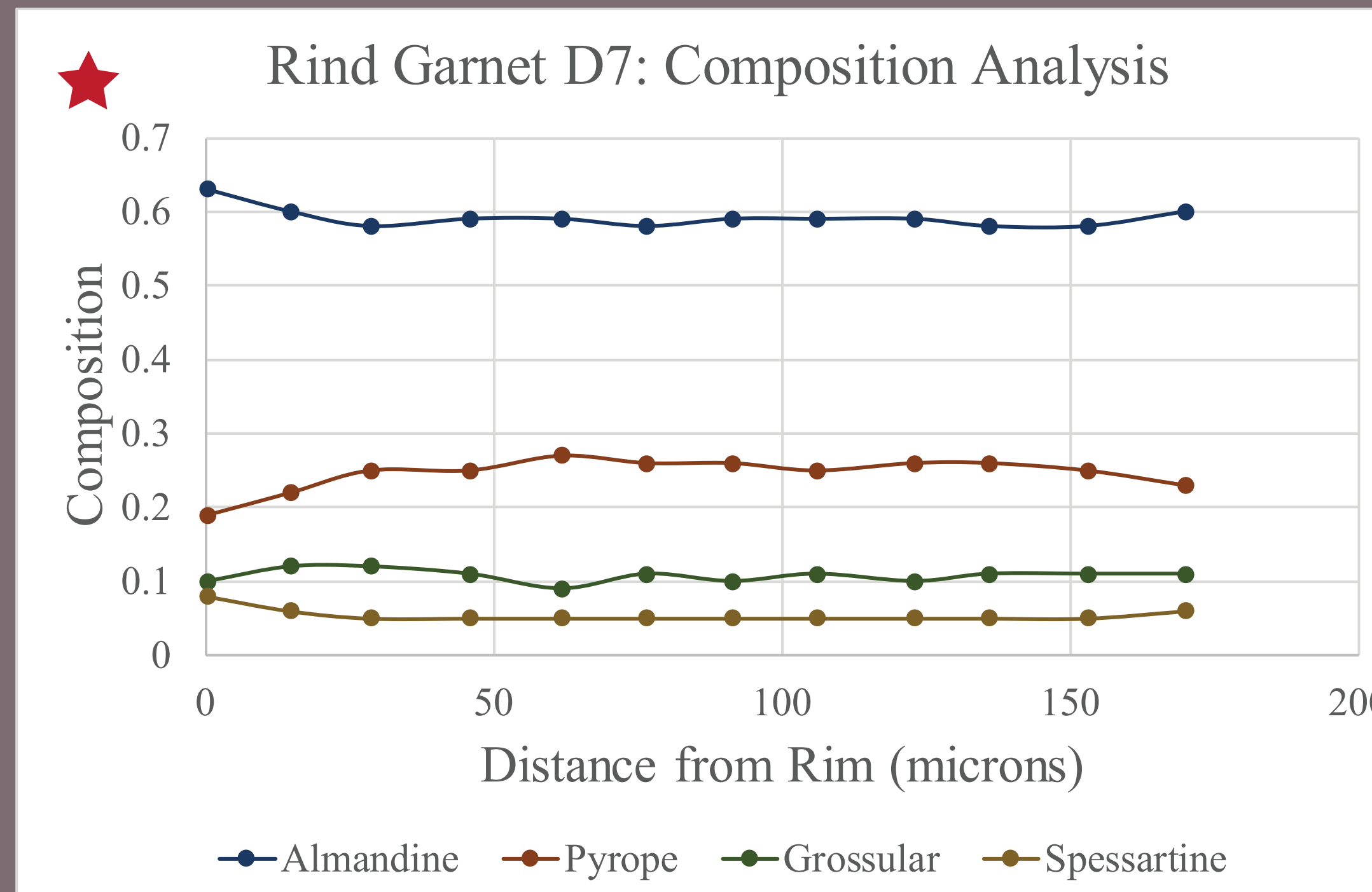
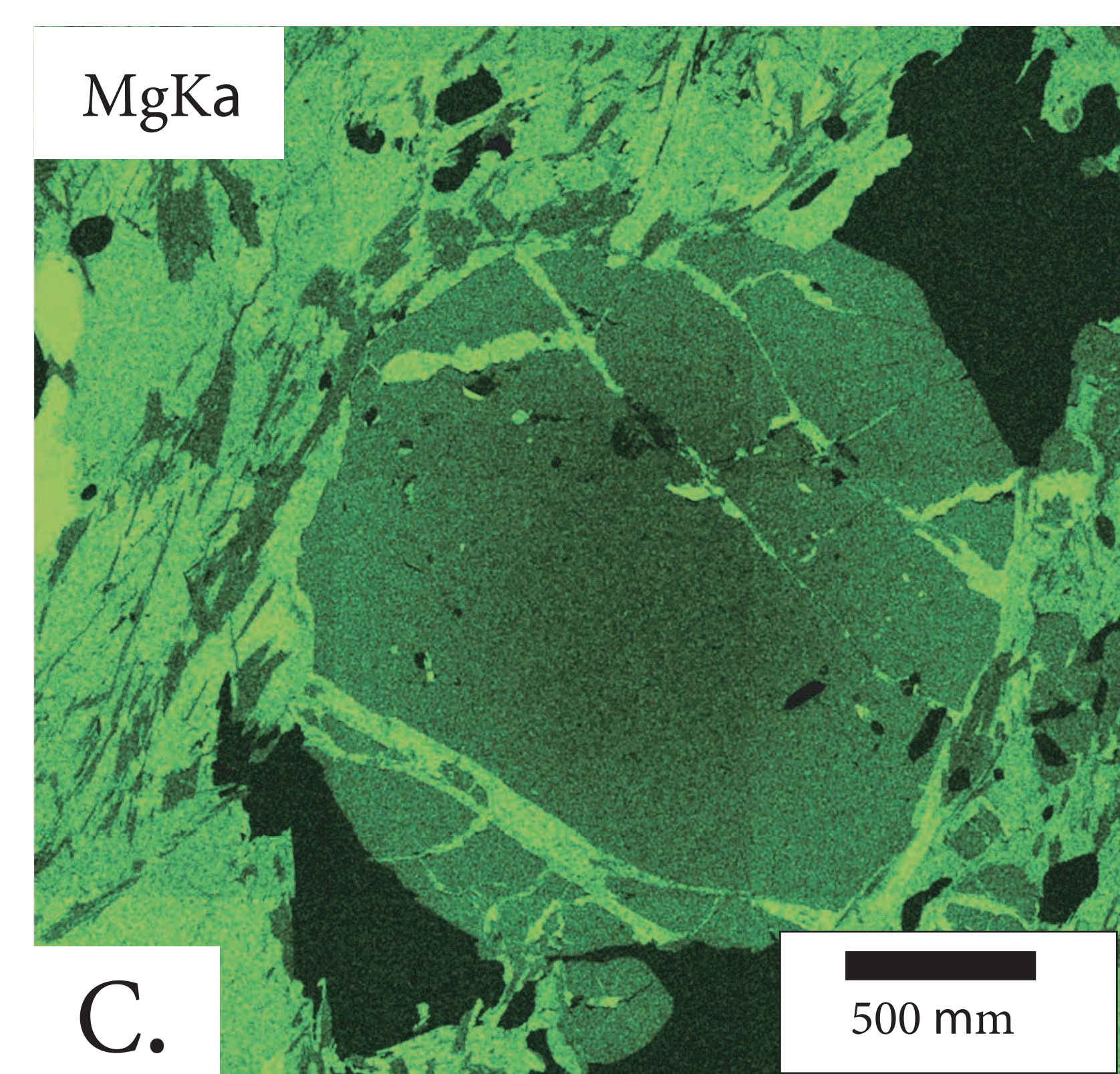
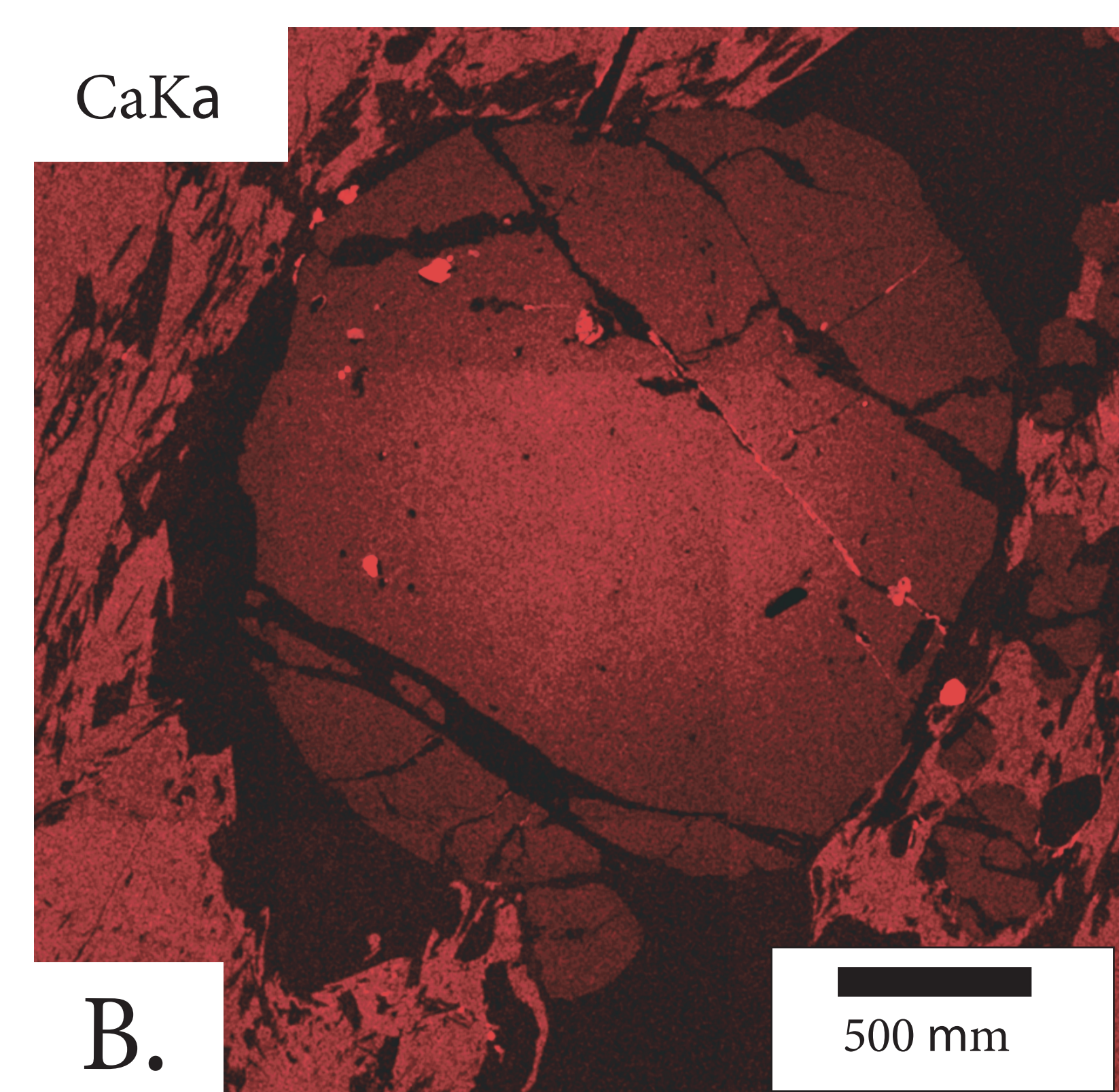


Figure 7. Small garnet crystals in rinds are homogeneous in major elements and resemble large rind garnet rims.

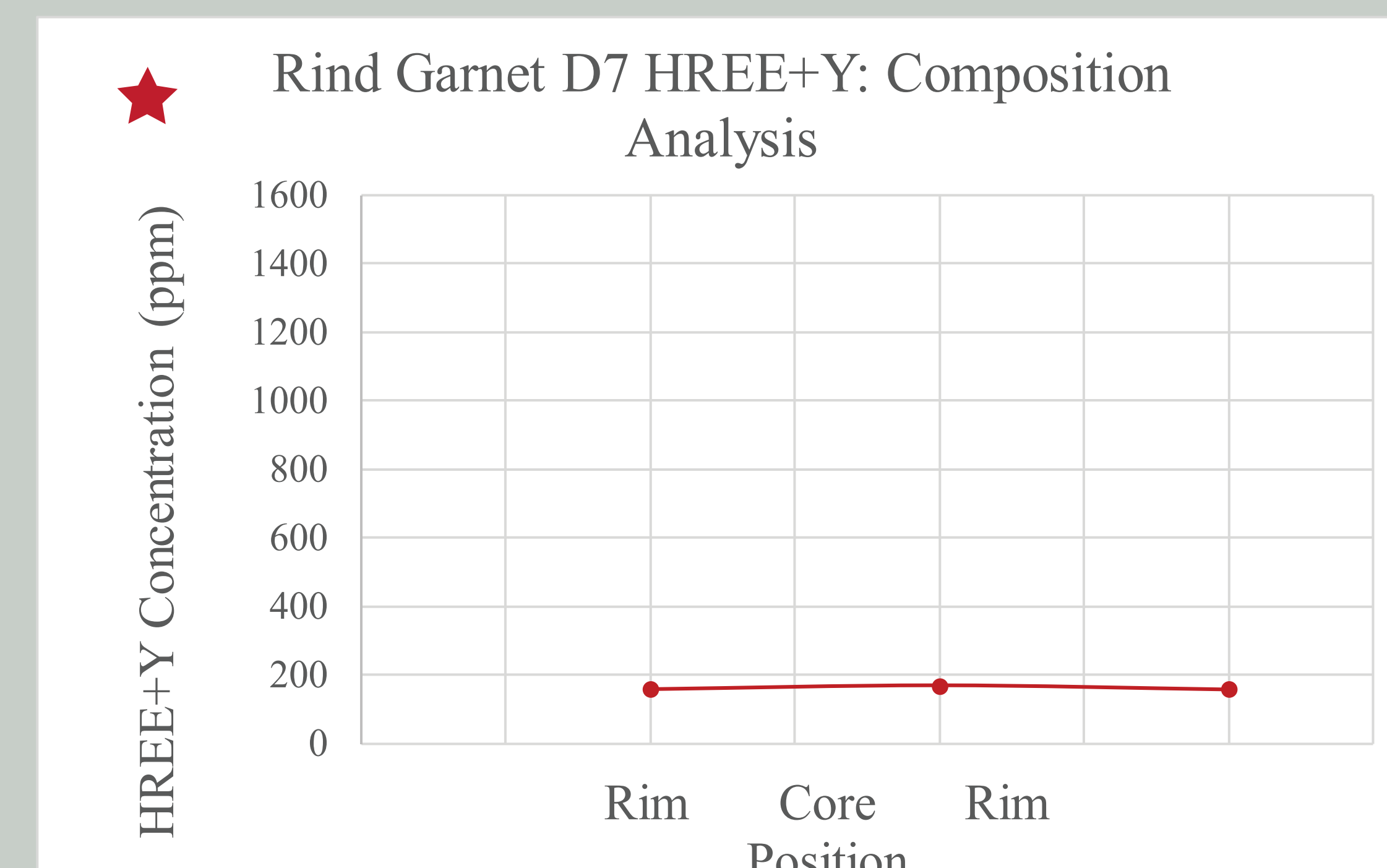


Figure 10. 200mm small rind garnet crystal has low HREE+Y concentrations (similar to large rind garnet rims) and minimal zoning.

References

- Leung, M.C., Page, F.Z., Penniston-Dorland, S.C., Kitajima, K., and Valley, G.W., 2016, Constraints on garnet-bearing metasomatic rind growth in subduction mélangé through SIMS analysis of oxygen isotopes: Geological Society of America Abstracts with Programs, Denver, Colorado.
- Penniston-Dorland, S.C., Gorman, J.K., Bebout, G.E., Piccoli, P.M., and Walker, R.J., 2014, Reaction rind formation in the Catalina Schist: Deciphering a history of mechanical mixing and metasomatic alteration: Chemical Geology, v. 384, p. 47-61.
- Platt, J.P., 1975, Metamorphic and deformational processes in the Franciscan Complex, California: some insights from the Catalina Schist terrance. Geol. Soc. Am. Bull. 86, 1337-1347.

Acknowledgements

Special thanks to the Departments and Facilities at Pomona College and Oberlin College, the Catalina Island Conservancy, ClaraMargaret Flood, Nicolette Mitchell, Nigel McMillion, and Kyle McCarty. This study was funded by the Keck Geology Consortium and the National Science Foundation (REU1659322). The Oxtoby I isotope Lab was funded by a grant from the Moore Foundation (GBMF5417). The SEM at Oberlin College was funded by a grant from the National Science Foundation (MRI162627).

STRUCTURAL EVOLUTION OF A SEGMENTED NORMAL FAULT TRANSFER ZONE, SEVIER FAULT, SOUTHERN UTAH

BENJAMIN SURPLESS, Trinity University

INTRODUCTION

While it has long been recognized that major normal fault systems are commonly segmented in map view, as opposed to continuous, planar surfaces (e.g., Goguel, 1952; Tchalenko, 1970; Wallace, 1970; Schwartz and Coppersmith, 1984), only recently have researchers made significant advances in the role that segmentation plays in the evolution of these fault systems (e.g., Biddle and Christie-Blick, 1985; Crone and Haller, 1991; Peacock and Sanderson, 1996; Peacock, 2002). The geometry and relative strength of links between fault segments can strongly influence the propagation of slip during an earthquake (e.g., King and Nabalek, 1985; Crone and Haller, 1991; Zhang et al., 1991), and the perturbations of the local stress field caused by interaction of fault segments can influence the formation of relay ramps, minor faults, and associated fracture networks in transfer zones between synthetic normal fault segments (e.g., Peacock and Sanderson, 1996; Crider and Pollard, 1998; Faulds and Varga, 1998; Peacock, 2002).

In addition, the high fracture densities developed at these segment boundaries (e.g., Stock and Hodges, 1990; Hudson, 1992; Faulds, 1996) may enhance fluid flow, thus increasing rates of groundwater flow (e.g., Rowley, 1998), permitting hydrocarbon migration (e.g., Morley et al., 1990), and promoting more effective ore mineralization (e.g., DeWitt et al., 1986). Because normal faults that typically develop in sedimentary basins, where natural resources commonly occur, are relatively planar and steeply-dipping in cross-section, with displacements of up to hundreds of meters (e.g., Peacock, 2002), well-exposed fault systems with these characteristics permit researchers to shed light on the evolution of similar

faults in the subsurface. In this Keck Utah Advanced Project, students used the Sevier fault zone in southern Utah (Fig. 1), a segmented normal fault system with ~600 – 700 m dip-slip displacement, to investigate the structural evolution of a normal fault transfer zone across a range of spatial scales.

STUDY AREA

The Sevier normal fault, considered one of the most important structures in the Basin and Range province (e.g., Davis, 1999; Lund et al., 2008), is part of the Toroweap-Sevier fault system, which extends for more than 300 km from northern Arizona to southern Utah (Fig. 1). The fault has accommodated extension across the transition zone from the Basin and Range province to the relatively stable Colorado Plateau since the Miocene (e.g., Reber et al., 2001; Lund et al., 2008), and previous workers have noted the potential of the fault to produce significant earthquakes (Anderson and Rowley, 1987; Doelling and Davis, 1989; Anderson and Christenson, 1989; Lund et al., 2008). It is likely that many segments of the Sevier fault reactivate older high-angle, Laramide-age contractional structures (e.g., Stewart and Taylor, 1996; Schiefelbein and Taylor, 2000), which may explain why the steeply-west-dipping fault zone is segmented in map view, with variations in the geometry of the linkages between normal fault segments (e.g., Davis, 1999; Reber et al., 2001; Schiefelbein, 2002; Doelling, 2008).

In this project, students focused their investigations on a particularly complex portion of the Sevier fault zone, termed the Orderville geometric bend (e.g., Reber et al., 2001) (Fig. 2). The Orderville bend displays a range of geometries associated with the interactions of three fault segments, which include,

from south to north, the Mt. Carmel segment, the Highway 89 segment, and the Spencer Bench segment. The interaction of these 3 fault segments is likely responsible for the formation of the minor faults (displayed in white) and relay ramps shown adjacent to Red Hollow Canyon and Stewart Canyon (Fig. 2); these features likely evolved within the perturbed stress field associated with the transfer zones between dominant fault segments (Fig. 3).

STUDENT PROJECTS

The excellent vertical and lateral exposure of the Jurassic Navajo sandstone at the two primary study areas, at Red Hollow Canyon and Elkheart Cliffs (Fig. 2), provided students opportunity to directly observe faults, fractures, and deformation bands within these well-studied lithologies (e.g., Rogers et al., 2004; Schultz et al., 2010; Solom et al., 2010). The Elkheart Cliffs exposure (Fig. 2) displays the simplest fault geometry because the Mt. Carmel segment accommodates all E-W extension. In contrast, at Red Hollow Canyon, extensional strain is accommodated by a more complex system that includes the Orderville relay ramp and several other faults (Fig. 2). This spatial variation in fault complexity allows student researchers to treat these two locations as end members, permitting them to evaluate how the evolution of different fault geometries damages adjacent rock volumes (Fig. 3).

To address fundamental questions about how rock volumes respond to the evolution of complex, segmented, normal fault systems, students applied a wide variety of approaches, including analysis of field data, 3D digital modeling of photographic data, ArcGIS analysis of major fracture sets, and geomechanical modeling of fault propagation through well-bedded sandstone layers. Their work improves our understanding of the 3D evolution of fracture networks in complex normal fault zones, which has important implications for natural resource exploration.

Charley Hankla (College of Wooster) interpreted field-based fracture data in the context of fault-zone evolution. He used fracture data from 8 different scanlines, which permit documentation of fracture

intensity and orientation along a horizontal line, as measured perpendicular to the dominant strike of the fracture set. To analyze the data, Charley plotted all fractures on stereonet and calculated basic statistics for each fracture population (e.g., average strike value). He then used these fracture orientation data in combination with precise, GPS-located map data and compressive strength data to relate fracturing to a newly-mapped fault segment within in the Red Hollow Canyon, named the Lion's Den fault (Fig. 2).

Charley clearly demonstrates that most fractures formed subparallel to the dominant fault segments in the area, with strikes of approximate 030° , supporting his hypothesis that the fault segments and fractures propagated within the same stress field, likely at the same time. Additionally, he notes the likelihood that fractures formed in the tip damage zone ahead of the propagating Lion's Den fault (Fig. 3C), reducing the cohesion of the rock and permitting northward propagation of the segment. Charley points out that fractures at significantly different orientations are consistent with joints documented in Zion National Park, to the east, where researchers suggest formation in a rotated regional stress field.

Caroline McKeighan (Trinity University) used a combination of field data and photographic data collected by unmanned aerial vehicle (UAV) to analyze variability in lateral and vertical fracture patterns. She compares fractures documented at the more complex Red Hollow Canyon (RHC) transfer zone (Fig. 2) to those from the Elkheart Cliffs locality, where all strain is accommodated by a single fault segment (Mt. Carmel segment, Fig. 2). As part of her project, she developed a new modeling protocol to efficiently document inaccessible fractures using Agisoft Photoscan Professional. Using a combination of these 3D digital outcrop models and field data, Caroline found that fracture intensities adjacent to the Mt. Carmel segment were significantly higher than from any location across the RHC transfer zone, where fractures were more broadly distributed. However, fracture intensity decreased rapidly with increasing distance from the Mt. Carmel segment, nearly disappearing when more than 100 meters from the fault contact, while fracture intensities remained relatively constant across the entire RHC transfer

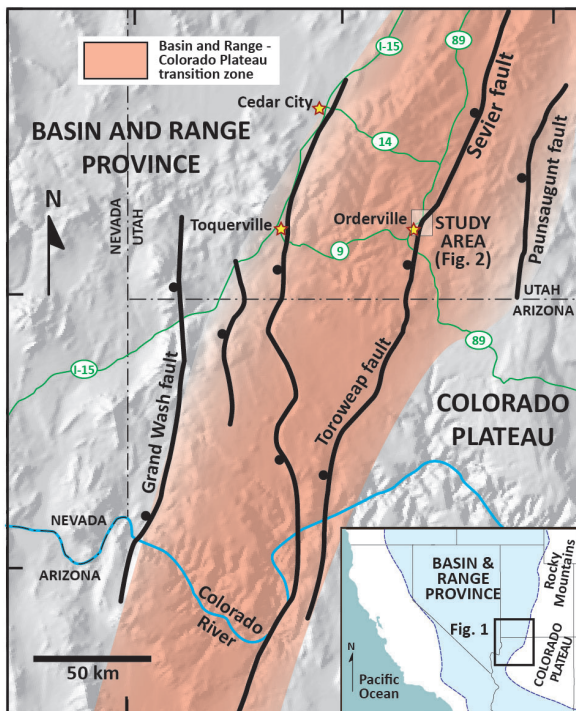


Figure 1. Physiographic context for the Sevier fault zone study area within the Basin and Range-Colorado Plateau transition zone (see inset). In combination with the Grand Wash, Hurricane, and Paunsaugunt faults, the Sevier-Toroweap fault helps accommodate extension across the transition zone. Ball is on the hanging wall of the west-dipping faults. Detailed geology of the Sevier fault study area (boxed) is displayed in Figure 2. Digital shaded relief modified from Thelin and Pike (1991). Figure significantly modified from Reber et al. (2001).

zone. In addition, she found that fracture intensities changed abruptly within the vertical stratigraphy, and zones of higher fracture intensity at one level rarely correlated with higher fracture intensities above or below.

These results suggest that fluid flow within fracture networks would likely be higher adjacent to a single fault segment but limited in lateral extent, while in a transfer zone, flow rates would be lower but with a broader distribution of flow. Vertical fracture data suggest that vertical fluid flow would be much more difficult to predict.

Curtis Segarra (Trinity University) utilized geomechanical finite-element modeling software, ABAQUS/CAE (by Dassault Systemes), to analyze the spatial distribution of stress and strain fields within well-layered sandstone bedding ahead of a propagating fault tip. The modeling software permitted Curtis to control a range of important

physical variables, including bed thickness, elastic moduli of fault blocks and bedding, friction between sedimentary rock layers, and fault geometry and displacement. He systematically tested for the displacement required to achieve initial plastic failure within modeled layers as well as for the displacement required to achieve throughgoing plastic failure through the layered stack. His results suggest that the initial stages of fault propagation within a layered system are characterized by complex patterns of stress and strain accumulation, with bedding contacts perturbing the stress field. Although somewhat predictable, the initial locations of high stress and strain are not along the projection of the fault, where expected, but are instead located meters off-plane, along bed contacts. However, by the

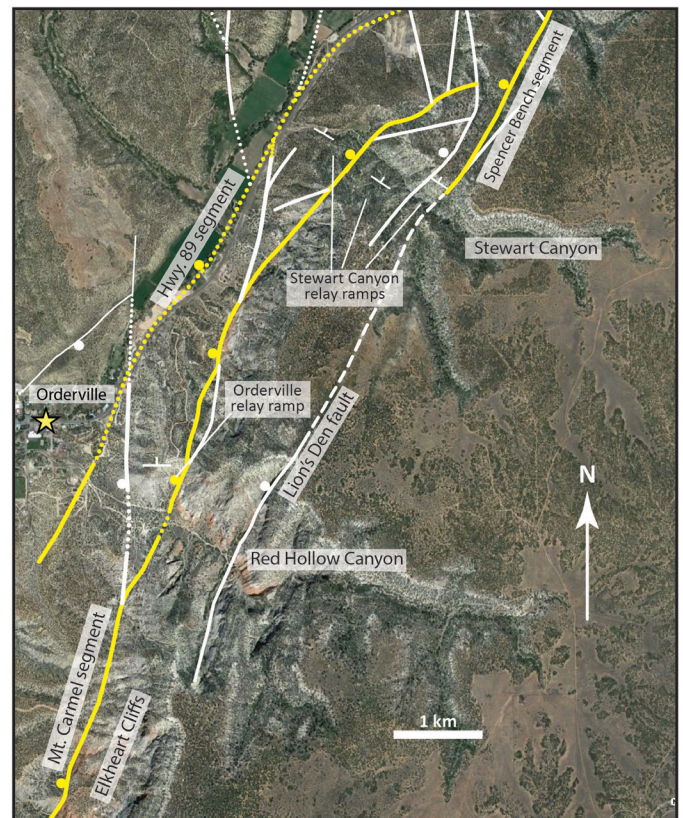


Figure 2. Fault map of the Sevier fault zone near Orderville, Utah. Yellow lines indicate normal faults that accommodate significant (>100 m) displacement or play an important role in fault linkage, and white lines indicate normal faults that play a role in strain accommodation but display lesser displacements. Ball symbols are on the hanging wall. Study locations include the Red Hollow Canyon transfer zone and the Elkheart Cliffs area, adjacent to the Mt. Carmel fault segment. Labels identify relay ramps within transfer zones. Faults and relay ramps shown here are based primarily on Schiefelbein (2002) and on the results of research completed as part of this Keck Advanced Project. See Figure 1 for location.

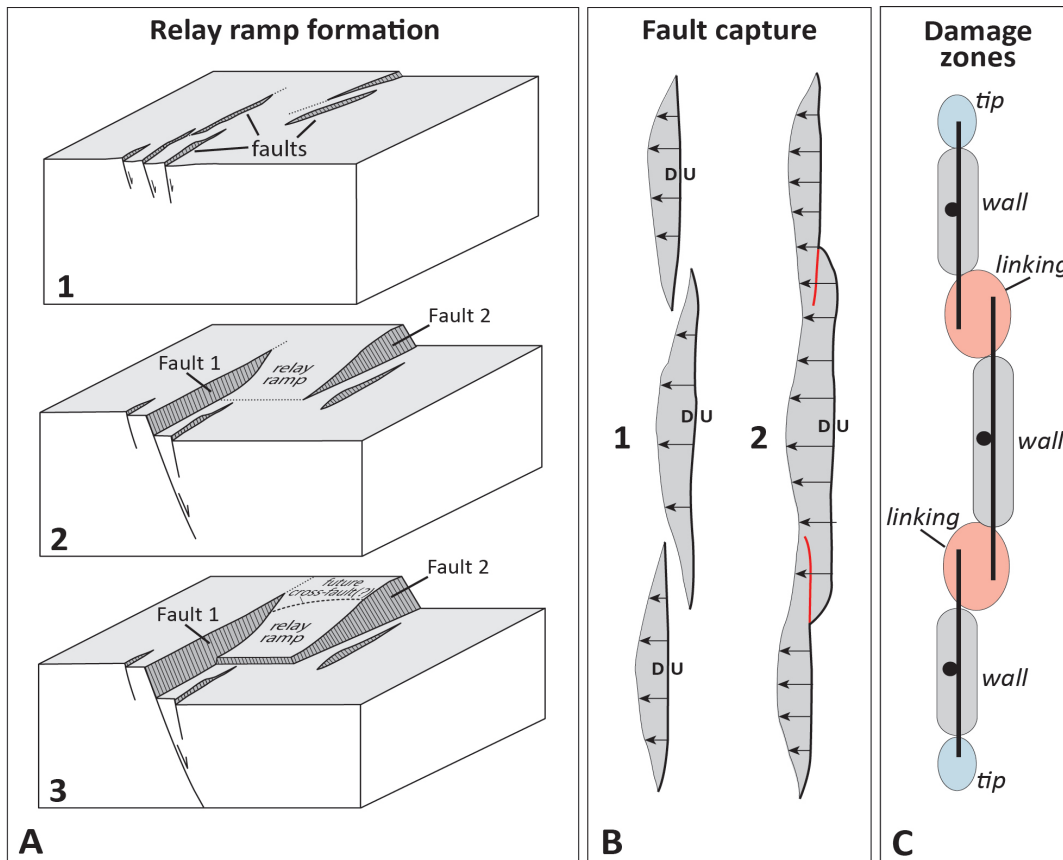


Figure 3. Diagrams displaying relay ramp development, fault capture, and damage zone classification. A) In all diagrams, the dark gray shaded area represents the magnitude of displacement, and the lines represent the slip direction as the hanging wall drops relative to the footwall. 1. A system of small-displacement faults develops to accommodate upper crustal stresses. The dotted lines represent the future propagation of the faults. 2. As displacement increases across the system, two faults (1 and 2) become dominant, both lengthening in map view and displaying increasing total displacement. A relay ramp forms in the zone of overlap between the faults. 3. Faults 1 and 2 link as a new cross-fault connects them. A future cross-fault may form where indicated, fully breaching the relay ramp. B) Map-view of a segmented fault system (bold lines are faults), with 1 and 2 representing progressive stages of fault segment linkage and capture. In 1, the three fault segments overlap but are only soft linked, and in 2, one of the segments has “captured” displacement from the other segments, isolating the overlapped portions of segments (red lines) that are no longer active. The segments are now hard linked and act as a single, corrugated fault. Arrows show the direction and relative magnitude of fault slip projected onto plan view. C) Schematic map view diagram of damage zone types associated with a segmented normal fault system (bold lines) with ball symbols on the hanging wall. Figure A. adapted from Peacock (2002) and Long and Imber (2011), Figure B. adapted from Reber et al. (2001), and Figure C. adapted from Kim et al. (2004).

time through-going failure occurs, these zones of strain accumulation (i.e., fractures) coalesce into a more coherent zone parallel to and in-plane with the propagating fault.

His research has significant implications for how tip damage zones evolve during fault propagation, which we can use to better understand results from field-based fracture studies like those undertaken by other students on this Keck Utah Project. More broadly, we can apply his results to the propagation of any fault through sedimentary layering, especially in the subsurface, where fracture networks cannot be directly

observed.

Madison Woodley (Mt. Holyoke College) focused on a detailed ArcGIS-based analysis of fracture networks, comparing data from the Red Hollow Canyon transfer zone to data from the Elkheart Cliffs, where a single fault segment accommodates all strain. She used a wide range of data, including orthorectified photography, digital elevation models, and high-resolution Google Earth imagery to build a detailed base map. Madison then added previous geologic mapping (Schiefelbein, 2002), so that she could use both rock unit distributions and faults

to provide context for her fracture analysis. She then built a fracture dataset as a layer in ArcMap, marking fractures and using ArcGIS tools to provide orientation data for each marked fracture. Finally, she used another tool to measure spacing between each fracture along well-defined scanlines, allowing her to assess both fracture intensity and relative clustering of fractures (clustering is quantified by the coefficient of variation, C_v ; see Woodley, *this volume*, for a detailed explanation).

Madison's data clearly show that the different fault zone geometries affect the orientations of fractures, fracture intensity, and relative clustering. At the Red Hollow Canyon transfer zone, her data suggest that more strain is accommodated over a larger area than at the Elkheart Cliffs locality, with greater clustering than at Elkheart Cliffs. She also points out that one fracture orientation dominates strain accommodation in the Elkheart Cliffs, while multiple fracture sets are present across the transfer zone. Madison proposes a model where the stress field within the rocks adjacent to the single fault segment locality was constant over time, while the presence of multiple faults linked across the transfer zone produce a more complex fracture network.

ACKNOWLEDGEMENTS

This material is based upon work supported by the Keck Geology Consortium and the National Science Foundation under Grant No. 1659322. Fieldwork was also supported by the Trinity University Department of Geosciences, and our time on Trinity University's campus was supported by the Trinity University Summer Undergraduate Research Program. Dr. Kevin Smart, at Southwest Research Institute, provided excellent guidance to Curtis Segarra, permitting Curtis to perform detailed and accurate geomechanical analysis.

REFERENCES

- Anderson, R.E., and Christenson, G.E., 1989, Quaternary faults, folds, and selected volcanic features in the Cedar City 1°x2° quadrangle, Utah: Utah Geological and Mineral Survey Miscellaneous Publication 89-6, 29 p.
- Anderson, J.J., and Rowley, P.D., 1987, Geologic map of the Panguitch NW quadrangle, Iron and Garfield Counties, Utah: Utah Geological and Mineral Survey Map 103, 8 p. pamphlet, scale 1:24,000.
- Biddle, K.T., and Christie-Blick, N., 1985, Strike – slip deformation, basin formation, and sedimentation, In: Biddle, K.T., Christie-Blick, N., Eds.: Strike– Slip Deformation, Basin Formation, and Sedimentation. Society of Economic Mineralogists Special Publication, v. 37, p. 375– 386.
- Crider, J., and Pollard, D., 1998, Fault linkage: Three-dimensional mechanical interaction between echelon normal faults: *Journal of Geophysical Research*, v. 103, p. 24,373 – 24,391.
- Crone, A.J., and Haller, K.M., 1991, Segmentation and the coseismic behavior of Basin and Range normal faults: examples from east-central Idaho and southwest Montana, U.S.A.: *Journal of Structural Geology*, v. 13, p. 151– 164.
- Davis, G., 1999, Structural geology of the Colorado Plateau region of southern Utah, with special emphasis on deformation bands: *Geological Society of America Special Paper* 342.
- DeWitt, E., Thompson, J., and Smith, R., 1986, Geology and gold deposits of the Oatman district, northwestern Arizona: U.S. Geologic Survey Open-File Report 86-0638, 34 p.
- Doelling, H.H., 2008, Geologic map of the Kanab 30'x60' quadrangle, Kane and Washington Counties, Utah, and Coconino and Mohave Counties, Arizona, 1:100,000-scale: Utah Geological Survey, MP-08-2DM.
- Doelling, H.H., and Davis, F.D., 1989, The geology of Kane County, Utah, with sections on petroleum and carbon dioxide by Cynthia J. Brandt: *Utah Geological and Mineral Survey Bulletin* 124, 192 p., scale 1:100,000, 10 plates.
- Faulds, J., 1996, Geologic map of the Fire Mountain 7.5' quadrangle, Clark County, Nevada, and

- Mohave County, Arizona: Nevada Bureau of Mines and Geology Map 106, scale 1:24,000 (with accompanying text).
- Faulds, J., and Varga, R., 1998, The role of accommodation zones and transfer zones in the regional segmentation of extended terranes, In Faulds, J.E., and Stewart, J.H., Eds., Accommodation zones and transfer zones: the regional segmentation of the Basin and Range province: Geological Society of America Special Paper No. 343, p. 1 – 45.
- Goguel, J., 1952, *Traite de Tectonique*: Masson, Paris (Translated by Thalmann, H.E., 1962). Tectonics: Freeman Publishing Company, San Francisco, 384 p.
- Hudson, M., 1992, Paleomagnetic data bearing on the origin of arcuate structures in the French Peak – Massachusetts Mountain area of southern Nevada: Geological Society of America Bulletin, v. 104, p. 581 – 594.
- Kim, K.-S., Peacock, D., and Sanderson, D., 2004, Fault damage zones: Journal of Structural Geology, v. 26, p. 503–517.
- King, G.C.P., and Nabalek, J.L., 1985, The role of bends in faults in the initiation and termination of earthquake rupture: Science, v. 228, p. 984 – 987.
- Long, J., and Imber, J., 2011, Geological controls on fault relay zone scaling: Journal of Structural Geology, v. 33, p. 1790 – 1800.
- Lund, W.R., Knudsen, T.R., and Vice, G.S., 2008, Paleoseismic reconnaissance of the Sevier fault, Kane and Garfield Counties, Utah: Utah Geologic Survey Special Study 122, Paleoseismology of Utah, v. 16, 31 p.
- Lowe, D., 2004, Distinctive image features from scale invariant keypoints: International Journal of Computer Vision, v. 60, p. 91–110, doi: 10.1023/B:VISI.0000029664.99615.94.
- Morley, C., Nelson, R., Patton, T., and Munn, S., 1990, Transfer zones in the East African Rift system and their relevance to hydrocarbon exploration in rifts: American Association of Petroleum Geologists Bulletin, v. 74, p. 1234 – 1253.
- Peacock, D.C.P., 2002, Propagation, interaction and linkage in normal fault systems: Earth-Science Reviews, v. 58, p. 121 – 142.
- Peacock, D.C.P., and Sanderson, D.J., 1996, Effects of propagation rate on displacement variations along faults: Journal of Structural Geology, v. 18, p. 311 – 320.
- Reber, S., Taylor, W., Stewart, M., and Schiefelbein, I., 2001, Linkage and Reactivation along the northern Hurricane and Sevier faults, southwestern Utah, In M.C. Erskine, J.E. Faulds, J.M. Bartley, P.D. Rowley, Eds., The Geologic Transition, High Plateaus to Great Basin – A Symposium and Field Guide, The Mackin Volume: Utah Geological Association Publication 30, Pacific Section American Association of Petroleum Geologists Publication GB78, p. 379 – 400.
- Rogers, C., Myers, D., and Engelder, T., 2004, Kinematic implications of joint zones and isolated joints in the Navajo Sandstone at Zion National Park, Utah: Evidence for Cordilleran relaxation: Tectonics, v. 23, TC1007, doi:10.1029/2001TC001329.
- Rowley, P., 1998, Cenozoic transverse zones and igneous belts in the Great Basin, Western United States: Their tectonic and economic implications In Faulds, J.E., and Stewart, J.H., Eds., Accommodation zones and transfer zones: the regional segmentation of the Basin and Range province: Geological Society of America Special Paper No. 343, p. 195-228.
- Schiefelbein, I., 2002, Fault segmentation, fault linkage, and hazards along the Sevier fault, southwestern Utah [M.S. thesis]: Las Vegas, University of Nevada at Las Vegas, 132 p.

- Schiefelbein, I., and Taylor, W., 2000, Fault development in the Utah transition zone and High Plateaus subprovince: Abstracts with Programs, v. 32, No. 7, p. 431.
- Schultz, R., Okubo, C., and Fossen, H., 2010, Porosity and grain size controls on compaction band formation in Jurassic Navajo Sandstone: Geophysical Research Letters, v. 37, L22306, doi:10.1029/2010GL044909.
- Schwartz, D.P., and Coppersmith, K.J., 1984, Fault behavior and characteristic earthquakes – Examples from the Wasatch and San Andreas fault zones: Journal of Geophysical Research, v. 89, p. 5681 – 5698.
- Solum, J., Brandenburg, J., Kostenko, O., Wilkins, S. and Schultz, R., 2010, Characterization of deformation bands associated with normal and reverse stress states in the Navajo Sandstone, Utah: AAPG Bull., v. 94, p. 1453–1475, doi:10.1306/01051009137.
- Stewart, M., and Taylor, W., 1996, Structural analysis and fault segment boundary identification along the Hurricane fault in southwestern Utah: Journal of Structural Geology, v. 18, p. 1017 – 1029.
- Stock, J., and Hodges, K., 1990, Miocene to recent structural development of an extensional accommodation zone, northeastern Baja California, Mexico: Journal of Structural Geology, v. 12, p. 312 – 328.
- Tchalenko, J.S., 1970, Similarities between shear zones of different magnitudes: Bulletin of the Geological Society of America, v. 81, p. 1625–1640.
- Thelin, G.P., and Pike, R.J., 1991, Landforms of the Conterminous United States - A Digital Shaded-Relief Portrayal: U.S.G.S. Geologic Investigations Series I – 2720.
- Wallace, R.E., 1970, Earthquake recurrence intervals on the San Andreas fault: Bulletin of the Seismological Society of America, v. 81, p. 2875 – 2890.
- Zhang, P., Slemmons, D.B., and Mao, F., 1991, Geometric pattern, rupture termination and fault segmentation of the Dixie Valley– Pleasant Valley active normal fault system, Nevada, U.S.A.: Journal of Structural Geology, v. 13, p. 165–176.

AN ANALYSIS OF FRACTURES AROUND THE SEVIER FAULT ZONE IN RED HOLLOW CANYON NEAR ORDERVILLE, UTAH

CHARLEY H. HANKLA, The College of Wooster
Research Advisor: Dr. Shelley Judge

ABSTRACT

Structural discontinuities - such as opening mode joints, shear fractures, and faults - tend to occur in close geographic proximity to one another; however, timing relationships between these structures are not always easy to discern in the field. In southwestern Utah, the Jurassic Navajo Sandstone is cut by large-scale normal faults associated with the Sevier Fault Zone, making it perfect for observing several fracture types. The aim of this study is to complete a dynamic and kinematic analysis of the fractures near a major fault and to determine the chronologic relationships between the fractures. Specifically, we observed an unnamed segment of the Sevier Fault Zone - herein referred to as the Mountain Lion Den Fault (MLD) - previously interpreted as a west dipping normal fault striking 030. The primary field area is the Red Hollow Canyon/Elkheart Cliffs region, located southeast of Orderville, Utah.

For this study, orientations (dip and dip direction) of fracture data within the Navajo Sandstone were measured and tracked on eight different scanlines. Scanline fractures were plotted on stereonet and averages determined. GPS locations were taken on a Trimble G7X at ends of each scanline for GIS mapping.

Fracture analyses show a general NNE strike similar to the MLD Fault strike. Despite a few outliers, scanline averages typically strike within 10°-15° of the 030 strike of the MLD Fault. We interpret movement along the fault initiated around the same time some of the fractures formed. The fractures likely formed in front of the MLD Fault at oblique angles to its strike as the fault propagated northward. These results suggest that

an area of weakness formed in Red Hollow Canyon, allowing the fault to propagate easily at 030. These results compare favorably to previous brittle fracture studies within propagating fault zones. Outliers in the data could be associated with NW rotation of σ_3 , similar to nearby joints in Zion National Park.

INTRODUCTION

In the western US, there are multiple physiographic provinces. In southern Utah, the Colorado Plateau and the Basin and Range provinces dominate, with the Transition Zone between them. Marked by changes in deformation, volcanism, topography, and crustal structure, the Colorado Plateau gradually gives way to the Basin and Range province in the west (Jackson, 1990b, 1990a; Porter et al., 2017). The Basin and Range is the result of large scale extension that created characteristic elongate valleys, north to north-northeast trending mountain ranges, and gently dipping strata. Extension produced large normal faults, horsts and grabens, as well as a variety of other structures including relay ramps (Stewart, 1998). The Transition Zone contains characteristics from both provinces and extension is interpreted to be ongoing (Eaton, 1982; Stewart, 1998).

In southern Utah there are four main faults/fault zones that accommodate extension across the Transition Zone, including the Grand Wash Fault Zone, the Hurricane Fault, the Sevier Fault Zone, and Paunsaugunt Fault. This study focuses on a portion of the Sevier Fault Zone (SFZ), near Orderville, Utah. This fault zone has many fault segments that accommodate regional extension. These segments are high angle, west-dipping normal faults generally striking 030. Initial displacement along the SFZ

started around 15 to 12 Ma, and the fault zone has produced two historical earthquakes, implying that it is still active (Eaton, 1982; Moores and Twiss, 1995; Davis, 1999).

Data collection for this study occurred in the Elkheart Cliffs and Red Hollow Canyon regions. In the Elkheart Cliffs area, only one fault accommodates extension, whereas Red Hollow Canyon (RHC) is in a transfer zone and contains multiple fault segments. Specifically, fracture data were gathered along the Elkheart Cliffs Fault (EHC), Mountain Lion Den Fault (MLD), and a potential small fault segment crossing the canyon between the MLD and EHC Faults (Doelling, 2008), which strikes at 025 and will be referred to as the Kimbler Fault (Figure 1). West of RHC is a fault that forms the Orderville Relay Ramp with the Elkheart Cliffs Fault and briefly follows Highway 89; this fault is referred to as the Highway 89 Fault (H89).

As subsidiary structures to faults, fractures are useful in interpreting the history of an area. Fractures are planar discontinuities that form to help accommodate stress. In the field, indicators of fractures included extremely flat faces along exposures, cracks in outcrops, and hackle plume structures. There are three main modes of fracturing: Mode 1 are opening fractures also called joints, Mode 2 are sliding fractures, and Mode 3 are tearing fractures. For dip-slip faults, Mode 2 tends to be on the top and bottom tips of fault planes, and fractures on the lateral tips tend to be Mode 3. These modes can form at the same time as Mode 1 fractures, creating zones of mixed mode fracturing (McGrath and Davison, 1995).

METHODS

Scanlines

While collecting fracture data in the canyons, scanlines were established. For purposes of this study, scanlines are used to measure fracture position relative to an arbitrary starting position (usually where good outcrop exposure made fracture documentation possible), approximately perpendicular to the orientation of a dominant fracture set. Positions (in meters) were recorded between each visible fracture greater than 4-m in height. There are large gaps in

some of the scanlines, indicating the absence of visible fractures or the lack of accessible outcrops. GPS locations were taken on a Trimble G7X to mark the beginning and end of each scanline.

Fracture Data

More than 200-m thick in the study area, the well-exposed Navajo Sandstone is excellent for data collection. When determining if a fracture's attitude was to be recorded, its length and accessibility were considered. If the visible portion of the fracture extended 4 or more meters (12 feet), its attitude (dip, dip direction) was recorded using a Brunton geologic compass. Fractures that were similar in attitude to the first fracture on the scanline were labeled 'typical' fractures, and those varying noticeably from that orientation were labeled 'diamond' fractures. It is important to note that fracture orientation data were collected by multiple geologists in the field, so there may be some human error included in the data collected. Sketches and photo documentation of fractures were done in the field as well.

Stereonets

Stereonet software (Allmendinger, 2018) was used to visualize fracture orientations. Fracture data were organized into .csv files, brought into Stereonet, and plotted. The stereographic projections were analyzed to find spatial patterns. Strike and dip averages were calculated using excel, not taking dip direction into account when determining the dip averages due to the uncertainty of the validity of the recorded dip direction.

RESULTS

Several trends are apparent in the scanline fracture data shown in Table 1. Numerically averaged dips for all fractures (except H \diamond) are within 14° of each other. Strike averages for scanlines A, B \diamond , C, C \diamond , D, E, and G only differ by a maximum of 18°, ranging from 019 to 037. The MLD Fault strikes at 030, the Kimbler Fault at 025, and the EHC Fault at 020 (Schiefelbein, 2002; Doelling, 2008); these faults correlate well to the above listed fracture averages. Though most fracture data trend NNE, scanline divisions E \diamond and H \diamond have strike averages that trend NNW.

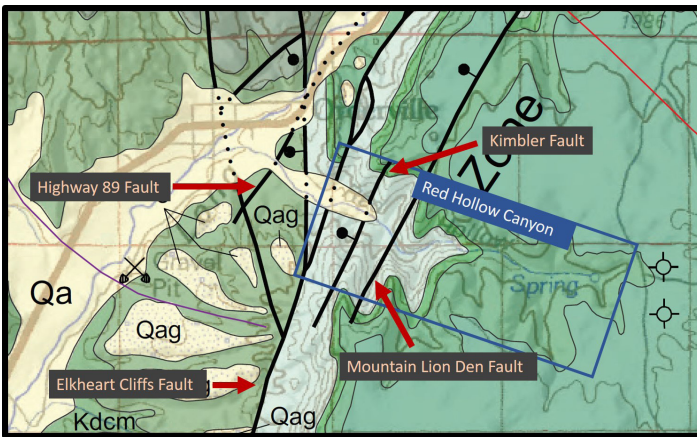


Figure 1. Geologic map of the portion of the SFZ in which the study was conducted. RHC emphasized with blue box (Modified from Doelling, 2008).

DISCUSSION

Fault-related Fractures

Fractures that form at tips of normal faults tend to be parallel or subparallel to the fault strike and form first, creating a weak zone for the fault to propagate through (McGrath and Davison, 1995; Kattenhorn et al., 2000). Fracture strike averages from near the MLD Fault are similar to the fault strike, seen in Figure 3, and the same holds true for the Elkheart Cliffs region. This suggests that the faults and fractures are genetically related. The similarity between these faults and fractures implies a close chronological relationship; the fractures around the MLD, Kimbler, and EHC Faults formed shortly before the faults, creating paths of least resistance in which the faults could form.

Isolated Fractures

Rogers et al. (2004) analyzed fractures in Zion National Park and found three main sets that trend NNE, NNW, and NW in chronological order from oldest to youngest. Since Rogers et al., (2004) were able to find timing relations between their observed fracture sets, they concluded that the regional stress regime rotated from NNE to NW over time. Zion is geographically close to both localities in this study, so there may be connections between the structures seen at both locations. Our data correlate to the older strike orientations of Rogers et al.'s (2004) sets; however, mostly NNE trending fractures were seen in RHC rather than the dominantly NNW fractures seen in

Rogers et al.'s (2004) paper.

Regional Stress Regime

For idealized Andersonian normal faults, σ_1 is perpendicular to the surface of Earth, and σ_3 is in the direction of extension. This means σ_3 is perpendicular to the fault strike (Peacock, 2002). Kattenhorn et al. (2000) found that fractures of similar age to a nearby normal fault will be parallel to sub-parallel to the fault strike. So, if a fault strikes at 025 (the average of the MLD, Kimbler, and EHC Faults), then the trend of σ_3 would be 115/295. Thus, a regional σ_3 trending ESE/WNW was present when the faults and related fractures formed. Rogers et al. (2004) also found a WNW trending σ_3 for a fracture set that over time changed to WSW and then to a SW trending σ_3 , indicating a rotation of the regional stress regime. Since we also see a difference in fracture strikes from NNE to NNW, our data support the σ_3 regional rotation hypothesis from Rogers et al. (2004).

Fault Propagation

The structural data presented here indicates that the fractures in RHC are close in age to the MLD Fault and associated nearby faults within the SFZ. For the MLD fault, the exact plane where the actual displacement occurred is difficult to define within the canyon due to erosion, landslides, and vegetation (Figure 4). However, displacement of the above Temple Cap

Table 1. Average strikes and numerical dip averages for typical and diamond fractures.

Scan-line	Number of Fractures	Typical Fractures Average		Diamond Fractures Average	
		Strike	Dip	Strike	Dip
A	102	020	88	-	-
B	81	054	88	027	81
C	47	030	84	025	75
D	31	021	74	-	-
E	18	019	82	348	84
F	39	010	82	-	-
G	24	032	79	-	-
H	33	037	85	352.5	63.5

Formation is clearly visible on the hanging wall on the north side of the canyon (Figure 4). Looking south along the approximate fault strike, no offset can be seen across the canyon. The offset and the oblique orientation of the fractures to the main fault plane indicate that the fault likely traveled north. Due to the absence of displacement of the Temple Cap on the south side of the canyon, our results suggest that the MLD segment began in RHC and propagated northward.

Northward propagation of the MLD Fault is likely

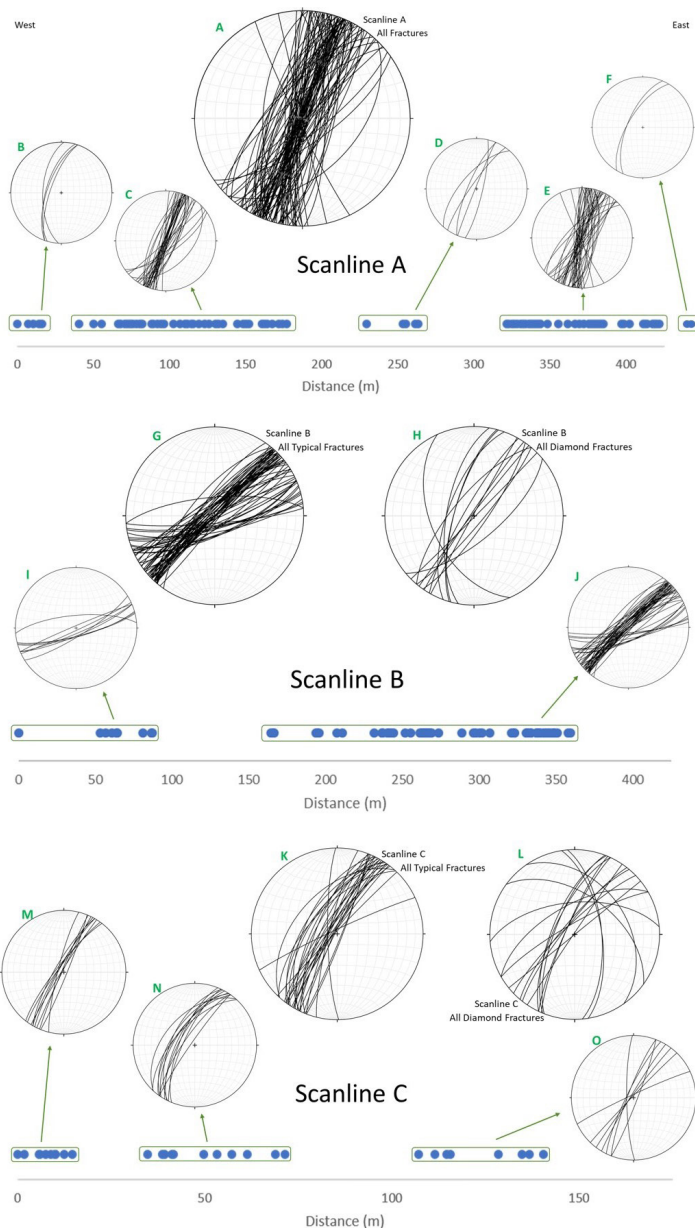


Figure 2. A-O. Stereonets of scanlines A, B, and C, plotted spatially along their respective scanline with groupings indicated by boxes.

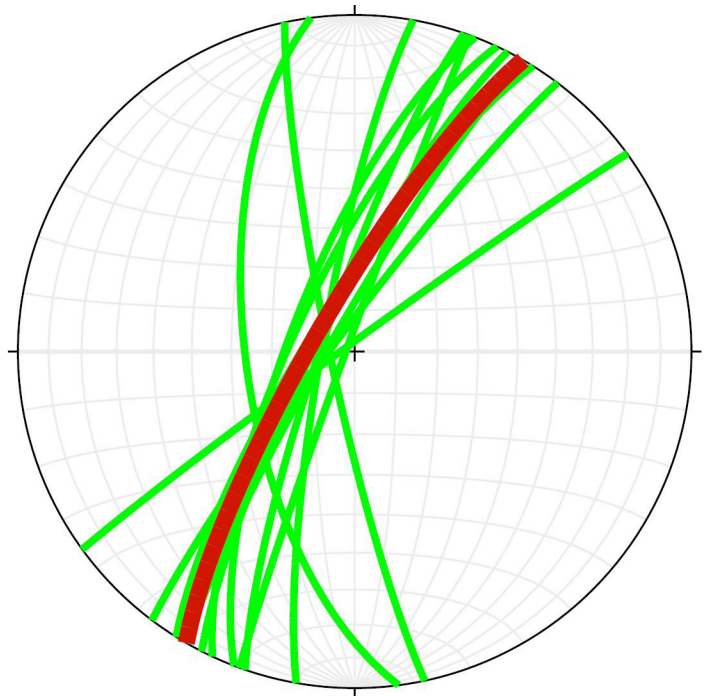


Figure 3. Stereonet showing typical and diamond fracture group averages from all scanlines (green) and the Mountain Lion Den Fault strike (red).

because the EHC Fault ends just northwest of the canyon, where a relay ramp connects it to the H89 Fault. The displacement of the EHC Fault stopped and additional offset accommodation was necessary, likely initiating the formation of the MLD Fault. However, because the H89 Fault also starts around where the EHC Fault stops, more research is needed to determine why the displacement was split between the MLD and H89 segments.

CONCLUSION

From these data, we conclude that:

- most fractures in Red Hollow Canyon and Elkheart Cliffs are related to the Mountain Lion Den, Kimbler, and Elkheart Cliffs Faults.
- the fault-related fractures are close in age to the fault(s) with which they are associated.
- data from this study supports the stress regime rotation theory of Rogers et al. (2004).
- the Mountain Lion Den Fault began in Red Hollow Canyon and propagated northward.



Figure 4. Photograph along the approximate MLD Fault strike. Temple Cap Formation sunlit in the background. Left side of the photo is the hanging wall and the right is the footwall. Estimated fault strike is circled. View to the NNE (Photo credit: Ben Surplless).

Studies of additional complex normal faulting regions in southern Utah would help support this study. To continue this research, more data could be collected along the Mountain Lion Den Fault, following it northward. Also, collecting more fracture data along the Elkheart Cliffs Fault, Kimbler Fault, and a heavily fractured zone east of this study's focus would provide valuable insight into how stress was accommodated in this complexly faulted region.

ACKNOWLEDGEMENTS

This material is based upon work supported by the Keck Geology Consortium and the National Science Foundation under Grant No. 1659322.

REFERENCES

- Allmendinger, R.W. Stereonet 10 | Rick Allmendinger's Stuff, <http://www.geo.cornell.edu/geology/faculty/RWA/programs/stereonet.html> (accessed October 2018).
- Davis, G.H., 1999, Structural Geology of the Colorado Plateau Region of Southern Utah, with Special Emphasis on Deformation Bands: Geological Society of America, 170 p.
- Doelling, H.H., 2008, Geologic map of the Kanab 30'x60' quadrangle: Kane and Washington counties, Utah, and Coconino and Mohave counties, Arizona: Utah Geological Survey Miscellaneous Publications 08-2DM.
- Eaton, G.P., 1982, The Basin and Range Province: Origin and Tectonic Significance: Annual Review of Earth and Planetary Sciences, v. 10, p. 409–440, doi:10.1146/annurev.earth.10.050182.002205.
- Jackson, G., 1990a, Tectonic Geomorphology of the Toroweap Fault, western Grand Canyon, Arizona: Implications for Transgression of Faulting on the Colorado Plateau: Arizona Geological Survey: Tucson, AZ, United States.
- Jackson, G.W., 1990b, The Toroweap Fault; one of the most active faults in Arizona: Arizona Geological Survey: Tucson, AZ, United States, p. 7–10.
- Kattenhorn, S.A., Aydin, A., and Pollard, D.D., 2000, Joints at high angles to normal fault strike: an explanation using 3-D numerical models of fault-perturbed stress fields: Journal of Structural Geology, v. 22, p. 1–23, doi:10.1016/S0191-8141(99)00130-3.
- McGrath, A.G., and Davison, I., 1995, Damage zone geometry around fault tips: Journal of Structural Geology, v. 17, p. 1011–1024, doi:10.1016/0191-8141(94)00116-H.
- Moores, E.M., and Twiss, R.J., 1995, Tectonics: New York, W.H. Freeman & Co, 415 p.
- Peacock, D.C.P., 2002, Propagation, interaction and linkage in normal fault systems: Earth-Science

Reviews, v. 58, p. 121–142.

Porter, R., Hoisch, T., and Holt, W.E., 2017,
The role of lower-crustal hydration in the
tectonic evolution of the Colorado Plateau:
Tectonophysics, v. 712–713, p. 221–231.

Rogers, C.M., Myers, D.A., and Engelder, T.,
2004, Kinematic implications of joint zones
and isolated joints in the Navajo Sandstone
at Zion National Park, Utah: Evidence for
Cordilleran relaxation: Tectonics, v. 23,
doi:10.1029/2001TC001329.

Schiefelbein, I.M., 2002, Fault segmentation, fault
linkage, and hazards along the Sevier fault,
southwestern Utah: University of Nevada, 132 p.

Stewart, J.H., 1998, Regional characteristics, tilt
domains, and extensional history of the late
Cenozoic Basin and Range Province, western
North America, in Faulds, J.E. and Stewart, J.H.
eds., Accommodation zones and transfer zones;
the regional segmentation of the Basin and Range
Province, Geological Society of America Special
Paper 323.

ANALYZING DEFORMATION WITHIN A NORMAL FAULT TRANSFER ZONE USING SFM 3D MODELING

CAROLINE MCKEIGHAN, Trinity University
Research Advisor: Benjamin Surpless

INTRODUCTION

Segmented normal fault systems increase the complexity and development of subsidiary structures such as joints, minor faults, and deformation bands. Where fault segments overlap, shear stresses are highest near the segment tips (e.g., Cowie and Shipton, 1998; Schiefelbein, 2002;), and as fault segments propagate and begin to interact, their paths may be deflected by local stress fields associated with other segments (e.g., Reber, 2001; Schiefelbein, 2002). Prior to linking, the structural discontinuity between the faults' propagating tips is a zone of distributed strain, a transfer zone (e.g., Taylor and Stewart, 1996; Ferrill and others, 1999), that commonly alters the mechanical and hydrologic properties of the rock (e.g., Davatzes, 2005). In many cases, these zones of amplified stress display fracturing (e.g. Davis, 1999) that may vary significantly depending on factors such as thickness of the beds, the weak or strong nature of the contact between beds, and other material properties of each layer (e.g., Cooke et al., 2000; McGinnis et al., 2015).

Thus, in transfer zones, where fracturing is commonly of higher intensity, fluid flow and permeability may be significantly enhanced, which impacts ore deposit formation, groundwater flow, and hydrocarbon migration (e.g., Sibson, 1987). In this study, we compare deformation within a well-documented normal fault transfer zone to deformation at a locality where a single fault accommodates all extension.

STUDY AREA

In southcentral Utah, three major high-angle normal

faults, including the Sevier fault zone, accommodate strain across the transition zone between the raised and relatively stable Colorado Plateau to the west and the highly-extended Basin and Range province to the east (e.g. Davis, 1997; Schiefelbein, 2002). The Orderville Salient, near the city of Orderville, Utah, displays two normal fault transfer zones along the Sevier fault zone (e.g., Schiefelbein, 2002). We focus on one of these transfer zones, located in Red Hollow Canyon, where two fault segments overlapped and linked (Reber et al., 2001; Schiefelbein, 2002) (Fig. 1). We also investigate strain accommodated by a single fault at Elkheart Cliffs, where the Mt. Carmel Segment of the Sevier fault zone is exposed (e.g., Schiefelbein, 2002).

The oldest sedimentary rock in the exposed stratigraphy is the Jurassic Navajo sandstone, which consists of a thick, cross bedded, fine- to medium-grained, well-sorted, and well-rounded quartz sandstone; the sandstone consists of a lower, red, oxidized unit and an upper, light-gray, bleached unit (e.g., Gregory, 1951; Hintze, 1973; Peterson and Pipiringos, 1979; Sargent and Philpott, 1987; Schiefelbein, 2002). Unconformably overlying the Navajo Sandstone is the Carmel formation, which is made up of alternating siltstone and limestone (e.g., Gregory, 1951; Hintze, 1973; Sargent and Philpott, 1987; Schiefelbein, 2002).

At both locations, I analyze the three-dimensional fracture network, focusing on lateral and vertical variations in fracture orientation and intensity. I also relate changes in fracture patterns to lithologic differences between exposed rock units, thus building a more complete picture of the relationship between normal faulting and fracturing. In order to achieve

these goals, I designed a workflow that has allowed me to construct 3D digital models of the fault and fracture network.

METHODS

Field Methods

In the field, we documented the position of fractures along scanlines oriented perpendicular to fracture strike. We only documented fractures with vertical height of greater than 4 meters to analyze orientation, position, and characteristics of the fractures. We used field photographs and detailed field notes to document the lateral and vertical fracture network and the position within the exposed stratigraphy. We recorded all field positions using handheld GPS units.

Unmanned Aerial Vehicle (UAV)

Although both localities display excellent bedrock exposure, the significant topography made documentation of field relationships impossible in many places. In order to gather data from the tall, vertical canyon and cliff walls, we applied an SfM (structure from motion) technique, which uses a series of overlapping photographs to create realistic digital 3D models (Johnson et al., 2014). We flew a Phantom 4 Professional UAV to record video of fault-related deformation to provide views of inaccessible lateral and vertical fracture networks associated with the Red Hollow Canyon and Elkheart Cliffs localities.

3D Model Workflow

I created a workflow (Fig. 2) to build realistic, sub-decimeter-resolution 3D models from videos captured during UAV flights. First, I clipped 4K images from the UAV videos at three-second intervals, using video editing software (VLC Media Player), ensuring a minimum of 70% overlap between images to guarantee accurate model building. In Agisoft Photoscan Professional, I imported a folder of these images as a “chunk” (terminology from Agisoft Photoscan) and applied an automated lens calibration to all images. Next, I aligned the photos within the software, which created a sparse point cloud of matched points, and I georeferenced (WGS 1984/UTM Zone 12N) obvious features from these

aligned photos. The program automatically attached all georeferenced markers, but I manually corrected the markers to ensure superior accuracy. Once all the markers are accurately aligned and georeferenced, I built a dense cloud. Next, I created a polygonal mesh then, I applied a texture to the mesh, based on imagery from the original-imported images, which constructs an accurate and realistic 3D model.

3D Model Annotation and Analysis

After I successfully built the digital 3D model, I annotated fractures and bed contacts in Photoscan. To ensure accuracy, I used a combination of the 3D model and original photographs. Next, I drew scanlines perpendicular to fracture orientation and kept the height of the scanline constant relative to bed contacts. If the outcrop shape varied significantly, I segmented the scanline to follow the same vertical position within the model and to keep the scanlines perpendicular to fracture strike.

RESULTS

Fracture Orientation

I analyzed 10 field and model scanlines located within and adjacent to the Red Hollow Canyon transfer zone (Fig. 1). The easternmost scanline, F1, is in the hanging wall of the Lion’s Den fault and is approximately 360 m above the base of the Navajo sandstone. Fractures from this scanline dominantly strike to the NNE and dip steeply ($>60^\circ$) to the WNW and ESE. Scanline M1 is in the hanging wall of the Lion’s Den fault, above the upper contact of the Navajo sandstone, within the basal unit of the Jurassic Carmel formation, and the dominant strike for the fracture set is to the NNE, with all fractures dipping from very steeply-WNW-dipping to vertical. Similarly, M2 is located in the hanging wall of the Lion’s Den fault and the dominant fracture strike is NNE, with similar very steep to vertical dips. This scanline is stratigraphically below scanline M1 and is located approximately 545 m above the base of the Navajo sandstone. Scanline M3, below M2, is also located in the hanging wall of the Lion’s Den fault, and is approximately 535 m above the base of the Navajo sandstone. The dominant fracture strike is NNE, with steep dips similar to those documented in M1 and M2.

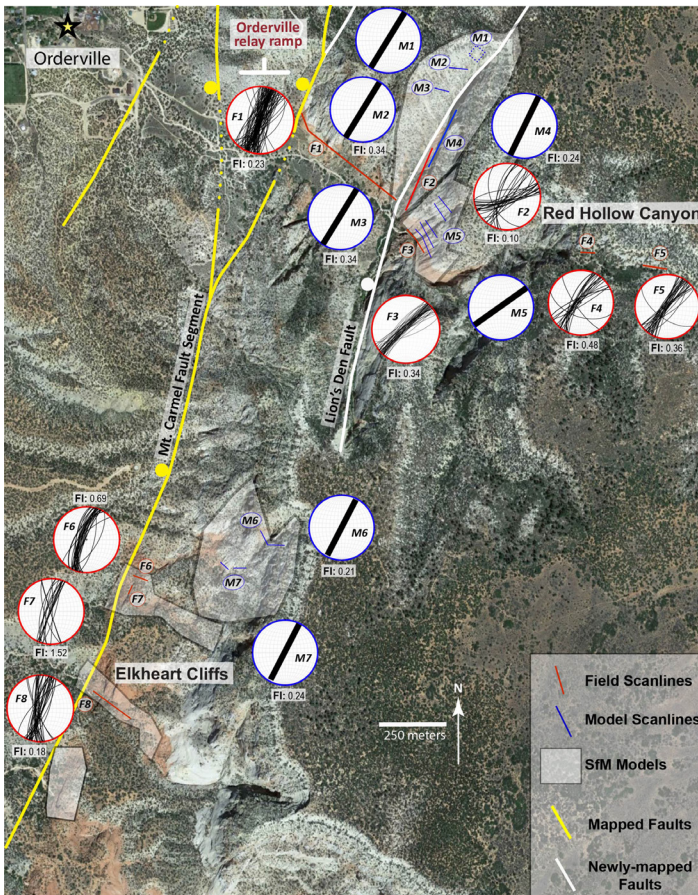


Figure 1. Orthophotograph displaying both the Red Hollow Canyon fault transfer zone to the north and Mt. Carmel segment fault locality at Elkheart Cliffs to the south. Field-based scanlines and stereonets are shown in red, and model scanlines and stereonets are shown in blue. Fracture intensity (FI) (m^{-1}) values are included for each stereonet. 6 locations where I built high-resolution SfM 3D models are outlined. The mapped and newly-mapped faults run from north to south (Schieffelbein, 2002).

Scanline M4 is from the footwall of the Lion's Den fault, within less than 10 m from the fault contact, and is approximately 485 meters above the base of the Navajo sandstone, with fractures that strike NNE and dip very steeply to vertically (Fig. 1). Scanline F2, stratigraphically below scanline M4, is in the footwall of the Lion's Den fault, approximately 360 m above the base of the Navajo sandstone, and is within approximately 10 m of the fault contact. Fractures from this scanline display a wider range in orientations than most localities, with strikes varying from NNE to ENE (Fig. 1). These ENE-striking fractures are not consistent with most fractures from the hanging wall of the Lion's Den fault (see scanline data from F1, M1, M2, and M3; Fig. 1). These fractures dip very steeply to vertically, with a range of dips from fractures that dip to the SE to fractures that dip to the

ENE.

Scanline F3 is about 360 m above the base of the Navajo sandstone and is adjacent to the Lion's Den fault. The dominant strike of this fracture set is NE and fractures steeply dip SE. Scanline M5 consists of 5 scanlines from different stratigraphic positions within the Navajo sandstone, from about 400 m to 550 m above the base of the unit. Similar to scanline F3, the fractures strike to the NE. Approximately 700 meters to east of the Lion's Den fault, along two scanlines (F4, F5) the dominant fracture strike is NE, with dips that range from steeply NW- or SE-dipping to vertical. Both scanlines are about 590 m above the base of the Navajo sandstone; these scanlines provide the stratigraphically-highest data from the Navajo sandstone.

We also analyzed fractures from 5 scanlines along the Elkheart Cliffs, where data are from the footwall of the Mt. Carmel segment, where a single fault accommodates all extension. To the south, three scanlines, F6-F8, in the footwall of the Mt. Carmel fault segment, are located about 220 meters above the base of the Navajo sandstone, and all record similar fracture orientations; fractures along scanlines F6, F7, and F8 strike NNE and steeply dip ESE or WNW. Scanline M6 is located about 465 m from the base of the Navajo sandstone and the dominant strike for this fracture set is NE, with steep to vertical dips. Scanline M7 is located about 355 m from the base of the Navajo sandstone, and the dominant fracture strike is NE, with all fractures displaying steep to vertical dips.

Variations in Lateral and Vertical Distributions

We found that where strain is accommodated by a single fault, the Elkheart Cliffs locality, intense fracturing and active erosion in the footwall (hanging wall rocks are not well exposed) make documentation of fractures within 30 meters of the fault impossible (Fig. 3). As shown on Scanline F8 (Fig. 3), from ~30 m to ~80 m from the contact, fracturing decreased in intensity with increasing distance, until fracturing sharply terminated at ~120 m from the fault. The average fracture intensity is 0.18 m^{-1} for the entire scanline (Table 1). Scanlines F6 and F7, located very close to the Mt. Carmel fault segment, have higher fracture intensities (0.69 m^{-1} and 1.52 m^{-1}) than all

other scanline locations. Across the transfer zone at Red Hollow Canyon, we found more broadly distributed fractures across >1000 m with values from 0.10 m⁻¹ to 0.48 m⁻¹ that displayed no relationship between fracture intensity and position relative to the fault contact.

Using a 3D digital model of the canyon wall near the Lion's Den fault, I documented fractures along five scanlines at different stratigraphic levels within the 200-m vertical exposure (Fig. 4). Along each scanline, positions of high fracture intensity do not correlate with scanlines above or below. In addition, the average fracture intensities vary significantly throughout exposed sections with values as low as 0.20 m⁻¹ at scanline M5A and M5C to 0.57 m⁻¹ at M5B (Fig. 4). Based on field observations and digital model data, these features of the fracture network appear to be related to changes in lithology and/or cross-bed set contacts that act as barriers to vertical fracture propagation.

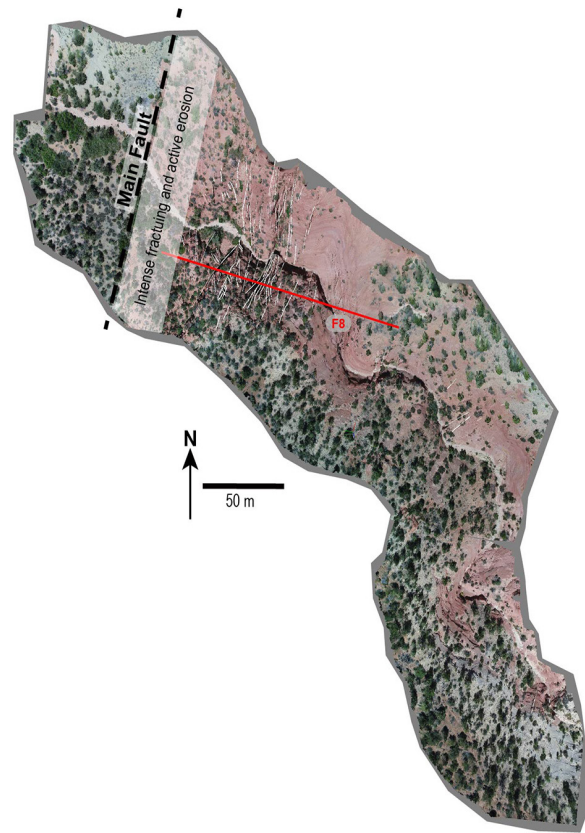


Figure 3. A high resolution 3D model of the single fault locality, the Mt. Carmel segment at Elkheart Cliffs, showing the main fault contact (dashed), fractures (white), and the field scanline F8 (red). The 30 m-wide zone of intensely-fractured rock and active erosion is highlighted.



Figure 2. Workflow used to build high-resolution 3D models in Agisoft Photoscan Professional.

DISCUSSION

At Elkheart Cliffs, fracture orientations from all field and model scanlines are sub-parallel to the Mt. Carmel fault segment, dipping the same direction as the fault. This includes scanlines M6 and M7, which are more than 250 m from the Mt. Carmel segment, suggesting that nearly all fractures formed in the same stress field as the fault, without any significant variations in local stresses. Similarly, in the Red Hollow Canyon transfer zone, fractures from scanlines F1 and M1-M4 strike NNE, sub-parallel to most faults across the transfer zone, suggesting fracture formation at those localities was nearly identical to that responsible for fault formation. However, to the east of the west-dipping Lion's Den fault, there is a 10-15° degree difference in the strike (NE) of fractures on scanlines F3-F5 and M5, with scanline F2, located within 10 m of the Lion's Den fault, displaying fractures with an even greater difference, ~20°, in fracture strike (ENE).

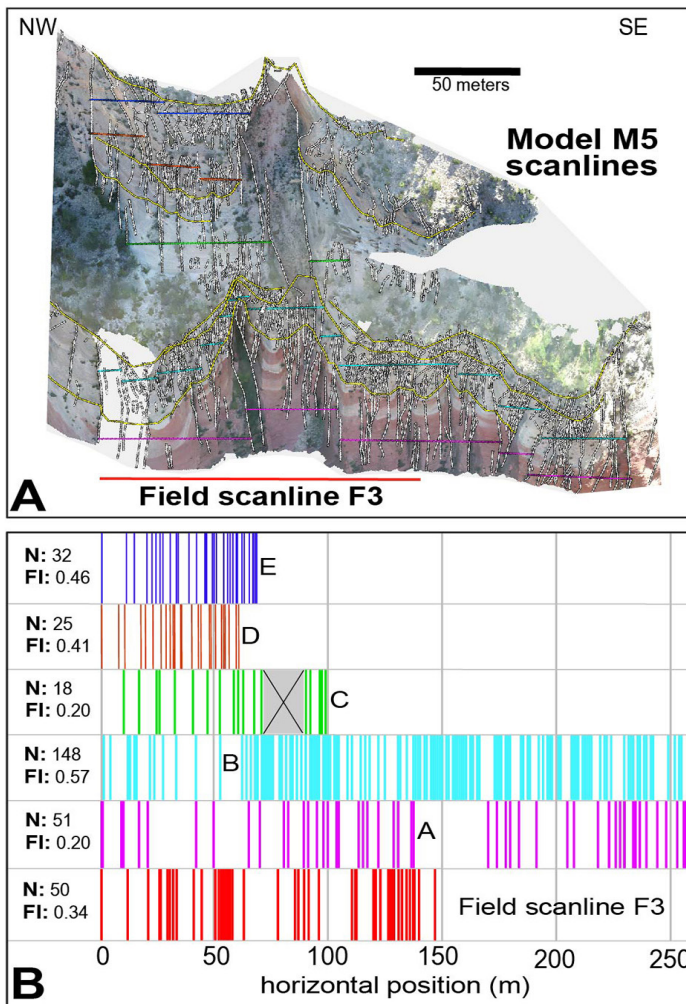


Figure 4. Transfer zone location displaying multiple scanlines. A. 5 vertically-stacked model scanlines, at location M5, including field scanline, F3. Scanlines are displayed on a screenshot of the 3D model built for this location. The model displays fractures (white) and bedding or changes in lithology (yellow). B. Fracture position with number of fractures measured (N) and fracture intensity (FI) (m-1).

I suggest that the Elkheart Cliffs fracture set is concurrent with the formation of the Mt. Carmel fault segment. However, further north, in Red Hollow Canyon, differences in fracture orientation laterally across Lion's Den fault indicate a more complicated fracture network with fractures that formed at different times relative to the faults. Fractures on the hanging wall, with the same orientation as the Lion's Den fault, likely formed at the same time as this fault and others in the transfer zone formed. Fractures that display different orientations, in the footwall of the fault, likely formed after the formation of the Lion's Den fault, with the fault acting as a stress barrier, preventing formation of fractures of those orientations in the hanging wall.

Importantly, fractures at all locations dip steeply ($>60^\circ$), indicating a stress field consistent with mixed mode failure in a tensile transitional stress field, with the minimum stress (tensional) oriented perpendicular to fracture strike. This stress field orientation is consistent with stresses responsible for Basin and Range extension in this region (e.g., Rogers et al., 2004), and the tensional minimum stress field is consistent fractures formed close to the surface, or at shallow depths with increased pore fluid pressures.

Fractures at the Red Hollow Canyon transfer zone locality are more broadly distributed, without changes in intensity associated with exposed faults, while at the single fault locality, Elkheart Cliffs, fracture intensity decreased rapidly with distance from the fault contact, with most fracturing focused adjacent to the fault contact. Thus, it is likely that the lateral distribution of stresses through rock volumes varied significantly between the two structural settings, creating fundamentally different fracture networks.

At Red Hollow Canyon, our data from different stratigraphic positions suggest that average fracture intensity and the position of high-intensity fracturing varies significantly in spite being in the same structural position relative to the Lion's Den fault. The significant variability from one vertical position to the next was most likely controlled by a combination of different mechanical behaviors (e.g., different elastic moduli) and by bed contacts within the Navajo sandstone acting as mechanical barriers to fracture propagation (e.g., McGinnis et al., 2015).

If the fracture network documented here was in the subsurface, our fracture data support a model where fluid flow would depend on structural position. At the transfer zone locality, the broader distributed fracture network would be expected to create a wide but diffuse zone of fluid flow, while the narrower but more intensely fractured zone adjacent to the single fault might create a more localized but perhaps more permeable pathway for fluids. The changes in the vertical fracture network is more complex, with a lack of vertical persistence through the stratigraphy. Although there were horizons with higher fracture intensities, these locations would be difficult to predict in the subsurface, and prediction of vertical connectivity of fluid pathways would also

Table 1. Fracture intensity (F.I.) values for field and model scanlines within the Jurassic Navajo sandstone.

Scanline Locations	Red Hollow Canyon									Elkheart Cliffs								
	F1	F2	F3	F4	F5	M2	M3	M4	M5					F6	F7	F8	M6	M7
									A	B	C	D	E					
Average F.I. (m⁻¹)	0.23	0.10	0.34	0.48	0.36	0.34	0.34	0.26	0.20	0.57	0.20	0.41	0.46	0.69	1.52	0.18	0.21	0.24

be challenging. Thus, while I might predict some features of the fracture network in relation to the different structural positions within the fault zone, it is far more difficult to determine how persistent these features are in three dimensions.

ACKNOWLEDGEMENTS

This material is based upon work supported by the Keck Geology Consortium and the National Science Foundation under Grant No. 1659322. Special thanks to my advisor, Dr. Ben Surpless, for his helpful advice and patience throughout this project. I would also like to thank Curtis Segarra, Charley Hankla, and Madison Woodley for making Utah an unforgettable experience.

REFERENCES

- Cooke, M., Mollema, P., Pollard, D., and Aydin, A., 2000, Interlayer slip and joint localization in the East Kaibab Monocline, Utah: field evidence and result from numerical modelling, In Cosgrove, J., and Ameen, M., eds.: *Forced Folds and Fractures*, Geological Society, London, v. 169, p. 23-49.
- Cowie, P.A. and Shipton, A.K., 1998, Fault tip displacement gradients and process zone dimensions: *Journal of Structural Geology*, v. 20, p. 983-997.
- Davatzes, N.C., and Aydin, A., 2003, Overprinting faulting mechanisms in high porosity sandstones of SE Utah: *Journal of Structural Geology*, v. 25, p. 1795–1813, doi: 10.1016/S0191-8141(03)00043-9.
- Davis, G.H., 1999, Structural geology of the Colorado Plateau region of southern Utah: *Geological Society of America Special Paper 342*, 127 p.
- Doelling, H.H, Davis, F.D., and Brandt. C.J., 1989, The geology of Kane County, Utah, *Geology, Mineral Resources, Geologic Hazards: Utah Geological and Mineral Survey Bulletin 124*, 192 p.
- Ferrill, D.A., Stamatakos, J.A., and Sims, Darrell, 1999, Normal fault corrugation- implications for growth and seismicity of active normal faults: *Journal of Structural Geology*, v. 21, p. 1027-1038.
- Gregory, H.E., 1951, The geology and geography of the Paunsaugunt region Utah: *U.S. Geological Survey Professional Paper 226*, p. 1-116.
- Hintze, L.F., 1973, *Geologic History of Utah: Brigham Young University Geology Studies 20*, 181 p.
- Johnson, K., Nissen, E., Saripalli, S., Arrowsmith, R., McGarey, P., Scharer, K., Williams, P., and Blisniuk, K., 2014, Rapid mapping of ultramafic fault zone topography with structure from motion: *Geosphere*, v. 10, p. 969 – 986.
- McGinnis, R.N., Ferrill, D.A., Smart, K.J., Morris, A.P., Higuera-Diaz, C., and Prawica, D., 2015, Pitfalls of using entrenched fracture relationships. Fractures in bedded carbonates of the Hidden Valley fault zone, Canyon Lake Gorge, Comal County, Texas: *American Association of Petroleum Geologists Bulletin*, v. 99, p. 2221-2245.
- Peterson, F., and Pippingos, G., 1979, Stratigraphic relations of the Navajo Sandstone to Middle Jurassic formations, southern Utah and northern Arizona: *Professional Paper*, doi: 10.3133/pp1035b.

- Reber, S., Taylor, W.J., Stewart, M., and Schiefelbein, I.M., 2001, Linkage and reactivation along the northern Hurricane and Sevier faults, southwestern Utah, in Erskine, M.C., Faulds, J.E., Bartley, J.M., and Rowley, P.M., eds., The geologic Transition, High Plateaus to Great Basin - a symposium and field guide: Utah Geological Association Publication 30 and Pacific Section American Association of Petroleum Geologists Guidebook GB 78, p. 379-400.
- Rogers, C., Myers, D., and Engelder, T., 2004, Kinematic implications of joint zones and isolated joints in the Navajo Sandstone at Zion National Park, Utah: Evidence for Cordilleran relaxation: *Tectonics*, v. 23, TC1007, doi:10.1029/2001TC001329
- Sargent, K.A. and Philpott, B.C., 1987, Geologic map of the Kanab quadrangle. Kane County, Utah, and Mohave and Coconino Counties, Arizona: U.S. Geological Survey Map GQ-1603.
- Schiefelbein, I., 2002, Fault segmentation, fault linkage, and hazards along the Sevier fault, southwestern Utah [M.S. thesis]: Las Vegas, University of Nevada at Las Vegas, 132 p.
- Sibson, R. H., 1987, Rupture interaction with fault jogs: *American Geophysical Union: AGU*, 37, p. 157-167, doi:10.1029/GM037p0157
- Taylor, W.J., Stewart, M.E., Orndorff, R.L., 2001, Fault segmentation and linkage: examples from the Hurricane fault, southwestern U.S.A., in Erskine, M.E., Faulds, J.E., Bartley, J.M., and Rowley, P.D., eds., The geologic Transition, High Plateaus to Great Basin - a symposium and field guide: Utah Geological Association Publication 30 and Pacific Section American Association of Petroleum Geologists Guidebook GB 78, p. 113-126.

GEOMECHANICAL ANALYSIS OF SEDIMENTARY LAYERING AS A STRUCTURAL CONTROL ON FAULT PROPAGATION

CURTIS SEGARRA, Trinity University
Research Advisor: Dr. Benjamin Surpless

INTRODUCTION

Deformation associated with normal fault propagation and displacement places controls on the distribution and flow of sub-surface fluids. With a better understanding of how sedimentary units deform in response to a propagating fault, scientists can better predict how fluids might flow through the system at different stages of displacement. Though previous researchers have acknowledged the effects of sedimentary layering as barriers to fault propagation (e.g. Cooke and Pollard, 1997; Cooke et al., 2001; Peacock, 2002; Hayano and Ishii, 2016), previous research has failed to produce a systematic, quantitative analysis of the role of mechanical layering on fault tip propagation. Therefore, building upon previous geomechanical modeling techniques (Smart et al., 2004, 2009, 2010b, 2010a, 2012; Doff, 2015; Sattari and Eaton, 2015), I use ABAQUS/Standard finite element modeling software (by Dassault Systemes, 2018) to create an experimental finite element model that permits me to analyze the influence of stratigraphic layering upon stress and strain ahead of a fault tip.

I use finite element analysis (FEA), a method for calculating a specific output quantity, such as stress or strain, as a solution to a defined mathematical problem, within a complex, multi-piece model (Cook, 1995). By dividing a model into “elements”, across which displacement, stress, and strain can be interpolated, I analyze the spatial distribution of stress and strain fields (Cook, 1995). I use this technique to address two research goals: 1. To systematically analyze the influence of planar bedding upon stress and strain fields ahead of a propagating normal fault;

and 2. To develop a predictive model of fracture distribution during propagation of a normal fault through bedded stratigraphy. This approach permits me to control the most important physical variables (e.g., bedding thickness, fault displacement, material properties of rock layers), and the software permits me to efficiently model changes in different factors (e.g., coefficient of friction between beds, number of beds) across a range of values.

METHODOLOGY

Model Development

My model replicates a 60°-dipping, planar, dip-slip normal fault, a geometry that represents normal fault systems at depths shallower than 10 km (Jackson and McKenzie, 1983). My model captures initial stages of propagation of a pre-existing fault into undeformed sandstone beds with thicknesses on the several-meter scale range; I do not examine initial fault formation, but instead, I focus my modeling efforts on initial stages of propagation through layered strata.

I use a model geometry similar to the geometry used by Smart et al. (2010a). The underlying fault block of the footwall (B1, Fig. 1) imposes displacement on the model. The overlying fault block of the footwall (B3, Fig. 1), provides an overburden load and is not restrained. Pinned fault blocks in the hanging wall (B2 and B3, Fig. 1) cannot move horizontally nor vertically, ensuring displacement occurs along the fault plane.

The mesh density, as defined by the size of “elements,” which each model piece is divided into for mathematical interpolation of stress and strain,

controls the permissible deformation of each model piece and the resolution of the results. Because I do not intend to deform the four bounding blocks of the model (B1 through B4), I define a coarse mesh for the four bounding blocks. Mesh resolution of the test beds is fine near the center of the beds and coarse near the edges of the model, ensuring higher-resolution analysis near the propagating fault. The vertical mesh resolution is constant; each element is 1 meter tall. Since the four fault blocks surrounding the test beds do not deform, the mesh resolution does not affect the results; coarser mesh in the fault blocks aids computational efficiency.

Following Smart et al.'s (2010a) modeling protocol, I employ elastic-plastic material behavior for the deformable beds and an elastic material with a high Young's Modulus (30 GPa) for the fault blocks (B1 through B4, Fig. 1); the material properties (Table 1) are held constant throughout each model.

Within my model, I define the fault surface and orientation as a planar, non-frictional contact. Similarly, I define contacts between the test beds and the fault blocks as planar, non-frictional contacts. I do not analyze the role of these outer contacts. The contacts between test strata (T1-T3, Fig. 1) are frictional planar contacts; I vary the coefficient of friction between test beds from 0.15 μ to 0.9 μ .

Within test strata, I prescribe a pre-existing internal stress state for all elements (stress tensor, Fig. 1); I pair this stress with inward forces applied to the top and sides of the model (Fig. 1), which simulate stresses due to a small overburden. There are no pre-existing weaknesses in the undeformed test beds.

Analysis

In the modeling presented here, I perform a three-step analysis. In the initial step, I apply boundary conditions. In the second step, I apply forces to the model, allowing the model to achieve equilibrium and begin displacement. Total displacement is incremented non-uniformly based upon the computational complexity of the model. Finally, once the displacement is complete, I review the results in the output step. I apply this procedure to one 20-meter-thick bed, two 10-meter-thick beds, three 6.67-meter-

thick beds, four 5-meter-thick beds, and five 4-meter-thick beds, which permits me to analyze the influence of planar bedding upon the stress and strain fields within the beds. Additionally, I vary the coefficient of friction between the beds, which permits me to assess the influence of inter-layer friction upon stress and strain field development.

RESULTS

Initial Plastic Failure

For each iteration of the model, initial plastic failure occurred at displacements between 0.030 meters and 0.040 meters and was spatially localized. Some models failed at only one region, others at two regions (Fig. 2), with failure restricted to the lowermost and uppermost layers of the test package (Fig. 2). This means that, where simultaneous initial failure occurred, initial plastic failure occurred close to the propagating fault tip (1-4 meters from the fault tip) as well as up to 19 meters from the propagating tip. The distribution of simultaneous initial failure, where three or more beds were deformed, is symmetrical about the center of the test strata (Fig. 2)

Stress Distribution

At displacements causing initial plastic failure, in-plane principal stress is highest in the uppermost and lowermost mechanical layers, reaching values of over 10 MPa (Fig. 2). Within a single layer, in-plane principal stress is highest in the base of the hanging wall of the test layer (Fig. 2). Additionally, the model with no layering exhibits a smooth gradient of stress

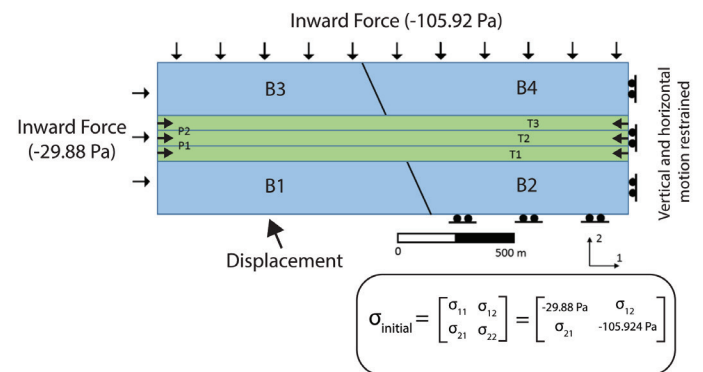


Figure 1. Example of model geometry and forces. This example shows three test beds (T1-T3).

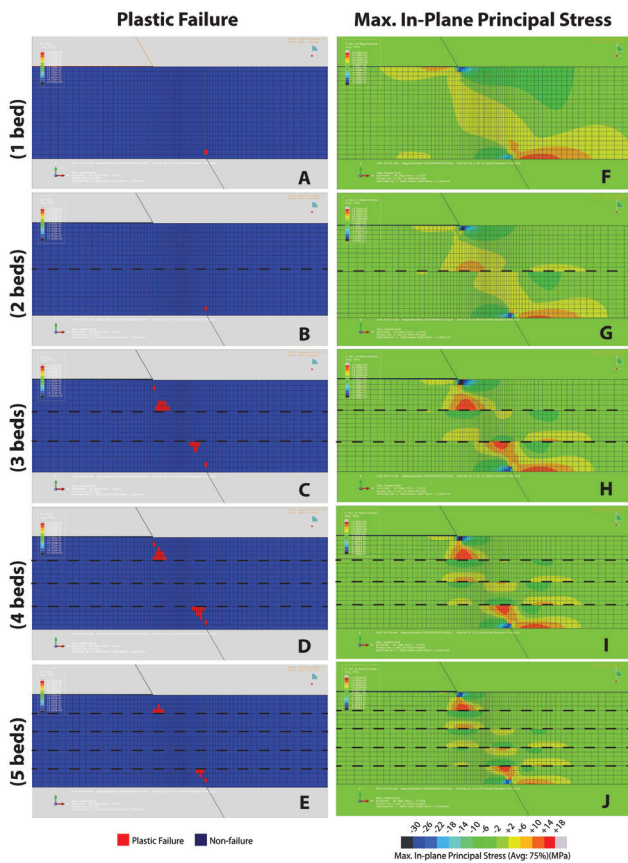


Figure 2. Initial plastic failure (A-E) and stress gradients (F-J) at low levels of displacement, with constant friction between layers (0.15μ). Dashed line indicates bedding plane. Note the presence of three or more beds (C-E) results in multiple locations of simultaneous plastic failure. Note that initial failure is confined to the lowermost and uppermost mechanical layers in each model (A-E). Note that mechanical layering (G) through (J) distorts the smooth gradient seen when no layering is present (F). Note how increasing mechanical layering allows for higher stress concentrations near the center of the test strata (G-J).

ahead of the propagating fault tip (Fig. 2). When mechanical layering is present, this smooth in-plane gradient becomes discontinuous, strongly affected by boundaries between mechanical layers (Fig. 2). In addition, in-plane principal stress near the center of the multi-bed package of test strata (in the center of the model) is elevated relative to the level of stress in the center of the single bed model. Although not explored in detail here, increased friction between mechanical layers results in the development of a more continuous gradient of in-plane principal stress from one mechanical boundary to the next (model not shown).

Strain Development

When only one mechanical layer is deformed in the

model, increased displacement leads to a smooth, along-fault-plane accumulation of in-plane principal strain. At displacement levels causing initial plastic failure, the presence of mechanical layering discretizes strain at the mechanical boundaries (Fig. 3). In every model with mechanical layering, logarithmic in-plane principal strain is maximized in the uppermost and lowermost mechanical layers (similarly indicated by the location of initial plastic failure) (Fig. 3).

Through-going Failure and Stress Distribution

With continued displacement (0.07 to 0.09 m), through-going plastic failure occurred throughout the entire 20 m test section (Fig. 4). This increased displacement caused stress gradients ahead of the propagating fault tips to become less discontinuous than in the earliest stages of propagation (Fig. 4). By the time through-going failure occurred, stress was relatively concentrated along the plane of the propagating fault, but off-fault-plane distributions of stress do occur. With increasing friction between layers, stresses are distributed further from the fault plane (model not shown).

DISCUSSION

I used 2D finite element modeling to assess the role of mechanical layering in the initial stages of normal fault tip propagation. By varying the number of mechanical layers present (one layer to five layers), I found that the presence of layers inhibits the development of a smooth stress gradient ahead of the propagating fault tip. This leads to simultaneous, discontinuous plastic failure at multiple locations ahead of the fault tip during the initial stages of propagation. With the material properties defined to represent a 20 m thick test section of sandstone, I find that a displacement of 0.03 to 0.04 meters is sufficient to cause plastic failure.

With continued displacement (0.07 to 0.09 m), through-going plastic failure occurred throughout the entire 20 m test section. This increased displacement caused stress gradients ahead of the propagating fault tips to become more continuous than in the earliest stages of propagation. As such, by the time through-going failure occurred, stress was primarily

Max. Log. In-Plane Principle Strain

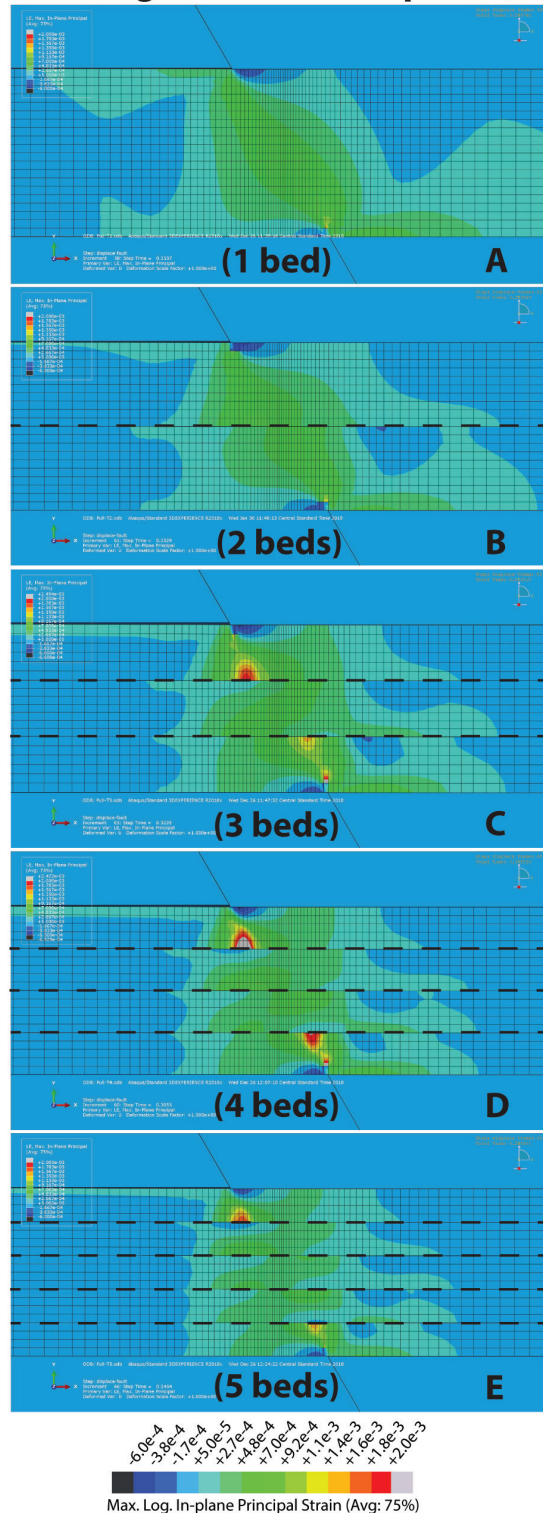


Figure 3. Maximum logarithmic in-plane principal strain gradients at low levels of displacement, with constant friction between layers (0.15μ). (A) No mechanical layering, (B) two layers, (C) three layers, (D) four layers, (E) five layers. Dashed line indicates bedding plane. Note that mechanical layering (B) through (E) distorts the smooth gradient seen when no layering is present (A). Note how increasing mechanical layering allows for strain accumulation in the uppermost and lowermost layers.

concentrated in-plane with the propagating fault.

I find that varying the coefficient of friction of the contacts between mechanical layers has minimal effect on the development of plastic failure; however, varying friction does affect the distribution of stress within the test strata. Increasing friction leads to a smoother stress gradient and minimizes the discontinuous localization of strain at mechanical layer boundaries.

At all levels of displacement, stress tends to accumulate in the hanging wall, out of plane from the fault. Under 0.07 m to 0.09 m displacement, increasing friction causes this accumulation of stress in the hanging wall to occur further from the fault plane.

My models suggest that the initial stages of fault tip propagation of a normal fault within a layered system are not characterized by linear stress gradients leading to in-plane plastic failure. Rather, the initial stages of propagation are characterized by complex patterns of stress accumulation. The presence of discontinuous regions of increased stress along layer boundaries leads to simultaneous plastic failure at multiple locations ahead of the propagating fault tip. This suggests that under low levels of displacement, a layered system is more likely to produce multiple, discontinuous fracture regions than in a single-layer system. Within a field setting, I would expect fracturing and potential fluid conduits to develop where the plane of a propagating fault tip intersects bedding planes. Additionally, my modeling suggests regions of increased stress off-plane from the propagating fault tip. In my model, these stress accumulations occurred in the hanging wall, but I would expect differing boundary conditions to lead to similar accumulations in the footwall. My results suggest that fracturing would be likely to occur away from the projected fault plane, localized along bedding plane boundaries.

As one of the first attempts to model the influence of planar bedding upon the stress and strain fields ahead of a propagating normal fault, my findings should be considered preliminary. However, these results reveal the power of finite element analysis to predict

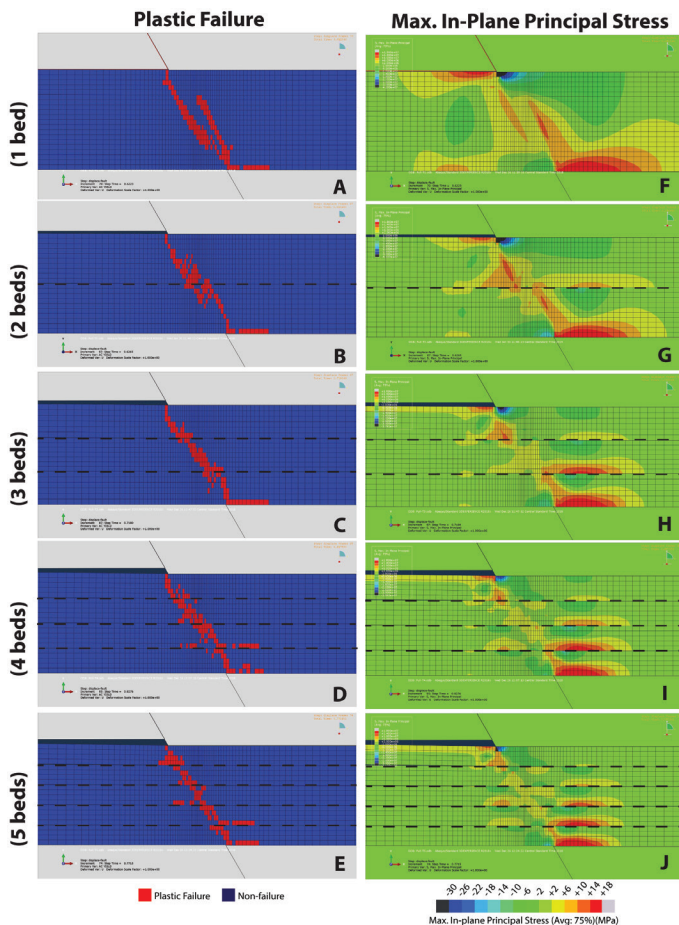


Figure 4. Initial plastic failure (A-E) and stress gradients (F-J) and at levels of displacement that cause through-going plastic failure, with constant friction between layers (0.15μ). Dashed line indicates bedding plane. Note the presence of four or more beds (D & E) results in plastic failure along multiple bedding planes. Note that failure accumulates where the hanging wall contacts the grey fault block (A-E). Note that mechanical layering (G-J) distorts the smooth stress gradient seen when no layering is present (F). Note how increasing mechanical layering allows for increased stress concentrations off-plane from the fault, in the hanging wall (F-J).

the distribution of fracture initiation relative to a fault propagating through bedding. Thus, an FEA approach may aid in subsurface resource conduit exploration and for modeling stress and strain fields near faults.

ACKNOWLEDGEMENTS

This material is based upon work supported by the Keck Geology Consortium and the National Science Foundation under Grant No. 1659322. Additionally, my research was funded, in-part, by the Trinity University Geosciences Department. Finally, I would like to thank Dr. Kevin Smart at SWRI for showing me how to use ABAQUS effectively.

REFERENCES

- Cook, R.D., 1995, Finite element modelling for stress analysis: John Wiley & Sons, Inc.
- Cooke, M.L., and Pollard, D.D., 1997, Bedding-plane slip in initial stages of fault-related folding: *Journal of Structural Geology*, v. 19, no. 3-4, p. 567-581.
- Cooke ML, and Underwood, C.A., 2001. Fracture termination and step-over at bedding interfaces due to frictional slip and interface opening, *Journal of Structural Geology*, 23: 223–238.
- Dassault Systèmes, 2018, ABAQUS/Standard 3DEXPERIENCE [Computer Software].
- Doff, J., 2015, Geomechanical modelling of a fault-propagation fold [bachelor's thesis]: TUDelft, 2015.
- Hayano, A., and Ishii, E., 2016, Relationship between faults oriented parallel and oblique to bedding in Neogene massive siliceous mudstones at the Horonobe Underground Research Laboratory, Japan: *IOP Conf. Ser.: Earth Environ. Sci.*, v. 44.
- Jackson, J., and McKenzie, D., 1983, The geometrical evolution of normal fault systems: *Journal of Structural Geology*, v. 5, p. 471-482.
- Peacock, D.C.P., 2002, Propagation, interaction and linkage in normal fault systems: *Earth-Science Reviews*, v. 58, p. 121-142.
- Sattari, A., and Eaton, D.W., 2015, 3D finite element modelling of fault-slip triggering caused by pore-pressure changes in *GeoConvention 2015: New Horizons*, Calgary, Canada.
- Smart, K.J., Ferrill, D.A., Sims, D.W., Franklin, N.M., Ofoegbu, G.I., Morris, A.P., 2004, Integrated structural analysis and geomechanical modelling: an aid to reservoir exploration and development: *Gulf Rocks 2004 – 6th North American Rock Mechanics Symposium: Rock Mechanics Across Borders & Disciplines*. Houston, TX, 5–9 June 2004: ARMA/NARMS Paper 04–470.

- Smart, K.J., Ferrill, D.A., and Morris, A.P., 2009, Impact of interlayer slip on fracture prediction from geomechanical models of fault-related folds: American Association of Petroleum Geologists Bulletin 93, 1447–1458.
- Smart, K.J., Ferrill, D.A., Morris, A.P., Bichon, B.J., Riha, D.S., and Huyse, L., 2010a, Geomechanical modelling of an extensional fault-propagation fold: Big Brushy Canyon monocline, Sierra Del Carmen, Texas: American Association of Petroleum Geologists Bulletin 94, 221–240.
- Smart, K.J., Ferrill, D.A., Morris, A.P., and McGinnis, R.N., 2010b, Geomechanical modelling of a reservoir-scale fault-related fold: the Bargy anticline, France: 44th U.S. Rock Mechanics Symposium, ARMA Paper 10–201.
- Smart, K.J., Ferrill, D.A., Morris, A.P., and McGinnis, R.N., 2012, Geomechanical modelling of stress and strain evolution during contractional fault-related folding: Tectonophysics, v. 576-577, p. 171-196.
- Smart, K.J., 2018, personal communication.

GIS ANALYSIS OF SUBSIDIARY STRUCTURES WITHIN A MAJOR NORMAL FAULT TRANSFER ZONE

MADISON WOODLEY, Mount Holyoke College
Research Advisor: Michelle Markley

ABSTRACT

This study focuses on fractures in the transition zone between the Basin and Range province and the Colorado Plateau. These fractures are in the segmented Sevier normal fault transfer zone near Orderville, Utah. This study incorporates ArcGIS to analyze mapped fractures using their orientations on a scanline in the exposed Jurassic Navajo sandstone for two localities: Red Hollow Canyon and Elkheart Cliffs. The Red Hollow Canyon and Elkheart Cliffs are in the steeply west-dipping Sevier fault zone. The first locality, at Red Hollow Canyon, is within a transfer zone between fault segments, where multiple faults and a relay ramp accommodate extension. The second locality, at Elkheart Cliffs, exposes deformation associated with a simple fault geometry, where the single fault accommodates for extension. The Red Hollow Canyon locality has two sets of fractures with different orientations in contrast to a single fracture set in the Elkheart Cliffs. The multiple faults in the Red Hollow Canyon locality caused substantial strain to the Navajo sandstone, which resulted in a higher rate of clustering for all fractures.

INTRODUCTION

The Sevier Fault is a segmented, steeply west-dipping normal fault system in the Basin and Range province (Davis, 1999; Lund et al., 2008). The fault zone extends for over 300 km, from northern Arizona to southern Utah (Reber et al., 2001). Since the Miocene, the Sevier Fault has accommodated for extension in the transition zone in southern Utah that lies between the Basin and Range province and the Colorado Plateau. The main study area in southern Utah is at the

Orderville geometric bend: a complex region of the Sevier fault zone characterized by different transfer zone geometries (Reber et al., 2001; Lund et al., 2008). The studied fractures in the Sevier fault zone are within the well-researched lithology of the exposed Jurassic Navajo sandstone (Schiefelbein, 2002; Simoneau et al., 2016).

The Sevier Fault near Orderville, Utah is a complex part of the fault zone, with relay ramps and multiple normal faults that accommodate significant displacement in the Red Hollow Canyon (Schiefelbein, 2002; Simoneau et al., 2016). The Red Hollow Canyon has two, possibly three, fault segments (Doelling, 2008) that intersect the mapped fracture network for this study. In the second locality, Elkheart Cliffs, the fault zone is less complicated and has only one fault that is to the western edge of the cliffs. This study's data shows that the stress fields and strain in the Navajo sandstone for each locality affected the relative orientations of fractures and their clustering.

METHODS

I built the primary ArcGIS map used in this study from orthorectified imagery (captured in 2011, 2014, and 2016), a 10-m resolution DEM for the region, and outlines of major geological features in the region compiled during a previous study (Simoneau et al., 2016). We exported spatial field data, including field observations and sample locations, from a handheld GPS unit and imported this information into ArcGIS. I added geologic map data from Schiefelbein (2002) to show rock units and major faults exposed in the area. I imported the map data and georeferenced it by matching contour lines in the plates to the contour

lines of the base topographic map I created in ArcGIS.

I merged the four individual DEMs into a single, simplified GIS layer. I created contour lines spaced 20 feet apart for this study by converting the lowest elevation value, 1492.61 meters, to feet and adding a z factor. The z factor changed all DEM values from meters to feet for the entire region.

I drew the major faults in ArcGIS using Schiefelbein's (2002) plates to create a separate Faults layer. I replaced the original orthorectified imagery with Google Earth imagery because of the higher resolution in the Google Earth images. To use the imagery from Google Earth Pro (Google Earth, 2018), I panned to select an area, exported and saved the image, added the image to ArcGIS, and then georeferenced it. I georeferenced each Google Earth by matching a minimum of three points from the base orthorectified images to verify the dimensions, latitude, and longitude for each imported image.

I created an ArcGIS layer to build a fracture dataset in which I drew lines on top of visible fractures in the Navajo sandstone. ArcGIS calculated the fracture orientations by adding a geometrical attribute called "Bearing" to each fracture. I quantified the inter-fracturing spacing with the Measure tool for the distances between each fracture along a specific scanline. The scanline is a projected horizontal line used to quantify discontinuities in rock units.

I excluded one region from my study. In Red Hollow Canyon, the canyon narrows and visibly warps any potential mapped fractures in the Google Earth images. This is likely due to the shading and extreme topographic relief in the canyon that is in the eastern part of Red Hollow Canyon.

EQUATIONS

In order to quantify fracture spacing and intensity, I created scanlines in ArcGIS by drawing lines perpendicular to fracture sets in a rock unit (Fig. 1C). The scanlines start from the first fracture in a scanline and end with the last fracture in the scanline. I calculated the fracture intensity by dividing the number of fractures by the length of the scanline. The

units for fracture intensity are fractures per meter.

$$\text{Fracture intensity (1)} = \# \text{ of fractures} / \text{scanline length (m)}$$

The average spacing between these fractures is the inverse of equation 3, or the length of the scanline divided by the number of fractures. The units for the average spacing between fractures are m/fracture.

$$\text{Average spacing (2)} = \text{scanline length (m)} / \# \text{ of fractures}$$

The relative clustering of fractures for each scanline is the coefficient of variation, C_v . The C_v is the standard deviation of the inter-fracture spacing population divided by the mean of the same population of fractures (Kagan and Jackson, 1991; Gillespie et al., 1999; Supak et al., 2006; Hooker et al., 2013). The relative clustering, C_v , is unitless.

$$C_v (3) = \text{standard deviation of spacing} / \text{mean of spacing}$$

If C_v equals 0, the inter-fracture spacing is considered regular and evenly spaced. If the C_v is equivalent to 1, the fractures are randomly spaced and considered more clustered. For C_v values greater than 1, the data reflects more clustering (Gillespie et al., 1999).

RESULTS

Red Hollow Canyon Scanlines

The fracture network for the first locality, Red Hollow Canyon, consists of two sets of fractures on 13 scanlines. The 13 scanlines are sub-divided into two regions: RHC-1 and RHC-2. These two regions each represent a single set of fractures that show different orientations across a major transfer zone in the Red Hollow Canyon. The first fracture set, RHC-1, is within the transfer zone between several fault segments in the locality. The other region, RHC-2, has fractures that lie in the footwall of the eastern-most fault in the major transfer zone.

The first region, RHC-1, in the Red Hollow Canyon has three locations: RHC_WT, RHC_MID, and RHC_NF1 (Table 1). The first two locations in this region trend NNE. These fractures have orientations that range from 23.6° to 30.1°. The third location in this region has a more northerly trend with a lower mean

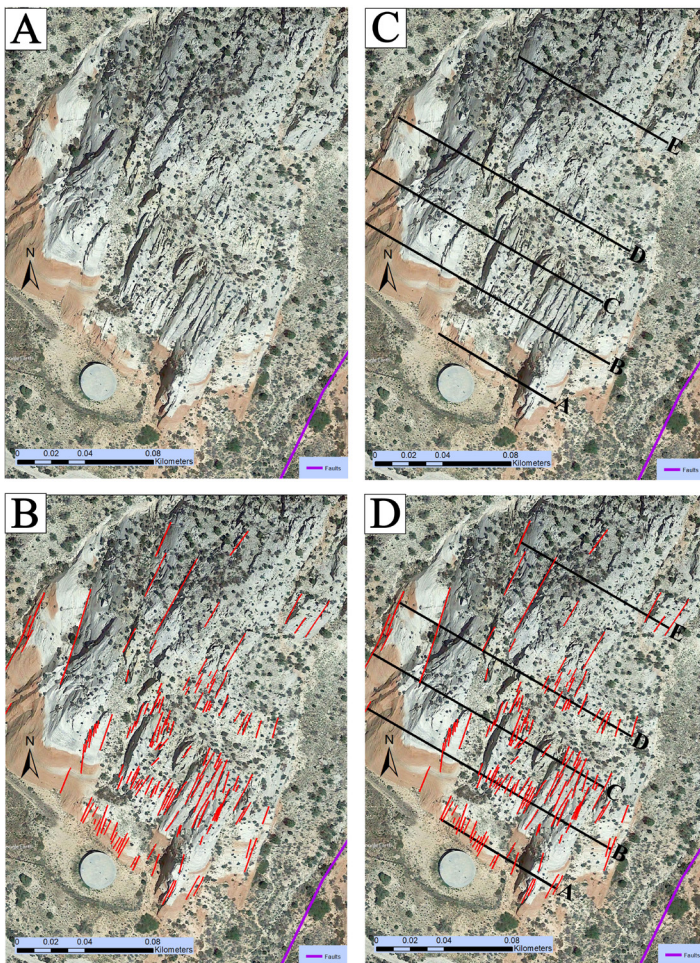


Fig. 1: Sequence of fracture mapping for the Red Hollow Canyon locality. The Red Hollow Canyon is located in southern Utah, outside the town of Orderville, Utah. This part of the locality is between multiple faults segments in a transfer zone. (A) Google Earth image of visible fractures in exposed rock at the western edge of the major transfer zone in Red Hollow Canyon. (B) Lines representing visible fractures in the exposed rock are shown in red. The purple line represents a fault segment. (C) The horizontal and parallel scanlines in black are perpendicular to the fracture network. The scanlines pictured are scanlines A to E in Table 1 (i.e. the RHC_WT lines). The scanlines start with RHC_WT1 at the base of the rock face and end with RHC_WT5 at the northernmost scanline. (D) The previous figures are layered into one image to show the scanlines with the mapped fractures.

bearing of 15.1° .

The second region, RHC-2, in the Red Hollow Canyon has only location, RHC_LD, compared to the three locations in RHC-1. The fractures in this region have RHC_LD in the beginning of their name in Table 1. RHC-2 has a second set of fractures that trend ENE with steeper orientations. These fractures trend ENE with a range of orientations from 54.1° to 61.3° .

These two sets of fractures are combined in a separate attribute called RHC-ALL. RHC-ALL combines

the two regions, RHC-1 and RHC-2, in Table 3 for side-by-side comparison to the Elkheart Cliffs data (ELHEART). The RHC-ALL and ELKHEART data do not show a significant relationship with fracture intensity.

Elkheart Cliffs Scanlines

The second locality, Elkheart Cliffs, has a single set of fractures on nine scanlines. The Elkheart Cliffs fractures are in an area with a simpler geometry than Red Hollow Canyon. These fractures are near a single fault segment versus a major transfer zone with multiple fault segments. The spacing between the fractures in the Elkheart Cliffs is smaller than the spacing in Red Hollow Canyon. This locality has orientations similar to the first region, RHC-1, in the Red Hollow Canyon data.

The Elkheart Cliffs data are separated into three locations: ELK_NS, ELK_MS, and ELK_SS. Each of these locations trend NNE and have fractures with a mean bearing similar to the RHC-1. The Elkheart Cliffs fractures show a larger range of orientations across all three locations than both regions in the Red Hollow Canyon. The orientations in the three locations in the Elkheart Cliffs ranges from 17.8° to 29.2° .

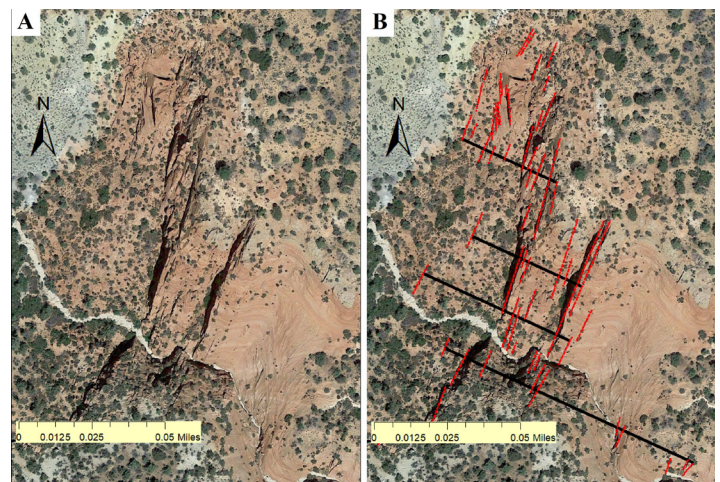


Fig. 2: The fracture mapping for the northernmost location, ELK_NS, of the Elkheart Cliffs data. (A) The exposed rock units visible with Google Earth Imagery without any mapped fractures. (B) The mapped fractures in red are perpendicular to the parallel scanlines in black. These scanlines include scanlines N to Q in Table 1 (i.e. the ELK_NS lines). The scanlines start with ELK_NS1 south of the white footpath and end with ELK_NS4 at the northernmost scanline.

Table 1: Raw Data of Fracture Mapping Grouped by Study Area

SCANLINE	LOCATION	MEAN BEARING (°)	LENGTH (m)	# OF FRACTURES	FRACTURE INTENSITY (fracture/m)	MEAN SPACING (m/fracture)
A	RHC_WT1	25.3	80.2	16	0.200	5.0
B	RHC_WT2	24.3	166.8	23	0.138	7.3
C	RHC_WT3	23.6	158.0	16	0.101	9.9
D	RHC_WT4	24.0	158.6	15	0.095	10.6
E	RHC_WT5	30.1	102.1	5	0.049	20.4
F	RHC_MID1	32.2	36.2	3	0.083	12.1
G	RHC_MID2	25.0	67.7	4	0.059	16.9
H	RHC_NF1	15.1	13.2	4	0.303	3.3
I	RHC_LD1	61.3	255.4	25	0.098	10.2
J	RHC_LD2	60.8	188.3	17	0.090	11.1
K	RHC_LD3	54.1	102.4	13	0.127	7.9
L	RHC_LD4	59.5	108.3	9	0.083	12.0
M	RHC_LD5	55.0	92.5	7	0.076	13.2
N	ELK_NS1	26.0	151.2	9	0.060	16.8
O	ELK_NS2	21.5	88.8	6	0.068	14.8
P	ELK_NS3	20.5	67.3	8	0.119	8.4
Q	ELK_NS4	19.0	57.7	10	0.173	5.8
R	ELK_MS1	17.8	190.9	6	0.031	31.8
S	ELK_MS2	29.2	24.2	4	0.165	6.1
T	ELK_MS3	27.5	42.4	3	0.071	14.1
U	ELK_MS4	22.9	47.5	7	0.147	6.8
V	ELK_SS1	19.6	25.2	6	0.238	4.2

Clustering

The calculated C_v for the Red Hollow Canyon locality is 1.2-1.3 for both fracture sets (Table 2). These values indicate a clustered and randomly spaced fracture network. The Elkheart Cliffs has a smaller C_v of 0.8 (Table 2). These fractures are more evenly spaced and less random than the Red Hollow Canyon fractures.

The scanline data and clustering of the fractures indicates that there are two sets of fractures for the Red Hollow Canyon locality with two different orientations. The first set of fractures in Red Hollow Canyon (RHC-1) are NNE, with azimuths close to 25 degrees. The second set of fractures (RHC-2) are ENE, with azimuths around 55 degrees. The fractures in Elkheart Cliffs are also NNE and have similar orientations to RHC-1. The fractures in Red Hollow Canyon show higher clustering than the more regular Elkheart Cliffs fractures.

DISCUSSION

The two fracture sets, RHC-1 and ELKHEART, have similar orientations, which suggests they formed at a similar time in the same stress field. The third fracture set, RHC-2, has a different trend and orientation so these fractures are from a second stress field in the Red Hollow Canyon. The complex system of multiple faults in the Red Hollow Canyon caused more strain on the Navajo sandstone rock unit. This increased strain in the rock increased the clustering in the Red

Hollow Canyon locality.

The variations in the fracture clustering between the two localities is likely related to fault zone dynamics. At Elkheart Cliffs, the Sevier fault zone has only one fault segment, and fracture clustering is relatively low. At Red Hollow Canyon, there are at least two significant normal faults that bookend a transfer zone, which resulted in a relatively higher amount of clustering. The rates of clustering in the Red Hollow Canyon are consistent for both regions: RHC-1 and RHC-2. The transfer zone with multiple faults and the higher strain on the Navajo sandstone in Red Hollow Canyon increased the clustering of fractures.

ACKNOWLEDGMENTS

This material is based upon work supported by the Keck Geology Consortium and the National Science Foundation under Grant No. 1659322. Thank you to Ben Surpress for his guidance in the field and with the subsequent analysis I completed during the following year. I also want to thank Michelle Markley for her support and critiques to help me write this contribution.

Table 2: Coefficient of Variation, C_v , by Scanline and Region

SCANLINE	LOCATION	C_v	REGION	MEDIAN C_v
A	RHC_WT1	1.3	RHC-1	1.3
B	RHC_WT2	1.7	RHC-2	1.2
C	RHC_WT3	1.3	RHC_ALL	1.3
D	RHC_WT4	1.2	ELKHEART	0.8
E	RHC_WT5	1.3		
F	RHC_MID1	0.9		
G	RHC_MID2	1.5		
H	RHC_NF1	0.7		
I	RHC_LD1	0.8		
J	RHC_LD2	1.4		
K	RHC_LD3	1.2		
L	RHC_LD4	1.6		
M	RHC_LD5	1.1		
N	ELK_NS1	1.1		
O	ELK_NS2	1.2		
P	ELK_NS3	1.2		
Q	ELK_NS4	0.7		
R	ELK_MS1	1.4		
S	ELK_MS2	0.7		
T	ELK_MS3	0.7		
U	ELK_MS4	0.8		
V	ELK_SS1	0.7		

Table 3: Summary of Fracture Mapping Data

REGION	MEDIAN BEARING (°)	# OF FRACTURES	MEDIAN FRACTURE INTENSITY (fracture/m)	MEDIAN SPACING (m/fracture)
RHC-1	24.7	86	0.098	10.2
RHC-2	59.5	71	0.090	11.1
RHC_ALL	30.1	157	0.095	10.6
ELKHEART	21.5	59	0.119	8.4

REFERENCES

- Davis, George Herbert. Structural geology of the Colorado Plateau region of southern Utah, with special emphasis on deformation bands. Vol. 342. Geological Society of America, 1999.
- Doelling, H. H. "Geologic map of the Kanab 30' x 60' quadrangle." Kane and Washington counties, Utah, and Coconino and Mohave counties, Arizona: Utah Geological Survey Miscellaneous Publications (2008).
- Google Earth 9.2.72.0. 2018. Red Hollow Canyon 37°16'15"N, 112°37'38"W, elevation ~1700m. 3D map, Satellite layer, viewed July 8th - 15th 2018. <<http://www.google.com/earth/index.html>>
- Gillespie, P. A., J. J. Walsh, J. Watterson, C. G. Bonson, and T. Manzocchi. "Scaling relationships of joint and vein arrays from The Burren, Co. Clare, Ireland." *Journal of Structural Geology* 23, no. 2-3 (2001): 183-201.
- Hooker, J. N., S. E. Laubach, and R. Marrett. "Fracture-aperture size—Frequency, spatial distribution, and growth processes in strata-bounded and non-strata-bounded fractures, Cambrian Mesón Group, NW Argentina." *Journal of Structural Geology* 54 (2013): 54-71.
- Kagan, Yan Y., and David D. Jackson. "Long-term earthquake clustering." *Geophysical Journal International* 104, no. 1 (1991): 117-133.
- Lund, W. R., T. R. Knudsen, and G. S. Vice. "Paleoseismic reconnaissance of the Sevier fault." Kane and Garfield Counties, Utah: Utah Geological Survey Special Study 122 (2008): 31.
- Reber, Spence, Wanda J. Taylor, Meg Stewart, and Ilsa M. Schiefelbein. "Linkage and reactivation along the northern Hurricane and Sevier faults, southwestern Utah." (2001): 379-400.
- Schiefelbein, I. "Fault segmentation, fault linkage, and hazards along the Sevier fault, southwestern Utah [MS thesis]: Las Vegas." University of Nevada at Las Vegas (2002).
- Simoneau, S., Surpless, B., and Mathy, H., 2016. "The evolution of subsidiary fracture networks in segmented normal fault systems." GSA National Meeting, Abstracts with Programs, Denver, Colorado (2016).
- Supak, S., D. R. Bohnenstiehl, and W. R. Buck. "Flexing is not stretching: An analogue study of flexure-induced fault populations." *Earth and Planetary Science Letters* 246, no. 1-2 (2006): 125-137.

PALEOENVIRONMENTAL ANALYSIS OF (PETRO)CALCIC SOIL HORIZONS IN THE MOJAVE DESERT

COLIN R. ROBINS, Claremont McKenna, Pitzer, and Scripps Colleges (The Claremont Colleges Consortium)

INTRODUCTION

Compared to humid environments, in which extensive chemical leaching and organic matter additions dominate soil formation pathways, arid soils are shaped much more by the accumulation of ions via evaporating, alkaline solutions and dust (Gile et al., 1981). Over time, this accumulation can completely cement desert soil horizons with pedogenic carbonates, sulfates, nitrates, halides, or even unique phyllosilicates (Dixon and Weed, 1989; Brady & Weil, 2008; Graham et al., 2008; Brock-Hon et al., 2012; Robins et al., 2012), and entire landforms can become armored by their soil profiles against erosion or further infiltration. Importantly, small changes in temperature or precipitation can impart larger magnitude responses in arid soil chemistry and mineralogy, plant growth and plant distributions, geomorphic stability, dust flux, and more (Chadwick and Chorover, 2001). Thus, in the face of warming global climate and increasing desert populations (Theobald et al., 2013), it is imperative to understand (1) how arid soils record past climate or geomorphic change, and (2) how arid soil-geomorphic surfaces are likely to respond to future climate change.

Calcite is among the most common pedogenic minerals to precipitate in arid climates, and soil classification systems worldwide note its importance (e.g., Soil Survey Staff, 2014; IUSS Working Group WRB 2006; and others). Given a stable climate and geomorphic surface, calcic soil horizons can evolve progressively from simple, “Stage I” horizons with thin dustings of carbonate through the soil matrix or along root traces, to “Stage III” horizons completely plugged by calcite that begin to inhibit infiltration, and finally, over 10⁶ timescales, into endmember

“Stage VI” petrocalcic horizons brecciated or partially dissolved and then recemented by pluvial-interpluvial climate fluctuations (Machette, 1985; Schoeneberger et al., 2012). This six-stage model ascribes relative ages to soil morphology in a way that Soil Taxonomy’s three-fold Bk (calcic), Bkk (calcic to petrocalcic), and Bkkm (petrocalcic) horizon classification (Soil Survey Staff, 2014) does only with less precision. However, rates of calcic and petrocalcic horizon genesis vary widely from site to site and between regions depending on parent material, climate, and dust flux, and the six-stage model is not perfect.

For instance, the model inadequately illustrates the mineralogical evolution of (petro)calcic horizons (e.g., Robins et al., 2012), each of which can include unique assemblages including palygorskite, sepiolite, and even barite (Brock-Hon et al., 2012) or fluorite (Bouza et al., 2007). Nor does the model address the timing and evolution of all micromorphological features found in calcic horizons, for instance excluding pedogenic ooids (Robins et al., 2015). Finally, the model is horizon-centric, meaning that individually tailored profile-scale models (e.g., Alonzo-Zarza et al., 1998; Brock and Buck, 2009; Alonzo-Zarza and Silva, 2002) must be developed on a site-by-site basis for polygenetic profiles, and for any soil with more than one calcic or petrocalcic horizon.

Ultimately, one of the most important applications of pedogenic carbonate analysis is the interpretation of paleoenvironmental data from stable isotope geochemistry (Zamanian et al., 2016). Isotopic analysis of pedogenic CaCO₃ ($\delta^{13}\text{C}$ and $\delta^{18}\text{O}$), phyllosilicates ($\delta^{18}\text{O}$), and barite ($\delta^{34}\text{S}$ and $\delta^{18}\text{O}$) from different soil developmental stages can yield useful insights into paleovegetation (e.g., Deutz et

al., 2001), paleotemperature (Quade et al., 2013), microbial activity (e.g., Jennings and Driese, 2014), and more. However, accurate interpretations rely on closed system assumptions that may be violated by partial or complete dissolution/precipitation of pedogenic calcite over time. Micromorphological context is also critical for accurate isotope interpretation because different micromorphological features form at different times within (petro) calcic horizons, and it is possible to mix data from calcite of different ages. Other pedogenic minerals in calcic horizons have not yet been well studied isotopically, and it is unknown whether the pedogenic phyllosilicates which form concurrently with calcite (Robins et al., 2012), for instance, better resist dissolution and later crystal growth additions than calcite.

The goal of Team Nevada (Figure 1), a Keck Geology Consortium Advanced Research project, was to advance the understanding of the mineralogic, geochemical, and micromorphological evolution of (petro)calcic horizons, using stage II-VI horizons from an ancient soil geomorphic surface in the Mojave Desert as a case study for processes relevant worldwide and in the stratigraphic record. These projects refine existing models of carbonate horizon development, and provide new isotope data for the Mormon Mesa surface in southeastern Nevada.

STUDY AREA

Mormon Mesa hosts perhaps the oldest, extant petrocalcic soil profile in North America (Figure 2). Its profile is a sequence of petrocalcic (Bkkm) horizons capping sediments of the Miocene-Pliocene Muddy Creek Formation (MCF) (Gardner, 1972; Brock and Buck, 2009; Soil Survey Staff, 2019). MCF deposits are fluvial and eolian sediments deposited in a closed basin prior to incision of the Virgin River upon interception by the lower Colorado River (Kowallis and Everett, 1986; Williams et al., 1997). Incision of the Virgin River to the east, and of Muddy Creek to the west produced ~200 m relief between the mesa and the floodplains (Fig. 2), with other fragments of the mesa surface preserved nearby as smaller mesas or buttes (e.g., Flat Top Mesa). Combined with an overall arid climate history, incision is hypothesized to have

ended any interaction of the Mormon Mesa soil with groundwater, however, there are no published stable isotope data to confirm this long-standing assumption. Onset of pedogenesis at Mormon Mesa is considered synchronous with incision of the lower Colorado River system ~5.6 - 4.2 Ma (Faulds et al., 2002; House et al., 2005), and a 5-4 Ma surface age is further supported by stratigraphic and morphostratigraphic correlation with isotopically dated tuffs and basalts (Schmidt et al., 1996; Williams et al., 1997; Faulds et al., 2002).

The Mormon Mesa soil profile (Figure 3) has been previously described and variably interpreted (Gardner, 1972; Bachman and Machette, 1977; Brock and Buck, 2009; Soil Survey Staff, 2019). Its currently accepted geomorphic history was interpreted by Brock and Buck (2009), and models for its mineral evolution (Robins et al., 2012) and the genesis of its pedogenic ooids (Robins et al., 2015) have been recently published also. The uppermost MCF strata exhibit carbonate nodules (a stage II paleosol), and are capped by a popcorn-textured, stage III “transitional” horizon forming the base of the Mormon Mesa profile (Brock and Buck, 2009). Subsequent sedimentation or erosion, followed by periods of geomorphic stability and pedogenesis, produced three to four more horizons (laminar layer, massive horizon, brecciated horizon, and a rubble layer interspersed with eolian sands) above the transitional (Brock and Buck, 2009). Locally, fluvial incision and backfilling has produced younger, nested profiles with petrocalcic horizons that cross-cut the older soil (Conley et al., 2018). Further, pedogenic laminae, pisoliths (e.g., irregular, > 2mm concretions indicative of rotation), dissolution voids and other features reflect complex episodes of calcite precipitation, horizon brecciation, and re-cementation (Brock and Buck, 2009; Robins et al., 2015).

Despite the research to date, Mormon Mesa’s polygenetic nature and micro-morphological and mineralogical complexity beg further study. None of the published models have been validated with stable isotope data. Detailed elemental geochemical comparisons have not been made for minerals between horizons nor between micromorphological features (e.g., laminae, pisoliths, matrix, dissolution voids). Importantly, models developed at Mormon Mesa can



Figure 1: Team Nevada concludes field work at Flat Top Mesa on June 26, 2018. From left to right: I. Futterman, P. Vorster, E. Conley, and K. Crandall.

be cautiously applied for insights into other (petro) calcic horizons and paleosols worldwide.

METHODOLOGY

This study involved four, closely-linked projects investigating the mineralogical, geochemical, and micromorphological evolution of the Mormon Mesa soil and geomorphic surface. Field work measuring section, describing soil profiles, and sampling was conducted in June, 2018. Three sites were chosen for detailed analysis: (1) the previously studied Mormon Mesa Riverside site (e.g., Brock and Buck, 2009; Brock-Hon et al., 2012; Robins et al., 2012; Robins et al., 2014; Robins et al., 2015), and two previously undescribed profiles in exposures at (2) Flat Top Mesa East, and (3) Flat Top Mesa West (Figure 2). Additionally, surface samples (top 10 cm) were collected for geochemical analysis from two Mormon Mesa transects, one Flat Top Mesa transect, and from representative geomorphic features on both mesas.

Intact, oriented and sometimes unoriented samples were collected using either a rock hammer and chisel, or a concrete cutting saw. Samples were labeled and stored in plastic boxes for transport to the laboratory. For geochemical study via x-ray fluorescence (XRF) and inductively coupled plasma (ICP) spectrometry, additional, surface samples were collected using a trowel and stored in plastic zip bags.

Initial sample processing was conducted in Claremont, CA. Billets were cut on a diamond-bladed tile saw and

shipped to Spectrum Petrographic Inc. (Vancouver, WA), for thin section preparation. Additional billets were polished for reflected light microscopy and/or scanning electron microscopy (SEM) with energy dispersive spectrometry (EDS) analysis. Samples for stable isotope analysis were trimmed to target specific micromorphological features including laminar caps, matrix, and pisoliths; these samples were divided into aliquots for carbonate isotope analysis and phyllosilicate analysis. Samples were shipped to Beloit College (Conley), Pitzer College (Crandall), Mount Holyoke College (Vorster), and Vassar College (Futterman) for individual projects.

Team Nevada presented preliminary findings at the 2018 Geological Society of America Meetings in Indianapolis (Conley et al., 2018), and continued their work through March, 2019.

STUDENT PROJECTS

Pedogenic ooids

Ethan Conley (Beloit College, WI) investigated the formation of pedogenic ooids – small, concentrically banded concretions - in (petro)calcic horizons with a systematic study of their morphology, and, importantly, presence or absence within individual horizons and features. Soil ooids are similar to sedimentological ooids - both are roughly spherical and composed of concentric authigenic mineral layers. However, pedogenic ooids exhibit a wider range of morphologies (e.g., with or without a single or complex nucleus), and compositions (calcite, clay, and/or oxide coats). Often this diversity of form and composition occurs in one spot, with different types of ooids immediately adjacent to one another in the soil. Further complicating matters, micromorphological terminology has proliferated within soil science, such that ooid-like features have variably been called coated grains, concretions, glaeboles, globules, granules, microaggregates, nodules, ooids, pellets, peloids, pisoids, pisolites, and other terms that have different meanings between or even within disciplines (see Bachman and Machette, 1977; Chafetz and Butler, 1980; Durand et al., 2010; Kendall et al., 2014; and others). Robins et al. (2015) suggested that chemical precipitation and the wetting of pedogenic

phyllosilicates within the ooid structure might explain much of the morphological variation observed in soils, but this model requires further testing.

Using optical light microscopy and SEM analysis, Ethan described, photographed, and classified ooids from 18 samples, comparing their morphology and context to published descriptions of ooids and comparable features in the literature. Ethan's analysis presents a new classification model positing three distinct genesis pathways for ooid occurrence in soils, including (1) simple, chemically precipitated grain coats, (2) biological, calcified excrements or castings, and (3) erosional features in horizon fracture and joint fillings.

Pedogenic laminae

Kurt Crandall (Pitzer College, CA) investigated correlations among the micromorphology, color, mineralogy, and geochemistry of pedogenic carbonate

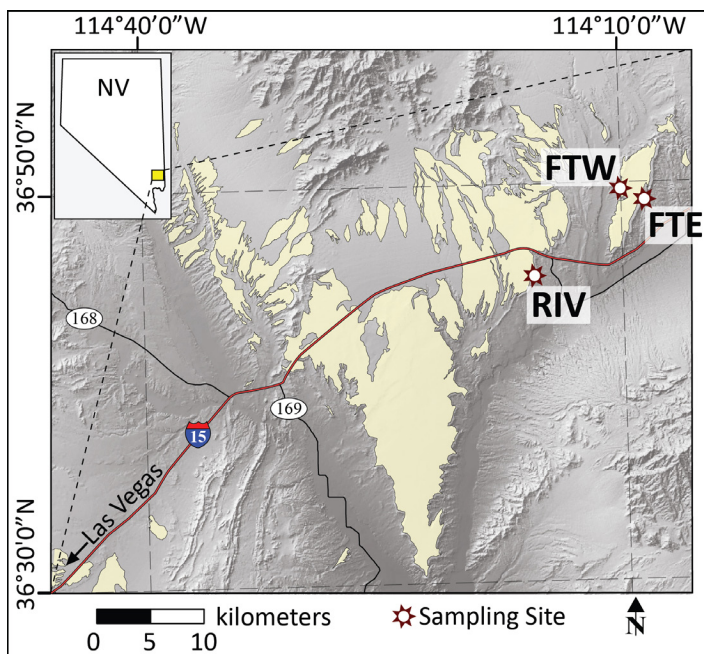


Figure 2: Location of the Mormon Mesa soil-geomorphic surface in southern Nevada; studied profiles include RIV = Riverside, FTW = Flat Top Mesa West and FTE = Flat Top Mesa East. Yellow polygons/shading represent approximate extent of the Mormon Mesa soil series (modified from Soil Survey Staff, 2006). Digital elevation base data modified from USGS (2005).

laminae in petrocalcic horizons, reconsidering existing hypotheses for laminar genesis. Importantly, in the six-stage model of progressive horizon calcification, > 1 cm thick sequences of laminae define transition from a Stage III calcic to a Stage IV petrocalcic horizon, when infiltration is restricted and percolating soil waters are diverted laterally across the top of the plugged horizon. However, the six-stage model does not address laminae formed by piping or other processes, and field observations suggest alternate pathways bear consideration.

Combining field observations, reflected and transmitted light microscopy, SEM-EDS, laser ablation ICP, and 3D surface scanning, Kurt defined six distinct laminar classes. Each differs in crystal size, mineralogy, and/or elemental abundances (especially Fe). These new data in context with field observations will help revise existing models for laminar genesis, and may help direct more targeted sampling protocols for stable isotope analysis.

Pedogenic barite

India Futterman (Vassar College, NY) conducted a landform-scale geochemical analysis to test competing hypotheses about Ba sources behind barite authigenesis in Mormon Mesa's petrocalcic horizons. Pedogenic barite confirmed in the Stage VI petrocalcic horizons at Mormon Mesa only recently (Brock-Hon et al., 2012), but may occur in other petrocalcic horizons around the world. This is significant because barite is a relatively insoluble mineral not previously thought to form in non-saline, arid-climate soils. Two competing hypotheses for Ba ion sources include (1) Ba weathered from parent material, especially volcanic ash, and (2) Ba input via eolian dust, especially from playas or from Ba-Mn oxides (hollandite) in desert varnish.

Using XRF and ICP analysis alongside geomorphic mapping, India measured the concentration of Ba and other ions in over 80 samples from three transects and numerous landform types across the Mormon and Flat Top Mesa surfaces. Her data show intriguing trends between Ba concentrations and surface geomorphology, suggesting that an eolian source may predominate over parent materials in barite authigenesis.

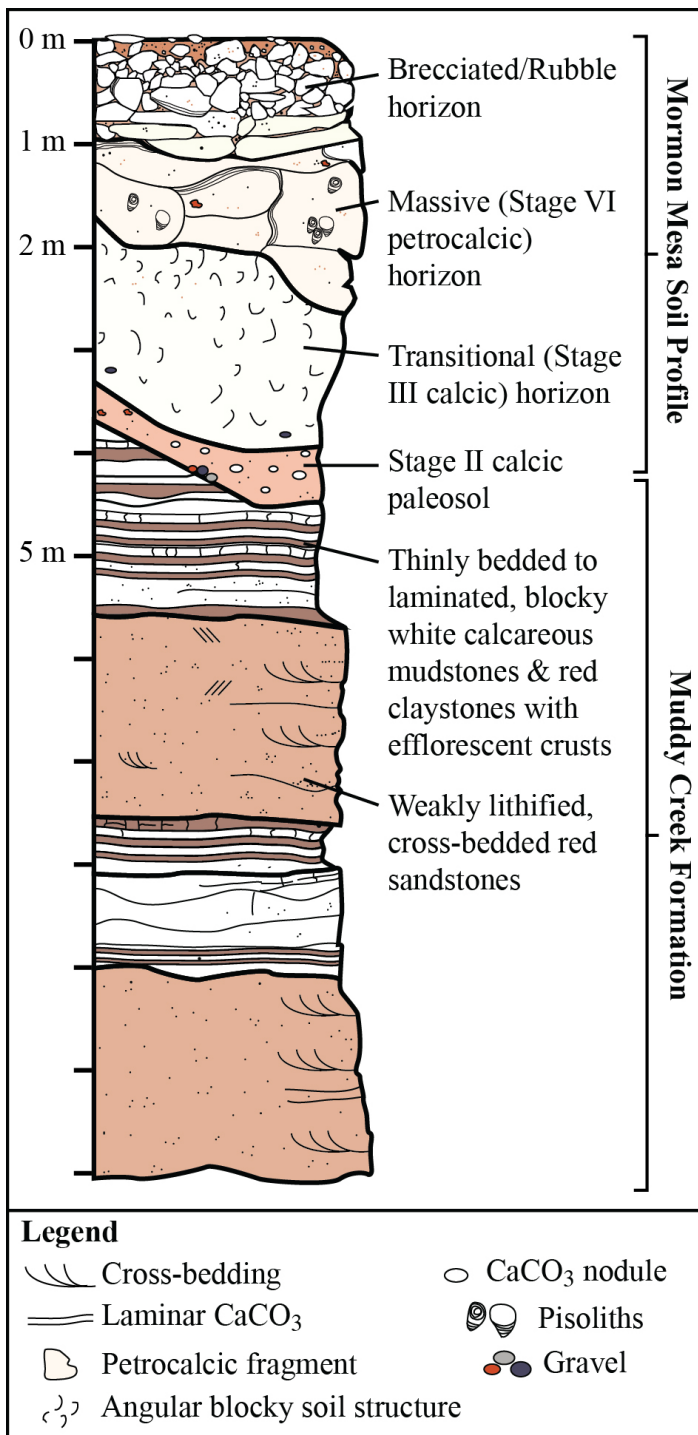


Figure 3: Generalized soil profile and stratigraphic section as measured at Riverside, using informal horizon nomenclature (e.g., Rubble, Brecciated, Massive, and Transitional horizons) of Brock & Buck (2009).

Stable isotope variation

Penelope Vorster (Mount Holyoke College, MA) used stable isotope geochemistry to seek differences in closed-system behavior between distinct micromorphological components of Mormon Mesa's

(petro)calcic horizons, especially nodules, pisoliths, laminae, and matrix. Importantly, Stage VI petrocalcic horizons develop like a conglomerate, containing brecciated fragments of precursor horizons that were variably eroded, redeposited, and recemented into a new horizon during Pleistocene climate oscillations. In targeting petrocalcic horizons for isotopic analysis and paleoenvironmental reconstruction, it is sometimes unclear whether the carbonate has resisted dissolution sufficiently to record the initial pedogenic environment, or whether it instead records younger calcite replacement or overprinting.

Penelope's analysis reveals widely variable (< 0.5 g to > 6.0 g per ~100 g of petrocalcic sample) phyllosilicate abundance across the massive horizon of Mormon Mesa, its laminae, pisoliths, and undifferentiated matrix, and her stable isotope analysis of the pedogenic carbonate shows intriguing trends between horizons with regard to their $\delta^{13}\text{C}$ signature (by contrast, $\delta^{18}\text{O}$ spanned a similar range across all horizons). These results provide important new data with which to test and refine models (Brock and Buck, 2009) for Mormon Mesa's evolution from the Pliocene to the Holocene.

SUMMARY AND CONCLUSIONS

The Mormon Mesa soil geomorphic surface continually proves more complex than previously imagined. These studies offer new models for the genesis of pedogenic carbonate laminae and ooids, and offer new insights into the origins of ions driving pedogenic barite crystallization. We anticipate additional phyllosilicate mineral and isotope data soon, as well as additional analyses of surface geochemistry that will shed further light on the evolution of polygenetic soil profiles with multiple calcic and petrocalcic horizons. Student research will help refine existing models for the development of petrocalcic horizons in modern soils as well as in paleosols.

ACKNOWLEDGEMENTS

This material is based upon work supported by the Keck Geology Consortium and the National Science Foundation under Grant No. 1659322, with

additional support from the Pomona College Geology Department, and the W.M. Keck Science Department of Claremont McKenna, Pitzer, and Scripps Colleges. I am indebted to J. Harris, K. McCarty, J.S. Lackey, M. Alfaro, B. Jaeger, K. Wirth, C. Davidson, M. Miller, and F. Bedoya for their assistance with the planning, administration, logistical operations, and analytical activities of this project. I thank S. Dunn, R. Gaines, E. Grosfils, K. Menking, and J. Rougvie for their generous on-campus mentorship and support of Team Nevada's research.

REFERENCES

- Alonso-Zarza, A., Silva, P.G., Goy, J.L., and Zazo, C., 1998. Fan-surface dynamics and biogenic calcrete development: Interactions during ultimate phases of fan evolution in the semiarid SE Spain (Murcia). *Geomorphology* 24: 147-167.
- Alonso-Zarza, A.M. and Silva, P.G., 2002. Quaternary laminar calcretes with bee nests: evidences of small-scale climatic fluctuations, Eastern Canary Islands. *Palaeogeography, Palaeoclimatology, Palaeoecology* 178: 119-135.
- Bachman, G.O., and Machette, M.N., 1977. Calcic soils and calcretes in the southwestern United States. U.S. Geological Survey Open File Report 77-794. U.S. Government Printing Office, Washington, DC.
- Bouza, P.J., Simón, M., Aguilar, J., del Valle, H., and Rostagno, M., 2007. Fibrous-clay mineral formation and soil evolution in Aridisols of northeastern Patagonia, Argentina. *Geoderma* 139 (1-2): 38-50.
- Brady, N.C. and Weil, R.R., 2008. *The nature and properties of soils, fourteenth edition (revised)*. Pearson Prentice Hall, Upper Saddle River.
- Brock, A.L. and Buck, B.J., 2009. Polygenetic development of the Mormon Mesa, NV petrocalcic horizons: Geomorphic and paleoenvironmental interpretations. *Catena* 77: 65-75.
- Brock-Hon, A.L., Robins, C.R., and Buck, B.J., 2012. Micromorphological investigation of pedogenic barite in Mormon Mesa petrocalcic horizons, Nevada USA: Implication for genesis. *Geoderma* 179-180: 1-8.
- Chadwick, O.A. and Chorover, J., 2001. The chemistry of pedogenic thresholds. *Geoderma* 100: 321-353.
- Chafetz, H.S. and Butler, J.C., 1980. Petrology of recent caliche pisolites, spherulites, and speleothem deposits from central Texas. *Sedimentology* 27: 497-518.
- Conley, E., Crandall, K., Futterman, I., Vorster, P., and Robins, C.R., 2018. Preliminary new insights into the evolution of an extant 4-5 Ma soil-geomorphic surface and its unique petrocalcic horizons, southern Nevada, USA. *Geological Society of America Abstracts with Programs* 50 (6): 193-2.
- Deutz, P., Montañez, I.P., Monger, H.C. and Morrison, J., 2001. Morphology and isotope heterogeneity of Late Quaternary pedogenic carbonates: Implications for paleosol carbonates as paleoenvironmental proxies. *Palaeogeography, Palaeoclimatology, Palaeoecology* 166 (3-4): 293-317.
- Dixon, J.B., and S.B. Weed, eds., 1989. *Minerals in soil environments*, 2nd edition. SSSA Book Series 1. Soil Science Society of America, Madison, WI.
- Durand, N., Monger, H.C., and Canti, M.G., 2010. Calcium carbonate features. In: Stoops, G., Marcelino, V., and Mees, F., Editors. *Interpretation of micromorphological features of soils and regolith*. Amsterdam: Elsevier: 149-194.
- Faulds, J.E., L.A. Gonzalez, M.E. Perkins, P.K. House, P.A. Pearthree, S.B. Castor, and Patchett, P.J., 2002. Late Miocene-Early Pliocene transition from lacustrine to fluvial deposition: inception

- of the lower Colorado River in southern Nevada and northwest Arizona. *Geological Society of America Abstracts with Programs* 34(4): 60.
- Gardner, L.R., 1972. Origin of the Mormon Mesa Caliche, Clark County, Nevada. *Geological Society of America Bulletin* 83: 143-156.
- Gile, L.H., Hawley, J.W. and Grossman, R.B., 1981. Soils and geomorphology in the Basin and Range area of Southern New Mexico - Guidebook to the Desert Project. New Mexico Bureau of Mines & Mineral Resources, Memoir 39. University of New Mexico, Socorro, 222 pp.
- Graham, R.C., Hirmas, D.R., Wood, Y.A. and Amrhein, C., 2008. Large near-surface nitrate pools in soils capped by desert pavement in the Mojave Desert, California. *Geology* 36(3): 259-262.
- House, P.K., Pearthree, P.A., Howard, K.A., Bel, J.W., Perkins, M.E., Brock, A.L., 2005. Birth of the lower Colorado River – Stratigraphic and geomorphic evidence for its inception near the conjunction of Nevada, Arizona, and California, in: Pederson, J., Dehler, C.M., eds., *Interior Western United States: Boulder Colorado*, Geological Society of America Field Guide 6. Geological Society of America, Boulder.
- IUSS (International Union of Soil Scientists) Working Group WRB, 2006. World reference base for soil resources 2006. *World Soil Resources Reports* No. 103. Food and Agricultural Organization of the United Nations, Rome.
- Jennings, D.S. and Driese, S.G., 2014. Understanding barite and gypsum precipitation in upland acid-sulfate soils: An example from a Lufkin Series toposequence, south-central Texas, USA. *Sedimentary Geology* 299: 106-118.
- Kendall, C., Alnaji, N., McCarney-Castle, K., Marshall, B., Editors, 2014. *Stratigraphy of Rocks and Sediments*. SEPM (Society for Sedimentary Geology) Strata Website: <http://www.sepmstrata.org/> [Accessed 8/22/2014].
- Kowallis, B.J., and Everett, B.H. 1986. Sedimentary environments of the Muddy Creek Formation near Mesquite, Nevada. *Sed. Assoc. Pub.* 15:69-75.
- Machette, M.N., 1985. Calcic soils of the southwestern United States. In: D.L. Weide (Editor), *Soils and Quaternary Geology of the southwestern United States*: 1-21.
- Quade, J., Eiler, J., Daëron, M. and Achyuthan, H., 2013. The clumped isotope geothermometer in soil and paleosol carbonate. *Geochimica et Cosmochimica Acta* 105(Supplement C): 92-107.
- Robins, C.R., Brock-Hon, A.L. and Buck, B.J., 2012. Conceptual mineral genesis models for calcic pendants and petrocalcic horizons, Nevada. *Soil Science Society of America Journal* 76(5): 1887-1903.
- Robins, C.R., Buck, B.J., Spell, T.L., Soukup, D.A. and Steinberg, S.M., 2014. Testing the applicability of vacuum-encapsulated $^{40}\text{Ar}/^{39}\text{Ar}$ geochronology to pedogenic palygorskite and sepiolite. *Quaternary Geochronology* 20: 8-22.
- Robins, C.R., Deurlington, A., Buck, B.J. and Brock-Hon, A.L., 2015. Micromorphology and formation of pedogenic ooids in calcic soils and petrocalcic horizons. *Geoderma*, 251-252: 10-23.
- Schmidt, D.L., W.R. Page, and Workman, J.B., 1996. Preliminary geologic map of the Moapa West Quadrangle, Clark County, Nevada. U.S. Geological Survey Open-File Report 96-521.
- Schoeneberger, P.J., Wysocki, D.A., Benham, E.C., Broderson, W.D., and Soil Survey Staff, 2012. *Field book for describing and sampling soils*, Version 3.0. Lincoln: Natural Resources Conservation Service, National Soil Survey Center.
- Soil Survey Staff. 2006. *Official Soil Series Descriptions*. USDA-NRCS <http://soils.usda.gov/technical/classification/osd/index.html> (accessed 1 April 2006).
- Soil Survey Staff, 2014. *Keys to Soil Taxonomy*,

Twelfth Edition. Lincoln: United States
Department of Agriculture Natural Resources
Conservation Service.

Soil Survey Staff, 2019. Official Soil Series
Descriptions. USDA-NRCS [http://soils.usda.gov/
technical/classification/ osd/index.html](http://soils.usda.gov/technical/classification/osd/index.html) (accessed
27 March 2019).

Theobald, D.M., Travis, W.R., Drummond, M.A., and
Gordon, E.S., 2013. The Changing Southwest.
In Garfin, G., Jardine, A., Merideth, R., Black,
M., and LeRoy, S., Eds., Assessment of climate
change in the Southwest United States: A report
prepared for the National Climate Assessment.
Washington, DC. Island Press: 37–55.

United States Geological Survey (USGS), 2005.
Seamless Data Distribution Digital Elevation
Models. U.S. Department of the Interior [http://
seamless.usgs.gov/](http://seamless.usgs.gov/) (accessed 1 Aug. 2005).

Williams, V.S., Bohannon, R.G. and Hoover, D.L.,
1997. Geologic map of the Riverside Quadrangle,
Clark County, Nevada, Geologic Quadrangle
Map GQ-1770.

Zamanian, K., Pustovoytov, K., Kuzyakov, Y., 2016.
Pedogenic Carbonates: Forms and formation
processes. *Earth Science Reviews* 157: 1-17.

MORPHOLOGY AND GENESIS OF PEDOGENIC OIDS IN CALCIC AND PETROCALCIC SOIL HORIZONS

ETHAN W. CONLEY, Beloit College
Research Advisor: Jim Rougvie

INTRODUCTION

Arid and semi-arid landscapes cover nearly a third of Earth's terrestrial environments, and support two billion people. With accelerated warming predicted for the Earth (Retallack, 2001), these landscapes must be thoroughly understood in both their current and future states. Arid soils are defined by the lack of available water for leaching, and instead often accumulate soluble salts such as calcite. Calcic and petrocalcic horizons form as secondary calcium and other carbonates accumulate in one or more parts (horizons) of the soil profile over time (Bockheim, 2014). Calcic and petrocalcic horizons provide important paleoenvironmental data through geochemical, stable isotopic, and micromorphological analysis of their CaCO₃ accumulation (Machette, 1985).

Calcic soil formation and evolution

Importantly, carbonate horizons evolve over time, transitioning from sparsely indurated, friable calcic horizons into completely cemented, hard petrocalcic horizons over 10³ to 10⁶ yr timescales. Petrocalcic horizons and paleosols (Soil Survey Staff, 2014) have long been recognized as soil and stratigraphic features although informally called caliche or calcrete in older geologic literature (Bachman and Machette, 1977). A six-stage model of calcic to petrocalcic horizon development illustrates the processes through which these soils evolve (Gile et al., 1966; Machette, 1985; Schoeneberger et al., 2012).

The rate of evolution from calcic (Stages I-III) to petrocalcic (Stages IV-VI) depends on the parent material (mineralogy and texture), geomorphic setting, and climate. But other studies demonstrate the need

to adapt the horizon-centric stage model for site-specific purposes addressing profiles with multiple (petro)calcic horizons or with dynamic climate or geomorphic histories (e.g., Zarza et al., 1992; Brock and Buck, 2009).

Micromorphology

The six stage model describes progressive morphological horizon development, but does not specifically address all micro-morphological features forming within the horizon during that evolution. Example features that are addressed by the model include pisoliths, pisoids, and laminae. Pisoliths are teardrop shaped structures that form when carbonate accumulations form pendants on the undersides of petrocalcic fragments sourced from the erosion and re-deposition of precursor calcic horizons, or other coarse fragments (Brock and Buck, 2009). Pisoids are round structures > 2 mm in diameter that have a varying range of internal morphologies (concentrically laminated or massive, nucleic or anucleic) (Robins et al., 2015). Pisoids are thought to form in stage VI as a result of the breaking up, transportation, and erosion of precursor, indurated matrix, nodules, or other features. Laminae are fine (mm scale) layers of carbonate, clay, or other pedogenic minerals < 1 cm thick (Zarza et al., 1992; Brock and Buck, 2009). The most prominent laminae sets are thought to develop as horizon caps (Stage IV) when pore spaces are plugged by Stage III carbonate accumulation and infiltration is restricted (stage IV) (Brock and Buck, 2009). Vertical laminae surrounding pisoids may correlate to erosional or dissolution events (piping) which can give insight into more recent climatic events, but their timing relative to horizontal laminae is less clear.

Importantly, ooids – a term borrowed from sedimentology – are intriguing micromorphological features that also often occur in (petro)calcic horizons, but which are not yet addressed by the six-stage model. Pedogenic ooids are concentric structures < 2 mm in diameter with variable internal morphologies (Halley, 1977). In calcic horizons they occur not only in isolation, but also in groups within larger macro-morphological features such as clast pendant laminae, pisoids, and laminae (Robins et al., 2015). Sedimentological ooids generally form in shallow, near-shore waters where waves or currents rotate grains in alkaline, calcite-precipitating waters, forming spherical secondary mineral coats around the nucleus grain. This model has been recreated in different lab settings (Deelman, 1978). By contrast, several competing hypotheses exist for pedogenic ooid origins. Robins et al. (2015) suggest ooids form in Stage I-III calcic horizons via combined: (A) mineralization during the evaporation of solutions held by surface tension around grains, clasts and other fragments, (B) hydration of plastically-behaving fibrous phyllosilicates, and (C) small, repetitive rotations caused by crystallization pressures from pedogenic minerals during soil solution evaporation (Robins et al., 2015). However, ooid occurrence has not been pervasively surveyed, and it remains possible that pedogenic ooids may also form in stage IV+ petrocalcic horizons.

This project systematically studies ooid presence and absence in stage II-VI (petro)calcic horizons to test existing hypotheses for their genesis. Understanding the timing of pedogenic ooid formation would refine models of petrocalcic horizon development and may assist paleoenvironmental reconstruction from petrocalcic horizons or paleosols.

METHODS

Site selection

Mormon Mesa, in South-Eastern Nevada, USA, is both remarkable and unique in terms of its age and soil profile characteristics. From the Miocene to the Pliocene, the tectonic basin which today hosts Mormon Mesa filled with alluvial, eolian, and lacustrine sediments of the Muddy Creek Formation

(MCF). Fluvial incision by the Virgin and Muddy Rivers (in response to Colorado River incision), plus continued Pliocene to Holocene alluvial fan sedimentation and eolian deposition formed the mesa and the Mormon Mesa soil series (Gardner, 1972). Flat Top Mesa is an isolated erosional remnant of Mormon Mesa's former extent and sits just east of the main soil geomorphic surface. Mormon Mesa makes an excellent ooid case study because its profile expresses stages II-VI, has been previously well described (Brock and Buck, 2009) and is known to exhibit pedogenic ooids in one or more horizons (Robins et al., 2015).

Field description and sampling

Three sites were chosen for soil-stratigraphic description and sampling in June, 2018, along roadcuts and the mesa's edge. Each exposure contained four main calcic or petrocalcic soil/paleosol horizons of interest = (Fig. 1). Ordered from bottom to top, the horizons are a stage II paleosol horizon within the upper MCF below the Mormon Mesa soil, followed, upwards in profile by: a stage III Transitional horizon (base of MM profile), Massive horizon (Stage VI), and brecciated rubble cap (Stage VI) intermixed with unconsolidated alluvium (Brock and Buck, 2009). Samples were taken from each of these horizons at three sites: Riverside (RR), Flat Top East (FTE), and Flat Top West (FTW).

Massive horizon samples were collected to capture different features including laminae, pisoliths, and pisoids, as well as several samples with no identifiable morphological features (massive matrix only). Transitional horizon samples averaging 3 cm in diameter were collected at random. Stage II MCF paleosol horizon, carbonate nodules were also randomly selected.

Laboratory methods

Eighteen billets were cut from the rubble layer and massive horizon for thin section preparation by Spectrum Petrographic Inc. (Vancouver, WA). Spurr low viscosity resin was used to epoxy friable transitional and MCF samples.

Thin sections were studied using optical light

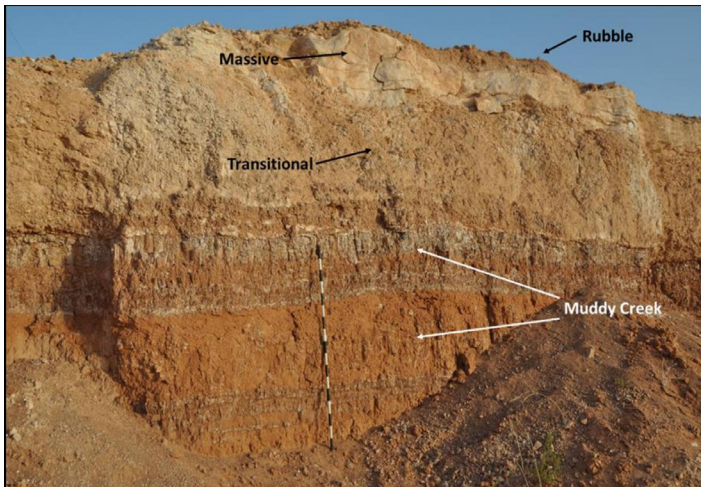


Figure 1: Mormon Mesa soil profile showing the four major horizons discussed in this study. The rubble horizon is a layer of weathered brecciated stage VI soil. The massive horizon is a stage VI petrocalcic horizon with a complex range of macro and micro-morphologic features. The transitional horizon is a moderately indurated stage III calcic horizon. The stage II MCF parent material is mixed alluvium and eolian sand. Mudstones with efflorescent crusts are also visible.

microscopy and scanning electron microscopy (SEM) at the Beloit College Geology Department. A random walk survey identified ooid locations in each slide. Each was photographed, and marked for subsequent SEM analysis.

SEM analysis employed the same billets from thin section preparation, but study was limited to massive horizon samples only due to time and logistical constraints. Billets were polished to remove saw marks and then etched in 10% HCl solution for 3 seconds to enhance contrast between minerals and features. Samples were immediately transferred to deionized water for rinsing and then air-dried. After etching, billets were Au sputter coated and imaged in a JEOL JSM-5900LV SEM at 15kV.

RESULTS

Ooids are not found in the MCF carbonate nodules. The carbonate nodules are irregular concretions; individual nodules with average diameters of 2-3 cm are surrounded by a sandy to silty matrix with a carbonate cement. Grains inside of the nodules lack visible grain coats and fabric is massive.

Transitional horizon samples yielded both micro and macro-morphological features including ooids

and pisoliths. Ooids exhibited three generalized morphologies (Fig.2). Category one ooids have nuclei composed only of clay or a collection of secondary minerals, and have a circular grain coating (Fig.2 A) (Fig.3). Category two ooids have nuclei composed of quartz, feldspar, and/or carbonates and the outer coats are neither circular nor concentric (Fig.2 B) (Fig.4 A&B). Instead, the grain coats conform to the nucleus's shape and fill all void space between grains (Fig.2 B). Category three ooids have nuclei composed of quartz, feldspar, and/or carbonates but the grain coats are circular and concentric (Fig.2 C&D) (Fig.4 C-F). Category two ooids are most prevalent in the transitional horizon. At all three sites, ooids are scattered within the transitional horizon and are not concentrated within any specific area nor feature.

Ooids in the massive horizon were less morphologically diverse, but occurred in the highest concentrations of any horizon. Both category two and three ooids were seen, with category three the most abundant. Ooids appear in all massive horizon sample areas, but the highest concentrations occur in thickly laminated zones, especially in RR and FTE samples.

The brecciated and rubble layer samples are more weathered than the previous horizons with commonly observed surface dissolution of pisoids and pisoliths. Both macro and micro-morphological features including laminae, pisoids, pisoliths, and ooids are present and similar to the massive horizon. Complex laminae surround and wrap around small pisoliths as well as pisoids, and ooids (< 2 mm) are visible within the laminae themselves. In grab samples, especially from Flat Top East, several large dissolution seams are present that contain entire sections of ooids. Grain size varies and several grains have carbonate bridges connecting the ooids in an hourglass shape.

DISCUSSION

In conjunction with previous research, these results help better illustrate the usefulness of pedogenic ooids as paleoenvironmental indicators and establish a place-holder for the timing of pedogenic ooid formation within the six stage model (Gile et al., 1966, Machette, 1985, Schoeneberger et al., 2012).

Ooid morphology

Category one ooids are interpreted as biogenic. They share similar diameters and mineralogical compositions with previously described calcite spherulites from animal dung (Canti, 1998). Another possible origin for this ooid class is development as filled root casings or deformed and enriched casts and imprints of cells from microbial mats that were present in the soil prior to the beginning of the calcification process (Gerdes et al., 1994). The structure of these grains would have started with an initial coating, but no nuclei because of their cellular structure. Over time, clays and possibly other minerals fill the void space in the center of the structure to give it an ooid appearance.

Category two ooids are interpreted as abiotic grain coats. These ooids have irregular structures (Fig. 4 A&B) and the grain coats consist of clay, or clay and carbonate. Some coatings do not completely encompass the grain, but rather truncate partway. Category two ooids are hypothesized to form as grain coats around a stationary nucleus with void space around it. The coatings are not rounded (Figure 2B), suggesting there was no motion forming the coat itself. Instead, the crystallizing coat filled all available voids around the central grain. This also explains why some grain coats do not completely surround

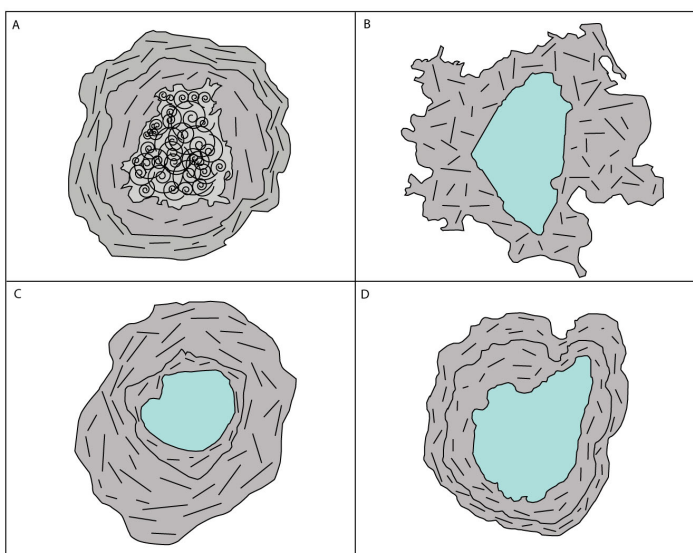


Figure 2: (A) Category one ooid (clay nuclei) interpreted as forming from termite/worm frass and or other biological processes. (B) Category two ooid (grain coat growing into void space) with quartz, feldspar, or carbonate nuclei, but irregular coating. (C) Category three ooid (spherical and concentric grain coat) with quartz, feldspar, or carbonate nuclei. (D) Category three ooid, but with an irregular nuclei.

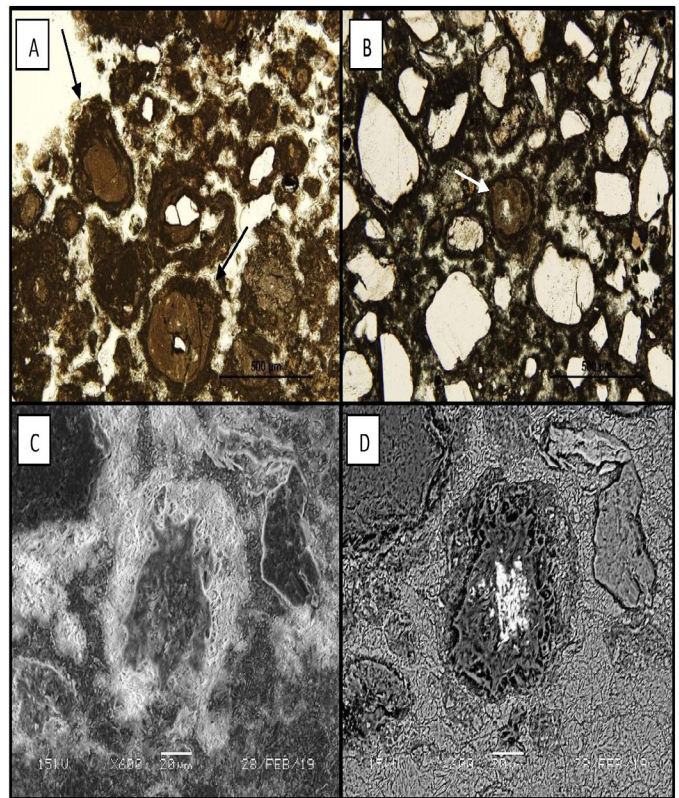


Figure 3: (A) Two category one ooids. (B) Category one ooid. (C) Secondary Electron Image of a category one ooid. (D) Backscatter Electron Image of a category one ooid found in C.

all grains because if there was initial grain-to-grain contact, there would be no void space for a coating to crystallize into. Some grains of this category only have a thin rind around them. In areas of tightly packed grains, with little available void space, a thinner coating develops instead.

Category three ooids are most abundant in the massive horizon and have high concentrations within laminae. Laminae form due to solution flow or pooling along impermeable contacts. In these areas, movement of grains is plausible. If this motion has a high enough energy to roll, rotate, and transport these grains, even in very small, episodic movements over multiple seasons or years, then the expected coat would grow and crystallize spherically. Thus, category three ooids likely form due to the result of some sort of motion.

Category two ooids are most abundant in the transitional horizon and category three ooids are most abundant within the massive horizon. These results support hypothesized processes in which

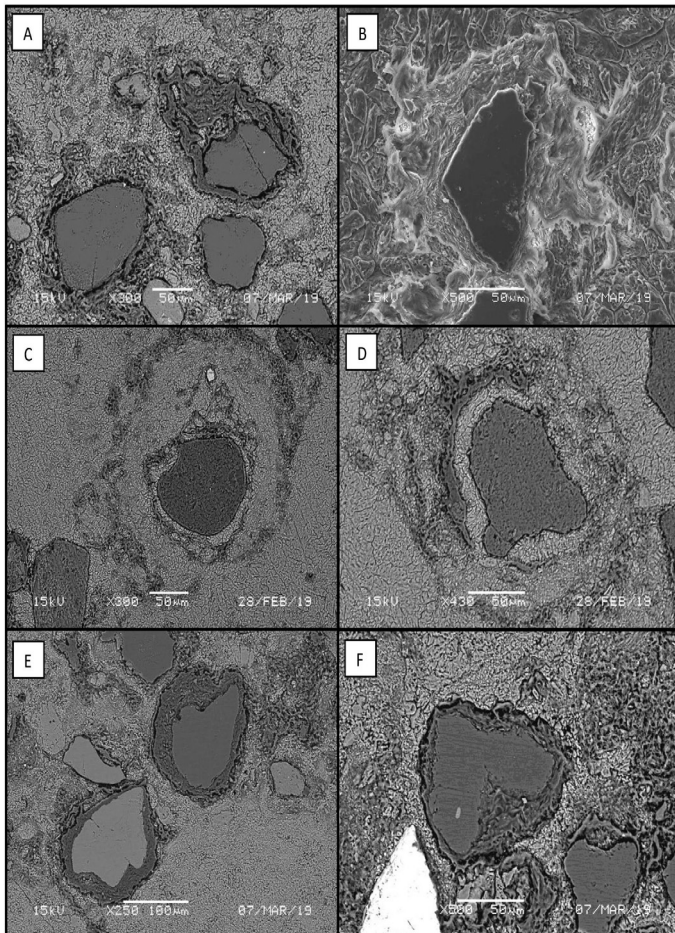


Figure 4: (A&B) SEM images of category two ooids lacking spherical and concentric grain coats. (C&D) SEM images of category three ooids with spherical and concentric grain coats. E&F) SEM images of category three ooids with spherical grain coatings despite irregular nuclei shape.

these two categories of ooids form because in the less indurated transitional horizon the need for void space is satisfied. Ooids in the massive, stage VI horizon form when joints, fractures, and pipes are opened during times of profile degradation, filled by new, younger material, and then recemented. These interpretations also explain the locations of the ooids within the different horizons. Pervasive porosity in the transitional would yield more scattered assemblage of category two ooid growth (Khresat, 2001). Fluid motion in these soils follows the paths of either fractures or impermeable surfaces which would make the formation locations of category three ooids more predictable.

Timing of Formation

Category one ooid formation begins within stage I as root casings and pores develop carbonate coatings.

These calcareous coatings retain the structure of the original roots and cells, but may not finish formation until stage III (Jaillard et al., 1991).

Category two ooids begin forming in stage III. During stage II, calcification and induration is incomplete and grains, especially those within the carbonate nodules, would not yet be immobile. Confining pressure is not achievable until Stage III, when the horizon is plugged by carbonate.

Category three ooids may form independently of category two ooids as a brand-new cycle sparked by motion or laminae formation. Another possibility is that category three ooids are older more developed versions of category two ooids. Category two ooids could be plucked out of place by infilling processes and laminae formation. These ooids could then become rounded from rolling and turning (Deelman, 1978) as they grow a new coating around the previously formed irregular coating. This would explain the concentric, rounded rings (spherical coats) marking individual growth periods or events. This could also explain why some massive horizon ooids still display characteristics of category two. If those grains were never moved, then they would have never developed a new, spherical coating.

CONCLUSIONS

The only ooids observed in this study meeting traditional ooid definitions (Deelman, 1978; Prothero and Schawb, 2014) in the geologic literature are category three because of their spherical, concentric grain coats and context (Robins et al., 2015). Category three ooids do not complete their formation until late stage III to stage VI. For the six-stage model of calcic horizon formation (Gile et al., 1966; Machette, 1985; Schoeneberger et al., 2012) this implies that the other two categories begin forming as early as stage I and certainly by early stage III. Thus, with at least three plausible modes of genesis, pedogenic ooids are useful paleoenvironmental indicators which tell the story of what has, and just as importantly, what has not happened to the soil profile in different climatic cycles.

ACKNOWLEDGEMENTS

This material is based upon work supported by the Keck Geology Consortium and the National Science Foundation under Grant No. 1659322. Additional support was provided by the Pomona College Geology Department, The W.M. Keck Science Department of Claremont McKenna, Pitzer, and Scripps Colleges, and by the Beloit College Geology Department. I thank C. Robins and J. Rougvie for advising this project and fellow Team Nevada colleagues K. Crandall, I. Futterman, and P. Vorster for their enthusiasm and friendship during the project, and continued collaboration during both research and writing.

REFERENCES

- Alonso-Zarza, A.M., Wright, V. P., Calvo, J. P., and Garcia del Cura, M.A., 1992. Soil-landscape and climatic relationships in the middle Miocene of the Madrid Basin. *Sedimentology* 39 (1):17-35.
- Bachman, G.O., and M.N. Machette, 1977. Calcic soils and calcretes in the southwestern United States. U.S. Geological Survey Open File Report 77-794. U.S. Government Printing Office, Washington, DC.
- Bockheim J.G., 2014. Calcic and Petrocalcic Horizons. In: Bockheim, J.G. *Soil Geography of the USA*. Springer Publishing
- Brock, A.L. and Buck, B.J., 2009. Polygenetic development of the Mormon Mesa, NV petrocalcic horizons: Geomorphic and paleoenvironmental interpretations. *Catena* 77: 65-75.
- Canti, M., 1998. Origin of calcium carbonate granules found in buried soils and Quaternary deposits. *Boreas*, 27 (4): 275-288.
- Deelman, J. C., 1978. Experimental ooids and grapestones; carbonate aggregates and their origin. *Journal of Sedimentary Petrology* 48 (2): 503-512.
- Gardner, L.R., 1972. Origin of the Mormon Mesa Caliche, Clark County, Nevada. *Geological Society of America Bulletin* 83: 143-156.
- Gerdes, G., Dunajtschik-Piewak, K., Riege, H., Taher, A. G., Krumbein, W. E., & Reineck, H. E., 1994. Structural diversity of biogenic carbonate particles in microbial mats. *Sedimentology* 41 (6): 1273-1294.
- Gile, L.H., Peterson, F.F., Grossman, R.B., 1966. Morphological and genetic sequences of carbonate accumulation in desert soils. *Soil Science* 101 (5): 347-360.
- Halley, R. B., 1977. Ooid fabric and fracture in the Great Salt Lake and the geologic record. *Journal of Sedimentary Petrology* 47(3): 1099-1120.
- Jaillard, B., Guyon, A., & Maurin, A. F., 1991. Structure and composition of calcified roots, and their identification in calcareous soils. *Geoderma* 50 (3): 197-210.
- Khresat, S. A., 2001. Calcic horizon distribution and soil classification in selected soils of north-western Jordan. Department of Natural Resources and the Environment, Jordan University of Science and Technology, 47(2): 145-152.
- Machette, M.N., 1985. Calcic soils of the southwestern United States. In: D.L. Weide (Editor), *Soils and Quaternary Geology of the southwestern United States*, pp. 1-21.
- Prothero D. R., Schwab, F., 2014. *Sedimentary Geology: an introduction to sedimentary rocks and stratigraphy*. W.H. Freeman, 3rd edition.
- Retallack, G.J., 2001. *Soils of the past: An introduction to paleopedology*. Blackwell Science, Malden, MA, 404 pp.
- Robins, C.R., Deurlington, A., Buck, B.J. and Brock-Hon, A.L., 2015. Micromorphology and formation of pedogenic ooids in calcic soils and petrocalcic horizons. *Geoderma*, 251-252: 10-23.
- Schoeneberger, P. J., Wysocki, D. A., Benham, E. C., Soil Survey Staff., 2012. *Field book for describing and sampling soils*. National Resources Conservation Service, National Soil Survey Center, Version 3.0.

Soil Survey Staff. 2019. Official Soil Series
Descriptions. USDA-NRCS [http://soils.usda.gov/
technical/classification/osd/index.html](http://soils.usda.gov/technical/classification/osd/index.html). Accessed
29 March 2019.

WHAT CAN PETROCALCIC LAMINAE TELL US ABOUT SOIL PROCESSES AND PALEOENVIRONMENTS?

KURT CRANDALL, Pitzer College

Research Advisor: Colin Robins (Claremont McKenna, Pitzer, and Scripps Colleges)

INTRODUCTION

Pedogenic carbonate forms in arid to semi-arid environments when infiltrating soil water evaporates and deposits solutes rather than leaching them through the soil profile. The amount and morphology of carbonate accumulation in soils, along with the overall degree of horizon and profile development, evolve over time (Brock & Buck 2009), reflecting relative age, and climate and/or geomorphic stability. The term “petrocalcic horizon” describes horizons in which carbonate accumulation has either completely engulfed and/or indurated the horizon, while “calcic horizon” reflects younger relative ages of less-extensive carbonate accumulation without complete horizon cementation (Soil Survey Staff, 2014).

Laminated horizon caps are the defining morphological indicator of the transition from calcic to petrocalcic horizon (Gile et al., 1966; Machette, 1985), but they are not always well described nor adequately understood. Laminae are defined as an internal fabric and are described according to thickness, regularity, and orientation (Bullock et al., 1985; Stoops, 2003). The accepted mode of formation of laminar caps is addressed by a broader model for calcic and petrocalcic horizon development (e.g., Schoeneberger et al., 2012). This progressive horizon development model was developed first as a four-stage model (Gile et al., 1966) including the laminar horizon at stage IV, and later refined to include two additional, later stages (Machette, 1985). However, other authors have shown the need to tailor all or part of this horizon-focused model to fit whole profiles, specific world regions, or to develop new models completely (Brock & Buck, 2009; Alonzo-Zara & Tanner, 2010; Robins et al.,

2015).

Internally or between horizons, pedogenic carbonate laminae often exhibit different morphologies, colors, mineral compositions, geochemistries, and architecture (Brock & Buck, 2009; Levine & Hendricks, 1990). Most are made of calcite or low-Mg calcite, but some include detrital quartz grains surrounded by cements which suggests dissolution, at least partial void filling by unconsolidated soil or sediment, and recrystallization (Stoops et al., 2010). Some laminae contain authigenic sepiolite and palygorskite clays (Robins et al., 2015; Hudnall et al., 2010, Vanden Huevel, 1966) in aggregates, as individual fibers, and as grain coatings. Moreover, other soil features contain or are surrounded by laminae in carbonate-cemented soils. For example, pisoliths are pointed, concentric, vertically tapering, accretionary structures thought to have formed through infilling of a dissolution void or fractured and eroded surface (Robins et al., 2012). After the void forms, rainfall washes solutes into these open or sand-infilled void spaces, coating grains and these spaces can be filled completely creating a calcified mass (Gile et al., 1966; Machette 1985). Pisoliths are common in petrocalcic soil horizons that are subject to alteration by chemical and mechanical weathering (Arakel, 1982; Robins et al., 2012; Dunham 1969).

Thus, published hypotheses regarding the origin of laterally continuous laminations in calcic and petrocalcic horizons include (1) formation as a cap, (2) formation due to biological processes, (3) dissolution and growth of calcite crystals in pores and cracks, (4) infusion and neof ormation of clays, and (5) formation in localized pedogenic structures.

Hypothesis 1 is the only hypothesis included in the VI Stage model (Machette 1985). More detailed analysis of the occurrence and morphology of laminae within calcic and petrocalcic horizons is needed to test and/or refine existing models for their genesis, mineralogy, and to address competing hypotheses about their genesis. An important first step in that analysis is the detailed micromorphological and mineralogical and classification of pedogenic laminae.

Objectives and Hypotheses

Using Mormon Mesa as a case study that may be broadly applicable to other petrocalcic soil and/or paleosol horizons around the world, it is hypothesized that mineralogy, elemental concentrations, and stable isotope geochemistry may vary among laminae of distinct morphologies, colors, or mineralogies, with implications for solution chemistry, and mode and depth of formation.

Thus, the overall goal of this project is to investigate the morphology and mineralogy of the calcic laminae in the petrocalcic horizons, to test and refine existing models for their genesis, especially the VI stage model. Questions explored included: (1) are there any top-bottom indicators in the laminae, (2) do the widely varied colors of laminae correlate with crystal size, detrital grain content, or mineralogy?

METHODS

Location and Sampling

The study sites for this project are located in the Mojave Desert at Mormon Mesa and Flat Top Mesa, Nevada, just outside of Mesquite Nevada, about 100 km northeast of Las Vegas. The formation of the Mormon Mesa soil in Muddy Creek Formation parent materials coincides with the incision of the Muddy Creek and Virgin Rivers in response to the down-cutting of the lower Colorado River.

Three informally-named sites with existing exposures of the soil profile and stratigraphic section were described and sampled at Mormon and Flat Top Mesas, NV: (1) Riverside, (2) Flat Top East (FTE), and (3) Flat Top West (FTW). The Riverside exposure occurs in a road cut along an abandoned highway that

exposes tall ~5-12 m soil profiles and stratigraphic sections. The Flat Top East exposure also lies in a short ~100 m long roadcut, made to assist in installing powerlines in the area. Additionally, the cut extends to edge of the mesa and is about 3-8 m tall in some locations. By contrast, Flat Top West is a natural, 12 m vertical exposure along the Mesa's edge and is harder to access than the other locations.

Samples were chosen in a targeted rather than random fashion, by searching the massive horizon for laminae. I limited my search to areas exhibiting large amounts of layers of laminae as to maximize my study. I also tried to find samples and areas that showed laminae in multiple directions, as well as ones that were only going in one direction, in order to sample the most complete range of contexts possible. I also targeted different colors and shapes of laminae for a complete and thorough comparison, using a Munsell Soil Color Book to normalize color descriptions. Samples were photographed in situ in the field and described in detail before collection.

Optical Microscopy

A Nikon LV100 Universal microscope with an automated motorized stage was used to describe soil mineralogy and micromorphology in thin section. Optical images collected using cross- or plane-polarized transmitted light were compared to digital photographs of billets in hand sample (reflected light) to identify different laminae types based on color in the field and in hand sample. The main magnification used was 4x, though 10x was often used to image smaller features. Metrics used to describe samples are based on the soil micromorphology guidelines from Stoop et al. (2003) and Bullock et al. (1985). Metrics included: contact distinctness & shape; thickness; color; mineralogy; crystal size, and fabric.

Modifications to standard terminology were required for clarity in a number of instances. In particular, Stoops (2003) and Bullock et al. (1985) define shape in a binary classification system as only either parallel or convolute. In this study, a third shape category is added. Shape then varies from straight to wavy to irregular to broken. Wavy can vary anywhere (and is stated) from parallel to wavy. The definition of wavy is $\frac{1}{2}$ wavelength > amplitude. Irregular is defined as

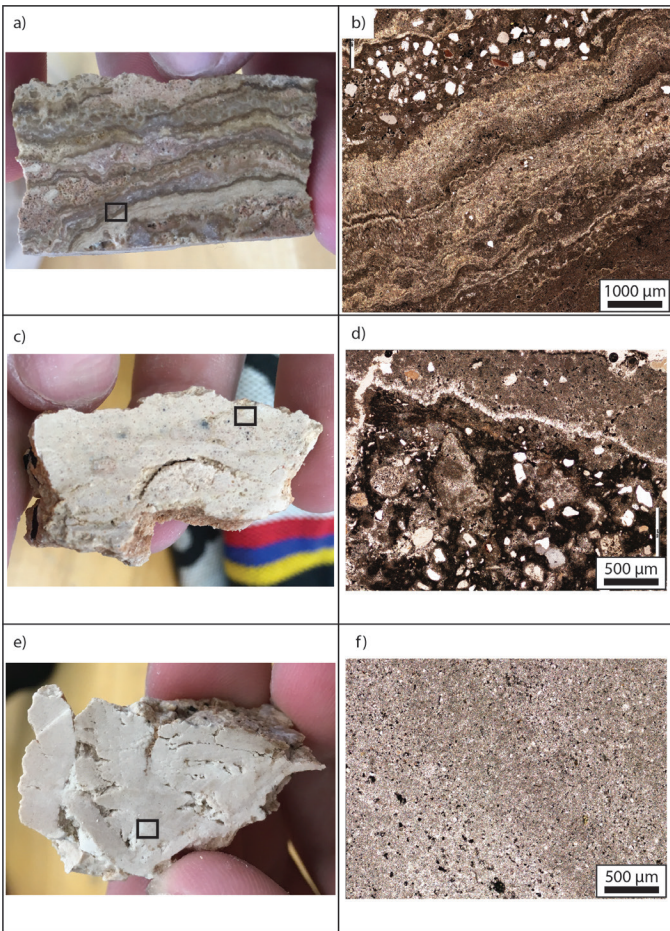


Figure 1: Three different examples of white laminae/sections. (a) Hand sample from Flat top East (FTEKCM4) collected from the top of the massive section. It shows a white section of laminae towards the bottom. This sample is oriented with the top facing upwards. (b) Thin section showing the white laminae in thin section in the SE corner. The white layer in thin section is dark brown and homogenous. (c) Hand sample from Flat top West (FTWK3) collected from an erosional surface of the laminar cap on the top of the transitional. Few laminae are present. (d) Thin section showing the dark mass similar to b but with more quartz sand grains and more heterogeneity throughout perhaps indicating a younger age. One laminae of crystals of calcite is seen. (e) Fragment from Flat top West (FTWV2) collected from the muddy creek section b unit 2. (f) Nearly all calcite crystals. Slight banding is seen from NW to SE of picture. The alternating sections differ only by crystal size. The larger crystal sections display elongation of pore spaces.

$\frac{1}{2}$ wavelength < amplitude. A broken shape is where there is a discontinuity in the laminae.

RESULTS

Profile Morphology and occurrence of laminae in the field profiles

All types of laminae were seen at all three sites

visited (MM, FTE, and FTW) and in horizons at different depths throughout the profile. Laminae were observed in many directions, not only horizontal to the surface extending for continuous lengths of 10s of cm. Laminae were however found roughly horizontal to the surface either in a draping manner or in horizontal cracks consistent with Bullock et al. (1985). Additionally, six different colors of laminae were identified: white, red, dark olive gray, pale brown, pink, and light brown.

Optical Microscopy

Contacts between laminae in thin section range from very sharp ($< 2 \mu\text{m}$) to diffuse (color/particle size transition $> 60 \mu\text{m}$ wide) (Stoops, 2003; Bullock et al., 1985). Most contacts between differing laminae are pronounced and abrupt, but on some, especially the alternating pink and light brown laminae, the contact was not easily discernible in thin section. Most laminae are wavy (53.2%), but some are irregular (29.8%) and some are broken (14.9%). Only 2.1% have a straight contact.

Most laminae could be traced laterally across the entire thin section (88.1%), with a few that were only 50% traceable throughout the thin section (9.5%). Infilled voids and cracks were prominent, recognizable due to their composition of sediments of silt/clay/sand that contrasted with the matrix and laminae, or by larger ($> 50 \mu\text{m}$) calcite crystals growing in radially from the void edges.

Colors distinct in hand sample remained distinct at the microscopic scale, correlating with grain size (pedogenic crystal size) and mineralogy. “White” laminae were generally comprised of very fine grained ($< 50 \mu\text{m}$) calcite mixed with clay and fine matrix, though sizes range from micrite ($< 4\mu\text{m}$ crystals) to microsparite (4 – $50\mu\text{m}$) (Bullock et al., 1985). In most samples, the white laminae fabric is homogenous and dark brown to black in thin section (Fig. 1a, b). In some cases, white layers contained quartz sand grains that were rounded to subrounded (Fig. 1c, d). In one case where the entire hand sample was white (Fig. 1e, f), the laminae within were almost entirely crystalline calcite. In this sample, weak banding was seen as a slight variation in crystal size possibly indicating different periods of growth.

Red laminae show crenulated calcite layering rich in oxides and clays. Some laminae exhibit a convolute (Stoops et al. 2003) or irregular ($\frac{1}{2}$ wavelength < amplitude) orientation. Some red laminae are present in very distinct bands or sections where several laminae are seen to have a red tint (Fig 2a, b). These bands are often thin (<1000 μm), long (>3cm), and continuous across the sample. Other red laminae/sections occur in larger swaths or areas (Fig. 2c, d). In these sections, the redness seems to be a haze over the entire area, where underlying laminae and sections are still visible with varying degrees of light and dark red.

The dark olive gray laminae in thin section show fine to coarse interlocking sparry calcite (10 – 300 μm) that ranges from equigranular hypidiotopic to equigranular idiotopic (Bullock et al., 1985) and fine clays. The sparry calcite crystals seem to grow in bands possibly parallel to overall laminae orientation; they also radiate perpendicularly from darker masses that are consistent with white areas in hand sample (Fig. 3a, b). Dark laminae can also form in cracks where they are made up of radiating calcite crystals (Fig. 3c, d).

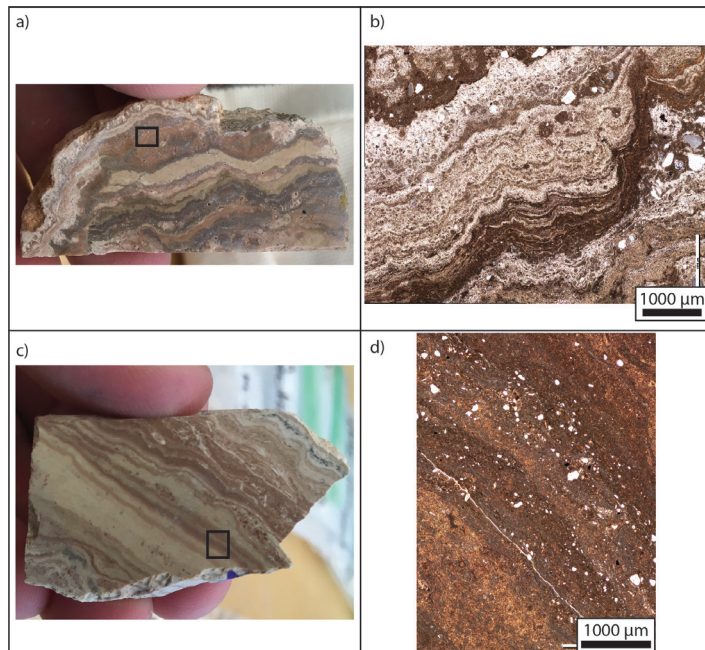


Figure 2: Two different examples of red laminae/sections. (a) Hand sample from Flat top East (FTEKCM2) collected from the upper part of the massive section. (b) Thin section showing a very distinct red laminae section. (c) Hand sample from Flat top East (FTEKCM6) collected as a grab sample(not in situ). (d) Thin section showing prominent red laminae. Redness is almost a tint or haze over entire area.

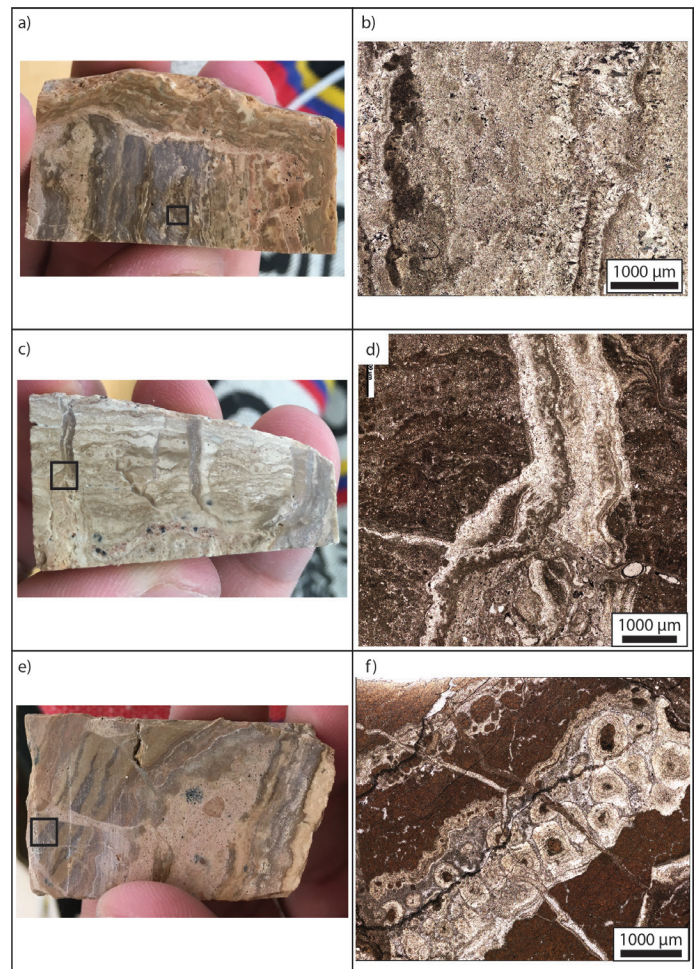


Figure 3: Three different examples of dark olive grey laminae. (a) Hand sample from Flat top East (FTEKCM1) collected from the upper middle part of the massive. (b) Thin section showing large calcite crystals. Some crystals seem to be growing off of or radiating from darker laminae segments, which are identified as white or lighter sections in hand sample. (c) Hand sample from Flat top East (FTEKCM3) collected from the upper section of the massive. (d) Thin section showing a crack filled dark laminae. The calcite crystals are radiating and forming in bands off of the darker areas which are white in hand sample. (e) Hand sample from the Riverside site at Mormon Mesa (MMRKC31L) cut with a saw and oriented. (f) Thin section showing concentric ooids with radiating calcite forming the darker laminae layer.

In some cases, dark laminae are largely comprised of numerous, adjacent ooids (concentric calcite concretions) (Fig. 3e, f). These findings, especially the ooids, corroborate reporting by Stoops et al. (2010).

The pale brown laminae are mostly comprised of densely packed, predominately phyllosilicate aggregate clusters, though some areas show loosely packed aggregates (Bullock et al., 1985). The aggregates in the pale brown laminae or sections range from being more matrix supported (Fig. 4a, b) to being more clast supported (Fig. 4c, d). In some cases,

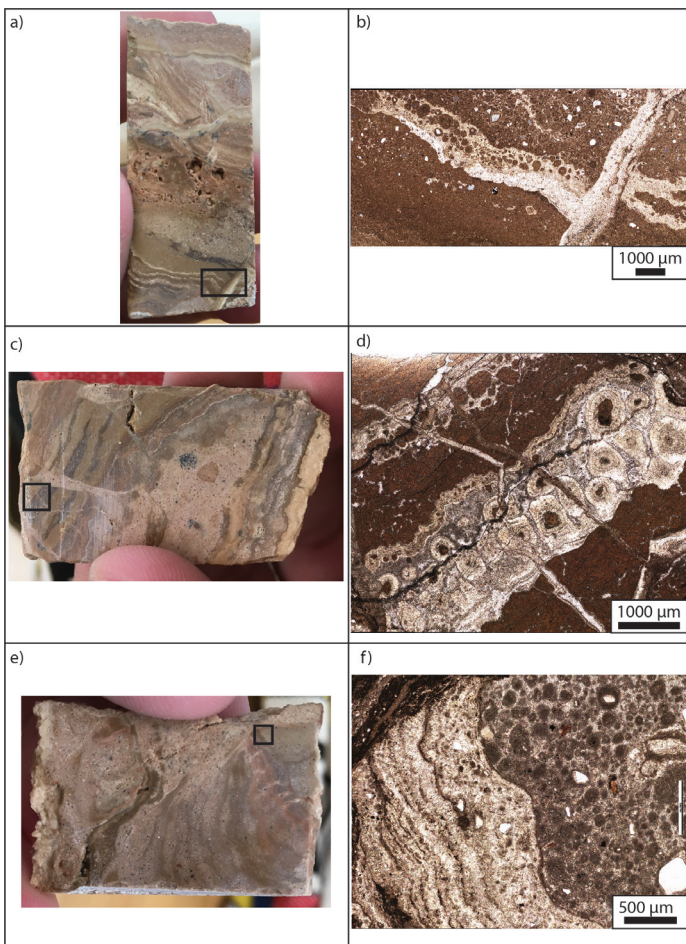


Figure 4: Three different examples of pale brown laminae/sections. (a) Hand sample from the Riverside site at Mormon Mesa (MMRKC32) cut with a saw and oriented. (b) Thin section showing aggregates clustered together in the NE part of the picture. The aggregates in the laminae are more ooid like with space and growth around them, but the aggregates above in the NE seem to be more stuck together. (c) Hand sample from Riverside site at Mormon Mesa (MMRKC31L) cut with a saw and oriented. (d) Thin section showing pale brown laminae on both sides of an ooid layer (dark olive grey laminae). Aggregates seem very together and only are barely visible in the bottom half of the picture. (e) Hand sample from Flat top West (FTWKC4) collected from the stage IV laminar cap. (f) Thin section showing the aggregate clustered together in the pale brown area.

there is almost no space between aggregates and the layer appears to be completely or nearly completely homogenous (Fig. 4e, f).

The differences in the pink and light brown laminae are difficult to see in thin section. Both are made up of mostly calcite with larger quartz grains scattered throughout in bands parallel to the laminae orientation and clays and exhibit an internal fabric of microlamination (Stoops et al. 2003). It is easier to tell them apart when they are adjacent to each other in the sample. One sample collected shows a thick section

of many alternating light brown and pink laminae, which is typical (Fig. 5a, c). The thin section shows alternating layers of reddish tinted mass and layers with a higher quartz grain content. The layers with more quartz are the pink layers and the layers with more of a red hue are the light brown layers (Fig. 5b). Alternating pink and light brown laminae are very common and occur in many places throughout the Mormon Mesa and Flat Top Mesa.

DISCUSSION

Interpretations of micromorphology

The laminae orientation seems to not be solely parallel to the overall landscape of the Mormon Mesa and Flattop Mesa. This means that laminae are forming not only as a cap but throughout the massive section



Figure 5: Examples of light brown and pink laminae. (a) Thin section billet showing where thin section picture c is taken. (b) Large hand sample from the Riverside site at Mormon Mesa (MMRKCMA4) cut out of the massive horizon with a saw and oriented. Large section of alternating light brown and pink laminae are seen as well as larger pisoliths. Laminae in large part is parallel to horizon. (c) thin section strip showing pink and light brown laminae. The pink, or lighter, laminae are those sections that have a higher quartz grain content. The light brown, or darker, laminae have a reddish tint and have less quartz comparatively to the pink laminae.

filling voids and fractures/joints.

Interpretations of mineralogy seen in microscope

Some basic differences between the six main types of laminae are noted. The white laminae are usually very fine-grained sections that appear to have no crystalline structure being homogeneously dark brown under the microscope. Some larger white layers could also be made up of wholly calcite crystals with banding. The red laminae appear to be oxidized and are very distinct. In some cases, there is a red haze seen in the laminae. The dark olive grey laminae are comprised of large sparry calcite crystals that are a secondary feature due to dissolution and recrystallization. These crystals radiate away usually from white laminae, or sometimes from other colors of laminae and most likely had the most time to grow. Some dark laminae could be attributed to concentric radially growing ooids. The pale brown laminae are almost entirely made up of small aggregates that can range from slight matrix supported to clast supported. Sometimes the aggregates will be so smashed up against each other that it is very difficult to point out the individual aggregates. The pink and light brown laminae are very similar in composition, and almost always alternate between one another. The difference is that the pink laminae and sections seem to have a higher quartz or sand grain content as opposed to the light brown laminae. Both seem to have a red hue under the microscope.

CONCLUSIONS

Several conclusions can be drawn. First, top-bottom indicators do exist, at least as a rule, though some laminae do not form from the top down. There are too many examples of laminae forming in cracks and voids that appear similar in shape and size to vertical forming laminae. Second, the wide variety of laminae colors represent differences in crystal size, detrital grain content, and mineralogy. The differences are seen in Figures 1-5. Third, laminae do form differently when in cracks and fractures than those seen forming in soil matrix. The laminae in cracks and voids seem to be either infill of aggregates/clay/sand, or growth of sparry calcite crystals. This study fills a gap in existing models of (petro)calcic horizon and profile

development and any insights gained from Mormon Mesa petrocalcic horizons can hopefully be applied to other arid soils and paleosols worldwide.

ACKNOWLEDGEMENTS

This material is based upon work supported by the Keck Geology Consortium and the National Science Foundation under Grant No. 1659322. I thank Colin Robins, who lead our project, and team members Ethan Conley, India Futterman, and Penelope Vorster. Bob Gaines of Pomona College Geology and Kyle McCarty have lent a tremendous hand in guidance and lab technical work.

REFERENCES

- Alonso-Zarza, A.M., Tanner, L.H., 2010. Paleoenvironmental record and applications of calcretes and palustrine carbonates. *Geologic Society of America Special Paper* 416, 1–15.
- Arakel, A. V. 1982. Genesis of calcrete in Quaternary soil profiles, Hutt and Leeman Lagoons, Western Australia. *Journal of Sedimentary Petrology*, 52(1), 109-125.
- Bigham, J.M., Jaynes, W.F., Allen, B.L. 1980. Pedogenic Degradation of Sepiolite and Palygorskite on the Texas High Plains. *Soil Science Society of America Journal* 44 (1) 159-167.
- Brock, A.L. and Buck, B.J., 2009. Polygenetic development of the Mormon Mesa, NV petrocalcic horizons: Geomorphic and paleoenvironmental interpretations. *Catena* 77: 65-75.
- Bullock, P., Fedoroff, N., Jongerius, A., Stoops, G., Tursina, T. 1985. *Handbook for Soil Thin Section Description*. Waine Research.
- Gile, L.H., Peterson, F.F. and Grossman, R.B., 1966. Morphological and genetic sequences of carbonate accumulation in desert soils. *Soil Science* 101(5): 347-360.
- Russell, D., Hudnall, W.H., Allen, B.L. 2010.

- Micromorphology investigation of sepiolite bearing petrocalcic horizons formed from lacustrine sediments on the southern high planes of Texas and New Mexico. Australian Clay Minerals Conference, 21, 43-46.
- Levine, S.J., Hendricks, D.M. 1990. Carbonate forms in Residual Horizons of Limestone Derived Soils in Northern Arizona. *Developments on Soil Science*, Volume 19, 373-380.
- Machette, M.N., 1985. Calcic soils of the southwestern United States. In: Weide, D.L. *Soils and Quaternary Geology of the southwestern United States*. Geologic society of America Special Paper 203: 1-21.
- Monger, H. C. and L. A. Daugherty, 1991. Neoformation of Palygorskite in Southern New Mexico Aridisols. *Soil Science Society of America Journal*. 55:1646-1650.
- Robins, C.R., Deurlington, A., Buck, B.J., and Brock-Hon, A.L., 2015. Micromorphology and formation of pedogenic ooids in calcic soils and petrocalcic horizons. *Geoderma* 251-252: 10-23.
- Schoeneberger, P.J., Wysocki, D.A., Benham, E.C., Broderson, W.D., and Soil Survey Staff, 2013. *Field book for describing and sampling soils*, Version 3.0. Lincoln: Natural Resources Conservation Service, National Soil Survey Center.
- Soil Survey Staff, 2014. *Keys to Soil Taxonomy*, 12th ed. USDA-Natural Resources Conservation Service, Washington, DC.
- Stoops, Georges, et al. 2003 *Guidelines for Analysis and Description of Soil and Regolith Thin Sections*. Soil Science Society of America.
- Stoops, Georges, et al. *Interpretation of Micromorphological Features of Soils and Regoliths*. Elsevier, 2010.
- Vanden Heuvel, R. C., 1966. The Occurrence of Sepiolite and Attapulgite in the Calcareous Zone of a Soil Near Las Cruces, New Mexico. *Clays and Clay Minerals*. 13:193-207.

INTERPRETING POTENTIAL BARIUM SOURCES AT MORMON MESA, NV USING GEOCHEMICAL AND GEOMORPHOLOGICAL DATA

INDIA FUTTERMAN, Vassar College
Research Advisor: Kirsten Menking

INTRODUCTION

Soil profiles, horizons, structures, and geochemistry are direct reflections of environments of formation. Calcic soils are a particularly interesting example which occur in arid to semi-arid environments, and are defined by a subsurface horizon of accumulated secondary calcium carbonate (Machette 1985). With steady climate over time, calcium carbonate accumulates to varying degrees and in varying structures as atmospherically-sourced Ca (and other) ions are translocated down through the soil profile. Ion translocations reach deeper in wetter climates and shallower in more arid periods, rendering their occurrence at different depths a potential proxy for paleoclimate reconstruction. Steady calcite accumulation over time produces a progressive developmental sequence that can be seen in calcic soils throughout the world, given a tectonically stable soil geomorphic surface. A six-stage model currently describes this developmental sequence, with Stage I horizons as the product of minimal CaCO₃ accumulation and Stage VI as the most highly indurated, physically and chemically complex, and typically oldest horizons that have been broken up and recemented at least once (Machette 1985). This breaking up occurred during wetter climate periods as flash flooding resulted in higher surface physical and chemical erosion rates (Robins et al 2012). The oldest soil profiles contain the most highly-developed petrocalcic horizons which serve as a nearly comprehensive record of climate and geomorphic events, and are thus powerful tools for paleoclimatological reconstruction.

One particularly well-developed, well-preserved

petrocalcic soil can be found at Mormon Mesa in the Mojave Desert of southwestern Nevada, USA (Gardner 1972). Developed over the past 4-5 million years in alluvial siliciclastic sediments of the Muddy Creek Formation (Gardner 1972), the Mormon Mesa soil displays the complex morphology of Stage VI petrocalcic horizon development, including brecciation, re-cementation, and vestiges of multiple erosional events. Its complexity has been the subject of many studies (Gardner 1972, Brock-Hon et al., 2012, Robins et al. 2012, and others), investigations which tend to present as many new questions about the development of this ancient soil as they do answers.

Previous work revealed a suite of intriguing minerals present in Mormon Mesa, including authigenic barite (BaSO₄) (Brock-Hon et al., 2012). The presence of authigenic barite in this soil is perplexing, as it implies the presence of mobile Ba ions, which were typically assumed to be insoluble under arid, alkaline conditions (Robins et al., 2012). Pedogenic barite is usually found in low-pH, aquic soils with high base saturation (Stoops and Zavaleta 1978, Sullivan and Koppa 1993), conditions which are not met at Mormon Mesa. However, experimental evidence indicates that Ba²⁺ solubility increases in the presence of Na⁺ and Mg²⁺ (Hanor 2000, Blount 1977). Because Ba ions are not readily oxidized nor reduced and do not bind strongly to organic compounds, their transport depends on solubility (Menzie et al. 2008). Considering the net addition of ions over time to Mormon Mesa soil, the influx of ions required to increase Ba solubility for barite authigenesis is plausible.

However, the question remains: what is the source of barium ions in Mormon Mesa soil? Two possibilities

present themselves: (1) barium could be sourced from Muddy Creek parent material, or (2) Ba ions could be transported to the mesa surface from distal locations.

Barium is not a rare element, most commonly found in the Earth's crust in K-bearing minerals such as alkali feldspars and biotite (Hanor 2000). The underlying Muddy Creek Formation in which the Mormon Mesa soil sequence developed is made up largely of well-sorted, loosely consolidated quartz sand with intercalated beds of claystone and gypsum crusts (Scott 1988). Younger parent materials contributing to the profile consist primarily of siliciclastic alluvium deposited from the Mormon Mountains to the North (Gardner 1972). Soil formation in this region is also heavily influenced by eolian dust inputs (Reynolds et al. 2005), and several studies of dust flux over time in the area point to nearby Owens and Amargosa Valleys as highly probable sources of Ba-rich dust (Reheis et al. 2009; Reheis et al. 2002; Reheis et al. 1996). Ba in these dust inputs can be traced back to granitic rocks eroded from the Sierra range (Reheis et al. 2002), and/or from manganese oxides such as hollandite, a constituent of desert varnish and some basaltic lavas that has been found in dusts deposited in southern Nevada (Reheis et al. 1996; Garvie et al. 2008; Fodor et al. 1994; Kabata-Pendias 2011). Additional evidence for eolian or atmospheric ion inputs is the fact that authigenic barite crystals were found primarily in the massive horizon (which caps the sequence), suggesting potential translocation from the surface of the mesa. While the eolian hypothesis is supported by many previous studies, the heterogeneity of the Muddy Creek parent material should be investigated as another potential source of Ba ions.

The goal of this study is to identify the most likely source of barium ions, which may reveal the nuances of the chemical mobilization pathways that are fundamental to the development of all soils. Additionally, the results of this study may illuminate the processes by which authigenic barium occurs in other calcic soils of the world. It was hypothesized that mapping of elemental concentrations across the mesa surface and across representative soil profiles would show wind-caused variations in geochemistry and reveal potential correlation with geomorphic features. Specifically, a downwind-directional

decrease in Ba concentration would suggest a primarily eolian source for Ba. Conversely, lack of variability of Ba between horizons or across the mesa surface could support a parent material source.

METHODS

Map unit description

A geomorphic map of the mesa surface was created based on remote sensing interpretations, field observations, and using the image classification spatial analyst tool in ArcMap (USDA-FSA-APFO 2017; see Fig. 1). Five geomorphic units were defined: sand dunes, or modern eolian features composed primarily of red quartz sand; gullies, or dendritic, vegetated intermittently wetted subsurface drainage networks; depression pits, or the round, vegetated water collection points for gully drainage; arroyos, or ephemerally wet stream beds actively eroding inwards from the edges of the mesa; and undifferentiated mesa surface, defined as sparsely vegetated eolian sands mantling alluvial fan gravels.

Surface site locations and sampling

Field work for this study was conducted in June, 2018. 86 samples were collected in total; of these, 36 were analyzed using inductively coupled plasma mass spectrometry (ICP-MS). Two groups of surface samples were collected: geomorphic unit samples collected to ensure adequate representation of the mesa surface in our dataset and to assess the influence of geomorphic processes on soil geochemistry, and surface transects for a systematic study of surface variability, especially as it relates to eolian dust flux. At each sampling site, 200-1000 g of substrate were collected. Two arroyos, three sand dunes, four depression pits, and two drainage gullies were sampled at Mormon Mesa (Fig. 2). Additionally, one sand dune and three depression pits were sampled at adjacent Flat Top Mesa, a separate, isolated remnant of the once more continuous paleo-Mormon Mesa soil geomorphic surface. 20 samples were taken parallel to the northernmost road on Mormon Mesa, at a distance of 0.2 km north of the road and at intervals of approximately 0.5 km along the transect (Fig 2). 10 samples were collected along a transect parallel to a shorter, more southern Mormon Mesa road, at 0.2

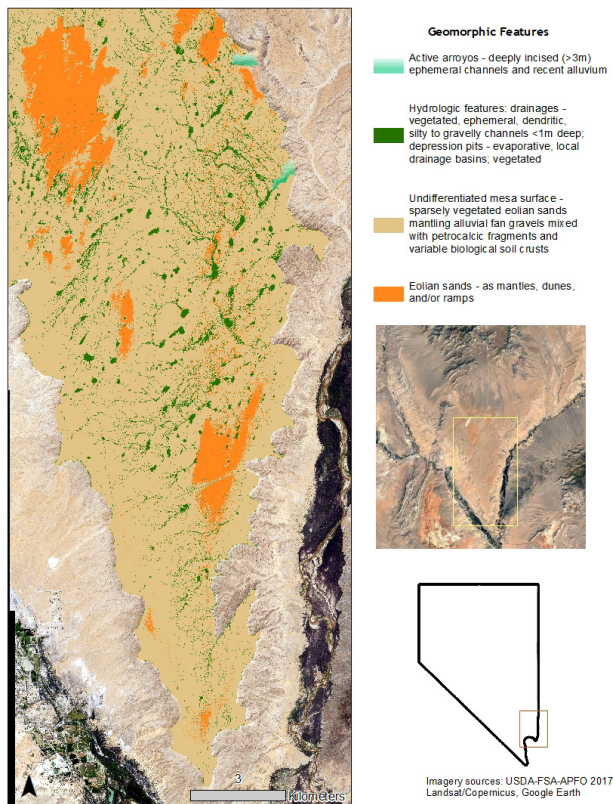


Figure 1: Geomorphic map of mesa surface study area.

km south of the road and at intervals of approximately 0.4 km along the transect (Fig. 2). Eight samples were collected along a Flat Top Mesa transect at intervals of approximately 0.25 km.

Profile locations and sampling

Two complete profiles were sampled at both Mormon Mesa (Riverside and Overton sites) and Flat Top Mesa (Flat Top East and Flat Top West; see Fig. 3). The Riverside and Overton sites are well-studied (Brock-Hon et al. 2012, Robins et al 2012), whereas both Flat Top Mesa profiles had not previously been sampled. 200-1000 g of substrate were collected from each horizon: Muddy Creek (parent material), lower, middle, and upper transitional subhorizons, massive, and brecciated. The highly indurated massive horizon was sampled using a concrete saw.

Laboratory preparation and geochemical analysis

Unconsolidated samples (e.g., all surface samples) were sieved to separate the fine fraction (>2 mm) from large organic matter and clasts. The coarse fraction, largely or entirely composed of petrocalcic fragments,

was retained. Indurated or partially cemented samples (e.g., all petrocalcic horizon samples) were pulverized in steel rock chippers and disc mills to achieve fine fractionation. 0.5 g of each sample was digested using EPA Method 3050b, Section 7.5 (for improved solubilities and recoveries of Ba). Digests were analyzed for elemental content using the Thermo Scientific iCapRQ ICP-MS run in KED mode at the Chemistry Department of Vassar College.

PRELIMINARY RESULTS

Elemental concentrations (Table 1) among each of the five depression pit samples tested are fairly consistent. These samples contain notably high concentrations of Al, K, and Fe. Excluding outliers, depression pit samples also contain comparatively high concentrations of barium and manganese. Ca concentrations are not notable among these samples. The single playa sample is relatively abundant in Al and K. Ca is very high. Mn concentrations are similar to those in depression pit samples. Fe and Ba are relatively abundant. K, Ca, and Fe concentrations among all undifferentiated surface samples are relatively consistent and tend towards somewhat high concentrations. Al, Mn, and Ba concentrations vary among these samples. Al ranges from moderate to high abundance; Mn ranges from low to moderate abundance, and Ba ranges from low to moderate concentration. Concentrations of all elements, besides Fe, were relatively low among sand dune samples. Ba concentrations are lowest among these samples. Ca concentrations range from low to moderate among samples. Concentrations of other elements remain consistently low among samples. Elemental concentrations between the two drainage samples tested are quite consistent. Al, K, Ca, and Mn are present at moderate concentrations. Fe and Ba are present at moderate to high concentrations. Some elemental concentrations between both arroyo samples are inconsistent. Al ranges from low to moderate, and Mn ranges from low to very high. Ca, Fe, and Ba are consistently relatively moderate.

Elemental concentrations vary among the horizon samples tested (Fig. 3 and Table 1). Among these samples, Al, K, and Fe concentrations are highest in the rubble horizon. Ca concentrations are highest in

the massive and transitional horizons. Mn is notably high in the transitional horizon, and Fe is particularly high in the rubble layer. The massive horizon contains by far the highest Ba concentration, with half as much in the transitional layer, and comparatively very little in the rubble layer. Between the two horizons, there is a general decreasing trend in Ba concentration with depth.

DISCUSSION

Preliminary ICP-MS results of Ba and other elemental concentrations present a puzzle. Because this study is primarily concerned with barium sources, interpretation will focus of Ba concentrations among samples and any apparent relationship between Ba and the presence of other ions. The high Ba concentrations (as much as 428.4 ppb) detected in the massive and transitional horizons are consistent with previously published observations of barite crystals in these

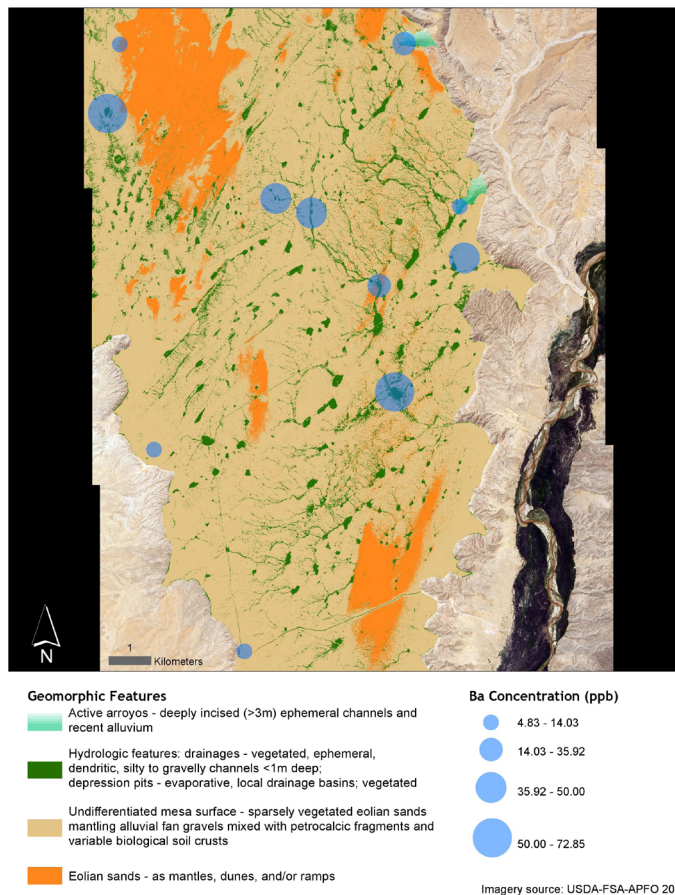


Figure 2: Selected elemental concentrations (ppb) from surface transect and geomorphic feature samples, Mormon Mesa.

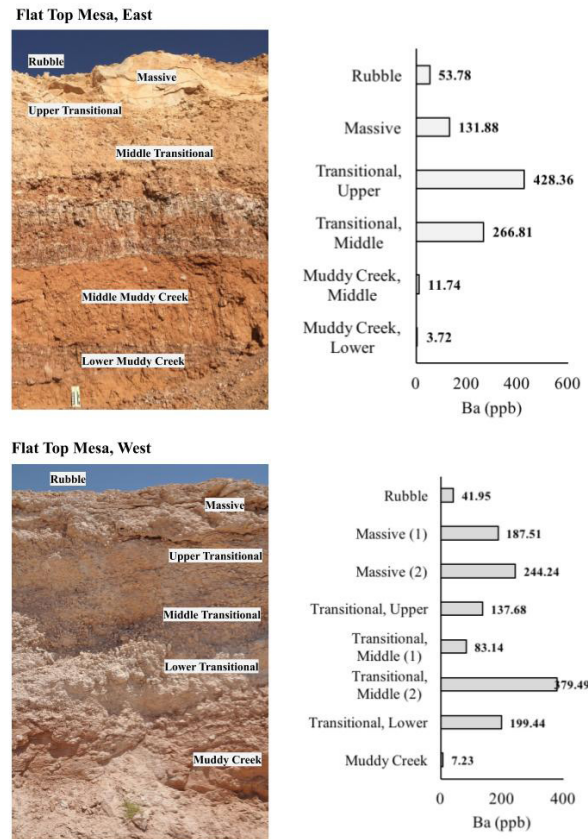


Figure 3: Ba concentrations within soil horizons: Flat Top Mesa East and West.

horizons from SEM imagery (Brock-Hon et al., 2012). These high Ba concentrations are likely the result of continuous accumulation of atmospherically-sourced ions in geomorphologically stable, relatively shallow horizons over an extended period of time. As an actively eroding surface, the uppermost rubble layer of the Mormon Mesa soil sequence would not be able to accumulate much atmospherically-sourced Ba. Additionally, according to the eolian/atmospherically-sourced Ba hypothesis, with increasing profile depth one would expect to see decreasing Ba concentrations as the translocated ions are sequestered in the shallower horizons.

Relatively high concentrations of Ba among depression pit samples perhaps point to the significance of hydrology in modern Ba solubility trends. As fluid collection points within an apparent hydrological network of drainage gullies on the mesa surface, they are likely to have more concentrated

	Al	K	Ca	Mn	Fe	Ba
Depression pit	3693.18	863.83	4276.66	114.80	4268.03	72.85
Depression pit	3291.90	653.08	7057.28	108.50	3756.95	65.38
Depression pit	2738.23	558.79	3908.38	95.77	3528.28	50.00
Depression pit	3808.70	912.06	5758.02	119.83	4289.36	69.70
Depression pit	2080.57	372.17	8789.04	75.58	2946.28	42.44
Playa	2937.69	631.44	26698.07	101.44	3580.14	50.48
Undifferentiated surface	1958.53	353.90	7281.74	71.31	3021.84	38.76
Undiff. surface	2095.99	326.75	9497.81	70.49	3046.29	48.21
Undiff. surface	919.56	114.95	2072.41	32.67	2071.36	14.03
Undiff. surface	1641.92	288.32	6617.07	107.62	2656.71	29.13
Sand dune	620.35	62.34	803.15	31.77	2917.76	8.52
Sand dune	282.58	16.87	1936.69	16.32	1139.15	4.83
Sand dune	559.90	87.13	339.20	18.59	1475.05	6.75
Sand dune	345.43	14.68	1504.20	12.59	844.36	4.69
Transitional horizon	937.62	63.99	65070.56	255.35	667.86	266.81
Massive horizon	892.23	34.36	54813.03	6.45	564.42	428.36
Rubble horizon	1813.87	283.04	13032.41	50.78	2706.00	53.78
Drainage gully	2610.98	557.65	5137.50	98.78	3501.64	48.39
Drainage gully	1894.83	394.62	3409.72	78.03	2855.12	35.92
Arroyo	1483.18	210.90	9020.06	36.88	2056.70	30.16
Arroyo	571.27	142.75	16597.30	753.81	1193.06	12.80

Table 1: ICP-MS results for selected elemental concentrations (ppb) of selected samples.

dissolved ions. These may prove to be ideal circumstances for increasing the solubility of barium, explaining why the data show somewhat elevated Ba concentrations among these samples, and also accounting for the somewhat lower Ba concentrations in drainage gully samples. If Ba were primarily sourced from the Muddy Creek Formation, these concentrations would be low relative to those parent materials. Future studies should also investigate the influence of biologically-aided mineral precipitation on elemental concentrations in these sporadically moistened locations.

The relatively high Ba concentration in the playa sample may support the eolian hypothesis as well, as the fine evaporitic sediments in playas to the west of the mesa may be blown onto the mesa surface. Future studies should sample additional adjacent playas for more comprehensive geochemical data. Further support for the eolian hypothesis stems from the presence of barium in “undifferentiated

surface” samples. Complete transects are being analyzed to assess a downwind trend in decreasing Ba concentration, which would also lend credence to the eolian hypothesis.

The apparently very low elemental concentrations among sand dune samples may be attributed to the fact that substrate samples, composed mainly of silicate minerals, were not digested in hydrofluoric acid. Complete digestions of all samples would yield more accurate data, and should be pursued in subsequent studies.

The lack of consistency in the geochemical makeup of both arroyo samples may be due to the active erosion occurring at these sites only. Active erosion would likely result in a chaotic mixing of lithic fragments, soil horizons material, and transported grains, producing somewhat outlier results.

CONCLUSIONS

This study incorporated data from ancient soil horizons as well as geomorphically active surface sediments to investigate the potential sources of Ba for authigenic barite in the massive horizon of this soil (Brock-Hon et al. 2012). By mapping the spatial variations in the concentration of barium and other associated elements in surface and profile samples, potential relationships between geomorphic features and chemical composition could be illuminated. ICP-MS data suggest that Ba ions are more concentrated towards the surface of the mesa, in the transitional, massive, and rubble horizons, as well as in the depression pits that dot the mesa surface. Somewhat elevated Ba concentrations in depression pit samples may also suggest a hydrological component to barite neoformation in Mormon Mesa soils. As more samples are analyzed and results are mapped, more definitive conclusions may be drawn. Identifying the mechanisms that drive barite authigenesis can deepen our understanding of soil formation and ion mobilization, as well as allow us to anticipate the geochemical impacts of climate change on our soils.

ACKNOWLEDGEMENTS

This material is based upon work supported by the Keck Geology Consortium and the National Science Foundation under Grant No. 1659322. Special thanks to Colin R. Robins, Penelope Vorster, Ethan Conley, and Kurt Crandall for their support in the field and laboratory. Major support from the Keck Geology Consortium was provided by Cam Davidson, Karl Wirth, Marga Miller, and Jonathan Harris. This project would not have been possible without the advising of Kirsten Menking in the Vassar College Earth Science Department. Other Vassar staff involved in this project include Rick Jones, Jeff Walker, and Joseph Tanski. Neil Curri provided invaluable assistance with GIS operations. Special thanks to Dr. Karen Wovkulich for her patient help with ICP and XRF analyses. Thanks also to Amy Brock-Hon for her foundational research on barite in Mormon Mesa soils. Matthew Rahn Manon and the Union College Department of Geology provided access to laboratory space and use of their handheld XRF. Permission to sample was provided by the Clark County Bureau of Land Management through a letter of understanding (680 NVS0100).

REFERENCES

- Beattie, J., & Haldane, A. (1958). The occurrence of palygorskite and barytes in certain parna soils of the Murrumbidgee region, new South Wales". *The Australian Journal of Science*, 20, 274-275.
- Blount, C. (1977). Barite solubilities and thermodynamic quantities up to 300 C and 1400 bars. *American Mineralogist*, 62, 942-947.
- Brock-Hon, A., Robins, C.R., & Buck, B.J. (2012). Micromorphological investigation of pedogenic barite in Mormon Mesa petrocalcic horizons, Nevada USA: Implication for genesis. *Geoderma*, 179-180, 1-8.
- Buck, B., Lawton, T., & Brock, A. (2010). Evaporitic paleosols in continental strata of the Carroza Formation, La Popa Basin, Mexico: Record of Paleogene climate and salt tectonics. *GSA Bulletin*, 122(7/8), 1011-1026.
- Fodor, R., Jacobs, R., & Bauer, G. (1994). Hollandite in Hawaiian basalt: a relocation site for weathering-mobilized elements. *Mineralogical Magazine*, 58, 589-596.
- Gardner, L. (1972). Origin of the Mormon Mesa Caliche, Clark County, Nevada. *Geological Society of America Bulletin*, 83, 143-156.
- Garvie, L., Burt, D., & Buseck, P. (2008). Nanometer-scale complexity, growth, and diagenesis in desert varnish. *Geology*, 36(3), 215-218.
- Jones, R. (1986). Barium in Illinois Surface Soils. *Soil Science Society of America Journal*, 50, 1085-1087.
- Kabata-Pendias, A. (2011). *Trace Elements in Soils and Plants*. (4, Ed.) Boca Raton, FL: CRC Press.
- Machette, M. (1985). Calcic soils of the southwestern United States. *Geological Society of America Special Paper*, 203, 1-21.
- Menzie, C., Southworth, B., Stephenson, G., & Feisthauer, N. (2008). The Importance of Understanding the Chemical Form of a Metal in the Environment: The Case of Barium Sulfate (Barite). *Human and Ecological Risk Assessment*, 14, 974-991.
- Reheis, M., Budahn, J., & Lamothe, P. (2002). Geochemical evidence for diversity of dust sources in the southwestern United States. *Geochimica et Cosmochimica Acta*, 66(9), 1569-1587.
- Reheis, M., Budahn, J., Lamothe, P., & Reynolds, R. (2009). Compositions of modern dust and surface sediments in the Desert Southwest, United States. *Journal of Geophysical Research*, 114, 1-20.
- Reheis, M., Goodmacher, J., Harden, J., McFadden, L., Rockwell, T., Shroba, R., . . . Taylor, E. (1995). Quaternary soils and dust deposition in southern Nevada and California. *GSA Bulletin*, 107(9), 1003-1022.
- Reynolds, R., Reheis, M., Yount, J., & Lamothe, P. (2006). Composition of aeolian dust in natural traps on isolated surfaces of the central Mojave

Desert - sights to mixing, sources, and nutrient inputs. *Journal of Arid Environments*, 66, 42-61.

Robins, C., Brock-Hon, A., & Buck, B. (2012). Conceptual Mineral Genesis Models for Calcic Pendants and Petrocalcic Horizons, Nevada. *Soil Science Society of America Journal*, 1-17.

Stoops, G., & Zavaleta, A. (1978). Micromorphological evidence of barite neoformation in soils. *Geoderma*, 20, 63-70.

Sullivan, L., & Koppi, A. (1995). Micromorphology of authigenic celestobarite in a duripan from central Australia. *Geoderma*, 64, 357-361.

$\delta^{13}\text{C}$ AND $\delta^{18}\text{O}$ GEOCHEMISTRY OF PEDOGENIC CARBONATES OF MORMON MESA, SOUTHEASTERN NEVADA, USA

PENELOPE VORSTER, Mount Holyoke College
Research Advisor: Steve Dunn

INTRODUCTION

The Early Pliocene, extant paleosol at Mormon Mesa in Southeast Nevada is a rare example of advanced calcium carbonate pedogenesis, forming multiple well-indurated petrocalcic horizons and a set of morphologic features such as carbonate laminae, concretionary pisoids, and pedogenic ooids encased in a carbonate matrix (Brock and Buck, 2009). The soil represents a record of geomorphic conditions in the Mojave over approximately 4-5 million years (Bachman and Machette, 1977; Brock and Buck, 2009; Robins et al., 2012).

Most of the Mormon Mesa soil horizons are extremely calcic, with an average of 70.4% CaCO_3 reported from one profile (Robins et al., 2012). The remainder of the soil mineralogy is composed of detrital grains of lithic parent material, volcanic ash, and fibrous phyllosilicates interpreted as pedogenic palygorskite and sepiolite from Scanning Electron Microscopy with Energy Dispersive Spectrometry (SEM-EDS) corroborated by X-Ray Diffraction (XRD) (Brock and Buck, 2009; Robins, 2010). Formation of authigenic minerals is dependent on ratios of mineral forming components in solution within the soil, as well as on soil pH. (Brock and Buck, 2009; Robins et al., 2012; Zamanian et al., 2016). Detrital silicate grains and volcanic ash contribute Si to the soil solution with force of calcite crystallization facilitating dissolution of quartz and ash. The available silica is incorporated into authigenic fibrous magnesium silicates such as palygorskite and sepiolite (Robins et al., 2012).

Of note for paleoenvironmental interests, pedogenic calcium carbonate accumulates in arid to semi-arid,

alkaline soil horizons like those at Mormon Mesa when Ca^{2+} ions from meteoric water combine with CO_2 from plant and microbial respiration, (Gile et al., 1966) and oxygen from soil water (Cerling and Quade, 1993; Zamanian et al., 2016). CO_2 is largely contributed to soil air or released into solution by microbial activity and by respiration at the plant root. At Mormon Mesa, where soil organic matter (SOM) is $< 2.0\%$, (Robins et al., 2012) soil CO_2 concentrations may also be impacted by the diffusion of atmospheric CO_2 into the soil profile (Cerling, 1984; Zamanian et al., 2016). Importantly, plant community compositions influence soil carbonate $\delta^{13}\text{C}$ signature. C3 plants contribute to more negative $\delta^{13}\text{C}$ values in comparison to C4 plants (Quade et al. 1989; Alonso-Zarza, 1998; Zamanian et al., 2016). Oxygen in pedogenic carbonate is sourced from meteoric water, with $\delta^{18}\text{O}$ values fractionated by regional temperature. A model describing the introduction of isotopic signatures from environmental sources is shown (Figure 1). The goal of this research project is to address the following questions: Do pedogenic carbonate $\delta^{13}\text{C}$ and $\delta^{18}\text{O}$ values vary among horizons and between features sampled at Mormon Mesa? Where do authigenic phyllosilicates occur in the micromorphology of the soil, and are they likely to record $\delta^{18}\text{O}$ values similar to those of the calcite?

METHODOLOGY

Field Methods

We identified three field sites located on the edges of Mormon Mesa and Flat Top Mesa in Clark County, Nevada. The Riverside site (MMR) is located on the southeast edge of Mormon Mesa. The Flat Top East

site (FTE) and Flat Top West site (FTW) are located on the eastern and western sides, respectively, of Flat Top Mesa, which is located to the East of Mormon Mesa (Figure 2).

The Mormon Mesa soil profile overlies the Muddy Creek Formation, a variable package of fine grained sandstones, thinly bedded siltstones, and mudstones of Miocene age capped by stage II carbonate paleosol horizons. At Riverside, five distinct horizons were observed above the muddy creek unit: Muddy Creek showing stage II calcic pedogenesis, a stage III transitional horizon, stage IV laminar horizon, stage V-VI discontinuous and brecciated massive horizon (Figure 3a). The same five horizons were observed at Flat Top East and Flat Top West, with variations in thickness and morphology. For this study, one to three samples were collected at intervals (top, middle, bottom) from each horizon at each profile to create a vertical section using rock hammers, chisels, and/or a concrete cutting saw.

Stable isotope analysis

Field samples were prepared at Pomona College. For carbonate $\delta^{18}\text{O}$ and $\delta^{13}\text{C}$ analysis, samples were ground using steel rock crushers and disc mills to achieve a fine gravel/coarse sand size. For some massive horizon samples, pisoid and laminae macromorphological features were cut and isolated from the soil matrix using a diamond bladed tile saw. Pisolids, laminae, and matrix portions of each sample were kept separate for isotope analysis.

Aliquots of processed samples were analyzed in the stable isotope laboratory at the University of Massachusetts Amherst on a Finnigan Delta XL+ mass spectrometer with a Kiel III automated carbon device. Reproducibility on standards and duplicates is generally better than $\pm 0.2\%$. $\delta^{18}\text{O}$ and $\delta^{13}\text{C}$ values are reported relative to the VPDB standard.

Micromorphology and imaging

Rectangular billets of Stage V-VI soil containing the four major macromorphological soil features observed- pisolids, laminae, and matrix- were cut to approximately 3x4x1 cm in size. For disaggregated Stage I-III samples, pieces of the soil were set in

epoxy and cut into approximately 3x4x1 cm billets. At Mount Holyoke College, billets were polished and carbon sputter coated for backscatter and secondary electron imaging on a FEI Quanta 200 SEM. EDAX Genesis software was used for x-ray microanalysis.

RESULTS

Stable Isotopes $\delta^{13}\text{C}$ and $\delta^{18}\text{O}$

$\delta^{13}\text{C}$ values range between -6.01% and -3.33% across FTE, FTW, and MMR profiles and when grouped by profile (Figure 3a), all three $\delta^{13}\text{C}$ ranges overlap. However, there are generally more negative values in the FTE (median -4.92%) and MMR (median -4.46%) profiles, and higher values in FTW (median -3.87%). One way ANOVA results support a significantly distinct range for the FTW ($p < 0.05$) $\delta^{13}\text{C}$ compared to those of FTE and MMR, but MMR and FTE values are not statistically distinct from each other.

When grouped by carbonate development stage and morphology (Figure 3b), the narrower range (-4.78% to -3.98%) of the Stage II carbonate nodule samples (median $\delta^{13}\text{C}$ -4.47%), overlaps with the broader range (-5.42% to -3.54%) of the Stage III samples (median -4.38%). Meanwhile, the Stage V-VI inset features at FTW (median -3.62% , range -3.80% to -3.33%) and rubble layer samples median -4.07% ; range from -4.21% to -3.93%) fall at the high end of the stage III values. One way ANOVA does not support significant statistical differences between ranges.

$\delta^{18}\text{O}$ values range from -10.51% to -7.43% across the three profiles (Figure 3a) and show closer overlap among the three sites than $\delta^{13}\text{C}$, with one way ANOVA finding no significant distinction between ranges. The median value for FTE is -8.62% . For FTW, the median is -8.16% . For MMR, the median is -9.23% .

For grouped stages (Figure 3b), $\delta^{18}\text{O}$ values show overlapping clusters, with $\delta^{18}\text{O}$ values for Stage III transitional horizons (median -8.98%) distributed in a broad range (-10.5% to -8.17%). The Stage V-VI inset features at FTW (median -7.78%) have a narrower range (-8.14% to -7.78%) and differ significantly ($p < 0.05$) from Stage II values (median -9.04% , range -9.99% to -8.62%) based on one way ANOVA.

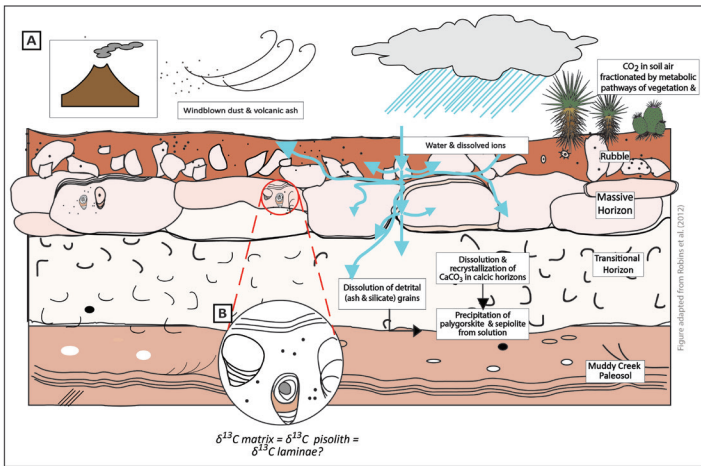


Figure 1. Illustrated model showing sources of carbon and oxygen fractionation, and of windblown parent minerals to authigenic calcite and silicates in Mormon Mesa soil. 1A shows introduction of lithogenic dust and ash, percolation of meteorically fractionated water, and metabolically fractionated CO_2 at plant roots. 1B shows a detailed view of Stage IV-VI morphological features.

Rubble layer samples report intermediate values (median -8.07‰ , range -8.05‰ to -8.09‰).

Micromorphology

A survey of the micromorphology and elemental composition of several thick sections of Stage V-VI pedogenic carbonate from MMR using SEM-EDS revealed a prevailing pattern to the micromorphology of the sample fabrics. Mineral identifications are supported by EDS spectra. Laminae features between $100\ \mu\text{m}$ and $1\ \text{mm}$ wide are observed in multiple samples. Laminae are defined by the alternation of lines of subangular to subrounded grains of detrital quartz in a calcium carbonate matrix with linear sections of homogenous carbonate (Figure 4a). Dissolution features in the carbonate matrix are common, especially at the contact between carbonate and detrital grains (Figure 4b). Within dissolution features, quartz grains show evidence of dissolution, with fibrous clay minerals interpreted as palygorskite and sepiolite (Robins et al., 2014) commonly filling dissolved areas between quartz grains and carbonate matrix (Figure 4a, b, c). Elemental composition of fibrous clays is shown in Figure 4d.

DISCUSSION

Values of $\delta^{13}\text{C}$ and $\delta^{18}\text{O}$ at FTE, FTW, and MMR are consistent with values for other calcic soils in similar

arid to semiarid soils in southern Nevada, which range from ca. -6‰ to 0‰ for $\delta^{13}\text{C}$ and ca. -10‰ to -4‰ for $\delta^{18}\text{O}$ (Quade et al., 1989). Additionally, trends of increasingly negative isotopic values for both $\delta^{13}\text{C}$ and $\delta^{18}\text{O}$ with increasing depth below the surface are consistent with previously published data (Cerling et al., 1984; Quade et al. 1989).

$\delta^{13}\text{C}$ values ranging -6.01‰ to -3.33‰ with mean -4.45‰ suggest the presence of both C3 and C4 vegetation, with an abundance of C4 vegetation approximately 22%. This is consistent with anticipated ratios of C3 and C4 communities in arid to semiarid climates (Ehleringer, 2005) and closely reflects previously published systematic surveys of vegetation on similar soils in the region (Quade et al., 1984). Significantly higher $\delta^{13}\text{C}$ values in the FTW profile imply greater exchange with respired CO_2 from C4 vegetation in the FTW profile than in either FTE or MMR. The implication of more pervasive C4 vegetation is greater local water stress at the time and location of carbonate precipitation.

The lack of significant distinction among $\delta^{13}\text{C}$ values for pedogenic carbonate stages and morphologies implies that proportions of C3 and C4 metabolic paths do not have a substantial effect. One explanation for the non-significantly high $\delta^{13}\text{C}$ of inset Stage V-VI features in FTW is that exchange between carbonate forming solution and atmospheric CO_2 was more active in the formation of these features. Atmospheric carbon diffusion enriches $\delta^{13}\text{C}$ values up to 4.4‰ (Cerling, 1984; Zamanian et al., 2016). The shallow depth of the inset features and the possibility of dissolution-recrystallization in these features supports the plausibility CO_2 diffusion.

The lack of statistically significant distinction between $\delta^{18}\text{O}$ ranges among the three profiles suggests similar regional temperature during pedogenic carbonate precipitation. The marginally higher $\delta^{18}\text{O}$ of FTW may reflect soil solution enrichment in $\delta^{18}\text{O}$ due to evaporation before carbonate precipitation (Quade et al., 1989). This is consistent with the hypothesized local water stress at FTW inferred from statistically high $\delta^{13}\text{C}$ in FTW carbonate.

Within grouped stages, significant distinction between the $\delta^{18}\text{O}$ ranges of inset Stage V-VI features

at FTW and Stage II values from all three profiles may represent precipitation under different regional temperatures. Lower $\delta^{18}\text{O}$ in Stage II carbonate indicates higher temperature at the time of carbonate precipitation compared to Stage V-VI, as the $\delta^{18}\text{O}$ value for meteoric water is decreased as evaporation increases. However, the possibility remains that relatively high $\delta^{18}\text{O}$ in FTW features is the result of evaporation of light oxygen from the carbonate-forming soil solution.

Each stage of carbonate pedogenesis has associated points of interest and challenges for interpreting paleoclimate from isotopic values. Stage II carbonate nodules represent only the earliest phase of carbonate pedogenesis, and thus do not present a full view of climate trends over time. Stage III is interpreted as forming over a very long time interval ($> 1 \text{ Ma}$) (Brock and Buck, 2009) and varies in thickness from approximately 60 cm at FTE to over 650 cm at FTW, complicating a comparative approach between profiles. Stage V to VI features are discontinuous, varied in their morphology, and show evidence of

dissolution-precipitation (Robins et al., 2014). Finally, the carbonate component of rubble layers are composed of fragments of one or more stage V-VII horizons. For these reasons, a more nuanced study is necessary to propose a climate history for Mormon Mesa.

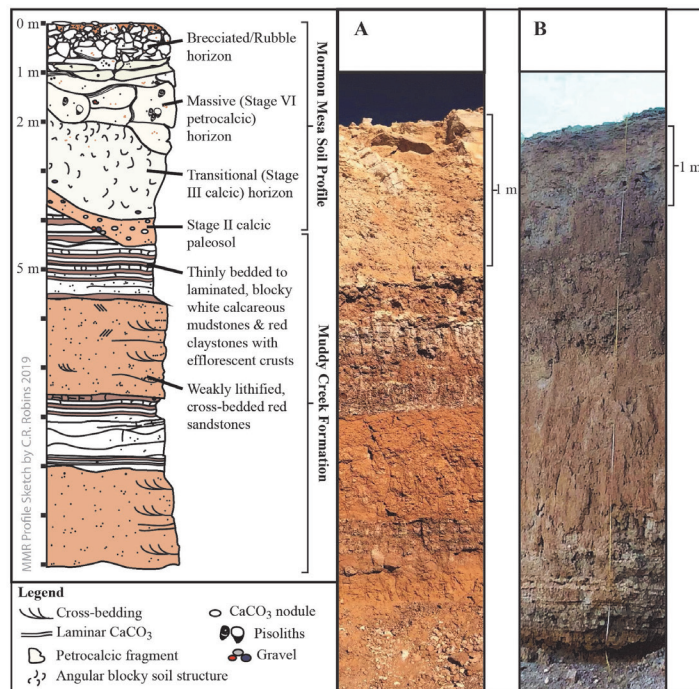


Figure 2. Sketch of MMR profile by C.R. Robins showing typical Mormon Mesa horizons. 2A field photo of FTE profile showing Muddy Creek Formation through Stage VI horizon. 2B field photo of FTW profile showing Muddy Creek Formation through Stage VI horizon.

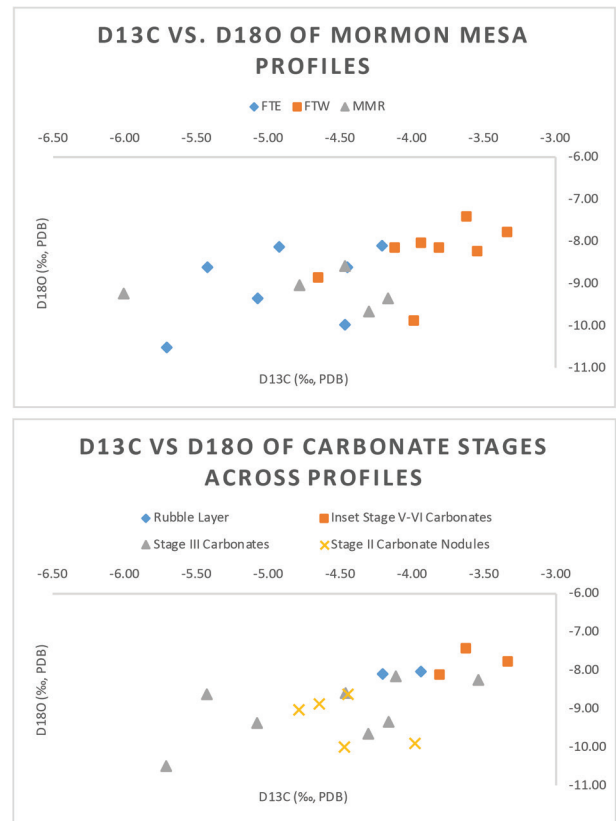


Figure 3. $\delta^{13}\text{C}$ vs. $\delta^{18}\text{O}$ stable isotope data in ‰ PDB compared between MMR, FTW, FTE profiles (top) and between carbonate stages II, III, V-VI, and rubble.

Occurrence of fibrous clay minerals interpreted as palygorskite and sepiolite from SEM-EDS secondary electron images and spectra is consistent with previously published mineralogy of Mormon Mesa soil (Robins et al., 2012; 2014). The observed morphology and spatial relationships between calcite, quartz, and phyllosilicate clay minerals supports the Robins et al. model of clay mineral authigenesis due to force of calcite crystallization. The implication of the observed morphology and indications of authigenesis is that a new set of hypotheses relating the oxygen component of Mormon Mesa soil solution and that of the pedogenic clays may be developed.

ACKNOWLEDGEMENTS

This material is based upon work supported by the Keck Geology Consortium and the National Science Foundation under Grant No. 1659322. Additional support for this project was provided by the Pomona College Geology Department, The W.M. Keck Science Department of the Claremont Colleges, and the Mount Holyoke Department of Geology and Geography. I thank The University of Massachusetts Amherst Department of Geosciences for stable isotope analyses. I thank my field colleagues Ethan Conley, Kurt Crandall, and India Futterman, my research advisors Colin Robins and Steve Dunn, and Mount Holyoke College Microscopy Director Sarah Kiemle.

REFERENCES

- Alonso-Zarza et al. 1998. Fan-surface dynamics and biogenic calcrete development: Interactions during ultimate phases of fan evolution in the semiarid SE Spain (Murcia). *Geomorphology*, 24, p.147-167.
- Bachman, G.O., Machette, M.N. 1977. *Calcic Soils and Calcretes in the Southwestern United States*. USGS: Open File Report 77-797, p. 163.
- Brock, A.L., Buck, B.J., 2009. Polygenetic development of the Mormon Mesa, NV petrocalcic horizons: Geomorphic and paleoenvironmental interpretations *Catena*, 77, p 65-75.
- Cerling, T.E., 1984. The stable isotopic composition of modern soil carbonate and its relationship to climate. *Earth and Planetary science letters*. 71, p. 229-240.
- Cerling, T.E., and Quade, J., 1993 Stable carbon and oxygen isotopes in soil carbonates. P. Swart, J.A. McKenzie, K.C. Lohman (Eds.), *Climate Change in Continental Isotopic Records*, American Geophysical Union, Washington DC. p. 217-231.
- Ehleringer J.R. 2005. The Influence of Atmospheric CO₂, Temperature, and Water on the Abundance

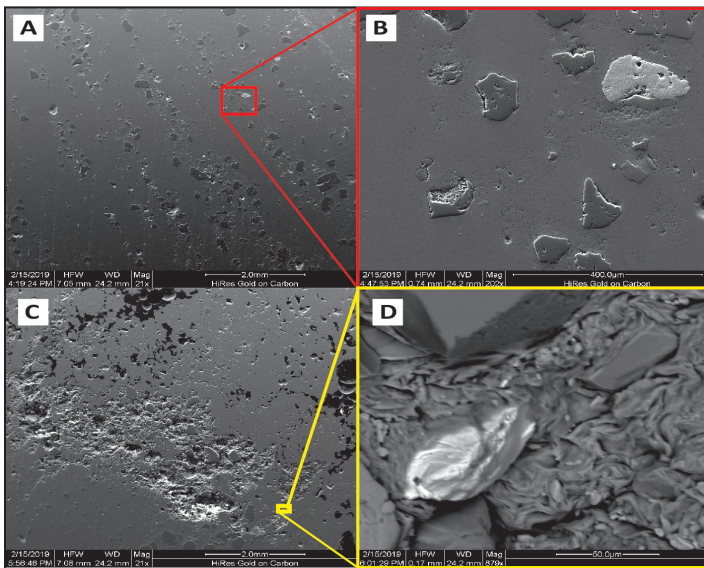


Figure 4. SEM secondary electron images showing micromorphology of sections of Stage V carbonate and clays. 4A image of laminae with bands of detrital quartz in calcite matrix. 4B enlarged view from 4A showing subangular quartz and oxide (light grain), with partial dissolution of quartz grain and precipitation of authigenic silicates. 4C image of carbonate matrix with quartz grains and dissolution features. 4D enlarged image from within dissolution feature of 4C showing fibrous authigenic phyllosilicates growing amid crystalline calcite.

CONCLUSIONS

Isotope data from pedogenic carbonate as a proxy for paleoclimate has contributed immensely to understanding of temperature and moisture regimes over recent geologic history. The use of pedogenic carbonate for regional temperature trends, however, relies on the assumption of authigenic carbonates as geochemically stable and does not account for dissolution and recrystallization of carbonate in soil. The implication of pedogenic carbonate recrystallization is an iteratively rewritten -and overwritten- climate history. Each successive phase of recrystallization captures new isotope values reflective of conditions at that moment, and ultimately contributes to time averaging of paleoclimate data. Authigenic phyllosilicate clay minerals in FTW, FTE, and MMR may be less prone to dissolution and recrystallization over the same time interval, and may as a result capture distinct signatures relevant to paleoclimate. Rather than relying on carbonate, $\delta^{18}\text{O}$ of authigenic phyllosilicates present in Mormon Mesa soil should be studied as a potential source of future paleoclimate models for this region.

of C3/C4 Taxa. In: Baldwin I. et al. (eds) A History of Atmospheric CO₂ and Its Effects on Plants, Animals, and Ecosystems. Ecological Studies (Analysis and Synthesis), vol 177. Springer, New York, NY. p 214 - 229

- Gile, L.H. et al., 1966. Morphological and genetic sequences of carbonate accumulation in desert soils. *Soil Science*. 1015, p. 345-360.
- Quade, J., Cerling, T.E., Bowman, J.R., 1989. Systematic variations in the carbon and oxygen isotopic composition of pedogenic carbonate along elevation transects in the southern Great Basin, United States. *GSA Bulletin*, 101, p. 464-475.
- Robins, C.R., 2010. Phyllosilicate mineralogy, ⁴⁰Ar/³⁹Ar geochronology, and genesis of petrocalcic soils in the Southwest U.S.A. Ph.D. Dissertation, University of Nevada, Las Vegas. 343p.
- Robins, C., Brock-Hon, A.L., Buck, B.J., 2012. Conceptual mineral genesis models for calcic pendants and petrocalcic horizons, Nevada Soil Science Society of America Journal. v. 76 n. 5, p. 1887-1903.
- Robins et al., 2014. Testing the applicability of vacuum-encapsulated ⁴⁰Ar/³⁹Ar geochronology to pedogenic palygorskite and sepiolite. *Quaternary Geochronology*. v. 20. P. 8-22.
- Zamanian, K., Pustovoytov, K., Kuzyakov, Y., 2016. Pedogenic Carbonates: Forms and formation processes. *Earth Science Reviews*. v. 157 p. 1-17.

GEOLOGY OF THE CHUGACH-PRINCE WILLIAM TERRANE IN NORTHERN PRINCE WILLIAM SOUND, ALASKA

JOHN I. GARVER, Union College
CAMERON DAVIDSON, Carleton College

INTRODUCTION

This six-student project focused on the geology of the Chugach and Prince William terranes in northern Prince William Sound, Alaska. The Chugach-Prince William (CPW) composite terrane is a Mesozoic-Tertiary accretionary complex that is well exposed for ~2200 km in southern Alaska and is inferred to be one of the thickest accretionary complexes in the world (Plafker et al., 1994; Cowan, 2003). The CPW terrane is bounded to the north by the Border Ranges fault, which shows abundant evidence of Tertiary dextral strike slip faulting, and inboard terranes of the Wrangellia composite terrane (Peninsular, Wrangellia, Alexander) (Pavlis, 1982; Cowan, 2003; Roeske et al., 2003). Throughout much of the 2200 km long belt of the CPW terrane it is bounded by the offshore modern accretionary complex of the Alaskan margin, but east of Prince William Sound the Yakutat block is colliding into the CPW and this young collision has significantly affected uplift and exhumation of inboard rocks.

Most of the Chugach and Prince William terranes are comprised of imbricated trench-fill turbidites deposited over a relatively short interval of time (Campanian to Paleocene – c. 75-52 Ma; Garver and Davidson, 2015; Davidson and Garver, 2017) and by some estimates the volume of sediment is between 1-2 million km³ (i.e. Decker, 1980; Sample and Reid, 2003). In Prince William Sound, the turbidites of the Chugach and Prince William terranes are known as the Valdez and Orca groups, respectively, and are separated by the Contact fault (Fig. 1). In northern Prince William Sound the Contact fault (aka Jack Bay fault) is dominated by strike-slip motion (Bol and

Roeske, 1993; Haeussler and Nelson, 1993), and in the west, it is less well defined, but shows evidence for dip-slip motion (Bol and Gibbons, 1992). The turbidites are interbedded with mafic igneous rocks (pillow basalts and locally full ophiolitic suites of Resurrection Bay, Knight Island, and Glacier Island). In sharp contrast to the published literature, we suggested that the ophiolites were actually formed in a supra-subduction zone setting that coincided with oblique rifting of the Orca basin (Davidson and Garver, 2017). A critical part of our argument is that the “ophiolite” rocks are interbedded with the Orca turbidites, and their geochemistry suggests that depleted mantle melts are modified by assimilation of the sediments (Noseworthy, this volume).

Very soon after imbrication and accretion to the continental margin, rocks of the CPW were intruded by near-trench plutons of the Sanak-Baranof belt that has a distinct age progression starting in the west (63 Ma in the Sanak-Shumagin areas far to the west) and getting progressively younger to the east (53-47 Ma on Baranof Island; Bradley et al., 2000; Haeussler et al., 2003; Kusky et al., 2003; Farris et al., 2006; Wackett et al., in revision). In western Prince William Sound, these rocks were also intruded by the 37-41 Ma Eshamy Suite of plutons (Johnson, 2012; Garcia, this volume).

Paleomagnetic and geologic data indicate that the CPW has experienced significant coast-parallel transport in the Tertiary (see Garver and Davidson, 2015). The CPW has apparent equivalents to the south, and this geologic match suggests that in the Eocene, the southern part of the Chugach-Prince William terrane was contiguous with the nearly

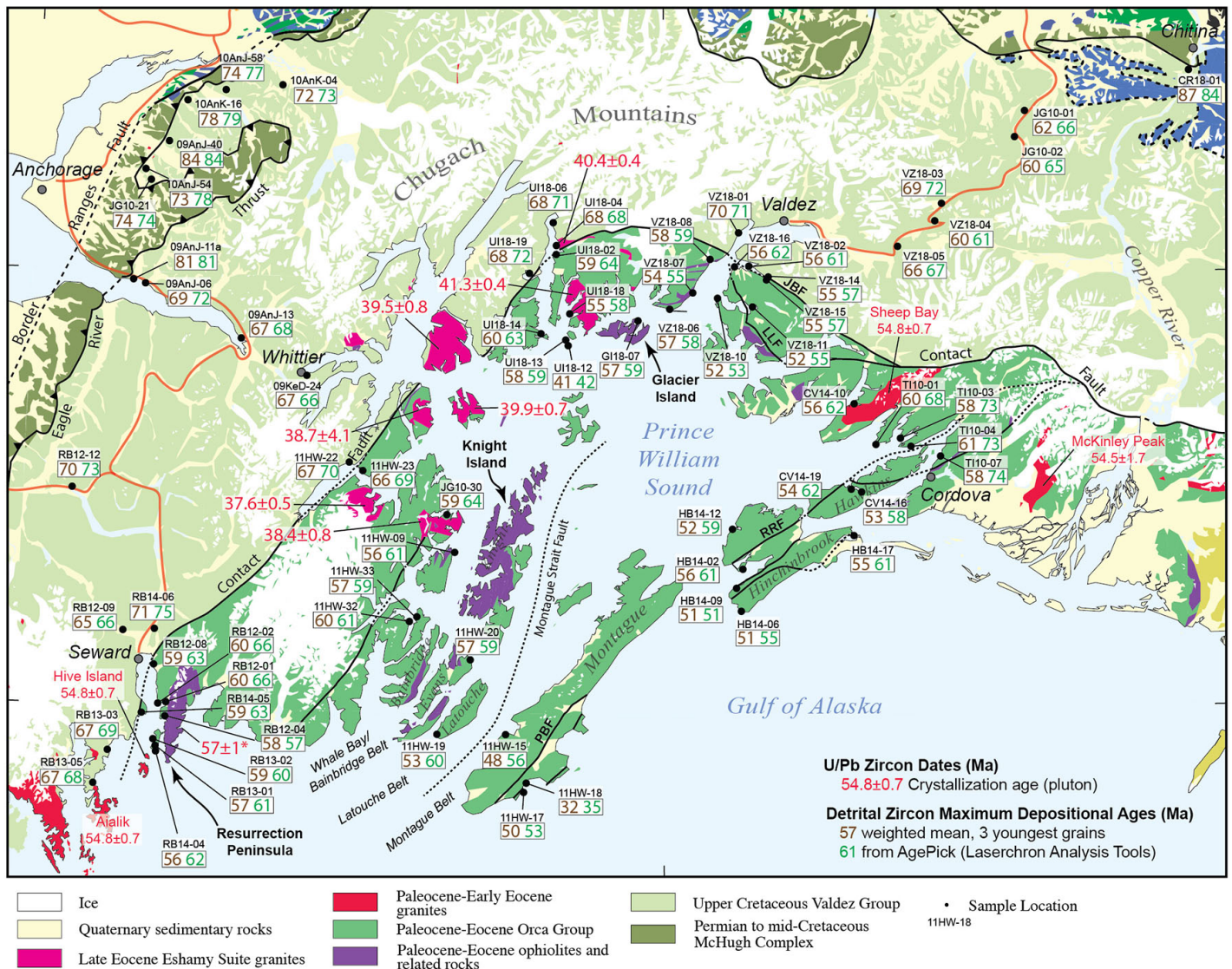


Figure 1. Geologic map of southern Alaska (modified from Bradley et al., 2003). Sample locations with maximum depositional ages (Ma) and pluton ages (Ma) are shown. The focus for the 2018 field season was northern Prince William sound near Valdez and along the Richardson highway.

identical Leech River Schist exposed on the southern part of Vancouver Island (Cowan, 1982; 2003). The geological implication of this hypothesis is profound yet elegant in the context of the Cordilleran tectonic puzzle: the CPW is the Late Cretaceous to Early Tertiary accretionary complex to the Coast Mountains Batholith Complex that intrudes the Wrangellia composite terrane and North America. Thus, the CPW is inferred to have accumulated in a flanking trench to the west and then soon thereafter these rocks were accreted to the margin. This geologic match is elegant because it suggests that the CPW accumulated outboard the Coast Mountains Batholith Complex (Gehrels et al., 2009) and that the CPW essentially is the erosional remnants of that orogenic belt.

RESEARCH

We had a terrific group of six students from four different colleges and universities (Fig. 2). Below we describe the four main research questions we studied and where the students made their contributions.

1) Provenance and maximum depositional ages of sandstones and conglomerates of the Valdez and Orca Groups in Northern Prince William Sound.

One of the primary goals of this research was to work out the relationship between the turbidites of the Valdez and Orca Groups in Prince William sound. Previous preliminary work along the Richardson highway (Fig. 1) suggests that the Valdez Group might



Figure 2. The 2018 Keck Alaska team collecting a detrital zircon sample in Unakwik Inlet.

be as young as 60 Ma, and the age and provenance of the Orca and Valdez group using detrital zircons in this area had not been studied until now.

Will Fisher (Union College) focused on the age of detrital zircon from the Orca Group and was able to show that there are four distinct zircon facies defined by maximum deposition age and grain-age distributions. He also used shale geochemistry collected from the Orca and Valdez Groups to show that there is very little difference in the trace element composition suggesting that the source area for shales in these rocks is indistinguishable. An important implication of Will's work is that the differences in provenance implied by the different zircon facies is not reflected in shale geochemistry suggesting that at least for this area and time period, shale geochemistry is too coarse a tool to help work out the provenance of these rocks.

Nick Gross-Almonte (Carleton College) studied the age of detrital zircon from the Valdez Group and was able to confirm the existence of young packages of turbidites (60-62 Ma) within the older (>66Ma) Valdez Group rocks along the Richardson highway. Based on maximum deposition age and grain-age distributions, he defines four different zircon facies including a Paleocene facies, and three distinct Cretaceous facies. This work is important because it shows that the Valdez Group is younger than previously described and that these younger rocks were either folded into the older Valdez Group turbidites, or were emplaced as structural slices during accretion.

Mollie Pope (Union College) focused on the origin and age of pebble and 6/10/19 boulder conglomerates found in the Orca Group. She shows that in more than one location, the age of well-rounded sandstone clasts are the same age as the matrix (within error). Furthermore, some of these clasts have hydrothermal veins with greenschist facies minerals including epidote suggesting that these rocks were deposited, buried, and exhumed in a short period of time.

2) Significance of the Contact Fault in Prince William Sound. The contact between the Valdez and Orca Groups in Prince William Sound has traditionally been mapped as the Contact fault and is the proposed terrane boundary between the Chugach and Prince William terranes (e.g. Plafker et al., 1994). A number of workers have questioned the importance of this structure (Bol and Gibbons, 1992; Bol and Roeske, 1993), or whether a fault even exists (e.g. Dumoulin, 1988).

Alysala Malik (Carleton College) studied detrital zircon ages from either side of the Contact fault system across Prince William Sound to look for discontinuities in depositional age and grain age distributions in the Orca and Valdez groups as would be predicted if the fault is a terrane bounding structure. She was able to show that the Jack Bay fault in Valdez Arm does not separate rocks of different age or significantly different zircon populations; but the Eaglik fault in Unakwik Inlet does. She also shows that there is a panel of turbidites that are significantly younger (~52 Ma) than rocks immediately north or south, and appear to correlate with rocks of similar age and stratigraphic character farther south on Hinchinbrook island.

3) Petrology and age of the Cedar Bay and Miners Bay plutons. Previous work on the Cedar Bay and Miners Bay plutons suggest that these plutons belong to the 37-40 Ma Eshamy Suite which intrude the Valdez and Orca Groups in western Prince William Sound (Johnson, 2012). However, the geochronology from these rocks was ambiguous (Nelson et al., 1999).

Victor Garcia (University of Texas, Austin) collected and analyzed 14 samples from the Miners Bay and Cedar Bay plutons for whole rock geochemistry and five samples for U-Pb zircon dating

and Hf isotope geochemistry. He shows that these plutons yield ages between 40.4 - 41.5 Ma, and do indeed correlate in age with the Eshamy suite. The Hf isotope ratios are similar as well and suggest these rocks were derived from a rather primitive source region ($\epsilon\text{Hf} = +4$ to $+10$).

4) Petrology of the Glacier Island ophiolite complex. Mafic volcanic rocks, mostly pillow basalt, are an important part of the Orca Group and are found interbedded with turbidites throughout Prince William Sound. Locally, these rocks dominate and in places appear to form what have been described as ophiolites complete with sheeted dike complexes and in some cases ultramafic rocks (Nelson and Nelson, 1992).

Caitlin Noseworthy (St Norbert College) collected 14 samples from the Glacier Island ophiolite complex and three samples from mafic volcanic rocks interbedded with turbidites for whole rock geochemistry. She also determined the maximum depositional age of a sandstone bed cut by a dike on Glacier Island. She shows that the Glacier Island ophiolite came from a depleted mantle (NMORB) source and is similar in age and geochemistry to the Resurrection and Knight Island ophiolites in western Prince William Sound.

ACKNOWLEDGEMENTS

This research was funded by a collaborative grant NSF EAR 1728013 (to J. Garver, Union College) and EAR 1727991 (to C. Davidson, Carleton College) and by the NSF Grant 1659322 to the Keck Geology Consortium (Macalester College). We are indebted to the extraordinary efforts by D. Giesler, M. Pecha and G. Gehrels at the Arizona LaserChron Center, which is an NSF multi-user facility at the University of Arizona. Hamilton Analytical Laboratory provided XRF and ICP-MS analyses for major and trace element data. We appreciate the visit, help in the field, and mentoring efforts of Prof. Tim Flood (St. Norbert College) and the mentoring efforts of Prof. Daniel Stockli (UT-Austin).

REFERENCES

- Bol, A.J. and Gibbons, H., 1992, Tectonic implications of out-of-sequence faults in an accretionary prism, Prince William Sound, Alaska: *Tectonics*, v.1, p. 1288-1300.
- Bol, A.J., and Roeske, S.M., 1993, Strike-slip faulting and block rotation along the contact fault system, eastern Prince William Sound, Alaska. *Tectonics* 12, 49–62.
- Bradley, D. C.; Parrish, R.; Clendenen, W.; Lux, D.; Layer, P.; Heizler, M.; and Donley, D. T., 2000, New geochronological evidence for the timing of early Tertiary ridge subduction in southern Alaska: US Geological Survey Professional Paper, 1615:5-21.
- Bradley, D.C., Kusly, T.M., Haeussler, P.J., Goldfarb, R.J., Miller, M.L., Dumoulinf, J.A., Nelson, S.W. & Karl, S. M., 2003, Geologic signature of early Tertiary ridge subduction in Alaska: Geology of transpressional orogen developed during ridge-trench interaction along the North Pacific margin: Geological Society of America Special Paper, v. 371, p. 19-49.
- Cowan, D.S., 1982, Geological evidence for post-40 m.y. B.P. large-scale northwestward displacement of part of southeastern Alaska, *Geology*, v. 10 p. 309-313.
- Cowan, D.S., 2003, Revisiting the Baranof-Leech River hypothesis for early Tertiary coastwise transport of the Chugach-Prince William terrane. *Earth and Planetary Science Letters*, v. 213, 463-475.
- Decker, J.E., Jr., 1980. Geology of a Cretaceous subduction complex, western Chichagof Island, Southeastern Alaska. PhD. Thesis, Stanford University, 135 p.
- Davidson, C. and Garver, J.I., 2017, Age and origin of the Resurrection Ophiolite and associated turbidites of the Chugach-Prince William terrane, Kenai Peninsula, Alaska. *Journal of Geology*, v. 125, p. 681–700. doi:10.1086/693926.

- Farris, D.W., Haeussler, P., Friedman, R., Paterson, S.R., Saltus, R.W. & Ayuso, R. 2006, Emplacement of the Kodiak Batholith and slab-window migration, *Geological Society of America Bulletin*, vol. 118, no. 11-12, pp. 1360-1376.
- Garver, J. I., and Davidson, C., 2015, Southwestern Laurentian zircons in Upper Cretaceous flysch of the Chugach-Prince William terrane in Alaska: *American Journal of Science*, 315:537-556.
- Gehrels, G.E., Rusmore, M., Woodsworth, G., Crawford, M., Andronicos, C., Hollister, L., Patchett, J., Ducea, M., Butler, R., Klepeis, K., Davidson, C., Mahoney, B., Friedman, R., Haggard, J., Crawford, W., Pearson, D., Girardi, J., 2009, U-Th-Pb geochronology of the Coast Mountains Batholith in north-coastal British Columbia: constraints on age, petrogenesis, and tectonic evolution. *Bulletin of the Geological Society of America*, v. 121, p. 1341-1361.
- Haeussler, P.J., and Nelson, S.W., 1993, Structural evolution of the Chugach-Prince William terrane at the hinge of the orocline in Prince William Sound and implications for ore deposits, in Dusel-Bacon, Cynthia, and Till, A.B., eds., *Geologic Studies in Alaska by the U.S. Geological Survey, 1992: U.S. Geological Survey Bulletin 2068*, p. 130-142.
- Haeussler, P.J., Bradley, D.C., Wells, R.E. & Miller, M.L. 2003, Life and death of the Resurrection Plate; evidence for its existence and subduction in the northeastern Pacific in Paleocene-Eocene time, *Geological Society of America Bulletin*, vol. 115, no. 7, pp. 867-880.
- Johnson, E., 2012, Origin of Late Eocene granitoids in western Prince William Sound, Alaska; *Proceedings from the 25th Keck Geology Consortium Undergraduate Research Symposium*, Amherst MA, p. 33-39.
- Kusky, T.M., Bradley, D.C., Donely, D.T., Rowley, D. & Haeussler, P.J. 2003, Controls on intrusion of near-trench magmas of the Sanak-Baranof Belt, Alaska, during Paleogene ridge subduction, and consequences for forearc evolution; *Geology of a transpressional orogen developed during ridge-trench interaction along the North Pacific margin*, Special Paper - Geological Society of America, vol. 371, pp. 269-292.
- Nelson, S. W.; and Nelson, M. S., 1993. *Geochemistry of ophiolitic rocks from Knight Island, Prince William Sound, Alaska: U. S. Geological Survey Bulletin*, p. 130-142.
- Nelson, S. W., Miller, M.L., Haeussler, P.J., Snee, L. W., Phillips, P.J., and Huber, C., 1999, Preliminary geologic map of the Chugach National Forest Special Study Area, Alaska: U.S. Geological Survey Open-File Report 99-362, scale 1:63,000.
- Pavlis, T.L., 1982, Origin and age of the Border Ranges Fault of southern Alaska and its bearing on the late Mesozoic Tectonic Evolution of Alaska: *Tectonics*, v. 1, n. 4, p. 343-368.
- Plafker, G., Moore, J.C. & Winkler, G.R. 1994, *Geology of the Southern Alaska margin in The geology of Alaska*, eds. G. Plafker & H.C. Berg, Geological Society of America, Boulder, CO, United States (USA), United States (USA).
- Roeske, S.M., Snee, L.W. & Pavlis, T.L. 2003, Dextral-slip reactivation of an arc-forearc boundary during Late Cretaceous-early Eocene oblique convergence in the northern Cordillera; *Geology of a transpressional orogen developed during ridge-trench interaction along the North Pacific margin*, Special Paper - Geological Society of America, vol. 371, pp. 141-169.
- Sample, J.C. & Reid, M.R. 2003, Large-scale, latest Cretaceous uplift along the Northeast Pacific Rim; evidence from sediment volume, sandstone petrography, and Nd isotope signatures of the Kodiak Formation, Kodiak Islands, Alaska; *Geology of a transpressional orogen developed during ridge-trench interaction along the North Pacific margin*, Special Paper - Geological Society of America, vol. 371, pp. 51-70.

ZIRCON FACIES IN THE PALEOCENE-EOCENE ORCA GROUP INDICATE A PROVENANCE LINK TO THE CHUGACH TERRANCE, PRINCE WILLIAM SOUND, ALASKA

WILL SPARKHAWK FISHER, Union College
Research Advisor: John Garver

INTRODUCTION

Much of the southern Alaska continental margin is made up of marine sedimentary rocks and distinct terranes that have been deposited and accreted from the Cretaceous to the present (Plafker et al., 1994). The Upper Cretaceous to Eocene Chugach-Prince William (CPW) terrane is interpreted to be one of the thickest accretionary complexes in the world, and it is bounded to the north by the Border Ranges fault and Wrangellia composite terrane (Garver and Davidson, 2015). The CPW terrane is inferred to be the Mesozoic accretionary complex of southern Alaska (Amato et al., 2013), but alternate hypotheses suggest it originally formed far to the south (Cowan, 2003). The CPW consists of inboard mesomélange (the McHugh Complex & Potter Creek Assemblage) and stratigraphically younger outboard flysch facies (the Valdez & Orca groups) and associated volcanics (Plafker et al., 1989; Garver and Davidson, 2015; Amato et al., 2013). The blueschist to greenschist Potter Creek Assemblage formed in Cretaceous-Early Jurassic subduction (Amato et al., 2013). The McHugh Complex is made up of mélangé and deformed conglomerates and sandstones and ages range from the Jurassic to mid Cretaceous (Amato et al., 2013). The majority of the CPW terrane (>90 %) is comprised of the outboard flysch facies of the Late Cretaceous to Eocene Valdez and Orca groups juxtaposed along the Contact fault system (Garver and Davidson, 2015; Dumoulin, 1987; Fig. 1). The CPW terrane was intruded by the 61-50 Ma Sanak-Baranof belt (SBB) near-trench plutons that are diachronous (Bradley et al., 2003; Cowan, 2003). There are two predominant hypotheses concerning the intrusion of these plutons

and the amalgamation and translation of the CPW terrane. The Baranof-Leech River hypothesis suggests the CPW terrane formed to the south and was then translated along the margin (Cowan, 2003). A more northern hypothesis where CPW terrane formed in situ and the Resurrection Plate subducted underneath it (Haeussler et al., 2003). These alternate hypotheses each require a different sediment provenance for the CPW terrane outboard flysch assemblages.

The goal of this study is to determine the depositional age, provenance, and original tectonic setting of the flysch facies of CPW terrane, with an emphasis on the younger Orca Group. Using maximum depositional ages (MDA) and the KS test, we delineate four distinctive zircon facies: 1) Miners Bay (~61-59 Ma, n=2244 grains); 2) Sawmill (59-55 Ma, n=1340); 3) Hawkins (55-50 Ma, n=1914); and 4) Montague (52-31 Ma, n=1144) (Fig. 2). A major stratigraphic conundrum is that the oldest Orca is age-correlative and has a similar provenance to the youngest Valdez Group at 61-60 Ma, and the location of these rocks casts doubt of models that rely on the Contact fault system as a terrane-bounding fault.

BACKGROUND & GEOLOGICAL SETTING

The Valdez Group

The Campanian-Paleocene Valdez Group consists of thick, deformed turbidites with minor tholeiitic basalts (Plafker et al., 1989; Davidson and Garver, 2017; Gross Almonte et al., 2019). The sedimentary and volcanic rocks of the Valdez Group were

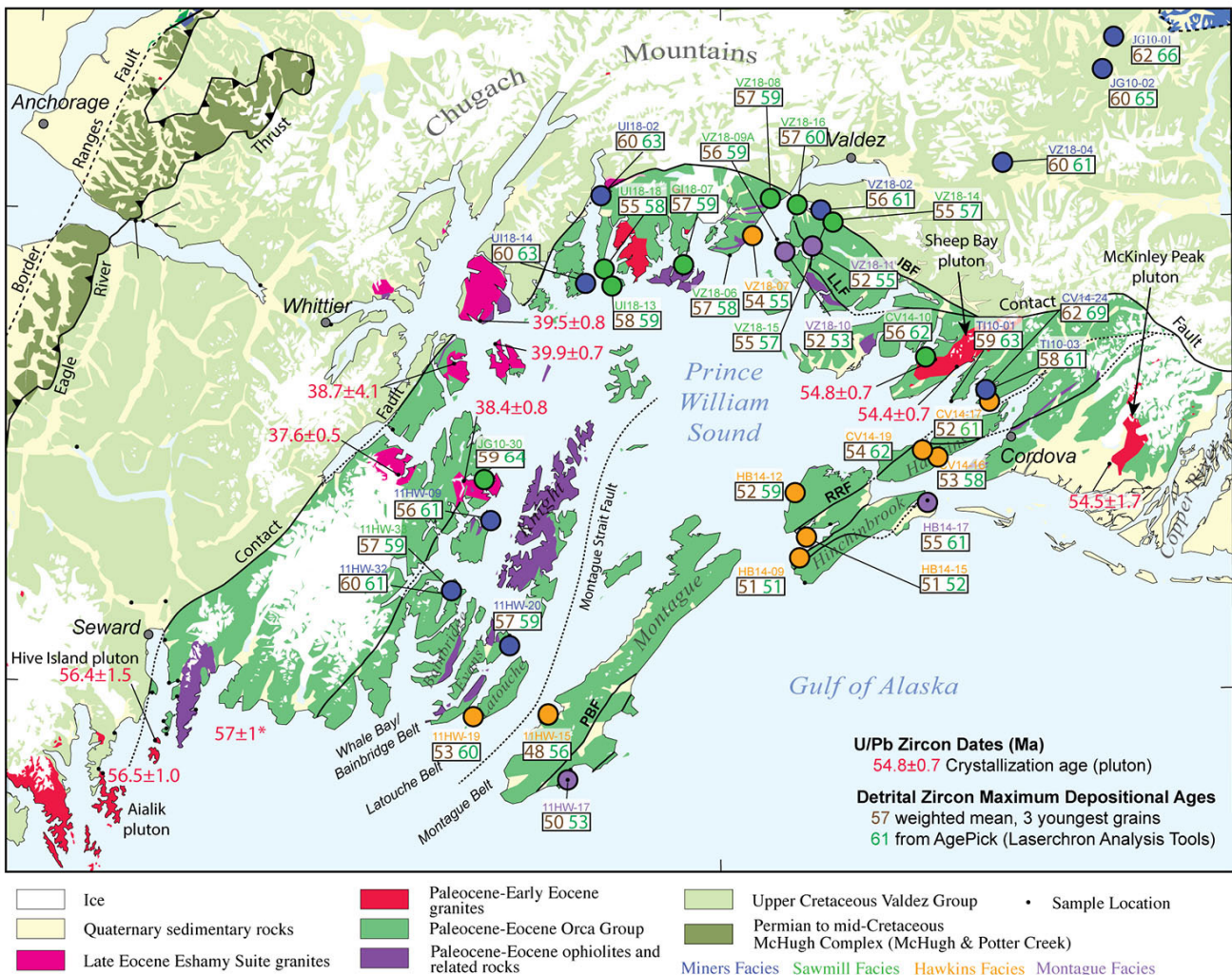


Figure 1: Geologic map of Prince William Sound showing sample locations used in this study. The inboard Valdez Group is juxtaposed against the outboard Orca Group across the Contact fault system. (Figure modified from Wilson et al., 2015).

originally defined by Schrader (1900) and Grant and Higgins (1910). Regionally the Valdez Group is metamorphosed to lower greenschist facies (Plafker et al., 1989, Dusel-Bacon, 1991). The Valdez Group is primarily comprised of medium-grained sandstones, locally with biotite, muscovite and intermittently veined shales (Grant and Higgins, 1910). Traditionally the age has been interpreted to be Campanian to Maastrichtian based on a few widely dispersed fossils (Jones and Clark, 1973).

The Orca Group

The Orca Group consists of a thick (6-10 km) sequence of marine turbidites well-exposed extending in Prince William Sound (PWS), and west to Kodiak (Fig. 2; Plafker et al., 1994). This belt makes up the Prince William terrane, and it is juxtaposed by the Contact fault system to the adjacent Valdez Group

(Chugach terrane) to the north (Tysdal and Case, 1979). The Orca Group was defined as consisting of thick-bedded, gray- to brown-weathering sandstones, with black limestones, arkoses, interbedded with typically thin layers of dark shale and slate, and minor conglomerates (Schrader, 1900; Grant and Higgins, 1910). The Orca Group is interpreted to have a lower metamorphic grade (zeolite – prehnite pumpellyite) (Schrader, 1900; Dusel-Bacon). The Orca Group is in depositional contact with ophiolitic rocks of Knight Island, Resurrection Peninsula, and Glacier Island (Tysdal and Case, 1977; Wilson and Hults, 2012; Davidson and Garver, 2017; Noseworthy et al., 2019). The occurrence of foraminifers in rocks of eastern Prince William Sound, Hinchinbrook Island, Porcupine Point, and Hawkins Island indicate a probable age range of Paleocene to early and middle Eocene (Plafker et al., 1985). U-Pb geochronology

of detrital zircon in these rocks partly reaffirms early paleontological studies (Davidson and Garver, 2017).

The Contact Fault

The Geology of PWS has a complicated history in the literature that largely revolves around the relationship between the Valdez and Orca Groups. The two dominant rock groups in PWS, the Orca and Valdez Groups, were essentially given de facto group status in 1910 (Grant and Higgins). A metamorphic break was initially described, and interpreted as an angular unconformity with the younger Orca resting unconformably on the older Valdez; however, it was also proposed that perhaps the units were in fault contact (i.e. Capps and Johnson, 1915; but see discussion in Moffit, 1954). By the 1970s, it was commonly accepted that there is a series of faults juxtaposing the inboard Valdez Group to the north against the outboard Orca Group to the south. Plafker et al. (1977) formally defined these faults as the Contact fault system. Upon further examination, it became evident that the Contact fault system is comprised of multiple fault segments, some with complex dextral strike-slip fault histories (Bol and Roeske, 1993), but its significance as a terrane boundary was less clear because the units are commonly indistinguishable in the field (Domoulin, 1987; Bol and Gibbons, 1992; Malik et al., 2019). These concerns leave two fundamental questions about the Contact fault: are the Orca and Valdez Groups a depositional continuum potentially with an unconformity or are the Orca and Valdez Groups from two distinct source terranes that have been placed next to each other along the Contact fault.

METHODS

U-Pb detrital zircon ages were obtained from samples taken along several transects across the Contact fault in northern PWS (this study; Malik et al., 2019) and along the Richardson Highway (Gross Almonte et al., 2019). In addition, Pope et al. (2019) focused on conglomerates of the Orca. Coarse-grained sandstones were sampled for detrital zircon U-Pb dating at the University of Arizona LaserChron Center. Zircons were extracted from the rock sample using standard rock pulverization techniques, followed by density

separation. In this study 100 or 300 zircons were randomly selected and individually dated using LA-ICP-MS to determine grain-age populations. Shale samples were taken from representative locations in northern PWS for major and trace element analysis at the Hamilton Analytical Laboratory at Hamilton College. The goal of sampling different blocks of Orca Group shale is to ascertain whether there are geochemically distinct tectonic blocks within the Orca Group (Fig. 3). For detrital zircon work the maximum depositional age (MDA) was calculated using the weighted mean of the three youngest grains in a sample and using AgePick (LaserChron Analysis Tools). Probability density functions (PDFs) are used to show grain-age distributions. Using maximum depositional ages (MDA), the KS test, and PDFs, I define four distinct zircon facies in the Orca Group (Fig. 2). To understand the significance of the sediment contribution from the adjacent Chugach terrane, a synthetic DZ signal was made from the Valdez Group (n = 3354), McHugh Complex (n = 916), and Potter Creek assemblage (n = 874), the three primary elements of the Chugach terrane (Fig. 4; Amato and Pelvis, 2010, Amato et al., 2013). These composites were used in a three-component model to estimate the maximum sediment contribution (MSC) of the Chugach terrane to the Orca. The MSC was modeled by taking the maximum component of Valdez at 72 Ma, the age of the primary population in the Valdez Group.

RESULTS

Combining our new U-Pb MDAs from northern PWS with previously published results (Davidson and Garver, 2017), the timing of deposition of the Orca Group is at least 61.5-31.0 Ma or younger in Prince William Sound. There are four distinctive MDA defined KS-supported facies within the Orca Group. The Miners facies (~61-59 Ma) consists of a primary 71 Ma population and secondary 108 Ma population (Fig. 2). The Sawmill (59-55 Ma) facies is characterized by a primary population at 59 Ma and secondary 108 Ma population and a significant decrease in Precambrian grains (Fig. 2). The Hawkins facies has three primary populations at 62, 71, and 88 Ma with a minor secondary grain-age population at 121 Ma (Fig. 2). The Hawkins facies is the only facies

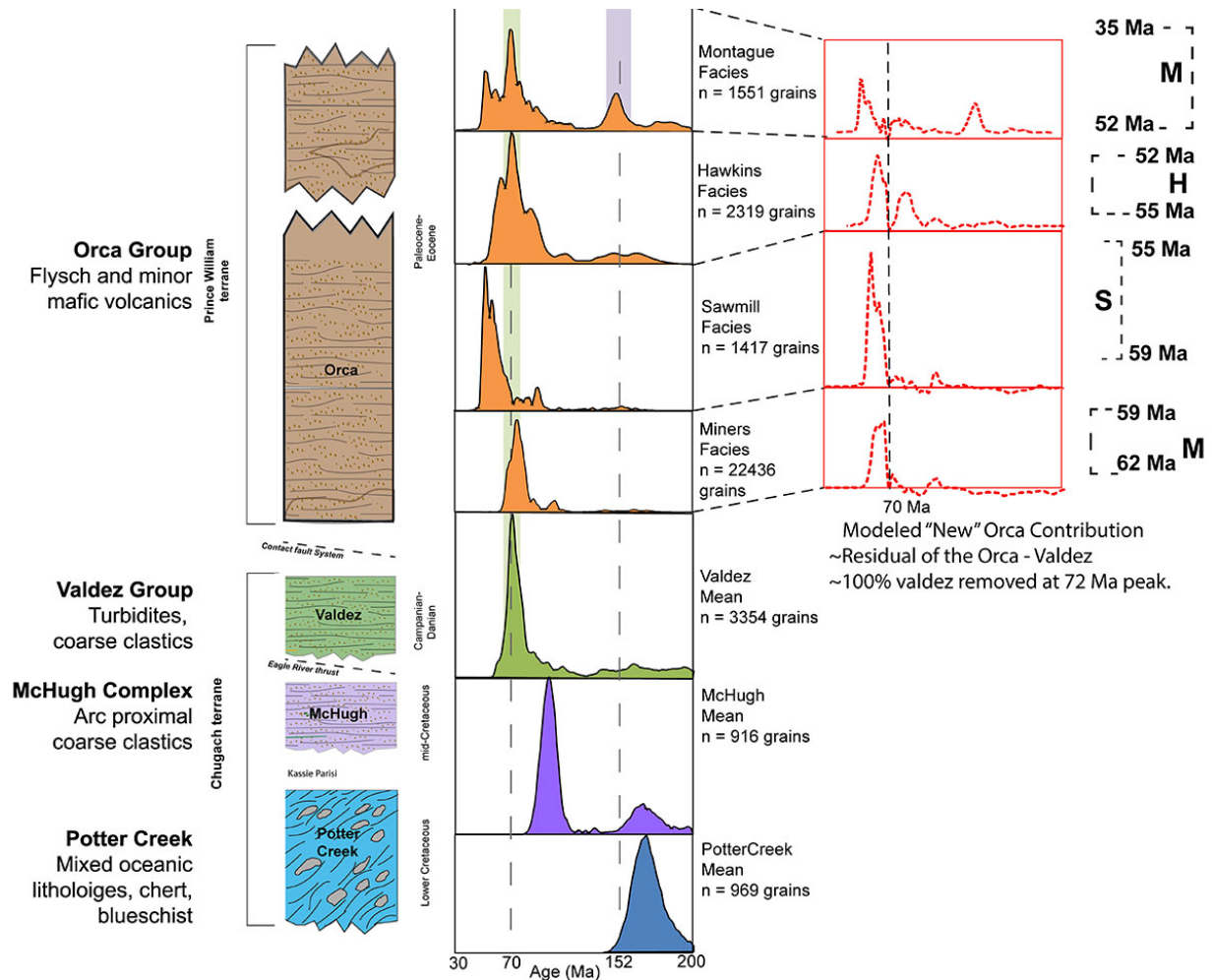


Figure 2: Stratigraphic column for the Chugach-Prince William terrane and correlative composite probability density functions ($n = \#$ of zircon grains). Black dashed time bins (Upper right) represent MDA time bins for the Orca Group facies. Pottercreek and McHugh zircon data from Amato and Pavlis, 2010 and Amato et al., 2013. Red dashed line graphs are the residual PDF with the Chugach MSC removed in each Orca Group zircon facies (see text).

recording a primary 88 Ma grain-age population. The young Montague facies (58-50 Ma) has a primary grain-age population at notably 53 and 73 Ma with a secondary grain age population at 152 Ma (Fig. 2). The source of the Orca Group was probably a Paleocene arc (~61-50 Ma) built on a Cretaceous and Jurassic metaplutonic basement along with significant sediment contribution from the Valdez Group (84-61 Ma). This relationship is substantiated by near identical shale geochemistry across the Orca and Valdez groups (Fig. 3).

The maximum sediment contribution (MSC) into the Orca basin from the adjacent Chugach terrane may be represented by three possible units: 1) Potter Creek Assemblage; 2) McHugh Complex; and 3) Valdez Group. If any unit contributed significant zircon to the Orca basin, it would be the Valdez Group

because it is regionally extensive and it dominates in volume. Modeling the MSC of the Valdez Group into the Orca Group shows that the Miners facies could have received as much as ~88% of its zircon from the Valdez Group. The Sawmill facies received the smallest MSC of the Valdez Group accounting for only up to ~35% of its sediment. The Hawkins facies MSC of the Valdez Group could have been up to ~55% derived from the Valdez Group. Similarly, the Montague facies, the most outboard facies, the MSC was as much as ~55%. The Potter Creek, and McHugh, with distinctive JK populations, cannot have been a significant sediment source in the Orca Group. They were found to be <1% in the modeled Orca Group zircon facies, and this result may suggest the Eagle River thrust is a significant terrane bounding structure and that these units were not present in the source region.

DISCUSSION

The zircon facies of the Orca Group show a changing provenance over time and the maximum sediment contribution model suggests a depositional setting in close proximity to the Valdez Group. The Valdez Group and the Orca Group have similar zircon facies and sedimentary provenance. The Orca Group can be modeled as containing a maximum of ~35-85% zircon recycled from the Valdez—or identical source. The Orca Group has clasts of the Valdez Group (Pope et al., 2019), which means there must have been some erosion of the Valdez Group.

How can depositional models incorporate rocks of practically the same age (60-61 Ma) with differing degrees of metamorphism, but similar provenances? A possible model for the deposition of the Orca Group and similarly aged, but metamorphosed Valdez Group is to underplate and quickly exhume Valdez Group rocks in an accretionary wedge complex with the exhumed Valdez Group rocks supplying the majority of the sediment for the Orca Group. This exhumation may have dominated the sediment supply (>50%) of the Orca Group with the exception of the Sawmill facies. Note that deposition of the Sawmill facies was synchronous with ophiolite emplacement and intrusion of the SBB plutons in PWS (Davidson and Garver, 2017); perhaps this magmatism temporarily rearranged drainage systems and diluted the Valdez Group signal.

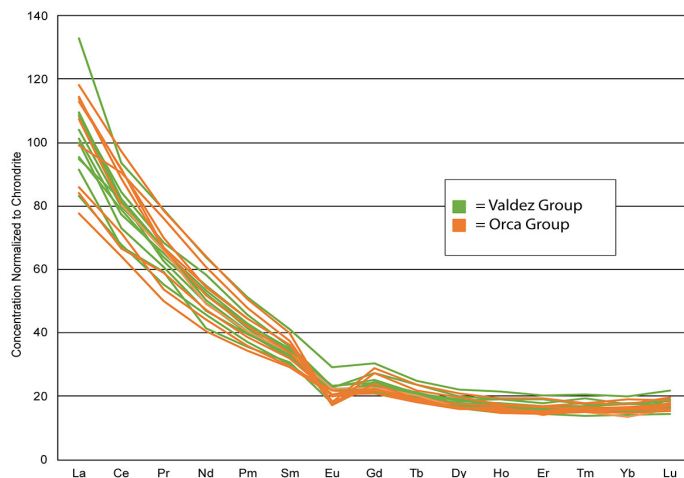


Figure 3: Rare Earth Element concentrations of shale samples from the Orca (orange, $n=9$) and Valdez (green, $n=11$) Groups. Normalized to chondrite compositions of McDonough and Sun (1995).

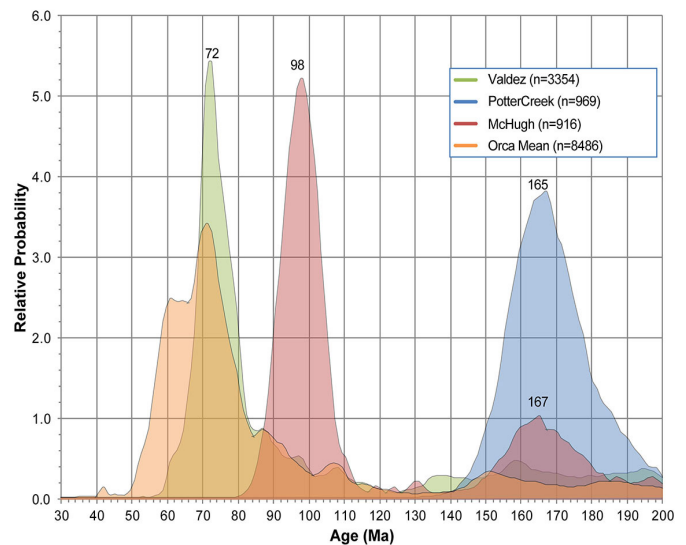


Figure 4: Probability density functions of the three main sandstone-bearing protectonic assemblages of the Chugach terrane: Valdez Group ($n = 3354$), McHugh Complex ($n = 916$), and the Pottercreek Assemblage ($n = 874$). McHugh and Potter Creek data from Amato and Pavlis (2010) and Amato et al. (2013).

The Hawkins and Montague facies have similar components, but reflect more complicated mixing. The Hawkins facies in particular records a “new” 88 Ma sediment flux only seen from 55-52 Ma, and the Montague facies records a 53 Ma grain-age population perhaps indicating a short-lived arc rejuvenation.

Because volcanic clasts dominate the lithic types in the Valdez and Orca Groups, the source terrane was likely an arc environment (Dumoulin, 1987). The similarities in sediment composition between the Valdez and the Orca Groups would suggest a single source terrane that evolved over time (Dumoulin, 1987). Likewise, the shale geochemistry of rocks across the Contact fault system in northern PWS have almost identical rare earth element abundances in the Valdez and Orca Groups.

One proposed source region for the Orca and Valdez Group is the Coast Mountains Plutonic Complex (CMPC) (Hollister, 1982, Farmer, et al., 1993). The CMPC is a 1700 km long belt of Jurassic to Paleogene plutonic rocks located to the south of the current location of the Orca and Valdez Groups (Farmer, et al., 1993; Cecil et al., 2011). Metamorphism and subsequent exhumation suggests rapid uplift of the CMPC (up to 30 km) occurred between 62-48 Ma producing up to 3×10^5 km³ clastic during the Paleocene and Eocene, when the Orca Group

was being deposited (Hollister, 1982). The CMPC also experienced crustal thickening from 85-58 Ma followed by a period of transtension from 58-50 Ma resulting in decompression and crustal thinning (Hollister and Andronicos, 2006).

Zircon facies within the Orca Group may allow for the depocenter to be determined. There are two possible situations in which the Valdez and Orca became juxtaposed. The Valdez Group could have been stitched to the Orca Group and traveled along the margin eroding into the Orca group. Alternatively, the Valdez Group could have been in its modern position by ~61 Ma and each Orca Group zircon facies represents slivers tapping into different source terranes. The Miners and Sawmill facies could be dominated by detritus from erosion of the Valdez Group or material from the original source. The MSC residuals show that the Montague and Hawkins facies are unique and distinct from one another and show a new source rock entered the basin (Fig. 2). The Montague facies may represent the position of the Orca Group depocenter farthest away from the south.

CONCLUSIONS

The provenance of the Orca and Valdez Groups is a fundamental element for understanding the geologic framework in southern Alaska. Previous petrographic studies (Dumoulin, 1987), structural analyses (Bol and Gibbons, 1992), and this study of detrital zircon grain-age populations and shale geochemistry suggest that the Contact fault system is not a terrane bounding fault. Our modeling suggests that Chugach-supplied sediment in the Orca Group may be as high as 75-88%, and this result implies that significant recycling of the Valdez Group into the Orca Group occurred from 62-52 Ma. If the Orca and Valdez Groups originated in the south, thickening of the CMPC could have supplied the Valdez Group and rapid exhumation could have continued to supply sediments to the Orca Group. The difference in metamorphic grade between the Valdez and Orca Groups could be explained by rapid underplating, exhumation and erosion of greenschist facies rocks of the Valdez Group. Thus, the similarities between the units suggest the Valdez and Orca groups are not separate terranes rather the depositional continuum of each other from a common

source terrane. The relationship of the PotterCreek and McHugh to Valdez is unclear, but these facies do not appear in the Orca Group (if recycled), indicating the Eagle River thrust could be a major terrane bounding fault. The Chugach terrane in this model is a composite terrane and may best be viewed as Potter Creek + McHugh as separate from the Valdez and Orca Groups which are similar, but with differing degrees of metamorphism.

ACKNOWLEDGEMENTS

I would like to thank Dr. John Garver for all of his support, thoughtful advice, and always trying to look at the problem a new way. I would also like to thank Dr. Cameron Davidson for all of his patience, handwork, and support. I would like to acknowledge our field team: Mollie Pope, Nicholas Gross-Almonte, Victor Garcia, Caitlin Noseworthy, and Alysala Malik. I would like to recognize Alysala Malik and Nicholas Gross-Almonte for their mineral separation work and the Carleton College Geology Department for SEM work. This material is based upon work supported by the Keck Geology Consortium and the National Science Foundation under Grant No. 1659322. The field work was made possible by: NSF EAR 1728013 (Garver); NSF EAR 1727991 (Davidson). U-Pb geochronology work was supported by the Arizona LaserChron Center, run by George Gehrels and Mark Pecha.

REFERENCES

- Amato, J.M. and Pavlis, T.L., 2010. Detrital zircon ages from the Chugach terrane, southern Alaska, reveal multiple episodes of accretion and erosion in a subduction complex. *Geology*, 38(5), pp.459-462.
- Amato, J.M., Pavlis, T.L., Clift, P.D., Kochelek, E.J., Hecker, J.P., Worthman, C.M. and Day, E.M., 2013. Architecture of the Chugach accretionary complex as revealed by detrital zircon ages and lithologic variations: Evidence for Mesozoic subduction erosion in south-central Alaska. *Bulletin*, 125(11-12), pp.1891-1911.
- Bol, A.J., Coe, R.S., Grommé, C.S. and Hillhouse,

- J.W., 1992. Paleomagnetism of the Resurrection Peninsula, Alaska: Implications for the tectonics of southern Alaska and the Kula-Farallon ridge. *Journal of Geophysical Research: Solid Earth*, 97(B12), pp.17213-17232.
- Bol, A.J. and Gibbons, H., 1992. Tectonic implications of out-of-sequence faults in an accretionary prism, Prince William Sound, Alaska. *Tectonics*, 11(6), pp.1288-1300.
- Bol, A.J. and Roeske, S.M., 1993. Strike-slip faulting and block rotation along the Contact fault system, eastern Prince William Sound, Alaska. *Tectonics*, 12(1), pp.49-62.
- Bradley, D.C., Kusly, T.M., Haeussler, P.J., Goldfarb, R.J., Miller, M.L., Dumoulin, J.A., Nelson, S.W. & Karl, S. M., 2003, Geologic signature of early Tertiary ridge subduction in Alaska: Geology of transpressional orogen developed during ridge-trench interaction along the North Pacific margin: Geological Society of America Special Paper, v. 371, p. 19-49.
- Cecil, M.R., Gehrels, G., Ducea, M.N. and Patchett, P.J., 2011. U-Pb-Hf characterization of the central Coast Mountains batholith: Implications for petrogenesis and crustal architecture. *Lithosphere*, 3(4), pp.247-260.
- Cowan, D.S., 2003. Revisiting the Baranof–Leech River hypothesis for early Tertiary coastwise transport of the Chugach–Prince William terrane. *Earth and Planetary Science Letters*, 213(3-4), pp.463-475.
- Davidson, C. and Garver, J.I., 2017. Age and origin of the resurrection ophiolite and associated Turbidites of the Chugach–Prince William terrane, Kenai peninsula, Alaska. *The Journal of Geology*, 125(6), pp.681-700.
- Dumoulin, J.A., 1987. Sandstone composition of the Valdez and Orca Groups, Prince William Sound, Alaska (No. 1774). US Government Printing Office. P. 1-34.
- Dusel-Bacon, C. E., *Metamorphic history of Alaska*, in *The Geology of North America*, vol. G-1, *The Geology of Alaska*, edited by G. Plafker and H. C. Berg, pp. 495-533, Geol. Soc. Am., Boulder, Colo., 1994.
- Farmer, G.L., Ayuso, R. and Plafker, G., 1993. A Coast Mountains provenance for the Valdez and Orca groups, southern Alaska, based on Nd, Sr, and Pb isotopic evidence. *Earth and Planetary Science Letters*, 116(1-4), pp.9-21.
- Grant, U.S. and Higgins, D.F., 1910. Reconnaissance of the geology and mineral resources of Prince William Sound Alaska. Washington: Government Printing Office. P. 22-32.
- Garver, J.I., Davidson, C. and Northfield, M.N., 2012. Tectonic evolution of the Chugach-Prince William terrane in Prince William Sound and Kodiak Island, Alaska. In *Proceedings from the 25th Keck Geology Consortium Undergraduate Research Symposium*, Amherst (pp. 1-7).
- Garver, J.I. and Davidson, C.M., 2015. Southwestern Laurentian zircons in upper Cretaceous flysch of the Chugach-Prince William terrane in Alaska. *American Journal of Science*, 315(6), pp.537-556.
- Gross Alamonte, N., Fisher, W.S., Malik, A.M., Garver, J.I., and Davidson, C.M. 2019. Age and provenance of the Upper Cretaceous to Paleocene Valdez Group of the Chugach terrane from the Richardson Highway and northern Prince William Sound, Alaska. *Geological Society of America Abstracts with Program, Cordilleran Section - 115th Annual Meeting, Portland Oregon*. v. 51, n. 4. doi: 10.1130/abs/2019CD-329673.
- Haeussler, P.J., Bradley, D.C., Wells, R.E. and Miller, M.L., 2003. Life and death of the Resurrection plate: Evidence for its existence and subduction in the northeastern Pacific in Paleocene–Eocene time. *Geological Society of America Bulletin*, 115(7), pp.867-880.
- Hollister, L.S., 1982. *Metamorphic Evidence For Rapid (2 mm/yr) Uplift of A Portion*

- of the Central Gneiss Complex, COAST MOUNTAINS, BC. *Canadian Mineralogist*, 20, pp.319-332.
- Hollister, L.S. and Andronicos, C.L., 2006. Formation of new continental crust in Western British Columbia during transpression and transtension. *Earth and Planetary Science Letters*, 249(1-2), pp.29-38.
- McDonough, W.F. and Sun, S.S., 1995, *The Composition of the Earth; Chemical Geology*, v. 120, p. 223-253.
- Malik, A.M., Fisher, W.S., Gross Alamonte, N., Garver, J.I., Davidson, C.M., 2019. U-Pb dating of detrital zircon from turbidites of the Chugach and Prince William terrane in Prince William Sound, Alaska: Implications of the significance of the Contact fault system as a terrane boundary. *Geological Society of America Abstracts with Program, Cordilleran Section - 115th Annual Meeting, Portland Oregon*. v. 51, n. 4. doi: 10.1130/abs/2019CD-32939.
- Plafker, G., Jones, D.L. and Pessagno Jr, E.A., 1977. A Cretaceous accretionary flysch and melange terrane along the Gulf of Alaska margin. *The United States Geological Survey in Alaska: Accomplishments during*, pp.B41-B43.
- Plafker, G., Nokleberg, W.J. and Lull, J.S., 1989. Bedrock geology and tectonic evolution of the Wrangellia, Peninsular, and Chugach terranes along the Trans-Alaska Crustal Transect in the Chugach Mountains and southern Copper River Basin, Alaska. *Journal of Geophysical Research: Solid Earth*, 94(B4), pp.4255-4295
- Plafker, George, and Berg, H.C., 1994, Introduction, in Plafker, George, and Berg, H.C., eds., *The Geology of Alaska: Geological Society of America*, p. 1-16.
- Pope, Mollie, Fisher, Will S., Malik, Alysala M., Garver, John I. and Davidson, Cameron, 2019. Provenance of Sandstone Clasts From Conglomerate of the Paleocene-Eocene Orca Group in Prince William Sound, Alaska. *The Geological Society of America: Cordilleran Section*.
- Schrader, F.C., 1900, A reconnaissance of a part of Prince William Sound and the Copper River district, Alaska, in 1898: U.S. Geological Survey Annual Report, 20, pt. 7, p. 341-423.
- Tysdal, R.G. and Case, J.E., 1979. Geologic map of the Seward and Blyng Sound quadrangles, Alaska (No. 1150), p. 9-12
- Wilson, F.H., Hults, C.P., Mull, C.G, and Karl, S.M, comps., 2015, Geologic map of Alaska: U.S. Geological Survey Scientific Investigations Map 3340, pamphlet 196 p., 2 sheets, scale 1:1,584,000, <http://dx.doi.org/10.3133/sim3340>.

CRYSTALLIZATION AGES AND GEOCHEMISTRY OF THE MINERS BAY AND CEDAR BAY PLUTONS, PRINCE WILLIAM SOUND, ALASKA

VICTOR R. GARCIA JR., The University of Texas at Austin
Research Advisor: Daniel F. Stockli

INTRODUCTION

The Late Eocene Eshamy Suite plutons (ESP) intrude turbidites of the Chugach-Prince William (CPW) terrane in western Prince William Sound. The Prince William Sound region of South-Central Alaska consists of the Chugach-Prince William Terrance (CPW), containing the Valdez and Orca Group separated by the Contact fault. The Valdez Group is Late Cretaceous in age and is characterized by a thick sequence of interbedded siltstone, greywacke, and pebble conglomerate likely deposited as turbidites on submarine fans (Tysdal and Plafker, 1978). South of the Valdez is the Orca Group of Paleocene to Eocene age, characterized by folded and faulted rocks that have been intruded by younger plutons (Davidson and Garver, 2017). The CPW has been traditionally interpreted as a Late Cretaceous to Paleocene accretionary wedge complex that was either formed in situ or was deposited farther south and subsequently transported a significant distance along the continental margin (cf. Cowan, 2003; Haeussler et al., 2003).

The ESP is a bimodal suite of granites dominated by biotite granites and leucogranites with subordinate gabbro. Questions for the ESP include the crystallization ages for the plutons, their relationship to igneous rocks found farther inboard, and the nature of the tectonic setting. For this study, we examined a set of granites from Miners Bay and Cedar Bay to compare with the rocks from the Nellie Juan and Eshamy Bay plutons to the southwest (Fig. 1), and the Caribou Creek volcanics (CCV) that occur 200 km inland. Our results show that the Miners and Cedar Bay plutons fall within the age range of the CCV and are marginally older than the Nellie Juan (NJP)

and Eshamy Bay plutons (EBP) (Cole et al., 2006; Johnson, 2012). However, preliminary geochemical data suggest that the ESP may not be directly related to the CCV and therefore may have formed in a different tectonic setting.

FIELD AND PETROGRAPHIC DESCRIPTIONS

This study focuses on the Miners Bay diorite and leucogranite which intrude the Valdez turbidites, and the Cedar Bay pluton which intrudes the Orca Group in Prince William Sound (Fig. 1). The Miners Bay diorite is truncated along its southern margin by the Miners Bay fault and the Miners Bay leucogranite occurs as a small intrusive body along the northern margin of the diorite (Fig. 1B). The diorite is black and white, equigranular hypidiomorphic containing plagioclase, clinopyroxene, and hornblende with minor biotite and ilmenite (Fig. 2A). The Miners Bay leucogranite is white, equigranular hypidiomorphic containing plagioclase, perthitic orthoclase, and quartz with trace biotite (Fig. 2B). The Cedar Bay pluton is dominated by light grey leucogranite with rare mafic enclaves and crops out south of Miners Bay (Fig. 1B). It is primarily equigranular hypidiomorphic containing plagioclase, orthoclase and quartz with trace biotite. In most samples the feldspars are partially to completely replaced by fine grained sericite and epidote (Fig. 2C).

ANALYTICAL METHODS & RESULTS

Fourteen whole-rock samples from the Miners Bay and Cedar Bay plutons including three mafic enclaves

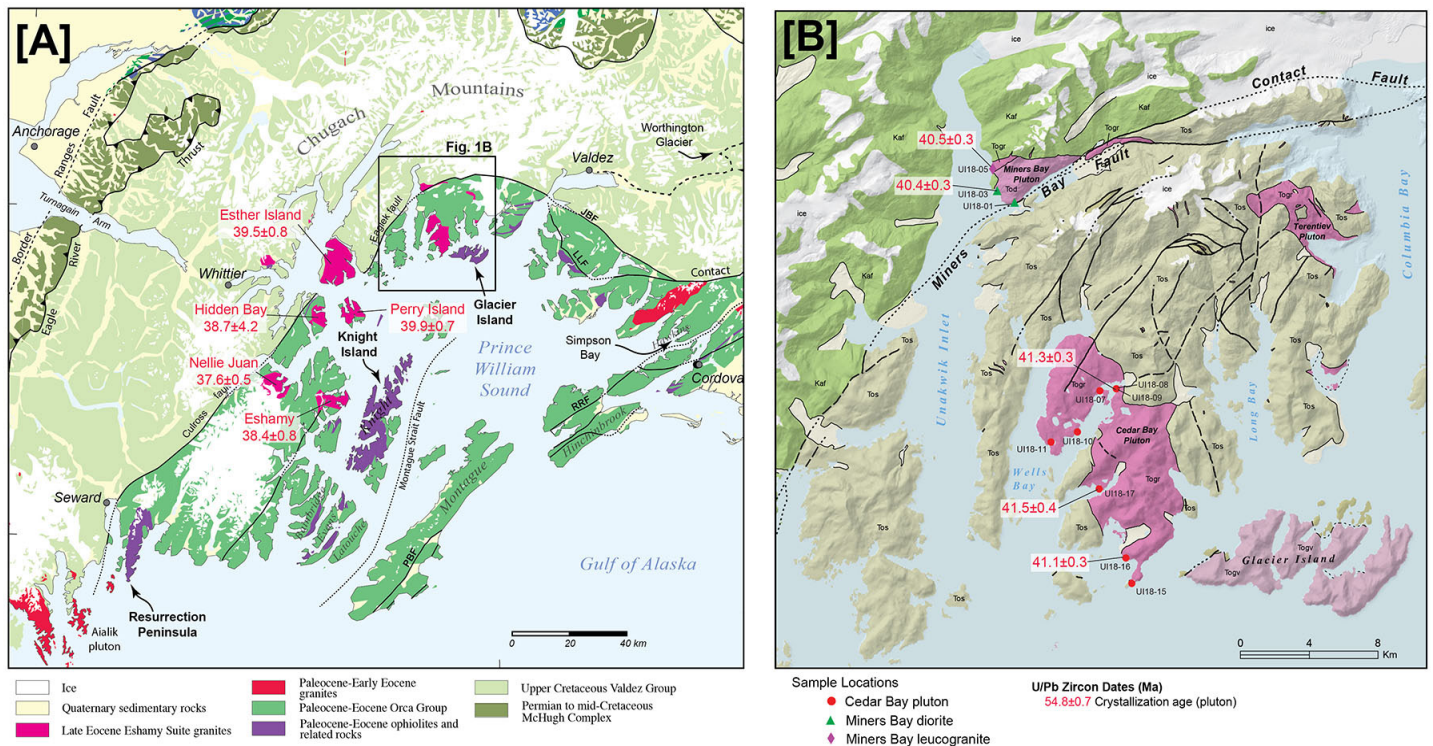


Figure 1. A) Geologic map of the CPW terrane (modified from Bradley et al., 2003). U/Pb ages of the Eshamy Suite plutons from Davidson and Garver (2017) and this study. Box shows approximate location of Fig. 1B. B) Geologic Map of northern Prince William Sound showing the Miners Bay and Cedar Bay plutons (modified from Wilson et al., 2015).

were analyzed at the Hamilton Analytical Laboratory using XRF for major elements and LA-ICP-MS for trace elements. In addition, zircon from the Miners Bay diorite (UI18-03), leucogranite (UI18-05), and from three samples from the Cedar Bay pluton (UI18-09, 16, 17) were extracted and U/Pb dated using LA-ICP-MS at the University of Arizona Laserchron Center. Approximately 35 zircons were analyzed for each sample, and BSE and CL images were used to discriminate between inherited cores (rare) and magmatic rims.

Geochemistry

The Miners Bay diorite contains ~53 wt% SiO₂ and plots as a gabbroic diorite on a plutonic TAS classification diagram (Fig. 3A). The Miners Bay leucogranite and all host-rock samples from the Cedar Bay pluton contain 72-77 wt% SiO₂ and plot in the granite field, and the three mafic enclaves contain 66-72 wt% SiO₂. All samples are calc-alkalic to calcic on the modified alkali index of Frost (2008) and are magnesian with the exception of the leucogranite and mafic enclave from the Miners Bay leucogranite which plot in the ferroan field (Fig. 3). All of the

rocks are peraluminous except for the Miners Bay diorite, the enclave from the Miners Bay leucogranite, and two samples from the Cedar Bay pluton (UI18-15&17; Fig. 3C).

Selected trace elements in the Miners Bay and Cedar Bay plutons are shown in Figure 4. REE concentrations from the Cedar Bay leucogranites and their xenoliths and the Miners Bay leucogranite are remarkably similar and are enriched in the LREE's and show a pronounced negative Eu anomaly (Fig. 4A). The xenolith from the Miners Bay leucogranite is enriched in HREE's relative to its host, has a pronounced negative Eu anomaly, and is slightly depleted in the LREE's compared to the HREE's. The Miners Bay diorite had a flatter REE profile, is depleted relative to the granites, and shows a small positive Eu anomaly relative to chondrites. All samples have low Sr/Y ratios except for the Miners Bay diorite which has low Y and high Sr/Y ratios (Fig. 4B).

U/Pb Geochronology and Hf Isotope Geochemistry

The weighted mean ages of the five samples dated

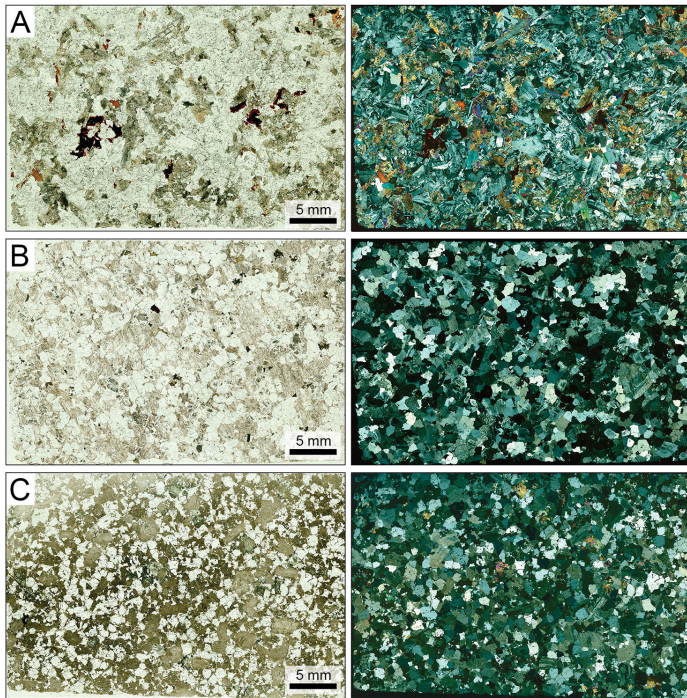


Figure 2. Photomicrographs (PPL and XPL) from the Miners Bay and Cedar Bay plutons. A) Miners Bay diorite (UI18-03). B) Miners Bay leucogranite (UI18-05A). C) Cedar Bay leucogranite (UI18-16) showing near complete replacement of feldspars with sericite and fine-grained epidote. High interference colors in XPL are coarse-grained (secondary) epidote.

in this study are shown in Table 1. The Miners Bay diorite (UI18-03) and leucogranite (UI18-05A) yielded ages of 40.41 ± 0.32 Ma and 40.45 ± 0.36 Ma, respectively. Cedar Bay pluton samples (UI18-09, 16, 17) yielded ages of 41.27 ± 0.37 Ma, 41.53 ± 0.35 Ma, and 41.06 ± 0.37 Ma, respectively. Most of the samples show no inheritance with the exception of a 61.5 Ma zircon in the Miners Bay leucogranite. Zircons from the Miners Bay diorite (UI18-03), leucogranite (UI18-05A), and Cedar Bay leucogranite (UI18-16) were also analyzed for Hf isotope ratios (Fig. 4; Table 1). Most zircons yield juvenile signatures ($\epsilon_{\text{Hf}} \sim +4$ to $+10$), but the Miners Bay leucogranite contains zircon with ϵ_{Hf} as low as -14.7 (Fig. 4).

DISCUSSION

The Miners Bay and Cedar Bay leucogranites are aluminum-rich, calc-alkalic to calcic plutonic rocks and appear to be similar to the Eshamy and Nellie Juan plutons of the Eshamy suite that crop out to the southwest (Figs. 1&3). However, the leucogranites have fewer mafic minerals and appear to be more

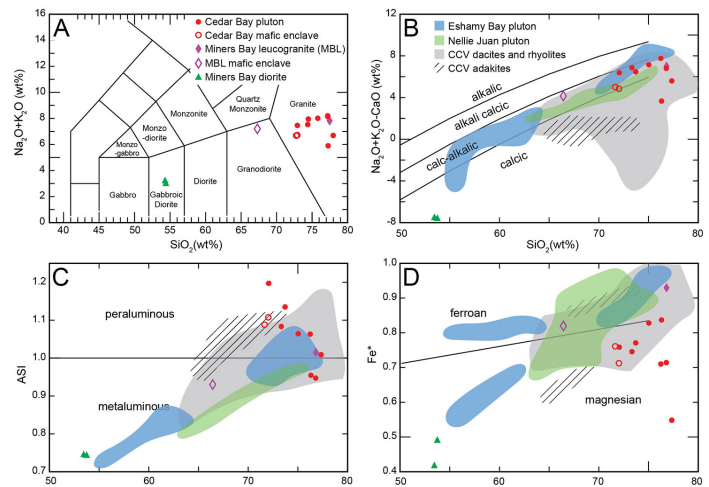


Figure 3. Major element geochemistry of the Miners Bay and Cedar Bay plutons. A) TAS classification for plutonic rocks (Middlemost, 1994). B) Modified alkali-lime index, C) aluminum-saturation index (ASI), and D) Fe index from Frost and Frost (2008). Data for the Eshamy Bay and Nellie Juan plutons from Johnson (2012) and data from the Caribou Creek volcanics (CCV) from Cole et al. (2006).

magnesian than the rest of the Eshamy suite (Fig. 3D).

The ESP are similar to the CCV in terms of major elements. While samples from the Miners Bay and Cedar Bay pluton are magnesian, most of the ESP is ferroan (Fig. 3D). Although some of the CCV plots onto the magnesian field, most of the CCV samples are ferroan aligning with the ESP. The EBP/ NJP and CCV also plot in the metaluminous field along with some of the Miners Bay and Cedar Bay pluton plotting in the peraluminous field (Fig. 3C).

The negative Eu anomaly associated with samples from the Miners Bay and Cedar Bay pluton suggests that plagioclase is fractionating from the melt, whereas a positive anomaly suggests plagioclase accumulation. The REE signatures from the dacites and rhyolites of the CCV are similar to the ESP which both share a negative Eu anomaly, but with just a flatter profile and slightly enriched HREEs (Fig. 4A). The Miners Bay diorite has a positive anomaly indicating the possibility that these are the cumulates of the Miners Bay leucogranites. The MB diorite also compares to the CCV in terms of REE's and Sr/Y ratio, indicating that these diorites may have undergone the same magmatic processes or come from a similar source region (Fig. 4B).

Previously sampled granitoid intrusions from the EBP and NJP were emplaced between 37.6 ± 0.5 and 39.9

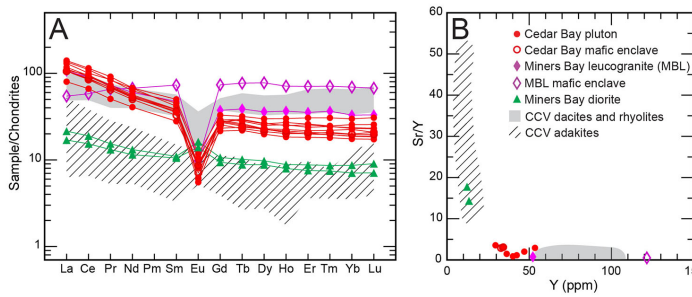


Figure 4. Trace element geochemistry of the Miners Bay and Cedar Bay plutons. A) REE's normalized to chondrites (Sun and McDonough, 1989). B) Sr-Y diagram. Data for the Caribou Creek volcanics (CCV) from Cole et al. (2006).

± 0.7 Ma (Johnson, 2012). The age range of 40.41 ± 0.32 Ma to 41.53 ± 0.35 Ma of the Miners Bay and Cedar Bay plutons confirm that they are part of the Eshamy Suite and also suggests an eastward age progression. In addition, a sandstone sample in UI18-12A in the Orca Group on Outpost Island (south of Unakwik Inlet) has an age of 40.9 ± 0.7 Ma suggesting it formed at the same time as the Eshamy Suite plutons and deposition occurred during intrusion. The CCV ranges from 52 to 36 Ma and fall within the age range of the ESP however may differ in source region and tectonic environment as they are located 200 km to the north of the ESP (Fig. 1; Cole et al., 2006). The Miners Bay and Cedar Bay plutons share a mostly juvenile Hf signature with the EBP and NJP however,

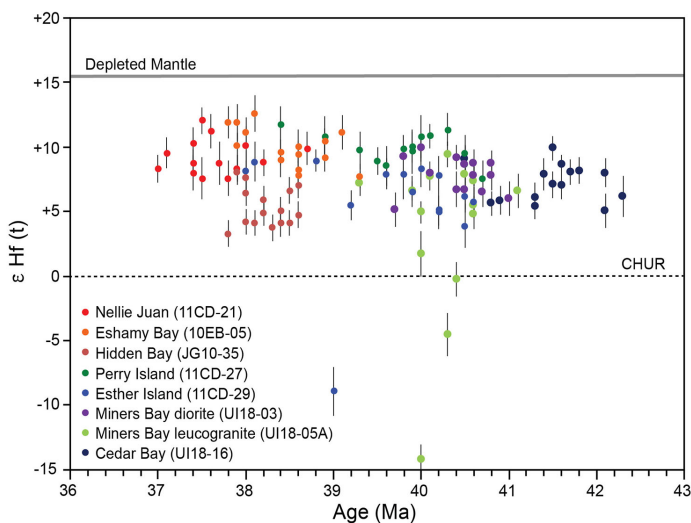


Figure 5. Zircon ϵ_{Hf} vs U/Pb age from the Eshamy Suite plutons (Fig. 1). Most zircons have a juvenile signature; however, the Esther Island pluton and Miners Bay leucogranite have negative ϵ_{Hf} values suggesting the incorporation of more evolved crustal material in the source region.

Table1: U/Pb and Hf isotope results of Miners Bay and Cedar Bay plutons from Prince William Sound

Sample	Location	Latitude	Longitude	U/Pb Age (Ma)	\pm	MWSD	No. of zircons analyzed	Mean ϵ_{Hf}	\pm
UI18-03 (gabbroic diorite)	Head of Miners Bay	61.0773	-147.5052	40.41	0.32	1.4	34	+8.0	0.6
UI18-05A (granite)	Miners Bay	61.0887	-147.5089	40.45	0.33	1.8	32	+4.7	0.6
UI18-09 (granite)	Cedar Bay	60.5827	-147.2340	41.27	0.33	1.9	33	N/A	N/A
UI18-16 (granite)	Cedar Bay (Fairmont Bay)	60.8876	-147.3836	41.53	0.35	0.99	30	+7.4	0.5
UI18-17 (granite)	Cedar Bay (Granite Bay)	60.9233	-147.4008	41.06	0.33	1.8	26	N/A	N/A

two samples from the Miners Bay pluton have a zircons with distinctly negative values suggesting that the source region for some of the plutons must involve partial melting and an incorporation of evolved crustal material (Fig 5).

CONCLUSIONS

The Miners Bay and Cedar Bay plutons are part of the Eshamy suite based on age and geochemistry. Although the CCV and ESP are similar by being ferroan and having comparable REE signatures, they differ by being primarily calcic and metaluminous with a high Sr/Y ratio in the CCV adakites. A similar tectonic environment may attribute to a possible linkage between the CCV and ESP, but it is unclear if they come from the same magmatic system and origin.

ACKNOWLEDGEMENTS

The material from this study is based upon work supported by the National Science Foundation (NSF) under Grant No. EAR 1727991 (to C. Davidson, Carleton College), Grant No. EAR 1728013 (to J.I. Garver, Union College), and by Keck Geology Consortium Grant No. EAR 1659322 (to J.I. Garver, Union College). I would also like to acknowledge Keck Member schools, Exxon Mobil, and the University of Arizona LaserChron Center and NSF-EAR Grant No. 1649254 (to M. Pecha and G. Gehrels) who made zircon analysis possible. I appreciate the Park Service permitting us access and permits to collect samples in the Chugach National Forest. Special thanks to Cameron Davidson, John Garver, and Daniel F. Stockli on their support in the lab and writing process as well as direction and advice

throughout this project. Lastly, I would like to thank Nick Gross Almonte, Alysala Malik, Mollie Pope, Caitlin Noseworthy, and Will Fisher for their unfailing support throughout this journey.

continuity of the Valdez Group, southern Alaska, in *Changes in Stratigraphic Nomenclature* by the U.S. Geological Survey, 1977: Geological Survey Bulletin 1457-A, v. 1422-A, p. A120–A132.

REFERENCES

Cole, R.B., Nelson, S.W., Layer, P.W., and Oswald, P.J., 2006, Eocene volcanism above a depleted mantle slab window in southern Alaska: *Bulletin of the Geological Society of America*, v. 118, p. 140–158, doi:10.1130/B25658.1.

Cowan, D.S., 2003, Revisiting the Baranof-Leech River hypothesis for early Tertiary coastwise transport of the Chugach-Prince William terrane: *Earth and Planetary Science Letters*, v. 213, p. 463–475, doi:10.1016/S0012-821X(03)00300-5.

Davidson, C., and Garver, J.I., 2017, Age and Origin of the Resurrection Ophiolite and Associated Turbidites of the Chugach–Prince William Terrane, Kenai Peninsula, Alaska: *The Journal of Geology*, v. 125, p. 681–700, doi:10.1086/693926.

Haeussler, P.J., Bradley, D.C., Wells, R.E., and Miller, M.L., 2003, Life and death of the resurrection plate: Evidence for its existence and subduction in the northeastern Pacific in Paleocene-Eocene time: *Bulletin of the Geological Society of America*, v. 115, p. 867–880, doi:10.1130/0016-7606(2003)115<0867:LADOTR>2.0.CO;2.

Johnson, E., 2012, Origin of the Late Eocene Eshamy Suite granitoids in Western Prince William Sound, Alaska: 25th Annual Keck Symposium: 2012, p. 33–39.

Sun, S. S. and McDonough, W. F., 1989, Chemical and isotopic systematics of oceanic basalts; implications for mantle composition and processes (in *Magmatism in the ocean basins*), *Geological Society Special Publications*, vol. 42 p. 313-345.

Tysdal, R.G., and Plafker, G., 1978, Age and

AGE AND PROVENANCE OF THE UPPER CRETACEOUS TO PALEOCENE VALDEZ GROUP OF THE CHUGACH TERRANE FROM THE RICHARDSON HIGHWAY AND NORTHERN PRINCE WILLIAM SOUND, ALASKA

NICHOLAS GROSS ALMONTE, Carleton College

Research Advisors: Cameron Davidson, Carleton College and John I. Garver, Union College

INTRODUCTION

The age and provenance of the southern Alaskan Campanian to Paleocene Valdez Group of the Chugach terrane and its relationship with the younger outboard Paleocene to Eocene Orca Group of the Prince William terrane is poorly understood but an important component of the Cordilleran collage (Plafker et al., 1994). The Valdez and Orca Groups are both part of the Chugach-Prince William terrane (CPW), which is a thick accretionary complex that extends 2200 km along the southern Alaskan margin (Fig. 1; Cowan, 2003). The deep-water turbidites of these terranes are quartzofeldspathic and volcanic-lithic sandstones and basaltic rocks (Dumoulin, 1987; Plafker et al., 1994). The CPW is intruded by near-trench plutons of the Sanak-Baranof belt (Davidson and Garver, 2017) and are believed to be related to a slab window that formed during subduction of Kula-Farallon or Kula-Resurrection spreading ridges (Marshak and Karig, 1977; DeLong et al., 1978; Moore et al., 1983; Kusky et al., 1997a; Bradley et al., 2003; Haeussler et al., 2003). There are two hypotheses for the formation of the CPW along the North American Cordilleran margin: 1) either the CPW terrane formed in situ by subduction of the Resurrection plate (Haeussler et al. 2003); or 2) the rocks formed in the Pacific Northwest or California and were transported at least 2000 km along coastwise strike-slip fault systems (Cowan, 2003; Garver and Davidson, 2015).

This study is an investigation into the age and provenance of the Valdez Group and its relationship with the Orca Group in the central Chugach Mountains

using detrital zircon U-Pb dates. New detrital zircon U-Pb dates and their grain-age distributions from the Valdez and Orca Group turbidites are combined with dates from Kochelek et al. (2011), Amato et al. (2013), and Davidson and Garver (2017) and then synthesized to understand the difference in age between the units and provenance. New and existing U-Pb dates indicate maximum depositional ages (MDA) of the Valdez Group are concentrated in three groups: 84-78 Ma, 74-65 Ma, and 62-60 Ma. The youngest group of MDAs are age-correlative with the Orca Group but were collected from rocks in areas mapped as Valdez Group, indicating that either Orca Group rocks occur in the Valdez Group or the youngest Valdez Group rocks are stratigraphically equivalent to those of the oldest Orca Group. If the latter, the Valdez Group is not Campanian to Maastrichtian in age as has been traditionally viewed (Plafker et al., 1994) but is Upper Cretaceous to Paleocene and in part correlative to the lowest part of the Orca Group.

GEOLOGIC SETTING

Chugach terrane

The Chugach terrane is composed of 1) Late Triassic to Jurassic glaucophane greenschist with local blueschist facies as young as Early Cretaceous (Day et al., 2016), 2) the Early Triassic to Early Cretaceous McHugh Complex, and 3) the Late Cretaceous Valdez Group (Plafker et al., 1994; Amato et al., 2013). The McHugh Complex is divided into two assemblages based on distinctive lithologies and MDAs: the 101-91 Ma McHugh Creek assemblage consisting of massive

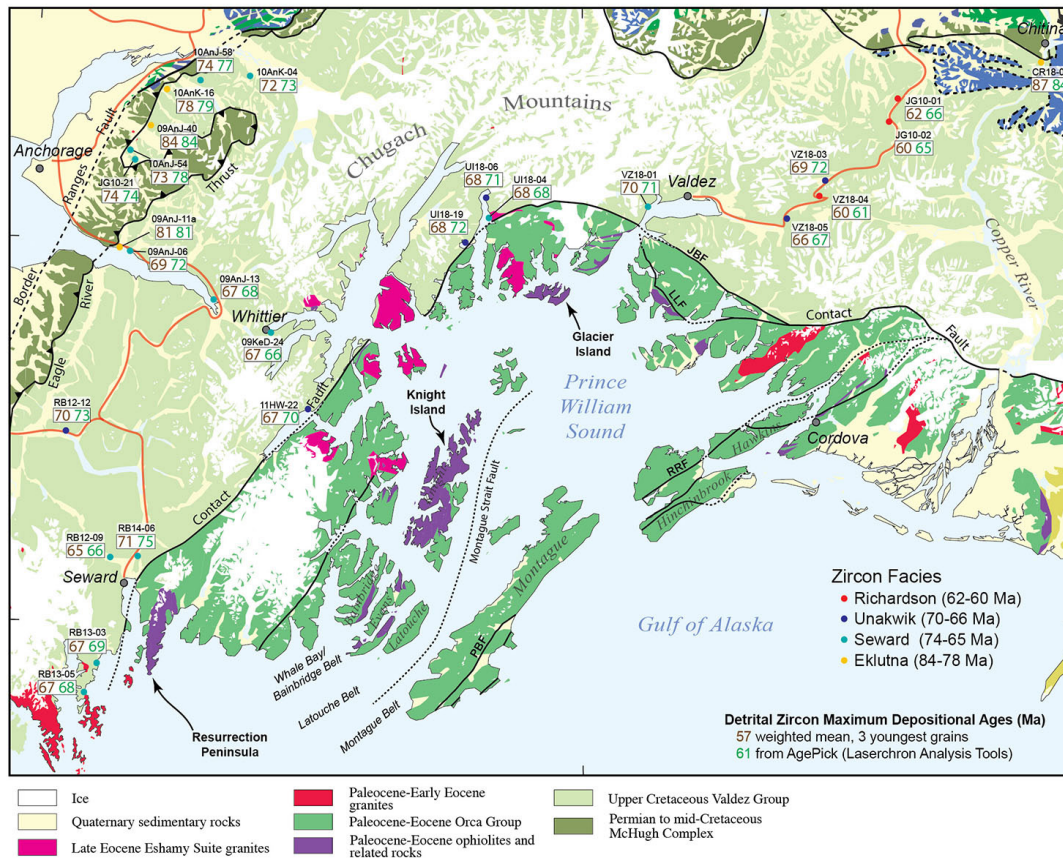


Figure 1. Geologic map of Prince William Sound, Alaska (modified from Bradley and Miller, 2006).

sandstones and conglomerates, and the 169-156 Ma Potter Creek assemblage consisting of chert, argillite, and volcanic rocks (Amato and Pavlis, 2010; Amato et al., 2013). The age of the Valdez Group has been previously constrained by sparse *Inoceramus* fossils from Turnagain Arm near Anchorage, indicating that the Valdez Group is no older than Late Cretaceous in age (Moffit, 1954). The Coast Mountains in British Columbia are inferred to be the primary source of the flysch (Plafker et al., 1994; Haeussler et al., 2006).

Prince William terrane

The Prince William (PW) terrane is composed of the Paleocene to Eocene Orca Group (Dumoulin, 1987; Plafker et al., 1994; Garver and Davidson, 2015). The Orca Group has a more diverse lithology than the Valdez Group with abundant volcanic rocks including breccias, sills, dikes, and pillows, all with a basaltic composition, and these rocks have experienced a lesser degree of metamorphism (Plafker and MacNiel, 1966).

Border Ranges Fault System

The Border Ranges fault (BRF) system is the tectonic boundary between the Chugach terrane and the inboard units of the Wrangellia composite terrane (MacKevett and Plafker, 1974; Pavlis, 1982; Pavlis et al., 1988, 2003; Pavlis and Crouse, 1989; Plafker et al., 1989, 1994; Cowan, 2003; Roeske et al., 2003; Pavlis and Roeske, 2007). If there has been coastwise translation of the CPW, it most likely was accommodated on the BRF (Cowan, 2003). The BRF system is responsible for underthrusting the Chugach terrane a horizontal distance of at least 40 km beneath the Wrangellia composite terrane (Plafker et al., 1994).

Contact Fault

Current mapping separates the older Valdez Group of the Chugach terrane from the younger Orca Group of the Prince William terrane along the Contact fault system (Bol and Roeske, 1993; Plafker et al., 1994; Wilson et al., 2015). The Contact fault is a strike-slip and dip-slip fault between the Chugach and Prince

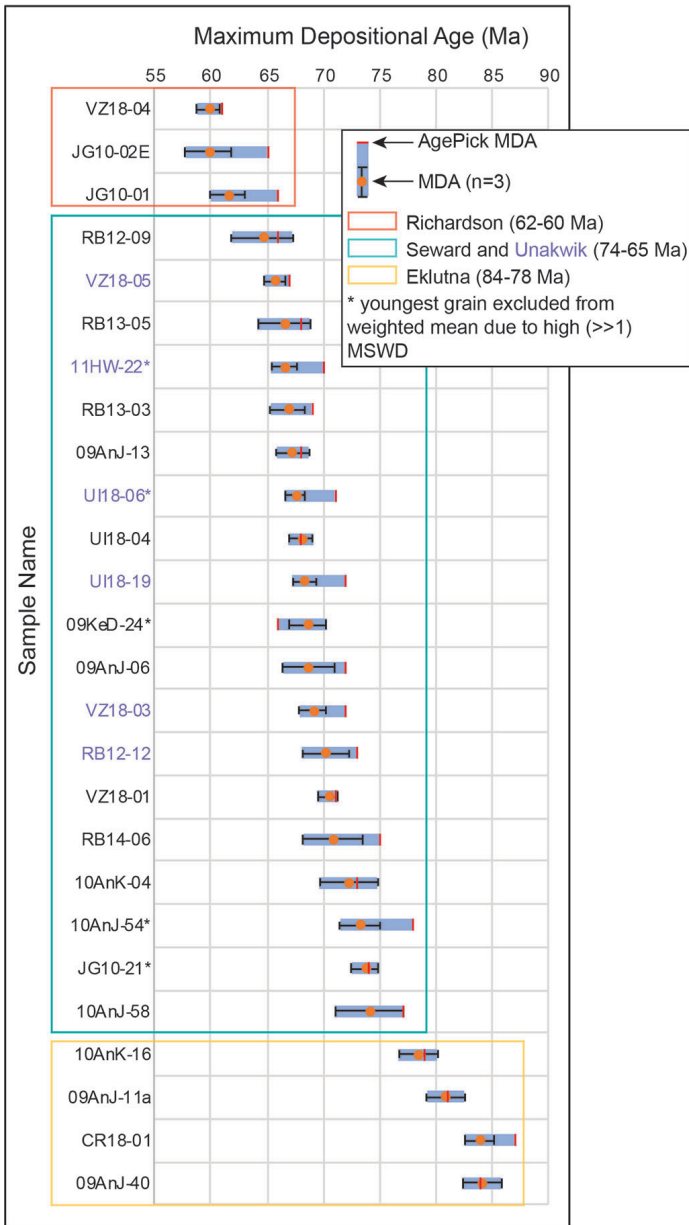


Figure 2. Maximum depositional ages (MDAs) of Valdez Group turbidites in Prince William Sound. MDA (n=3) is the weighted mean of the three youngest coherent zircons from a sample, and AgePick MDA was determined using the AgePick macro of Gehrels (2012). Blue bars show the range of uncertainty of the MDA for a sample.

William terranes and is locally called the Jack Bay fault in northern Prince William Sound. Bol and Roeske (1993) proposes the Contact fault is a strike-slip fault between the terranes, while Plafker et al. (1994) believes the Contact fault places the Orca Group underneath the Valdez Group. Malik et al. (2019), however, suggests the Contact fault may not actually be a terrane bounding fault. The Contact fault cuts rocks in an east-west arc through Valdez Arm and

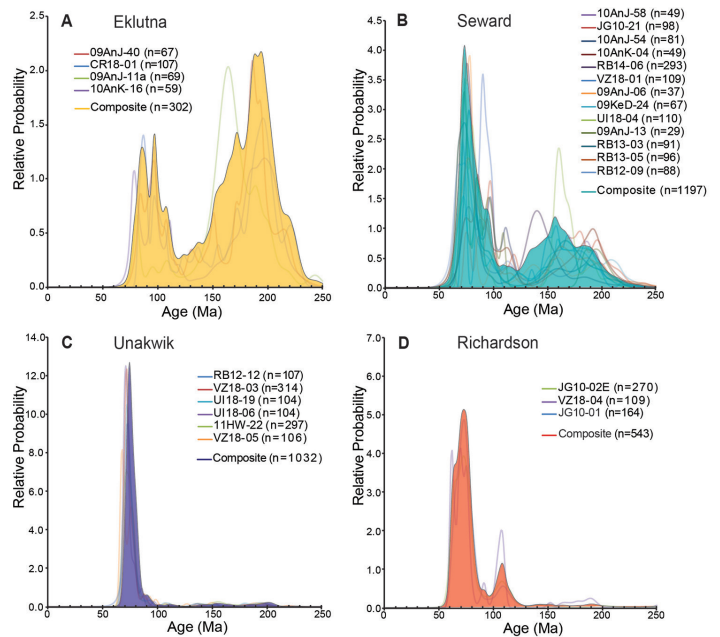


Figure 3. Probability density functions (PDFs) of detrital zircon U/Pb ages for the four zircon facies identified in the Valdez Group. Filled PDFs are composites of all samples in a facies. Legends are organized from oldest to youngest MDA in the group. (A) Eklutna facies with MDAs between 84-78 Ma, (B) Seward facies with MDAs between 74-65 Ma, (C) Unakwik facies with MDAs between 70-66 Ma, and (D) Richardson facies with MDAs between 62-60 Ma.

Unakwik Inlet in our study area.

METHODS

U-Pb ages of detrital zircons were determined from ten sandstone samples of the Valdez Group from northern Prince William Sound and the Richardson Highway as part of this project. For this study, zircon crystals were extracted from our samples with standard methods of crushing, grinding, Rogers Table, heavy liquids, and Frantz magnetic separation. Polished detrital zircons were then dated by U-Pb technique at the Arizona LaserChron Center with laser ablation inductively coupled plasma mass spectrometry (LA-ICP-MS) using standard methods to determine their age and provenance. Zircons were randomly chosen for analysis of 100 or 300 grains per sample.

RESULTS

U-Pb data were collected from a total of 1,063 zircon grains from eight sandstone samples of the Valdez Group from near Chitina, along the Richardson Highway, and northern Prince William Sound. Our

project contributes to a total of 3,074 grains dated (26 samples) from the Valdez Group. We exclude some published ages of the Valdez Group from Bradley et al. (2009), Kochelek et al. (2011), and Amato et al. (2013) due to poor precision (high 1σ error and high MSWD) and a low number of zircons analyzed.

Valdez Group samples are dominated by Early to Late Jurassic, Early to Late Cretaceous, and Paleocene populations with their MDAs ranging from 84.1 to 59.8 Ma. We divide the range of MDAs into three different primary groups by reason of age breaks in the MDAs: 84-78 Ma, 74-65 Ma, and 62-60 Ma (Fig. 2). Each group of samples share similar grain-age distributions and is supported by the Kolmogorov-Smirnov (K-S) test where the p-value between samples in the group is greater than 0.05 which corresponds to 95% confidence that the samples are not statistically different (Gehrels, 2012). Some samples fail the K-S test but are still considered part of a group because of similarities in grain-age distribution and MDA.

The oldest group, the Eklutna facies, includes previously published samples from Mount Magnificent, Turnagain Arm, and Eklutna River near

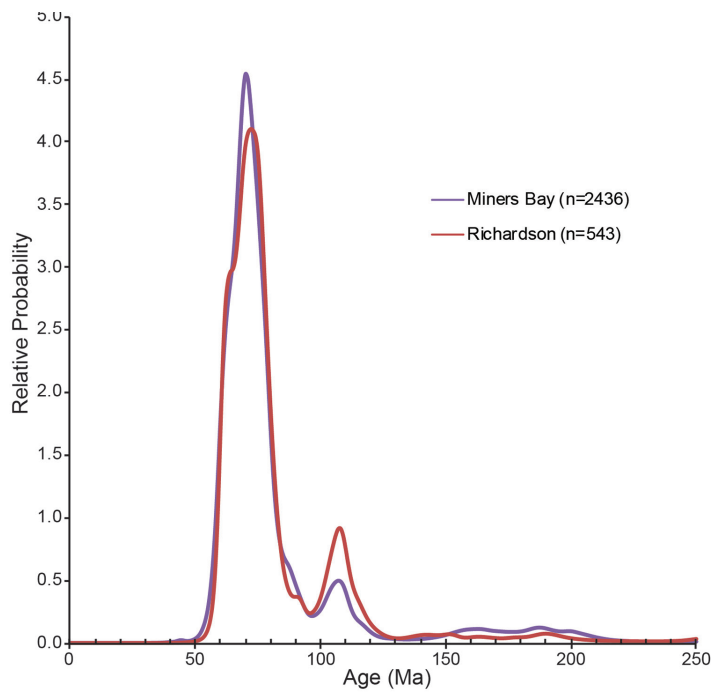


Figure 4. Composite probability density functions of the Richardson facies of the Valdez Group and Miners Bay facies of the Orca Group.

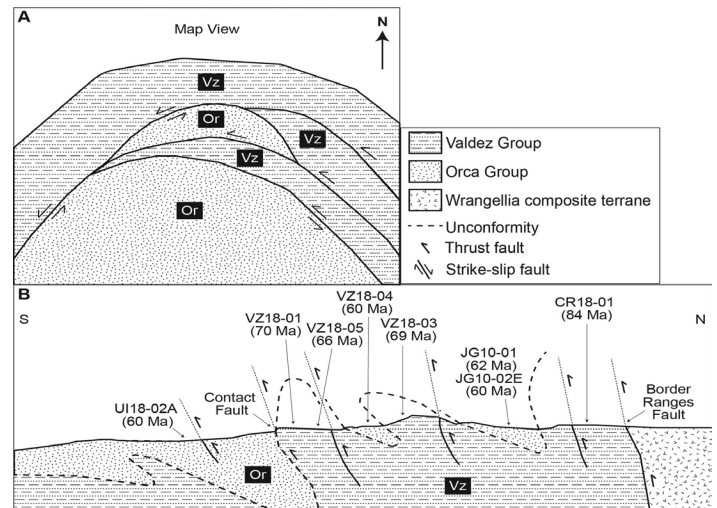


Figure 5. Two possible structural explanations for the occurrence of the young Richardson facies in the Valdez Group. A) The Paleocene rocks are correlative to the Orca Group and occur in the Valdez Group as structural slices. B) The Paleocene rocks were unconformably deposited on top of the Valdez and subsequently folded into the Valdez Group.

Anchorage and one from our study along the Copper River near Chitina (Fig. 1). These four samples (09AnJ-11a, 09AnJ-40, 10AnK-16, and CR18-01) have similar Late Cretaceous populations between 97 and 79 Ma and Early to Middle Jurassic populations between 197 and 164 Ma (Fig. 3A) with MDAs between 84-78 Ma. All samples share Precambrian detrital zircon grains with peaks at ~1465 Ma, ~1800 Ma, ~1980 Ma, and ~2705 Ma. All samples in this group pass the K-S test.

The middle group is the largest and includes nineteen samples: 09AnJ-06, 09AnJ-13, 09KeD-24, 10AnJ-54, 10AnJ-58, 10AnK-04, 11HW-22, JG10-21, RB12-09, RB12-12, RB13-03, RB13-05, RB14-06, UI18-04, UI18-06, UI18-19, VZ18-01, VZ18-03, and VZ18-05 (Fig. 1). The middle group is split into two sub-groups based on grain-age distribution. One sub-group, the Seward facies, has thirteen samples that have pronounced Early to Late Jurassic and Early Cretaceous populations between 192 and 140 Ma with MDAs between 74-65 Ma (Fig. 3B). This sub-group's Precambrian grains have a wide range of ages between ~560 to ~2760 Ma. The other sub-group, the Unakwik facies, includes six samples: 11HW-22, RB12-12, UI18-06, UI18-19, VZ18-03, and VZ18-05 (Fig. 3C). The Unakwik facies, with MDAs between 70-66 Ma, is remarkably uniform and is dominated by Late Cretaceous zircons between 76-68 Ma and do not

have older populations like the Seward facies. These samples share many Precambrian peaks between ~1730 to ~2310 Ma and between ~2550 to ~2740 Ma. VZ18-05 is the only sample in the sub-group that fails the K-S test.

The youngest group, the Richardson facies, includes three samples (JG10-01, JG10-02E, and VZ18-04) collected from rocks mapped as the Valdez Group along the Richardson Highway (Fig. 1) and are dominated by zircons with Late Cretaceous (72-70 Ma) and Early Cretaceous (109-106 Ma) peak ages (Fig. 3D) with MDAs between 62-60 Ma. The samples in this group also have a wide age range of Precambrian grains, but they all share peaks between ~1775 to ~2050 Ma. VZ18-04 fails the K-S test for this group, probably because of the large Cretaceous peak at 108 Ma (Fig. 3D).

DISCUSSION

Grain-age distributions of the Valdez Group are dominated by Paleocene and Cretaceous peaks, possibly originating from an active and partially dissected Late Cretaceous to Paleocene volcanic arc (Garver and Davidson, 2015). Many samples also have Jurassic populations which may come from meta-plutonic basement rocks built on the volcanic arc (Garver and Davidson, 2015). The grain-age distribution of the CPW terrane is strikingly similar to that of the Coast Mountains Batholith Complex (CMB) in British Columbia (Haeussler et al., 2006; Garver and Davidson, 2015), suggesting that the CPW terrane may have formed farther south and adjacent to the CMB (Garver and Davidson, 2015).

The MDAs of the Eklutna facies (84-78 Ma), Seward facies (74-65 Ma) and Unakwik facies (70-66 Ma) suggest that these rocks were deposited in the Cretaceous and are consistent with previous age estimates (Plafker et al., 1994). However, the Richardson facies (62-60 Ma) is Paleocene in age and is age-correlative with the Orca Group. A comparison of the Richardson facies of the Valdez Group with the Miners Bay facies (which includes the three samples that comprise the Richardson facies) of the Orca Group (Fisher, 2019) shows that these rocks are nearly identical (Figs. 1&4). A key question is the stratigraphic alliance of this

young facies (62-60 Ma) in the Valdez Group. Samples from the Richardson facies were collected 50 to 100 km away from the Contact fault and along Richardson Highway, an area long-mapped as Valdez Group (Fig. 1). We have two options for the occurrence of Orca Group age-correlative samples in areas mapped as the Valdez Group: 1) the Richardson facies is part of the Valdez Group and is stratigraphically equivalent to the oldest Orca Group (Miners Bay facies); or 2) the Richardson facies is part of the Orca Group and occurs in the Valdez Group as structural slices (Fig. 5A) or was deposited unconformably on top of the Valdez and subsequently folded into the Valdez Group (Fig. 5B).

CONCLUSIONS

Detrital zircon U-Pb ages from turbidites of the Valdez Group of the Chugach terrane in Prince William Sound demonstrate the complex relationship between the Valdez Group with the outboard turbidites of the Paleocene-Eocene Orca Group. New detrital zircon U-Pb data, however, suggests that the Valdez Group is Upper Cretaceous to Paleocene in age. MDAs of the Valdez Group form three groups: 84-78 Ma, 74-65 Ma and 62-60 Ma. The youngest MDA group, the Richardson facies, overlaps in age with the Miners Bay facies from the Orca Group (Fisher et al., 2019). This study supports the conclusions of Malik et al. (2019) that the Contact fault system may not be a terrane boundary (Malik et al., 2019).

ACKNOWLEDGEMENTS

The material from this study is based upon field work and analyses funded by the National Science Foundation (NSF) under NSF Grant “Collaborative Research: RUI: Translation and accretion of the Yakutat microplate and Prince William terrane, Alaska” No. EAR-1727991 (to C. Davidson, Carleton College) and No. EAR-1728013 (to J.I. Garver, Union College). We were also funded by the Keck Geology Consortium Grant “Geology of the Chugach-Prince William terrane in northern Prince William Sound” (to J.I. Garver, Union College) and partly funded by NSF Grant No. EAR-1659322 (to Keck Geology Consortium). I would also like to acknowledge the Arizona LaserChron Center funded by NSF-EAR Grant No. 1649254 who made zircon analysis possible. I would like to thank my project advisors Dr. Cameron

Davidson and Dr. John I. Garver for the opportunity to participate in this Keck REU project. Lastly, I would like to thank the other students in the research group for their diligent work on this project: W. Fisher, V. Garcia, A. Malik, C. Noseworthy, and M. Pope.

REFERENCES

- Amato, J.M., and Pavlis, T.L., 2010, Detrital zircon ages from the Chugach terrane, southern Alaska, reveal multiple episodes of accretion and erosion in a subduction complex: *Geology*, v. 38, p. 459-462.
- Amato, J.M., Pavlis, T.L., Cliff, P.D., Kochelek, E.J., Hecker, J.P., Worthman, C.M., and Day, E.M., 2013, Architecture of the Chugach accretionary complex as revealed by detrital zircon ages and lithologic variations: evidence for Mesozoic subduction erosion in southcentral Alaska: *Geol. Soc. Am. Bull.* 125:1891-1911.
- Bol, A.J., and Roeske, S.M., 1993, Strike-slip faulting and block rotation along the contact fault system, eastern Prince William Sound, Alaska: *Tectonics* 12:49-62.
- Bradley, D.C., Kusky, T.M., Haeussler, P.J., Goldfarb, R.J., Miller, M.L., Dumoulin, J.A., Nelson, S. S., and Karl, S.M., 2003, Geologic signature of early Tertiary ridge subduction in Alaska. In *Sisson, V. B., Roeske, S., and Pavlis, T. L., eds., Geology of a transpressional orogen developed during ridge-trench interaction along the North Pacific margin: Geol. Soc. Am. Spec. Pap.* 371:19-49.
- Bradley, D.C., and Miller, M.L., 2006, Field guide to south-central Alaska's accretionary complex, Anchorage to Seward: Anchorage, Alaska Geological Society, 32 p.
- Bradley, D., Haeussler, P., O'Sullivan, P., Friedman, R., Till, A., Bradley, D. and Trop, J., 2009, Detrital zircon geochronology of Cretaceous and Paleogene strata across the south-central Alaskan convergent margin (No. 1760-F): *US Geological Survey*, 36 p.
- Cowan, D.S., 2003, Revisiting the Baranof-Leech River hypothesis for early Tertiary coastwise transport of the Chugach-Prince William terrane: *Earth and Planetary Science Letters*, v. 213, p. 463-475.
- Davidson, C. and Garver, J., 2017, Age and origin of the Resurrection Ophiolite and associated turbidites of the Chugach-Prince William terrane, Kenai Peninsula, Alaska: *The Journal of Geology*, v. 125, p. 681-700.
- Day, E.M., Pavlis, T.L., Amato, J.M., 2016, Detrital zircon ages indicate an Early Cretaceous episode of blueschist-facies metamorphism in southern Alaska: Implications for the Mesozoic paleogeography of the northern Cordillera: *Lithosphere*, v. 8, no. 5; p. 451-462.
- Delong, S.E., Fox, P.J., and McDowell, F.W., 1978, Subduction of the Kula ridge at the Aleutian trench: *Geol. Soc. Am. Bull.* 89:83-95.
- Dumoulin, J.A., 1987, Sandstone composition of the Valdez and Orca Groups, Prince William Sound, Alaska: *U.S. Geological Survey Bulletin* 1774, p. 1-37.
- Fisher, W.S., Pope, M.D., Malik, A.M., Garver, J.I., and Davidson, C., 2019, Zircon facies in the Paleocene-Eocene Orca Group indicate a provenance link to the Chugach terrane, Prince William Sound, Alaska: *Geological Society of America Abstracts with programs*, v. 51, Portland, OR.
- Garver, J., and Davidson, C., 2015, Southwestern Laurentian zircons in Upper Cretaceous flysch of the Chugach-Prince William terrane in Alaska: *American Journal of Science*, v. 315, p. 537-556.
- Gehrels, G., 2012, Detrital Zircon U-Pb Geochronology: Current Methods and New Opportunities, in *Tectonics of Sedimentary Basins: Recent Advances*, C. Busby and A. Azor, editors, Wiley-Blackwell Publishing, p. 47-62.
- Haeussler, P. J., Bradley, D.C., Wells, R.E., and Miller, M.L., 2003, Life and death of the Resurrection plate: Evidence for its existence and subduction in the northeastern Pacific in Paleocene-Eocene time: *Geological Society of America Bulletin*, v.

- 115, p. 867-880.
- Haeussler, P.J., Gehrels, G.E., and Karl, S.M., 2006, Constraints on the age and provenance of the Chugach accretionary complex from detrital zircons in the Sitka Graywacke near Sitka, Alaska: U.S. Geol. Surv. Prof. Pap. 1709-F, 24 p.
- Kochelek, E.J., Amato, J.M., Pavlis, T.L., and Clift, P.D., 2011, Flysch deposition and preservation of coherent bedding in an accretionary complex; detrital zircon ages from the Upper Cretaceous Valdez Group, Chugach Terrane, Alaska: *Lithosphere*, v. 3, no. 4; 4, p. 265-274.
- Kusky, T.M., Bradley, D.C., and Haeussler, P., 1997a, Progressive deformation of the Chugach accretionary complex, Alaska, during a Paleogene ridge-trench encounter: *J. Struct. Geol.* 19:139-157.
- MacKevett, E., Jr., and Plafker, G., 1974, The Border Ranges fault in south-central Alaska: *U.S. Geol. Surv. J. Res.* 2:323-329.
- Malik, A.M., Fisher, W.S., Gross Almonte, N., Garver, J.I., and Davidson, C., 2019, U-Pb dating of detrital zircon from turbidites of the Chugach and Prince William terranes in Prince William Sound, Alaska: Implications for the significance of the Contact fault system as a terrane boundary: *Geological Society of America Abstracts with programs*, v. 51, Portland, OR.
- Marshak, R.S., and Karig, D.E., 1977, Triple junctions as a cause for anomalously near-trench igneous activity between the trench and volcanic arc: *Geology* 5:233-236.
- Moffit, F.H., 1954, Geology of the Prince William Sound region, Alaska: U.S. Geological Survey Bulletin 989-E, p. 225-310, 1 sheet.
- Moore, J.C., Byrne, T., Plumley, P.W., Reid, M., Gibbons, H., and Coe, R.S., 1983, Paleogene evolution of the Kodiak Islands, Alaska: consequences of ridge-trench interaction in a more southerly latitude: *Tectonics*, 2:265-293.
- Pavlis, T.L., 1982, Origin and age of the Border Ranges fault of southern Alaska and its bearing on the late Mesozoic tectonic evolution of Alaska: *Tectonics* 1:343-368.
- Pavlis, T.L., Monteverde, D.H., Bowman, J.R., Rubenstone, J.L., and Reason, M.D., 1988, Early Cretaceous near-trench plutonism in southern Alaska: atonalite-trondhjemite intrusive complex injected during ductile thrusting along the Border Ranges fault system: *Tectonics* 7:1179-1199.
- Pavlis, T.L., and Crouse, G.W., 1989, Late Mesozoic strike slip movement on the Border Ranges fault system in the eastern Chugach Mountains, southern Alaska: *J. Geophys. Res. Solid Earth* 94(B4):4321-4332.
- Pavlis, T.L., Marty, K., and Sisson, V.B., 2003, Eocene dextral strike slip within the Chugach terrane, southern Alaska: evidence from fabric studies along the Richardson Highway. In Sisson, V.B., Roeske, S., and Pavlis, T.L., eds., *Geology of a transpressional orogen developed during ridge-trench interaction along the North Pacific margin: Geol. Soc. Am. Spec. Pap.* 371:171-190.
- Pavlis, T.L., and Roeske, S.M., 2007, The Border Ranges fault system, southern Alaska. In Ridgway, K. D., Trop, J. M., Glen, J. M. G., and O'Neill, J. M., eds., *Tectonic growth of a collisional continental margin: crustal evolution of southern Alaska: Geol. Soc. Am. Spec. Pap.* 431:95-127.
- Plafker, G., and MacNeil, F.S., 1966, Stratigraphic significance of Tertiary fossils from the Orca Group in the Prince William Sound region, Alaska, in U.S. Geological Survey, Geological survey research 1966, Chapter B: U.S. Geological Survey Professional Paper 550-B, p. B62-B68.
- Plafker, G., Nokleberg, W.J., and Lull, J.S., 1989, Bedrock geology and tectonic evolution of the Wrangellia, Peninsular, and Chugach terranes along the Trans-Alaska crustal transect in the Chugach Mountains and southern Copper River Basin, Alaska: *J. Geophys. Res. Solid Earth* 94(B4):4255-4295.

- Plafker, G., Moore, J.C., and Winkler, G.R., 1994, Geology of the southern Alaska margin, in Plafker, George, and Berg, H.C., eds., *The geology of Alaska: Geological Society of America, DNAG Series, v. G-1*, p. 389-449.
- Roeske, S.M., Snee, L.W., and Pavlis, T.L., 2003, Dextral-slip reactivation of an arc-forearc boundary during Late Cretaceous-early Eocene oblique convergence in the northern Cordillera. In Sisson, V. B., Roeske, S., and Pavlis, T. L., eds., *Geology of a transpressional orogen developed during ridge-trench interaction along the North Pacific margin: Geol. Soc. Am. Spec. Pap. 371*: 141-169.
- Wilson, F.H., Hults, C.P., Mull, C.G, and Karl, S.M, comps., 2015, *Geologic map of Alaska: U.S. Geological Survey Scientific Investigations Map 3340*, pamphlet 196 p., 2 sheets, scale 1:1,584,000, <http://dx.doi.org/10.3133/sim3340>.

U-PB DATING OF DETRITAL ZIRCON FROM TURBIDITES OF THE CHUGACH AND PRINCE WILLIAM TERRANES, ALASKA: SIGNIFICANCE OF THE CONTACT FAULT SYSTEM AS A TERRANE BOUNDARY

ALYSALA MALIK, Carleton College
Research Advisor: Cameron Davidson

INTRODUCTION

The Gulf of Alaska is rimmed by a Mesozoic-Cenozoic accretionary wedge complex comprised of the Chugach and the Prince William terranes. This study focuses on understanding the history and relationship between turbidites of the Chugach and Prince William terranes in the Prince William Sound area: the Campanian-Maastrichtian Valdez Group and the Paleocene-Eocene Orca Group. Critical in understanding this system is the Contact fault system, a poorly understood collection of fault strands that has traditionally been viewed as the terrane boundary between the two (Winkler and Plafker 1975; Plafker et al. 1977; Tysdal and Case 1979; Dumoulin 1988; Bol and Gibbons 1992; Bol and Roeske 1993; Arkle et al. 2013). It was thought to be an original accretionary fault that separates terranes (Plafker et al. 1977; Nokleberg et al., 1986; Dumoulin, 1988); however, more recent work has characterized it as a sequence of faults that may be related to internal deformation of the accretionary complex (Bol and Gibbons, 1992; Bol and Roeske, 1993).

The main goal of this study is to determine whether the Contact fault functions as a terrane boundary across Prince William Sound by presenting new detrital zircon U-Pb ages from either side of the fault system (Fig. 1). First, we specifically focus on understanding the age relationships between the Valdez Group and the Orca Group on either side of the Jack Bay fault and the Landlock fault in Valdez Arm, northeastern Prince William Sound (Fig. 2). Second, we focus on strands of the Contact fault system in

three other locations: Unakwik Inlet, Kings Bay, and Seward (Fig. 3).

This second goal of this study is to determine the nature of the Landlock block, an area currently defined by the convergence of the Jack Bay and Landlock faults (Fig. 2). Early maps portrayed the Landlock block as Valdez Group (Moffit, 1954; Winkler and Plafker, 1975), but the current location of the Contact fault in Jack Bay includes the block as part of the Orca Group (Dumoulin, 1998; Bol and Roeske, 1993). Therefore, an important question is the affinity of the rocks of the Landlock block, whether they are Orca Group or Valdez Group.

GEOLOGIC SETTING

Northeastern Prince William Sound

In northeastern PWS near Valdez, the segments of the Contact fault of interest are the Jack Bay and Landlock Faults. The two faults divide the area into three lithotectonic belts that have been reported to differ in structural trends, deformation intensities, and metamorphic grade (Fig. 2; Bol and Roeske 1993). The Jack Bay fault is currently mapped as the contact between the Chugach and Prince William terranes, separating the Valdez Group and the Orca Group (Fig. 2; Dumoulin, 1998; Bol and Roeske, 1993; Wilson et al., 2015). The Jack Bay fault is also mapped as the northern edge of the Landlock block, an area defined by the convergence of the high-angle Jack Bay fault with the low-angle Landlock fault (Fig. 2). The Landlock block has been characterized

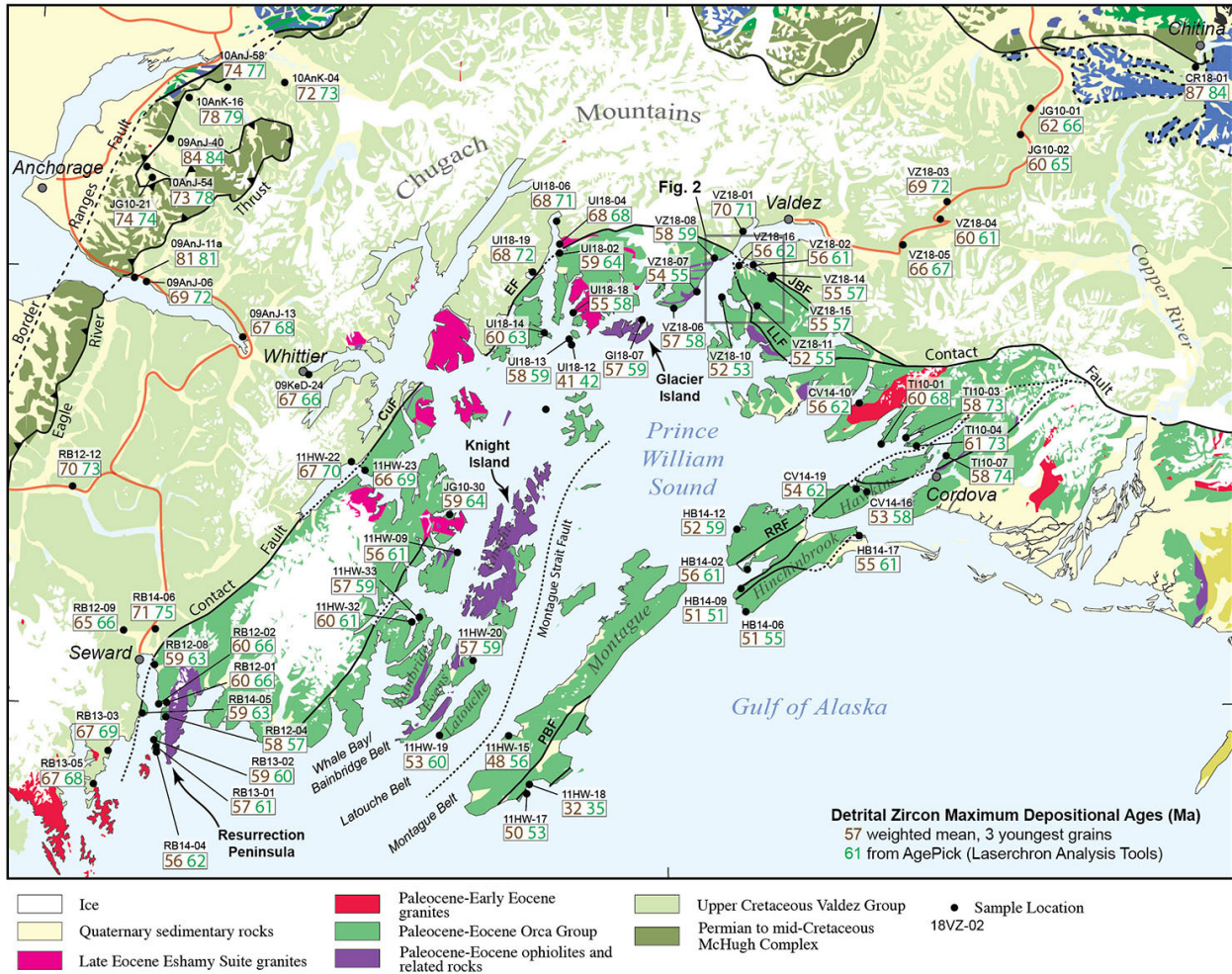


Figure 1. Geologic map of Prince William Sound, Alaska (modified from Bradley and Miller, 2006). CuF = Culross fault, EF = Eaglek fault, JBF = Jack Bay fault, LLF = Landlock fault.

by massive sandstone units with units of thinly interbedded sandstone and siltstone turbidites (Bol and Roeske, 1993). The metamorphic grade was mapped as phrenite-pumpellyite and rarely greater than lower greenschist facies, which is lower than surrounding units (Bol and Roeske, 1993). North of the Jack Bay fault the rocks are mainly fine-grained graywacke sandstones with greenschist facies mapped as the highest metamorphic grade (Bol and Roeske, 1993). However, in the field we observed that the north shore of the Landlock block was indistinguishable from massive, coarse-grained sandstone units north of the Jack Bay fault. It was only farther south in Galena Bay that we observed characteristic Landlock block outcrops of thinly bedded, medium-fine sandstone turbidites interbedded with shale (sample VZ18-11, Fig. 2).

Northern Prince William Sound

In northern PWS, the Eaglek fault is the fault strand mapped as juxtaposing the Prince William and Chugach terranes (Fig. 3; Tysdal and Case 1979; Nelson et al. 1985). It is visible as a deformation zone 10 to 100 meters wide that begins at Unakwik Inlet, passes through Eaglek Bay, and becomes obscured after Esther Island (Bol and Gibbons 1992; Plafter et al. 1977). The age of the fault is constrained by a cross-cutting relationship with the 41 Ma Miner’s Bay pluton (Garcia et al., 2019).

Western and Southwestern Prince William Sound

The location of the Contact fault has been difficult to define in western Prince William Sound because of similarities in lithology and structure of the Valdez and Orca Groups (Tysdal and Case, 1979; Dumoulin,

METHODS

Detrital zircon U-Pb ages were determined from sandstone samples collected along Valdez Arm and Unakwik Inlet to determine, in part, the age of units on either side of the Jack Bay, Landlock, and Eaglek faults (Figs. 2 & 3). Zircons were isolated using standard techniques of crushing, grinding, Rogers table, heavy liquids, and magnetic separation at Carleton College. Samples were dated at the Arizona Laserchron Center through Laser Ablation ICP Mass Spectrometry. Maximum depositional ages (MDA) were calculated using two different methods. The first method uses the weighted mean of the youngest three zircons from the youngest age cluster of a sample. The second method uses AgePick, an

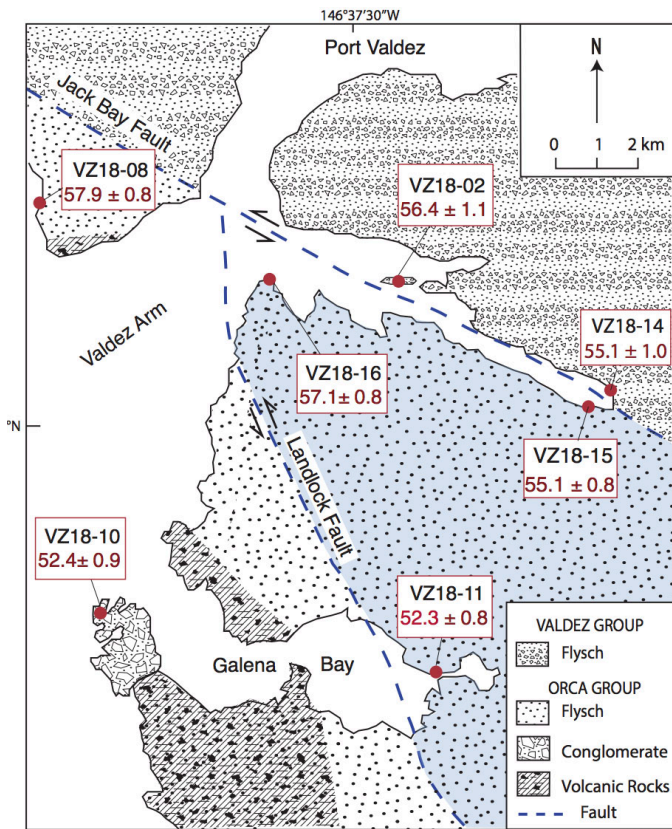


Figure 2. Geologic map of Valdez Arm in northeastern Prince William Sound. The Jack Bay and Landlock faults, sample locations, and geologic units are shown. Maximum depositional ages (MDAs) based on the weighted mean of the youngest three zircons are shown in red. All samples yielded Orca Group MDAs (Paleocene-Eocene). Adapted from Bol and Roeske (1993).

1988; Bol and Gibbons, 1992; Davidson and Garver, 2017). The Culross fault was originally mapped as the terrane-bounding segment of the Contact fault system (Tysdal and Case, 1979; Bol and Gibbons, 1992). The fault itself is highly obscured in locations such as Long Bay (west of Culross Pass) while extremely visible and located to within a few meters farther northeast (Fig. 3; Bol and Gibbons, 1992). The fault was initially mapped as a southern extension of the Eaglek fault (Tysdal and Case, 1979), however this has been disproven (Bol and Gibbons, 1992).

Similarly to western Prince William Sound, the location of the Contact fault has been difficult to define in southwest Prince William Sound. The fault was originally mapped along the Resurrection Peninsula (Tysdal and Case, 1979), however a recent study suggested that the Contact fault belongs along the western edge of Resurrection Bay (Davidson and Garver, 2017).

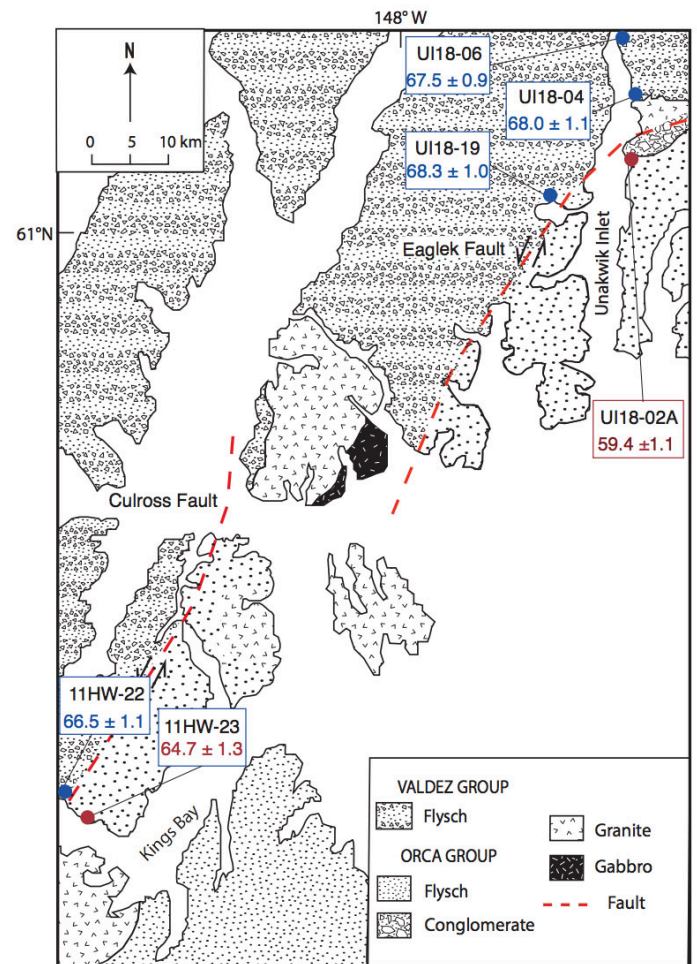


Figure 3. Geologic map of Unakwik Inlet and Kings Bay in northwest Prince William Sound. The Eaglek and Culross faults, sample locations, and geologic units are shown. Samples in red yield Orca Group MDAs (Paleocene-Eocene) while samples in blue yielded Valdez Group MDAs (Upper Cretaceous). Adapted from Bol and Gibbons (1992).

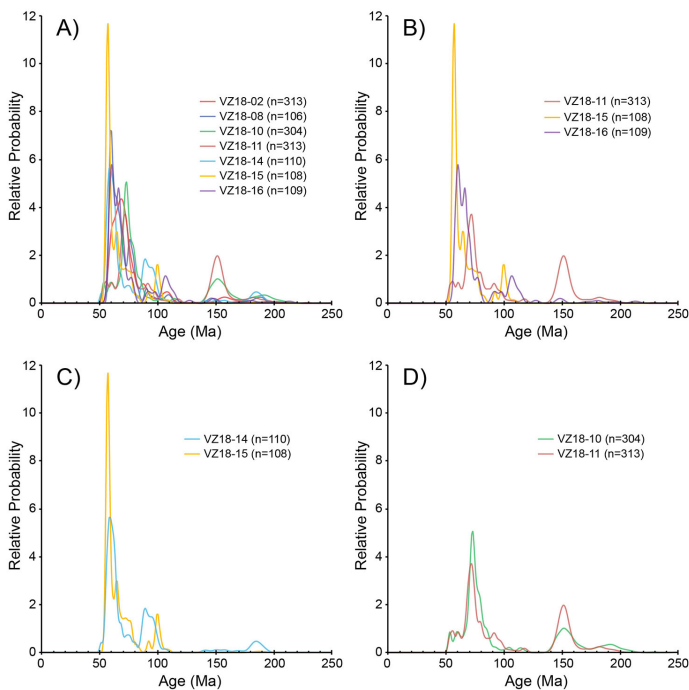


Figure 4. Normalized probability density functions (PDFs) of detrital zircon ages from the Valdez Arm area shown in Figure 2. A) All seven samples from Figure 2. B) Three samples from the Landlock block have different grain-age distributions and fail the K-S test. C) VZ18-14 and 15 from either side of the Jack Bay fault have similar grain-age distributions and pass the K-S test. D) VZ18-10 and 11 from either side of the Landlock fault have remarkably similar grain-age distributions and pass the K-S test.

Excel macro that identifies the youngest coherent peak in a grain-age distribution. The Kolmogorov-Smirnov statistical test (K-S test) was used to analyze whether samples have similar grain-age populations.

RESULTS

Seven samples collected from either side of the Jack Bay and Landlock faults in the Valdez Arm area yield Paleocene and Eocene MDAs (Fig. 2 & 4A). The three samples from the Landlock Block (VZ18-15, VZ18-16, and VZ18-11) have different grain-age distributions (Fig. 4B) and failed the K-S test suggesting they were not derived from the same source. Samples taken from either side of Jack Bay fault (VZ18-14 and VZ18-15) give the same MDA (55.1 Ma) and have similar grain-age distributions with a prominent Paleocene peak (57-59 Ma), and another prominent Late Cretaceous peak (90-100 Ma) and pass the K-S test (Fig. 4C). Two samples collected on either side of the Landlock fault (VZ18-10 and VZ18-11) have nearly identical Eocene MDAs (~52Ma), yield remarkably similar grain-age

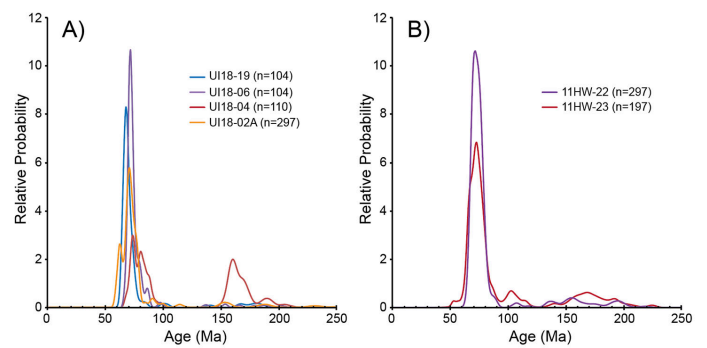


Figure 5. A) UI18-02A taken from the Orca Group side of the Eaglek fault has a Paleocene-Eocene grain-age peak while three samples taken from the Valdez Group side have late Cretaceous grain-age distributions. B) 11HW-22 and 23 from either side of the Culross fault have remarkably similar grain-age distributions, however fail the K-S test.

distributions with prominent Late Cretaceous and Jurassic peaks (Fig. 4D), and pass the K-S test ($p=0.412$).

In Unakwik inlet, UI18-02A taken from the southern side of Eaglek fault yielded a Paleocene MDA of 59.4 ± 1.1 Ma (Fig. 3). However, three samples taken from the northern side of the fault (UI18-04, UI18-06, and UI18-19) yield Late Cretaceous MDAs of 68.0 ± 1.1 , 67.5 ± 0.9 , and 68.3 ± 1.0 Ma (Fig. 3 & 4A). In western Prince William Sound, 11HW-22 and 11HW-23 occur on either side of the Contact fault but have similar MDAs (66.5 ± 1.1 Ma and 64.7 ± 1.3 Ma) and grain-age distributions with a significant Late Cretaceous peak at 73 Ma (Fig. 3 & 5B). 11HW-22 and 11HW-23 do not pass the K-S test ($p=0.002$).

DISCUSSION

Samples were taken from either side of the Jack Bay fault to analyze the relationship between the fault strand and the Valdez and Orca Group. Samples in the Valdez Arm area yield similar Paleocene and Eocene MDAs (Fig. 2) and some of the samples appear to be derived from the same source (Fig. 4). The presence of Orca Group age rocks north of the Jack Bay fault suggests that: a) the Jack Bay fault as mapped is not the boundary between the Chugach and Prince William terranes, or b) there are slivers of Orca Group along the fault zone on the northern arm of Jack Bay. Samples VZ18-02, 08, 14, and 16 have similar grain ages distributions and pass the K-S test; this suggests that there may be a coherent block of similar

provenance that becomes progressively older moving east to west (Fig. 2).

The similar MDAs and grain-age distributions of VZ18-10 and VZ18-11 on either side of the Landlock fault show that the rocks of the Landlock block are clearly allied with the Orca Group (Fig. 4D). The rocks in Galena Bay are younger than the Orca Group to the north in Jack Bay, but also younger than the Orca Group to south near Cordova (Fig. 1). Grimm (2015) reports similar Eocene age rocks to the south on Hinchinbrook Island (Fig. 1) that are markedly similar to the Orca units seen in Galena Bay (Fig. 2), characterized by thin- to medium-bedded fine sandstone and interbedded shale. Additionally, K-S test results indicate that VZ18-10 and VZ18-11 were drawn from the same population, and that HB14-06 and VZ18-11 were also drawn from the same population (at the 95 percent confidence level).

In the Unakwik inlet area (Fig. 3), samples taken from either side of the Eaglek fault yield MDAs and grain-age distributions that show that the Eaglek fault functions as the boundary between the Valdez Group and Orca Group (Fig. 5A). UI18-02A has an MDA of ~59 Ma while UI18-04, UI18-06, and UI18-19 yielded Late Cretaceous MDA's of ~68 Ma (Fig. 3). Results of the K-S test indicate that UI18-06 and UI18-19 were drawn from the same population. Examination of the PDF's of these three samples indicates that UI18-04 has a smaller proportion of Late Cretaceous grains than UI18-06 and UI18-19, which may have affected the results of the K-S test (Fig. 5A).

The location of the Contact fault in western Prince William Sound has been difficult to define due to similarities in appearance and structure of the Valdez and Orca Groups (Tysdale and Case, 1979; Dumoulin, 1988; Bol and Gibbons, 1992). U-Pb results from 11HW-22 and 11HW-23 collected on either side of the Culcross fault are somewhat ambiguous (Fig. 3). The MDAs are similar and fall near the K-Pg boundary, the traditional age break between the Valdez and Orca Groups (c.f. Davidson and Garver, 2017). The Phanerozoic grain age distribution of the two samples are strikingly similar (Fig. 5B), but they fail the K-S test, perhaps because of the difference in the sample size (n) between the two samples (Gehrels, 2012).

CONCLUSIONS

The Eaglek fault in northern Prince William Sound is the only strand of the Contact fault that may be a terrane boundary between the Valdez and Orca Groups. Our results show that the Jack Bay a fault in the Valdez Arm area is definitely not a terrane bounding fault and the Culcross strand in Kings Bay in Western PWS is ambiguous, and appears to separate rocks with similar MDA's and grain-age distributions. Our preferred interpretation is that the turbidites of the Chugach terrane (Valdez Group) and turbidites of Prince William terrane (Orca Group) should be considered together, and were deposited, accreted to the continental margin, and deformed over a protracted period of time from the Late Cretaceous to Early Eocene.

ACKNOWLEDGMENTS

This material is based upon work supported by the Keck Geology Consortium and the National Science Foundation. Field work and analyses were funded by NSF Grant "Collaborative Research: RUI: Translation and accretion of the Yakutat microplate and Prince William terrane, Alaska", NSF EAR 1727991. Additional funding was from Keck Geology Consortium NSF Grant No. 1659322, "Geology of the Chugach-Prince William terrane in northern Prince William Sound, Alaska." U-Pb data were collected at the Arizona LaserChron Center, the NSF multi-user facility run by Mark Pecha and George Gehrels at the University of Arizona funded by NSF-EAR Grant No. 1649254. Special thanks to project advisors Dr. Cameron Davidson and Dr. John Garver, and team members Nick Gross-Almonte, Mollie Pope, Victor Garcia, Caitlin Noseworthy, and Will Fisher.

REFERENCES

- Arkle, J. C.; Armstrong, P. A.; Haeussler, P. J.; Prior, M. G.; Hartman, S.; Sendziak, K. L.; and Brush, J. A. 2013. Focused exhumation in the syntaxis of the western Chugach Mountains and Prince William Sound, Alaska. *Geol. Soc. Am. Bull.* 125:776–793. doi:10.1130/B30738.1.
- Bol, A. J., and Gibbons, H. 1992. Tectonic implications of out-of-sequence faults in an accretionary prism, Prince William Sound, Alaska. *Tectonics* 11:1288–1300. doi: 10.1029/92TC01327.
- Bol, A. J., and Roeske, S. M. 1993. Strike-slip faulting and block rotation along the contact fault system, eastern Prince William Sound, Alaska. *Tectonics* 12:49–62. doi: 10.1029/92TC01324.
- Bradley, D. C.; Kusky, T. M.; Haeussler, P. J.; Goldfarb, R. J.; Miller, M. L.; Dumoulin, J. A.; Nelson, S. S.; and Karl, S. M. 2003. Geologic signature of early Tertiary ridge subduction in Alaska. In *Sisson, V. B.; Roeske, S.; and Pavlis, T. L., eds. Geology of a transpressional orogen developed during ridge-trench interaction along the North Pacific margin.* *Geol. Soc. Am. Spec. Pap.* 371:19–49.
- Bradley, D.C., and Miller, M.L., 2006, Field guide to south-central Alaska's accretionary complex, Anchorage to Seward: Anchorage, Alaska Geological Society, 32 p.
- Davidson, Cameron, and John I. Garver. "Age and Origin of the Resurrection Ophiolite and Associated Turbidites of the Chugach–Prince William Terrane, Kenai Peninsula, Alaska." *The Journal of Geology* 125.6 (2017): 681-700. Web.
- Dumoulin, J. A., Sandstone petrographic evidence and the Chugach-Prince William terrane boundary in southern Alaska, *Geology*, 16, 456- 460, 1988
- Fisher, W.S., Pope, M.D., Malik, A.M., Garver, J.I., and Davidson, C.M., 2019. Zircon facies in the Paleocene-Eocene Orca Group indicate a provenance link to the Chugach terrane, Prince William Sound, Alaska. *Geological Society of America Abstracts with Program, Cordilleran Section - 115th Annual Meeting, Portland Oregon.* v. 51, n. 4. doi: 10.1130/abs/2019CD-329384
- Garcia, Jr., V.R., Stockli, D.F., Davidson, C. and Garver, J.I. 2019. Crystallization ages and geochemistry of the Miner's Bay and Cedar Bay plutons, Prince William Sound, Alaska: *Geological Society of America Abstracts with programs*, v. 51, Portland, OR.
- Garver, J.I., and Davidson, C. 2015. Tectonic evolution of the Prince William terrane in Resurrection Bay and eastern Prince William Sound, Alaska: *Short Contributions, Keck Geology Consortium 28th Annual Symposium Volume, Union College, NY.*
- Gehrels, G., 2012, Detrital Zircon U-Pb Geochronology: Current Methods and New Opportunities, in *Tectonics of Sedimentary Basins: Recent Advances*, C. Busby and A. Azor, editors, Wiley-Blackwell Publishing, p. 47-62.
- Grimm, William. 2015, A tectonic and provenance study of the Chugach-Prince William terrane, Alaska, with specific focus on the Paleogene Orca Group, using U-Pb dating of detrital zircons, Senior Integrative Exercise, Carleton College, MN.
- Gross Almonte, N., Fisher, W.S., Malik, A.M., Garver, J.I., and Davidson, C.M. 2019. Age and provenance of the Upper Cretaceous to Paleocene Valdez Group of the Chugach terrane from the Richardson Highway and northern Prince William Sound, Alaska. *Geological Society of America Abstracts with Program, Cordilleran Section - 115th Annual Meeting, Portland Oregon.* v. 51, n. 4. doi: 10.1130/abs/2019CD-329673.
- Hudson, T.; Plafker, G.; and Peterman, Z. E. 1979. Paleogene anatexis along the Gulf of Alaska margin. *Geology* 7:573–577.
- Jones, D. L.; Silberling, N. J.; Berg, H. C.; and Plafker, G. 1981. Map showing tectonostratigraphic

- terrane of Alaska, columnar sections, and summary description of terranes. U.S. Geol. Surv. Open-File Rep. 81-792, 2 sheets, 20 p., scale 1:2,500,000.
- Moffit, F. H., 1954, Geology of the Prince William Sound region, Alaska: U.S. Geol. Survey Bull. 989-E, p. 225-310.
- Nelson, S.W., Dumoulin, J.A., and Miller, M.L., 1985, Geologic map of the Chugach National Forest, Alaska: U.S. Geological Survey Miscellaneous Field Studies Map MF1645-B, 16 p., 1 Pl., scale 1:250,000.
- Nokleberg, W. J., G. Plafker, and S. M. Roeske, Structural analysis and accretionary tectonics of Cretaceous and early Tertiary flysch sequences juxtaposed along the Contact Fault, eastern Chugach Mountains, Alaska, Geol. Soc. Am. Abstr. Programs, 18, 164, 1986
- Plafker, G.; Moore, J. C.; and Winkler, G. R. 1994. Geology of the southern Alaska margin. In Plafker, G., and Berg, H. C., eds. The geology of Alaska. Boulder, CO, Geological Society of America, p. 389–449.
- Plafker, G.; Jones, D. L.; and Pessagno, E. A., Jr. 1977. A Cretaceous accretionary flysch and mélangé terrane along the Gulf of Alaska margin. In Blean, K. M., ed. The U.S. Geological Survey in Alaska: accomplishments during 1976. U.S. Geol. Surv. Circ. 751B:B41–B43.
- Roeske, S. M.; Snee, L. W.; and Pavlis, T. L. 2003. Dextral slip reactivation of an arc-forearc boundary during Late Cretaceous-early Eocene oblique convergence in the northern Cordillera. In Sisson, V. B.; Roeske, S.; and Pavlis, T. L., eds. Geology of a transpressional orogen developed during ridge-trench interaction along the North Pacific margin. Geol. Soc. Am. Spec. Pap. 371: 141–169.
- Tysdal, R. G., and Case, J. E. 1979. Geologic map of the Seward and Blying Sound quadrangles, Alaska. Reston, VA, U.S. Geological Survey, 12 p., 1 sheet, scale 1:250,000.
- Winkler, G. R., and Plafker, G. 1975. The Landlock fault: part of a major early Tertiary plate boundary in southern Alaska. In Yount, M. E., ed. U.S. Geological Survey Alaska program, 1975. U.S. Geol. Surv. Circ. 722:49.

AGE AND TECTONIC SETTING OF THE PALEOCENE GLACIER ISLAND VOLCANIC SEQUENCE OF THE ORCA GROUP IN PRINCE WILLIAM SOUND, ALASKA

CAITLIN NOSEWORTHY, Saint Norbert College
Research Advisor: Tim Flood

INTRODUCTION

Southern Alaska has a long history of subduction, accretion, and coastwise transport of terranes (Coney et al., 1980; Monger et al., 1982; Plafker et al., 1994). The Chugach-Prince William (CPW) terrane is about 2200 km long and extends through much of southern Alaska (Plafker et al., 1994) (Fig. 1A). The inboard Chugach terrane can be divided into two parts, a *mélange* and sedimentary units that are Permian to Early Cretaceous in age and a turbidite sequence that is from the Upper Cretaceous (Plafker et al., 1994). In the Prince William Sound area, the outboard Prince William terrane is comprised of Paleocene to Eocene turbidites and associated basaltic rocks of the Orca Group (Davidson and Garver, 2017), and the turbidites of the inboard Chugach terrane are known as the Valdez Group. The turbidites are intruded by the Sanak-Baranof Belt (SBB), a group of 63-47 Ma plutons that are progressively younger to the east. The Border Ranges fault system marks the northern boundary of the CPW terrane, separating the Chugach terrane from the Wrangellia composite terrane and the Contact fault separates the Chugach and Prince William terrane (Fig. 1; Plafker et al., 1994).

There are three ophiolite sequences in the Orca Group: Knight Island (KI), Resurrection Peninsula (RP), and Glacier Island (GI) (Fig. 1B). The KI ophiolite contains a sequence of massive pillow basalts, sheeted dikes, and a minor amount of ultramafic rocks (Tysdal et al., 1977; Nelson and Nelson, 1992; Crowe et al., 1992). The RP ophiolite is a typical ophiolite sequence and has interbedded Paleocene turbidites (Davidson and Garver, 2017). Paleomagnetic data gathered from the RP ophiolite indicated a mean depositional

paleolatitude of $54^{\circ} \pm 7^{\circ}$ which implies $13^{\circ} \pm 9^{\circ}$ of poleward displacement (Bol et al., 1992). These data suggest that the RP ophiolite was translated northward to its current position after being formed in the Pacific Northwest, and thus the CPW terrane may have been originally located at $48-49^{\circ}$ north and at 50 Ma was transferred 1100 km to the north by strike-slip faulting (Cowan, 2003). However, an opposing hypothesis suggests that the terrane has not experienced significant displacement and formed in Alaska due to a now-subducted Resurrection plate (Haeussler et al., 2003).

KI and RP ophiolites have traditionally been assumed to be oceanic crust that was tectonically emplaced into the CPW terrane (Bol et al., 1992; Lytwyn et al., 1997). However, a more recent study suggests a hypothesis that the ophiolites originated in an upper plate setting and formed due to transtension (Davidson and Garver, 2017). Previous workers have used discriminant diagrams to identify the volcanic rocks of KI ophiolite and RP ophiolite as mid-ocean ridge basalts (Lytwyn et al., 1997; Miner, 2012). This project presents new geochemical and geochronological data from the GI ophiolite to determine its age and tectonic setting. The purpose of this study is to compare the data from GI with the data from KI and RP, and the comparison of the geochemical data will allow for a greater understanding of the tectonic setting of southern Alaska.

GEOLOGIC SETTING AND OUTCROP DESCRIPTION

The Orca Group is composed of turbidites that are

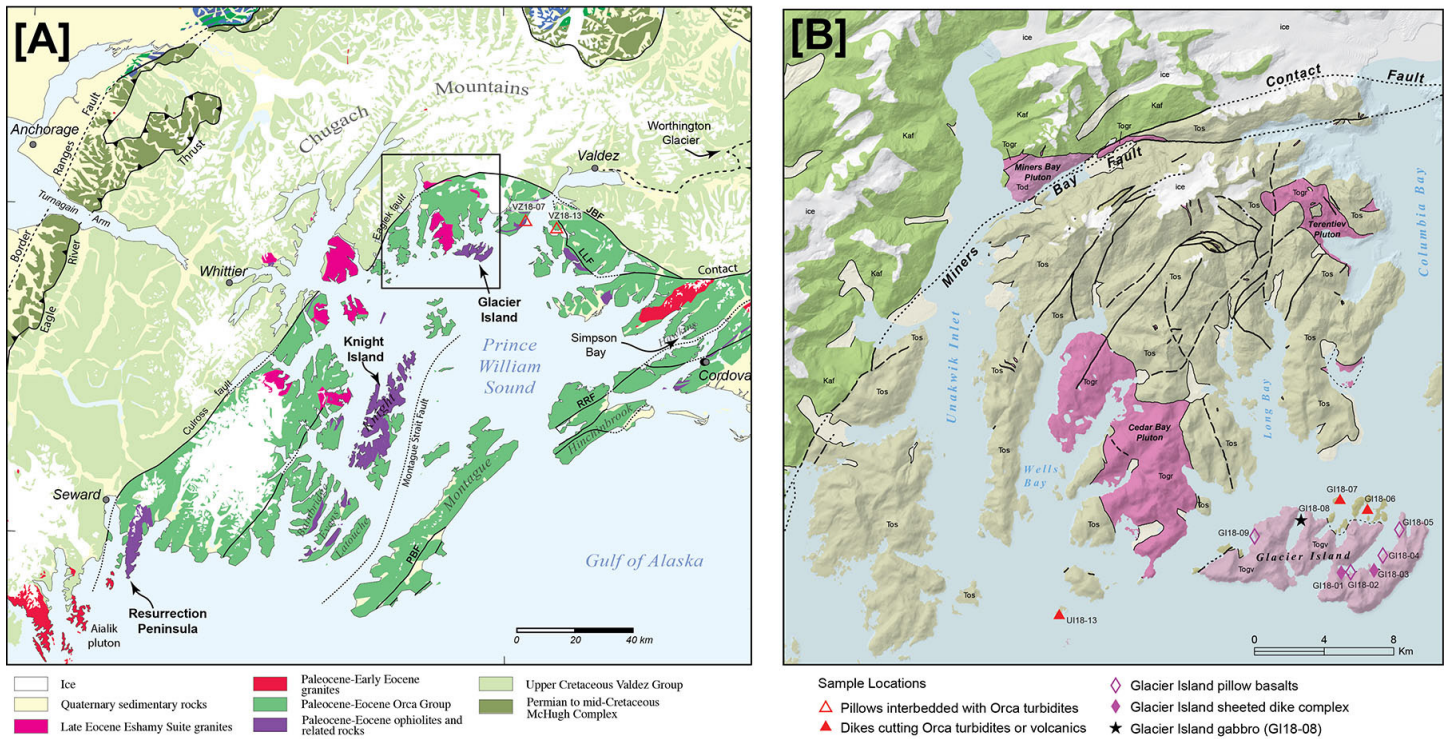


Figure 1: A) Geologic map of the CPW terrane (modified from Bradley et al., 2003). Box shows approximate location of Fig. 1B. B) Geologic Map of Glacier Island and Unakwik Inlet (modified from Wilson et al., 2015).

interbedded with pillow basalt and sheet flows, and is intruded by mafic dikes. The group is Paleocene to Eocene in age and is primarily exposed in Prince William Sound (Wilson and Hults, 2012). The Orca Group is also intruded by the SBB plutons and the Eshamy Suite plutons (Fig. 1). The Orca Group is variably metamorphosed from laumontite to lower-greenschist facies with metamorphic grade increasing to the north and northwest (Wilson and Hults, 2012).

The GI sequence in northern Prince William Sound is a volcanic sequence that has been described as an ophiolite (Nelson et al., 1999, Crowe et al. 1992; Bradley et al., 2003). The sequence contains volcanoclastic rocks, pillow basalts with some minor massive basalt flows, and sheeted dikes (Wilson and Hults, 2012). Geologic maps of GI indicate the majority of the island is composed of pillow basalts, but the southern part of the island has a sheeted dike complex (Wilson and Hults, 2012).

The sheeted dikes on Glacier Island range from 10 cm to 1.5 m thick (Fig. 2A) and many of the dikes have visible chill margins. One dike, sample G118-07B, intrudes a sandstone unit (Fig. 2C), that allows

the age of the dike to be constrained by dating zircons in the sandstone (see below). Some of the dikes and pillows have large (~4 mm) phenocrysts of plagioclase and all of the dikes have some amount of fracturing. The pillow basalts on Glacier Island have pillows that range in size from 0.25 m to 1.0 m in diameter (Fig. 2B) and some of the pillows have large vesicles. Some of the pillow basalts are also brecciated and disorganized likely due to the magma instantly hitting the water.

ANALYTICAL METHODS

Fourteen samples from Glacier Island and three samples of mafic volcanic rocks interbedded with or intruding turbidites of the Orca Group were collected for geochemical analysis (Fig. 1). The samples were sent to Hamilton College where major element geochemical data were determined using XRF. The glass beads were mounted and polished, and were then sent to Rensselaer Polytechnic Institute for trace element data collected using LA-ICP-MS. Zircons extracted from a sandstone sample from Glacier Island intruded by a mafic dike were analyzed for U/Pb at the Laserchron Lab at the University of Arizona.

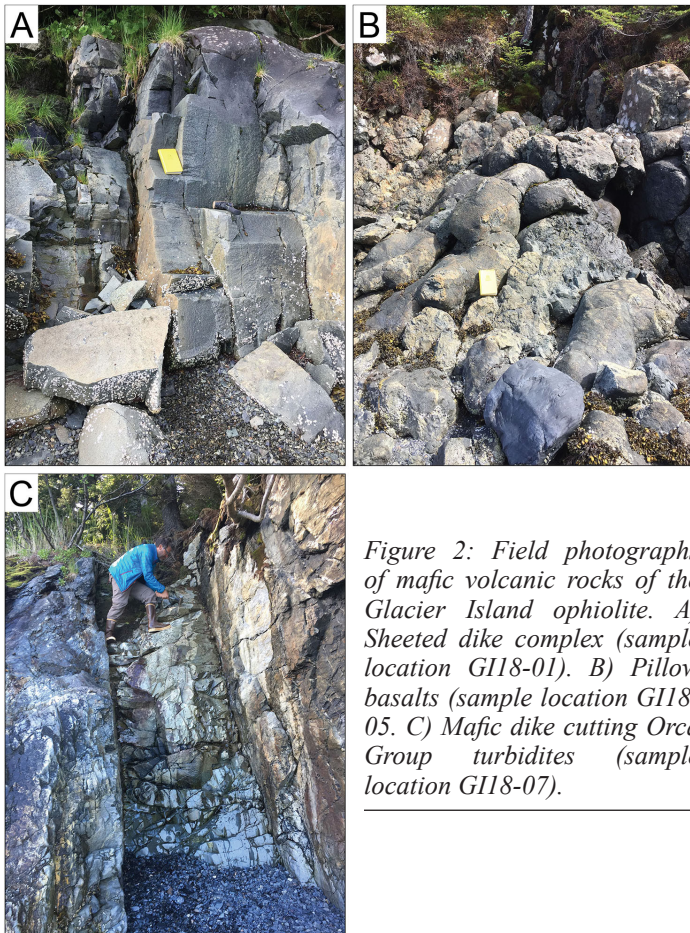


Figure 2: Field photographs of mafic volcanic rocks of the Glacier Island ophiolite. A) Sheeted dike complex (sample location GI18-01). B) Pillow basalts (sample location GI18-05). C) Mafic dike cutting Orca Group turbidites (sample location GI18-07).

U/PB RESULTS

The maximum depositional age (MDA) of the sandstone sample (GI18-07A) is 56.8 ± 0.6 Ma. This number was determined using U/Pb analysis of 110 zircon grains and calculating the weighted mean of the three youngest zircon grains (Davidson and Garver, 2017). GI18-07A is cut by a mafic dike assumed to be related to the GI volcanics. The dike intruding the sandstone suggests that volcanism and deposition of the turbidites in the Orca Group occurred together. MDA's of the surrounding Orca Group turbidites have a similar age to GI-07A (Malik et al., this issue; Fisher et al., 2019). The MDA indicates that the dike that intruded the area of the detrital sample must be younger than (or equal to) 56.8 ± 0.6 Ma. These data suggest that the GI, RP, and KI ophiolites are the same age (cf. Davidson and Garver, 2017).

GEOCHEMICAL RESULTS

All of the mafic volcanic rocks from Glacier Island

and northern Prince William Sound from this study plot as basalts and basaltic andesites (Fig. 3A) and are tholeiitic (Fig. 3B). Basalts with a tholeiitic composition are consistent with a mid-ocean ridge origin. On various discrimination diagrams, the GI rocks plot as ocean floor basalts and appear to be most closely aligned with N-MORB (Fig. 4).

Figure 5 shows the rare earth element (REE) abundances from this study and the KI and RP ophiolites. Overall, the majority of the samples from this study have a fairly flat REE pattern indicative of a depleted mantle source, with some samples from Glacier Island showing depletion in the LREE's typical of N-MORB.

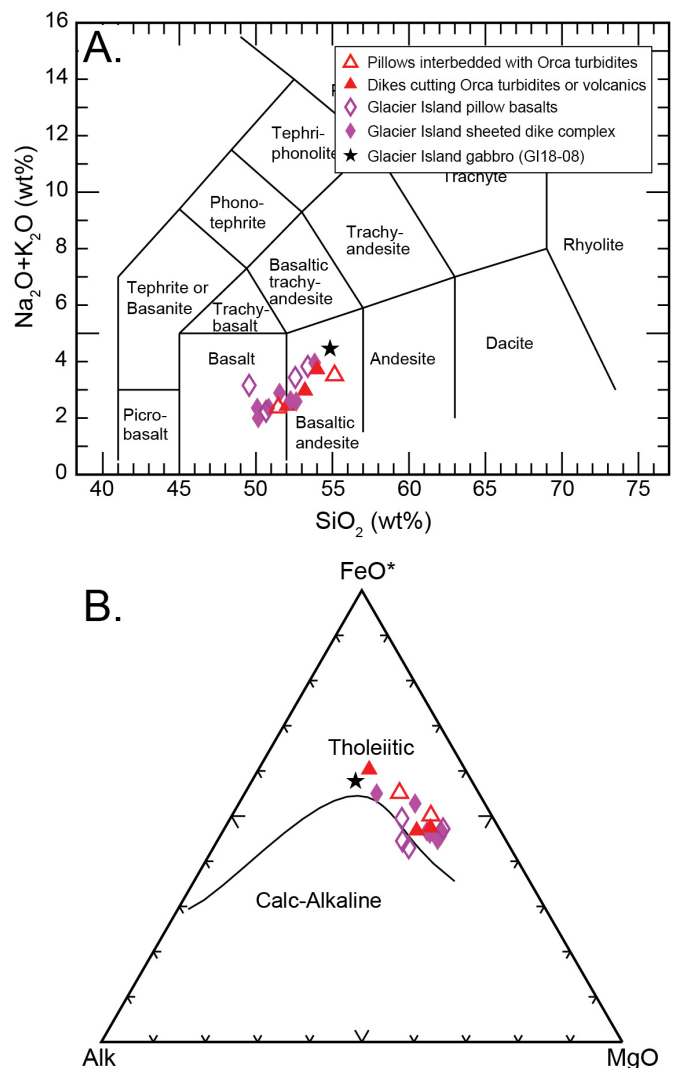


Figure 3: Rock classification diagrams for the Glacier Island ophiolite. A) TAS Diagram (LeBas et al., 1986). B) AFM Diagram (Irvine and Baragar, 1971). Symbols are the same as those shown in Figure 1.

Thin sections of the four pillow basalt samples from GI are mostly fine-grained and dominated by altered pyroxene and plagioclase. The plagioclase phenocrysts tend to be euhedral and elongated. Three of the thin sections contain amygdules. Overall, significant alteration of the groundmass is noted. This alteration is likely due to the fact that the pillows came in contact with seawater. The alteration seen in thin section is an alternative explanation for the depletion in the LREEs seen in some samples (Fig. 5).

Thin sections for the nine dikes range from fine-grained equigranular to coarse-grained porphyritic and are dominated by plagioclase and pyroxenes. The majority of the plagioclase grains are elongated and euhedral. Plagioclase grains exhibit slight to moderate dusty alteration. Pyroxenes are subhedral to anhedral. The pyroxenes range from unaltered to moderately

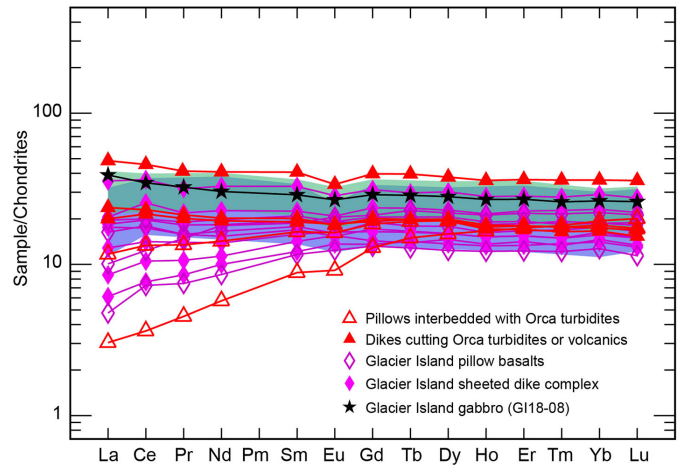


Figure 5: Rare earth element abundances for the Glacier Island, Knight Island, and Resurrection ophiolites normalized to chondrites after Sun and McDonough (1989). Symbols and shaded regions are the same as those shown in Figures 1 & 4.

altered. Variable amounts of opaque minerals are present in each of the thin sections.

DISCUSSION

The detrital zircon results from Glacier Island indicate that the GI ophiolite is ~57 Ma (or younger), and therefore approximately the same age as the RP ophiolite (Bradley, et al., 2003; Davidson and Garver, 2017). The RP ophiolite was directly dated at 57 ± 1 Ma by Nelson et al. (1989) using a plagiogranite assumed to be genetically related to the ophiolite, and Davidson and Garver (2017) dated a sandstone unit interbedded with pillow basalts at the top of the ophiolite that yielded an MDA of 57 Ma. The KI ophiolite has not been dated but it is inferred that the ophiolite is the same age as the RP and GI ophiolites because all three are interbedded with the Orca Group turbidites, occur along a strike in the same belt, and are composed of similar rock types (Figs. 4&5; Bradley, et al., 2003; Davidson and Garver, 2017).

Geochemical data show that the three ophiolites likely originated from the same source. Most of the KI volcanic rock samples are tholeiitic basalts (Lytwyn et al., 1997; Miner, 2012) and the mafic volcanic rocks from GI are also tholeiitic basalts (Fig. 3B). Major and trace element geochemistry from GI are similar to KI and RP basalts and suggest that the rocks originated from a complicated ridge setting (Lytwyn et al., 1997; Miner, 2012) where melts from a spreading

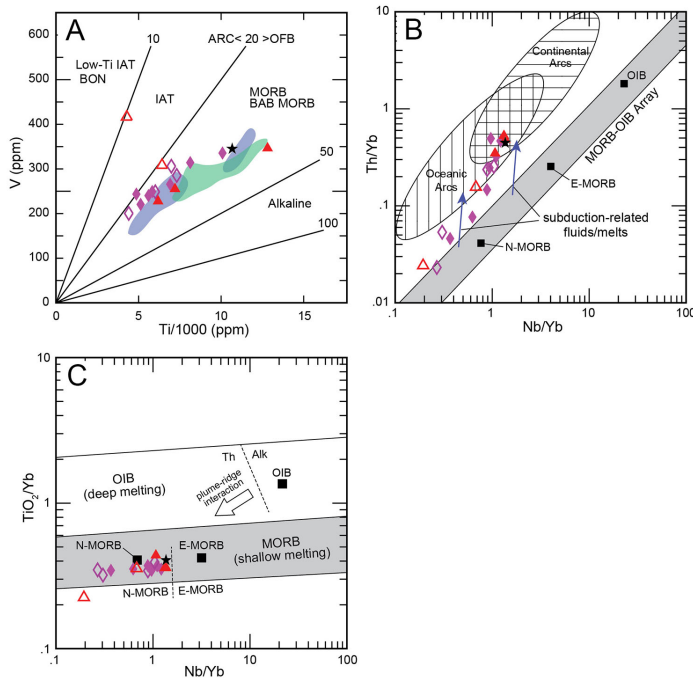


Figure 4: Discrimination diagrams for the Glacier Island ophiolite. Symbols are the same as those shown in Figure 1. A) Ti-V after Shervais (1982). Data from Lytwyn et al. (1997) shown as fields for the Resurrection ophiolite (green) and Knight Island ophiolite (blue). B) Th-Nb proxy from Pearce (2008). N-MORB, E-MORB, and OIB compositions from Sun and McDonough (1989). Blue arrows show the direction MORB compositions change when mixing with melts derived from a mantle wedge infiltrated by subduction-related fluids and melts. C) Ti-Nb proxy from Pearce (2008) that shows the depth/temperature dependence of mantle melts. The data from Glacier Island suggest shallow melting of an N-MORB source.

center (N-MORB) were mixing with melts derived from a mantle wedge that was previously altered by subduction-related fluids or melts (Fig. 4B). REE patterns are also similar between the three ophiolites (Fig. 5); however, the samples in this study were more depleted in LREEs than RP and KI, similar to N-MORB or possibly due to mobilization of the LREE during low-grade metamorphism and/or seafloor alteration.

CONCLUSION

Based on geochemical data and detrital zircon ages, the Glacier Island, Resurrection Peninsula, and Knight Island ophiolite sequences originated from the same depleted mantle source and within a short period time at ~57 Ma. The RP ophiolite has been shown to have translated northward by $13^{\circ} \pm 9^{\circ}$ since it formed (Bol et al., 1992). These data suggest that the RP ophiolite, and therefore the GI and KI ophiolites and associated Orca Group turbidites in Prince William Sound were translated northward to their current position after being formed in the Pacific Northwest at 57 Ma.

ACKNOWLEDGEMENTS

This material is based upon work supported by the Keck Geology Consortium and the National Science Foundation under Grant No. 1659322. This project is a part of a larger Keck Consortium project led by Cameron Davidson (Carleton College) and John Garver (Union College). Funding for this project is provided by NSF EAR 1728013 (Garver) and NSF EAR 1727991 (Davidson). XRF data were collected at Hamilton College, LA-ICPMS data were collected at Rensselaer Polytechnic Institute. and U/Pb data were collected at the University of Arizona Laserchron Center (NSF-EAR 1649254). Thank you to Tim Flood, Rebecca McKean, and Nelson Ham for being wonderful and supportive advisors throughout the last three years. A big thank you to John Garver and Cameron Davidson for their leadership. Lastly, I want to thank the 2018 Keck Alaska team for all of their hard work and dedication: Will Fisher, Victor Garcia, Nicholas Gross Almonte, Alysala Malik, and Mollie Pope.

REFERENCES

- Bol, A., and Coe, R., 1992, Paleomagnetism of the RP, Alaska: Implications for the Tectonics of Southern Alaska and the Kula-Farallon Ridge, *Journal of Geophysical Research*, Vol. 97, No. B12, p.17,213-17,232.
- Bradley, D.C., Kusky, T.M., Haeussler, P.J., Goldfarb, R.J., Miller, M.L., Dumoulin, J.A., Nelson, S.W. & Karl, S.M. 2003, Geologic signature of early Tertiary ridge subduction in Alaska; Geology of a transpressional orogen developed during ridge-trench interaction along the North Pacific margin, *Special Paper -Geological Society of America*, vol. 371, p. 19-49.
- Coney, P. J., Jones, D. L., and Monger, J.W.H., 1980, Cordilleran suspect terranes: *Nature*, V. 288, p. 329-333.
- Cowan, D.S., 2003, Revisiting the Baranof-Leech River hypothesis for early Tertiary coastwise transport of the Chugach-Prince William terrane. *Earth and Planetary Science Letters*, v. 213, 463- 475.
- Crowe, D.E., Nelson, S.W., Brown, P.E., Shanks, W.C., III, and Valley, J.W., 1992, Geology and geochemistry of volcanogenic massive sulfide deposits and related igneous rocks, Prince William Sound, southern Alaska: *Economic Geology*, v. 87, p. 1722-1746.
- Davidson, C. and Garver, J.I., 2017, Age and Origin of the Resurrection Ophiolite and Associated Turbidites of the Chugach–Prince William Terrane, Kenai Peninsula, Alaska. *The Journal of Geology*, 125(6), p.681-700.
- Fisher, W.S., Pope, M.D., Malik, A.M., Garver, J.I., and Davidson, C.M., 2019. Zircon facies in the Paleocene-Eocene Orca Group indicate a provenance link to the Chugach terrane, Prince William Sound, Alaska. *Geological Society of America Abstracts with Program, Cordilleran Section - 115th Annual Meeting, Portland Oregon*. v. 51, n. 4. Doi: 10.1130/abs/2019CD-329384
- Haeussler, P.J., Bradley, D.C., Wells, R.E. and Miller,

- M.L., 2003. Life and death of the Resurrection plate: Evidence for its existence and subduction in the northeastern Pacific in Paleocene–Eocene time. *Geological Society of America Bulletin*, 115(7), pp.867-880.
- Irvine, T.N., and Baragar, W.R.A., 1971, A guide to the chemical classification of the common volcanic rocks. *Can. J. Earth Sci.*, v. 8, p.523-548.
- LeBas, M.J., LeMaitre, R.W., Streckeisen, A., and Zanettin, B., 1986. A chemical classification of volcanic rocks based on the total alkali silica diagram. *J. Pet.* 27:745-750.
- Lytwyn, J., Casey, J., Gilbert, S., and Kusky, T., 1997, Arc-like mid-ocean ridge basalt formed seaward of a trench-forearc system just prior to ridge subduction: An example from subaccreted ophiolites in southern Alaska: *Journal of Geophysical Research*, v. 102, no. B5, p. 10225-10243.
- Malik, A.M., Fisher, W.S., Gross Almonte, N., Garver, J.I., Davidson, C.M., 2019. U-Pb dating of detrital zircon from turbidites of the Chugach and Prince William terrane in Prince William Sound, Alaska: Implications of the significance of the Contact fault system as a terrane boundary. *Geological Society of America Abstracts with Program, Cordilleran Section - 115th Annual Meeting, Portland Oregon*. v. 51, n.4. Doi: 10.1130/abs/2019CD-329396.
- Miner, L., 2012, Geochemistry of the KI Ophiolite and Chenega Island Volcanics, Prince William Sound, Alaska. *Proceedings of the Twenty-Fifth Annual Keck Research Symposium in Geology*, p. 40-47.
- Monger, J.W.H., Price, R. A., and Tempelman-Kluit, D. J., 1982, Tectonic accretion and the Origin of the Two Major Metamorphic and Plutonic Welts in the Canadian Cordillera: *Geology*, v. 10, p. 70-75.
- Nelson, S.W., Miller, M.L., and Dumoulin, J.A., 1989, The Resurrection Peninsula ophiolite, in Nelson, S.W., and Hamilton, T.D., eds., *Guide to the geology of the Resurrection Bay-Eastern Kenai Fjords area: Anchorage, Geological Society of Alaska, Guidebook*, p. 10-20.
- Nelson, S.W., Miller, M.L., Haeussler, P.J., Snee, L.W., Phillips, P.J., and Huber, C., 1999, Preliminary Geologic Map of the Chugach National Forest Special Study Area, Alaska: U.S. Geological Survey and U.S. Forest Service.
- Nelson, S.W., and Nelson, M.S., 1992, Geochemistry of ophiolitic rocks from Knight Island, Prince William Sound, Alaska: U.S. Geological Survey Bulletin 2068, p.130-142.
- Pearce, J.A., 2008. Geochemical fingerprinting of oceanic basalts with applications to ophiolite classification and the search for Archean oceanic crust. *Lithos* 100: 14-48.
- Plafker, G., Moore, J.C. & Winkler, G.R., 1994, Geology of the Southern Alaska margin in *The geology of Alaska*, eds. G. Plafker & H.C. Berg, Geological Society of America, Boulder, CO, v. G-1, p. 389–449.
- Shervais, J.W., 1982, Ti-V plots and the petrogenesis of modern and ophiolitic lavas, *Earth and Planetary Science Letters*, 59 (1), p. 101-118.
- Sun, S. S. and McDonough, W. F., 1989, Chemical and isotopic systematics of oceanic basalts; implications for mantle composition and processes (in *Magmatism in the ocean basins*), Geological Society Special Publications, vol. 42 p. 313-345.
- Tysdal, R. G.; Case, J. E.; Winkler, G. R.; and Clark, S. H. B. 1977. Sheeted dikes, gabbro, and pillow basalt in flysch of coastal southern Alaska. *Geology* 5:377–383.
- Wilson, F.H. and Hults, C.P., 2012. Geology of the Prince William Sound and Kenai Peninsula region, Alaska. *US Geol. Surv. Sci. Invest. Map*, 3110, p.37.
- Wilson, F.H., Hults, C.P., Mull, C.G, and Karl, S.M, comps., 2015, Geologic map of Alaska: U.S. Geological Survey Scientific Investigations Map 3340, pamphlet 196 p., 2 sheets, scale 1:1,584,000, <http://dx.doi.org/10.3133/sim3340>.

PROVENANCE OF SANDSTONE CLASTS FROM CONGLOMERATE OF THE PALEOCENE-EOCENE ORCA GROUP IN PRINCE WILLIAM SOUND, ALASKA

MOLLIE D. POPE, Union College

Research Advisors: John Garver, Cameron Davidson

INTRODUCTION

The thick flysch facies of the Cretaceous to Eocene Chugach-Prince William terrane (CPW) represents a thick accretionary complex that extends approximately 2200 km across southern Alaska, and in the central area is comprised mainly of the Valdez Group and the Orca Group (Fig. 1) (Garver and Davidson, 2015; Davidson and Garver, 2017). The Valdez Group is traditionally viewed as a Campanian to Maastrichtian turbidite deposit with mafic volcanic rocks that have experienced lower greenschist facies metamorphism (Dusel-Bacon, 1991; Gasser et al., 2012). The Orca Group is Paleocene to Eocene turbidite and volcanic deposit that, in most places, has undergone prehnite-pumpellyite facies metamorphism (Dusel-Bacon, 1991; Wilson et al., 2012).

The relationship between the Valdez Group and the Orca Group is poorly understood (Moffit, 1954). A common hypothesis suggested long ago is that they are stratigraphically related and are a continuous sequence (Capps and Johnson, 1915). Given recent zircon dating, the Valdez Group appears to have maximum depositional ages (MDA) of 75-65 Ma and the deposition of the Orca Group is between 60-50 Ma (Davidson and Garver, 2017). In this case, deformation of the Valdez Group may have occurred 65-60 Ma, just before the deposition of the oldest Orca Group turbidites began. Thus, the youngest strata of the Valdez Group must be older than the oldest strata of the Orca Group. An alternative hypothesis is that the Orca Group formed in a different location and was translated to its current position along strike slip faults after the deformation of the Valdez Group (cf. Plafker et al., 1994). This idea would mean that the

ages of the two groups may overlap in age, and the time of juxtaposition of the Orca Group to the Valdez Group is unknown but important. After the deposition of the bulk of the Orca Group was completed, the CPW experienced plutonism by the near-trench Sanak-Baranof Belt (SBB) and the Eshmay plutons (Cowan, 2003; Davidson and Garver, 2017).

If a pluton crosscuts two terranes then the age of that pluton is the minimum age that the two terranes were juxtaposed (Coney et al., 1980). The SBB plutons intruded the CPW from 63-47 Ma, with a distinct age progression from 63 Ma to the west to 50-47 Ma to the east (Davidson and Garver, 2017). In Prince William Sound the CPW terrane is also intruded by the Eshmay Suite Plutons (ESP) around 37-41 Ma (Fig. 1) (Johnson, 2012; Davidson and Garver, 2012; Garcia et al., 2019). The Eshmay suite plutons could be explained by high heat flow that melted Orca Group sediments and these melts then mixed in with mantle-derived basalts (Johnson, 2012). The ESP stitch the two terranes, as they occur on both sides of the Contact Fault System (Fig. 1) (Davidson and Garver, 2017).

A key link between the Orca and Valdez Groups may be conglomerates that occur in the Orca Group. There are five main localities of conglomerates in PWS, and some of the most significant exposures are in eastern and northern PWS. These conglomerates were described by Grant and Higgins (1910) as being near the bottom of the Orca Group stratigraphy, specifically at the basal unconformity. However, Capps and Johnson (1915) described the conglomerates as being at the top of the Orca Group, occurring after and interleaved with basaltic volcanic rocks (cf. Tysdal and

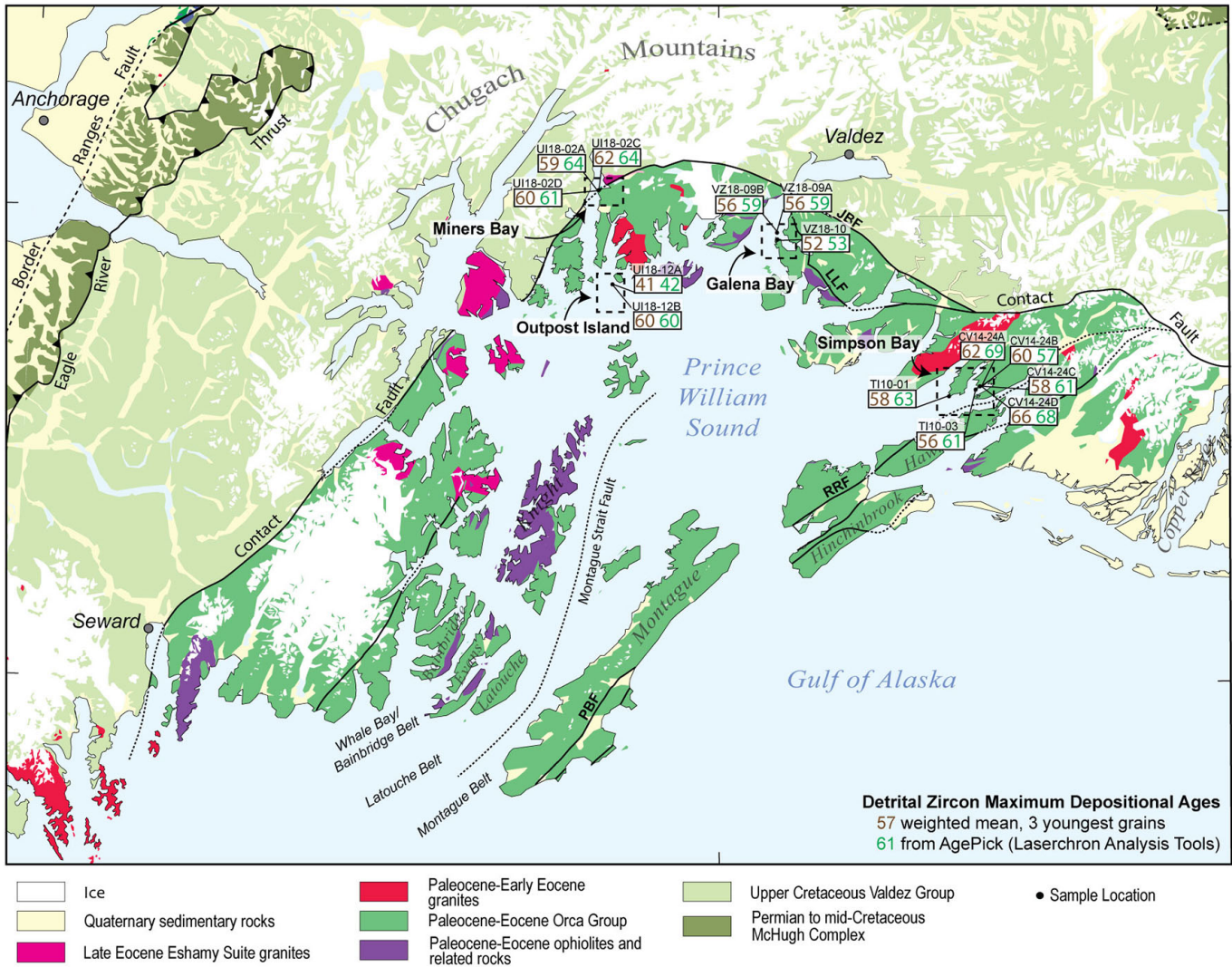


Figure 1. Map of study region in Prince William Sound. On this map the age of the the Sanak Baranof Belt and Eshamy Suite Plutons are indicated in red. Conglomerate matrix and clasts MDAs are all labeled at their sample site. The MDAs used in this paper are in brown, determined through the weighted mean on the youngest three grains (modified from Davidson and Garver 2017).

Case, 1979). If the Valdez Group is the source of the Orca Group conglomerate clasts, then the two terranes were adjacent at a time earlier than previously known (38-39 Ma) (Davidson and Garver, 2017).

Capps and Johnson (1915) proposed that the matrix of the conglomerates and the majority of the clasts were derived from the Valdez Group. They also suggest that a few clasts could be derived from the greenstones of the Orca Group. The provenance of the Orca Group conglomerates is important in our understanding of the relationship between the Valdez and Orca Groups as well as our overall understanding of the Cordilleran tectonics. This study will focus on understanding the Valdez Group and the Orca Group through the study of detrital zircons from sandstone clasts from the Orca Group Conglomerates and the host strata to those

conglomerates.

GEOLOGIC SETTING

In the PWS area, the Valdez Group, which makes up about 90% of the Chugach terrane, is generally viewed as being Campanian-Maastrichtian (75-65 Ma), deformed, metasedimentary graywacke, siltstone, and shale interbedded with meta-volcanic tholeiitic basalts and meta-intrusive rocks, that have undergone greenschist grade metamorphism (Dusel-Bacon, 1991; Plafker et al., 1994; Wilson and Hults, 2012). The Valdez Group is correlative with the Shumagin and Kodiak formations to the west, and parts of the Sitka Graywacke to the east, and together they extend for 2000 km along southern Alaska (Wilson and Hults, 2012). The Eagle River thrust bounds the flysch of the

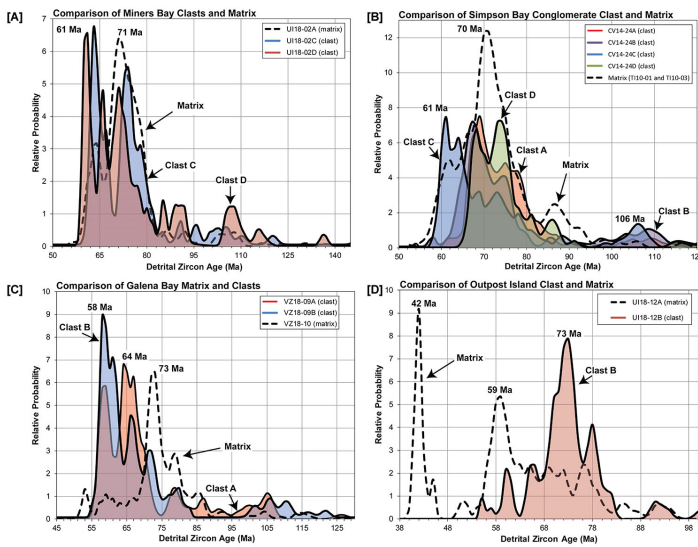


Figure 2. The probability density function (PDF) for each sample taken at the four conglomerate locations. [A] Probability density plot of Miners Bay conglomerate. The matrix UI18-02A (black dashed line) has a major population at 71 Ma, the clast UI18-02C (blue) has a major population at 63 Ma, and the clast UI18-02D (green) has a major population at 61 Ma. [B] PDF plot of the Simpson Bay conglomerate. The samples T110-01 and T110-03 (black dashed line) represent the matrix of the conglomerate. The clast has CV14-24C (blue) has a major population at 61 Ma and the matrix has a major age population at 70 Ma. [C] PDF plot of Galena Bay conglomerate clasts VZ18-09A (red) and VZ18-09B (blue) and matrix (black dashed line). The clasts age distribution has major population at 58 and 64 Ma. The matrix lacks these populations and instead has a large population at 73 Ma. [D] Probability density plot of Outpost Island conglomerate. The matrix UI18-12A (black dashed line) has a major population at 40 Ma and 59 Ma, and the clast UI18-12B (red) has a major population at 73 Ma.

Chugach terrane to the north, separating it from the older mélangé and the McHugh Complex and Potter Creek Assemblage (Amato et al., 2013; Davidson and Garver, 2017). The Border Ranges fault is the northern border of the Chugach terrane and it separates the terrane from the older more inland terranes of the Wrangellia composite terranes, and the southern boundary of the terrane is the Contact Fault and its equivalents (Davidson and Garver, 2017; Malik et al., 2019).

The Contact Fault system is thought to separate the Valdez Group to the North and the Orca Group to the south and it has an arcuate map trace across northern PWS (Malik et al., 2019). Across the fault, the Valdez Group and the Orca Group contain turbidites that have similar sandstone compositions, but overall the Valdez Group has undergone much more deformation (Plafker et al., 1994). In the east the Contact fault

system is primarily composed of steeply north-dipping dextral strike-slip faults, with the system in the west being very difficult to define (Bol and Gibbons, 1992; Davidson and Garver, 2017). South of the main arc of the Contact fault is the Prince William terrane, composed of the Orca Group (Davidson and Garver, 2017).

The Paleocene to Eocene Orca Group is a thick sequence of turbidities and conglomerates with ultramafic to mafic volcanic sequences, that are metamorphosed to prehnite-pumpellyite facies (Dusel-Bacon, 1991; Wilson and Hults, 2012). In PWS there are four locations of the Orca Group Conglomerates that were studied for this project: Miners Bay, Simpson Bay, Galena Bay, and Outpost Island (Fig. 1). Miners Bay is a poorly sorted, gravel to cobble (5-30 cm), clast-supported conglomerate with outsized clast (40 cm). The conglomerate contains primarily coarse-grained sandstone with some volcanic clasts. The Simpson Bay conglomerate is a clast supported, disorganized, sandstone-rich (80-90%) conglomerate with minor light-gray, felsic volcanic rocks. The conglomerate at Galena Bay is a massive, clast supported, cobble conglomerate with outsize clasts, a sandstone matrix, and no obvious bedding or grading. This conglomerate contains approximately 65% sandstone (of which 60% are veined), 15% shale, 20% volcanics, and <1% carbonate clasts. The conglomerate at Outpost Island is a cobble conglomerate with a coarse-grained sandstone matrix with approximately 80% of clast being fine-grained

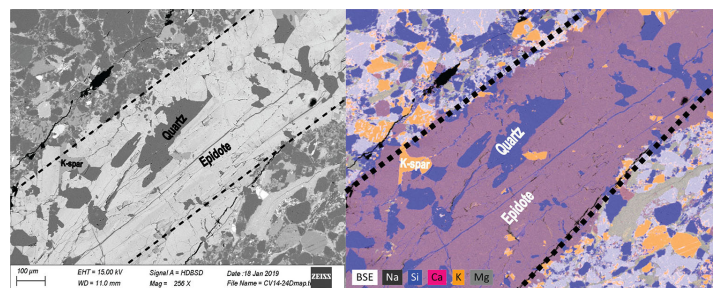


Figure 3. Mineral assemblage of veins from sample CV14-24D (MDA ~66 Ma), a clast from Simpson Bay. In both images the vein boundary is defined with a black dashed line and an example of each mineral phase (Quartz, K-spar, and Epidote) is labeled. In the EDS image minerals that are orange correspond to K-rich feldspar, purple is indicative of quartz, and pink is indicative of epidote. Similar veins can be observed in Simpson Bay clast CV14-24A (MDA ~62 Ma).

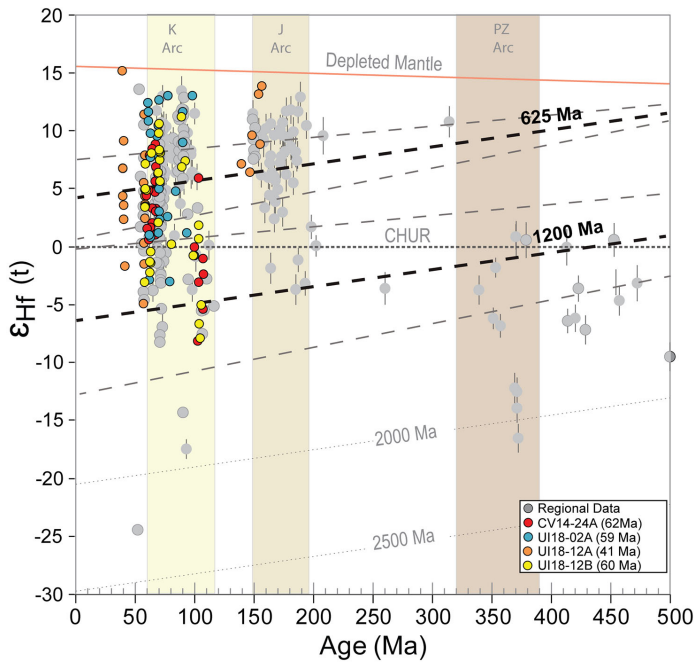


Figure 4. The $\epsilon_{\text{Hf}}(t)$ for 67 new detrital zircon samples compared to other locations in southeastern Alaska (Shumagin Islands, Kodiak Island, and other parts of Prince William Sound). Extraction age of the zircons with a crystallization age of ~ 70 Ma is 625 Ma and for those with a crystallization age of ~ 100 Ma it is 1200 Ma. This figure is adapted from Davidson and Garver (2017).

sandstone, 15-20% mudstone, and less than 5% porphyry volcanic.

METHODS

Sandstone clasts and matrix were sampled from each of the four conglomerate locations in PWS. Whole rock samples were sent to GeoSep Services in Idaho or Carleton College in Minnesota to undergo a mineral separation process where detrital zircons were isolated. This process involves a large piece of the whole rock (2-4 kg) crushed to sand sized particles that are then separated by density, first on a water table and then using heavy liquids. Magnetic separation was then used to isolate zircons. U/Pb geochronology and Hf isotope analysis was conducted on detrital zircons by laser ablation inductively coupled plasma mass spectrometry (LA-ICP-MS) at the University of Arizona LaserChron Center. The maximum depositional age (MDA) for each sample was determined by calculating the weighted mean of the three youngest zircon ages of each sample. Thin sections of sandstone clasts were imaged using a Zeiss EVO-MA15 scanning electron microscope (SEM)

and mapped using QUANTX Electron Dispersive Spectroscopy (EDS) at Union College.

RESULTS

The conglomerate at Miner's Bay (UI18-02) is a poorly sorted, gravel to cobble (5-30 cm), clast-supported conglomerate with outsized clasts (up to 40 cm). The conglomerate contains primarily coarse-grained sandstone with some volcanic clasts. The matrix of this sample (UI18-02A) yielded an MDA of 59.4 ± 1.1 Ma, and the clast, UI18-02C and UI18-02D, yielded MDAs of 61.6 ± 1.1 and 59.5 ± 1.0 Ma with major grain-age populations at 61 and 63 Ma, respectively.

The Simpson Bay conglomerate (CV14-24) near Cordova is a clast-supported, disorganized, sandstone-rich (80-90%) conglomerate with minor light-gray, felsic volcanic rocks. For this site, samples TI10-01 and TI10-3, from a location close to Simpson Bay, were used as matrix proxies (Izykowski, 2011), and were re-dated for this project. The clasts for this sample yielded MDAs of 61.5 ± 1.0 (CV14-24A), 60.3 ± 1.3 (CV14-24B), 58.4 ± 0.8 (CV14-24C), and 66.3 ± 1.1 Ma (CV14-24D), with major populations at 74 Ma, 69 Ma, 68 Ma, and 61 Ma (Fig. 2B). The matrix samples yielding a combined MDA of 57.4 ± 1.2 Ma. Clasts CV14-24A and CV14-24D have clear veins with a mineral assemblage consisting of zoned epidote, quartz, and potassium-rich feldspar (Fig. 3).

The conglomerate at Galena Bay Island is a massive, clast-supported, conglomerate with a fine-grained sandstone matrix. Clasts consist of sandstone, shale, volcanic, and carbonate. At this location three sandstone clasts were collected (VZ18-09A, VZ18-09B, and VZ18-09C), however, the matrix at this location was not easily sampled, so the matrix was collected from a nearby exposure on the mainland ~ 750 meters to the SSW (VZ18-10). An MDA of 56.4 ± 1.0 and 56.1 ± 1.0 was determined for VZ18-09A and VZ18-09B with major age populations at 58 Ma and 64 Ma, respectively (Fig. 2C). The nearby sandstone for this site (VZ18-10) has an MDA of 52.4 ± 0.9 .

The conglomerate at Outpost Island is a cobble conglomerate with a coarse-grained sandstone matrix

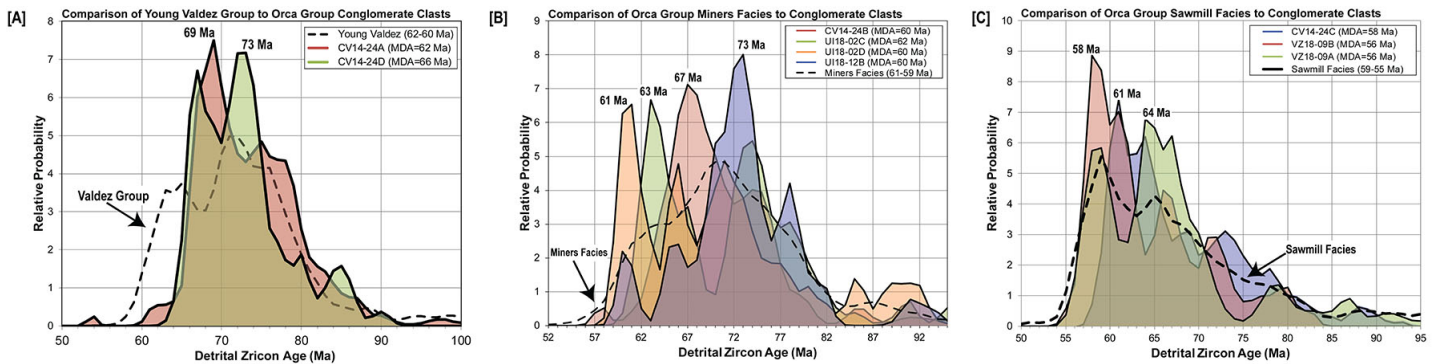


Figure 5. Probability density comparisons of sandstone conglomerate clasts to regional data. [A] Probability density plot of clasts CV14-24A (MDA ~62 Ma) and CV14-24D (MDA ~66 Ma) to the youngest Valdez Group samples (Gross Almonte et al., 2019). [B] Probability density plot of clasts CV14-24B (MDA ~60 Ma), UI18-02C (MDA ~62 Ma), UI18-02D (MDA ~60 Ma), and UI18-12B (MDA ~60 Ma) to the Miners Facies of the Orca Group (Fisher et al., 2019). [C] Probability density plot of clasts CV14-24C (MDA ~58 Ma), VZ18-09A (MDA ~56 Ma), and VZ18-09B (MDA ~56 Ma) to the Sawmill Facies of the Orca Group (Fisher et al., 2019).

dominated by volcanic and less common sandstone clasts. In this regard this unit is distinct and different from other conglomerates because it has an abundance of volcanic clasts. The matrix of this conglomerate (UI18-12A) yielded an MDA of 40.9 ± 0.7 Ma, and the clast (UI18-12B) yielded an age of 60.1 ± 0.8 Ma with a major grain age population of 73 Ma (Fig. 2D).

The data for this project includes Hf isotope values for 193 detrital zircon throughout PWS. Hafnium isotope measurements when combined with zircon crystallization ages can be used to understand crustal evolution. Measured $^{176}\text{Hf}/^{177}\text{Hf}$ values are normalized to the chondritic uniform reservoir (CHUR) and reported in epsilon notation [$\epsilon\text{Hf}(t)$] (Garver and Davidson, 2015). The $\epsilon\text{Hf}(t)$ values for this data set range from -8.3 to 15.1 with two exceptions that have values of -14.3 and -24.4 (Fig. 4).

DISCUSSION

The MDAs from this project provide insight into the position of the conglomerates in the stratigraphic column of the Orca Group (~61 to 35 Ma) (Davidson and Garver, 2017). The MDAs of the Miners Bay and Simpson Bay conglomerates fall within the earliest time frame of the Orca Group (57 to 60 Ma), which would suggest that they sit at or near the base of the Orca Group (at ~60 Ma; Fisher et al., 2019). Recent dates of the Valdez Group indicate that it is as young as ~61 Ma meaning that there is no gap in age between the deposition of the Valdez Group and Orca Group (Fisher et al., 2019; Gross Almonte et al., 2019). The conglomerate at Galena Bay has an MDA of 52

Ma, this falls between the middle and upper part of the Orca Group. The matrix of the conglomerate at Outpost Island (UI18-12A) has an MDA of 41 Ma, which corresponds to the youngest of the Orca Group and thus sits at the upper part of the stratigraphic column.

The ages of the Galena Bay and Outpost Island conglomerate correspond to the emplacement of plutons in this area. The nearby Sheep Bay Pluton of the SBB was emplaced at ~54 Ma, so the deposition of the Galena Bay conglomerate (~52 Ma) occurred just after the emplacement of the pluton (Davidson and Garver, 2017). The Eshamy Suite plutons were emplaced from ~38 to 41 Ma, so the MDA of Outpost Island (~41 Ma) overlaps with the emplacement of the Eshamy Suite plutons (~38 to 41 Ma) (Davidson and Garver, 2017). Thus, two conglomerates (Galena Bay and Outpost Island) appear to coincide, or nearly so, with pluton intrusion which raises the question of conglomerate sedimentation being a result of pluton emplacement, and perhaps disruption of the basin due to uplift and inflation.

Almost all conglomerate clasts dated yield ages that correspond to depositional ages associated with the Orca Group and probability density functions (PDF) that pass the K-S similarity test when compared to various Orca Group samples (Fig. 5) (Fisher et al., 2019). This result suggest that within a few million years of deposition the Orca Group was being uplifted and eroded. The veined sandstone clasts are mainly derived from the Orca Group cannibalization during this period. Two clasts from Simpson Bay, CV14-

24A (~62 Ma) and CV14-24D (~66 Ma), have MDAs that can be tied to the depositional age of the Valdez Group (Figure 5A). These clasts also contain distinct veins composed of epidote, quartz, and potassium-rich feldspar, indicating that it has undergone greenschist grade metamorphism (Fig. 3). The Orca Group as a whole did not experience this high of a grade of metamorphism so it is likely that these two clasts have a Valdez affinity. Thus, this result means that the Orca Group must have been adjacent to the Valdez Group by 57 Ma.

The majority of $\epsilon_{\text{Hf}}(t)$ data for clasts CV14-24A and UI18-12B are positive and corresponds to other regional data from the Shumagin Islands, Kodak Island, and other parts of Prince William Sound (Fig. 4). The $\epsilon_{\text{Hf}}(t)$ values collected for zircons with crystallization ages of ~70 Ma and ~100 Ma suggest the existence of two distinct juvenile arcs with mantle extraction ages of ~625 Ma and ~1200 Ma, respectively (Fig. 4). Overall, this suggest that during its formation, there was a large component of juvenile crust in the source region. The similarity between the clasts $\epsilon_{\text{Hf}}(t)$ data to the regional data set (largely Valdez and equivalents) implies that the provenance of the two clasts are consistent with a local source, such as the Valdez Group.

CONCLUSIONS

The new U/Pb detrital zircon data from the Orca Group Conglomerates shows that the MDAs of each conglomerate occur throughout the deposition of the Orca Group, so the conglomerates are located throughout the stratigraphic column. The MDAs and PDFs for the majority of the sandstone clasts correspond to the Orca Group, which implies that within a few years of its deposition the Orca Group was being uplifted and eroded. Two clasts from Simpson Bay have experienced greenschist metamorphism, and thus provide a link between the Orca Group and the Valdez Group. This means that the two groups must have been together by 57 Ma, much earlier than previously thought.

ACKNOWLEDGEMENTS

This material is based upon work supported by the Keck Geology Consortium and the National Science Foundation under Grant No. 1659322. Field work and analyses funded by NSF Grant “Collaborative Research: RUI: Translation and accretion of the Yakutat microplate and Prince William terrane, Alaska” NSF grants EAR-1728013 (Garver): NSF EAR 1727991 (Davidson), and NSF EAR 0619578 MRI (Garver and others at Union College). I want to thank the incredible field team Professor Tim Flood (St. Norbert College), Alysala Malik (Carleton College), Caitlin Noseworthy (St. Norbert College), Nick Gross Almonte (Carleton College), and Victor Garcia (University of Texas - Austin). I would also like to thank everyone at University of Arizona Laserchron Center an NSF supported multi-user facility ran by Mark Pecha and George Gehrels at the University of Arizona and that is funded by NSF-EAR Grant No. 1649254 for making the U/Pb and Hf analyses possible.

REFERENCES

- Amato, J.M., Pavlis, T.L., Clift, P.D., Kochelek, E.J., Hecker, J.P., Worthman, C.M. and Day, E.M., 2013. Architecture of the Chugach accretionary complex as revealed by detrital zircon ages and lithologic variations: Evidence for Mesozoic subduction erosion in south-central Alaska. *Bulletin*, 125(11-12), pp.1891-1911.
- Bol, A.J. and Gibbons, H., 1992. Tectonic implications of out-of-sequence faults in an accretionary prism, Prince William Sound, Alaska. *Tectonics*, 11(6), pp.1288-1300.
- Capps, S.R., and Johnson, B.L., 1915, The Ellamar District, Alaska: U.S. Geological Survey Bulletin 605, pp. 100-125.
- Coney, P.J., Jones, D.L. and Monger, J.W., 1980. Cordilleran suspect terranes. *Nature*, 288(5789), p.329.
- Cowan, D.S., 2003. Revisiting the Baranof–Leech River hypothesis for early Tertiary coastwise transport of the Chugach–Prince William terrane.

- Earth and Planetary Science Letters, 213(3-4), pp.463-475.
- Davidson, C. and Garver, J.I., 2017. Age and Origin of the Resurrection Ophiolite and Associated Turbidites of the Chugach–Prince William Terrane, Kenai Peninsula, Alaska. *The Journal of Geology*, 125 (6), pp.681-700.
- Dusel-Bacon, C., 1991. Metamorphic history of Alaska. US Geological Survey. Open-File Report 91-556.
- Fisher, W.S., Pope, M.D., Malik, A.M., Garver, J.I., and Davidson, C.M., 2019. Zircon facies in the Paleocene-Eocene Orca Group indicate a provenance link to the Chugach terrane, Prince William Sound, Alaska. *Geological Society of America Abstracts with Program, Cordilleran Section - 115th Annual Meeting, Portland Oregon*. v. 51, n. 4. doi: 10.1130/abs/2019CD-329384
- Garcia, V.R. Jr, Stockli, D.F., Davidson, C.M, Garver, J.I., 2019. Crystallization ages and geochemistry of the Miners Bay and Cedar Bay plutons, Prince William Sound, Alaska. *Geological Society of America Abstracts with Program, Cordilleran Section - 115th Annual Meeting, Portland Oregon*. v. 51, n. 4. doi: 10.1130/abs/2019CD-329495.
- Garver, J.I., Davidson, C. and Northfield, M.N., 2012. Tectonic evolution of the Chugach-Prince William terrane in Prince William Sound and Kodiak Island, Alaska. In *Proceedings from the 25th Keck Geology Consortium Undergraduate Research Symposium, Amherst* (pp. 1-7).
- Garver, J.I. and Davidson, C.M., 2015. Southwestern Laurentian zircons in upper Cretaceous flysch of the Chugach-Prince William terrane in Alaska. *American Journal of Science*, 315 (6), pp.537-556.
- Gasser, D., Rubatto, D., Bruand, E. and Stüwe, K., 2012. Large-scale, short-lived metamorphism deformation, and magmatism in the Chugach metamorphic complex, southern Alaska: A SHRIMP U-Pb study of zircons. *Bulletin*, 124(5-6), pp.886-905.
- Grant, U.S. and Higgins, D.F., 1910. Reconnaissance of the geology and mineral resources of Prince William Sound Alaska. Washington: Government Printing Office.
- Gross Almonte, N., Fisher, W.S., Malik, A.M., Garver, J.I., and Davidson, C.M. 2019. Age and provenance of the Upper Cretaceous to Paleocene Valdez Group of the Chugach terrane from the Richardson Highway and northern Prince William Sound, Alaska. *Geological Society of America Abstracts with Program, Cordilleran Section - 115th Annual Meeting, Portland Oregon*. v. 51, n. 4. Doi: 10.1130/abs/2019CD-329673.
- Haeussler, P.J., Bradley, D.C., Wells, R.E. and Miller, M.L., 2003. Life and death of the Resurrection plate: Evidence for its existence and subduction in the northeastern Pacific in Paleocene–Eocene time. *Geological Society of America Bulletin*, 115(7), pp.867-880.
- Izykowski, T.M., 2011, Detrital zircon fission track ages of the Paleocene Orca Group of Eastern Prince William Sound, near Cordova, Alaska [B.S. thesis]: Schenectady, Union College, 119 p.
- Johnson, E., 2012, Origin of the Late Eocene Eshamy Suite Granitoids in Western Prince William Sound, Alaska: 25th Annual Keck Symposium: 2012, p. 33–39.
- Malik, A.M., Fisher, W.S., Gross Almonte, N., Garver, J.I., Davidson, C.M., 2019. U-Pb dating of detrital zircon from turbidites of the Chugach and Prince William terrane in Prince William Sound, Alaska: Implications of the significance of the Contact fault system as a terrane boundary. *Geological Society of America Abstracts with Program, Cordilleran Section - 115th Annual Meeting, Portland Oregon*. v. 51, n. 4. doi: 10.1130/abs/2019CD-329396
- Moffit, F.H., 1954, Geology of the Prince William Sound region, Alaska, IN *Mineral resources of Alaska, 1951-53*: U.S. Geological Survey

Bulletin, 989-E, p. E225-E310, (incl. geologic map, scale 1:250,000)

Plafker, G., Keller, G., Nelson, S.W., Dumoulin, J.A. and Miller, M.L., 1985. Summary of data on the age of the Orca Group, Alaska: A section in The United States Geological Survey in Alaska: Accomplishments during 1984 (No. 967, pp. 74-76). US Geological Survey.

Pope, M.D., Fisher, W.S., Malik, A.M. Garver, J.I., and Davidson, C.M., 2019. Provenance of sandstone clasts from conglomerate of the Paleocene-Eocene Orca Group in Prince William Sound, Alaska. Geological Society of America Abstracts with Program, Cordilleran Section - 115th Annual Meeting, Portland Oregon. v. 51, n. 4. Doi: 10.1130/abs/2019CD-329392

Tysdal, R.G. and Case, J.E., 1979. Geologic map of the Seward and Blying Sound quadrangles, Alaska (No. 1150).

Wilson, F.H., Hults, C.P., Swint-Iki, T.R. and Ryan, D.A., 2012. Geology of the Prince William Sound and Kenai Peninsula Region, Alaska: Including the Kenai, Seldovia, Seward, BlyingSound, Cordova, and Middleton Island 1: 250,000-scale Quadrangles. US Geological Survey.

ASSESSING VEGETATION AND FLUVIAL RESPONSES TO THE PALEOCENE-EOCENE THERMAL MAXIMUM IN THE HANNA BASIN (WYOMING, U.S.A.)

ELLEN D. CURRANO, University of Wyoming
BRADY Z. FOREMAN, Western Washington University

INTRODUCTION

The Paleocene-Eocene Thermal Maximum (PETM) represents the largest and most abrupt global warming event of the Cenozoic Era (Koch et al., 1992; Zachos et al., 2001; McInerney & Wing, 2011) and is viewed as one of the premier geologic analogs for modern, anthropogenic warming. Fifty-six million years ago, a massive pulse of isotopically-light carbon was introduced to the world's oceans and atmosphere, and Earth's mean global temperature increased by at least 5°C (Zachos et al., 2001; McInerney & Wing, 2011). The event is recorded in numerous marine sediment cores whereas the continental record is limited to relatively few sites (McInerney & Wing, 2011). This difference in geographic data coverage has resulted in reasonably well-constrained and understood consequences for marine biologic systems, ocean chemistry, and ocean temperatures (McInerney & Wing, 2011), but a poorer understanding of the consequences for continental biologic and environmental conditions (Wing & Currano, 2013). North America contains the most extensive record of climate change spanning the PETM, with carbon isotope records identifying the PETM event in five basins (Koch et al., 1992; Bowen & Bowen, 2008; Clechenko et al., 2008; Foreman et al., 2012; Bataille et al., 2016). However, detailed sedimentologic descriptions of alluvial changes have only been performed at two locations (the Bighorn Basin, northwest Wyoming, and the Piceance Creek Basin, western Colorado) and paleobotanical changes documented at just one location (the Bighorn Basin) (Figure 1; Foreman et al., 2012; Wing and Currano, 2013; Kraus et al., 2015). With such limited

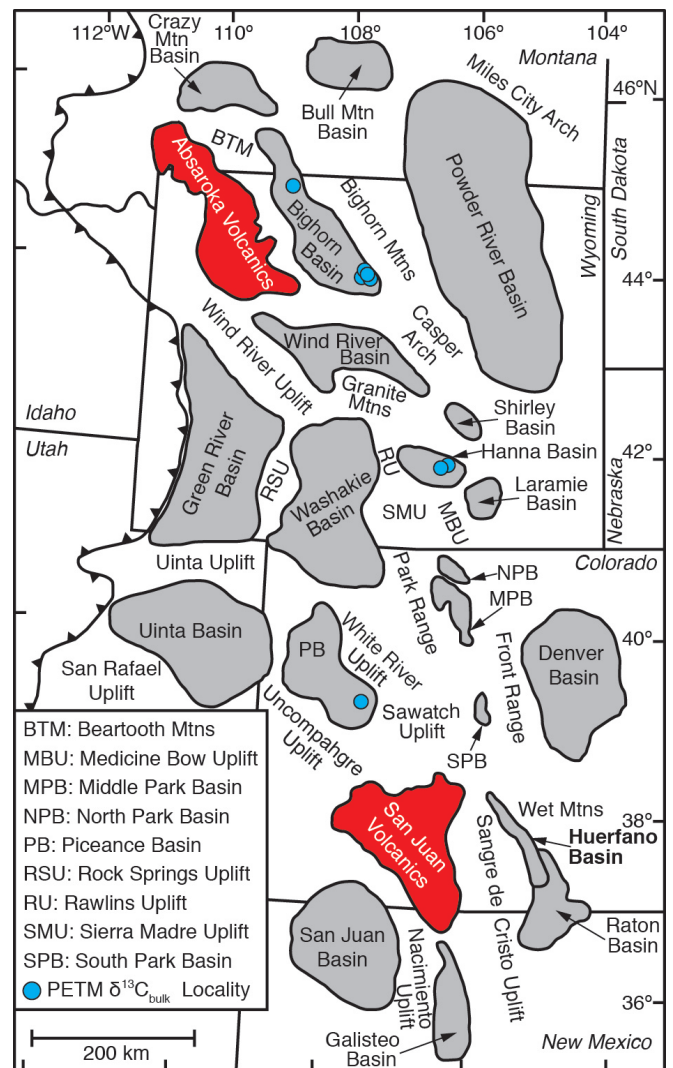


Figure 1. Map of Laramide basins with Paleogene sediments and surrounding uplifts. The negative carbon isotope excursion that marks the PETM has been previously identified in the Bighorn and Piceance Creek Basins. Data collected by the Keck Wyoming Project constrained the location of two additional PETM isotope excursions in the Hanna Basin.

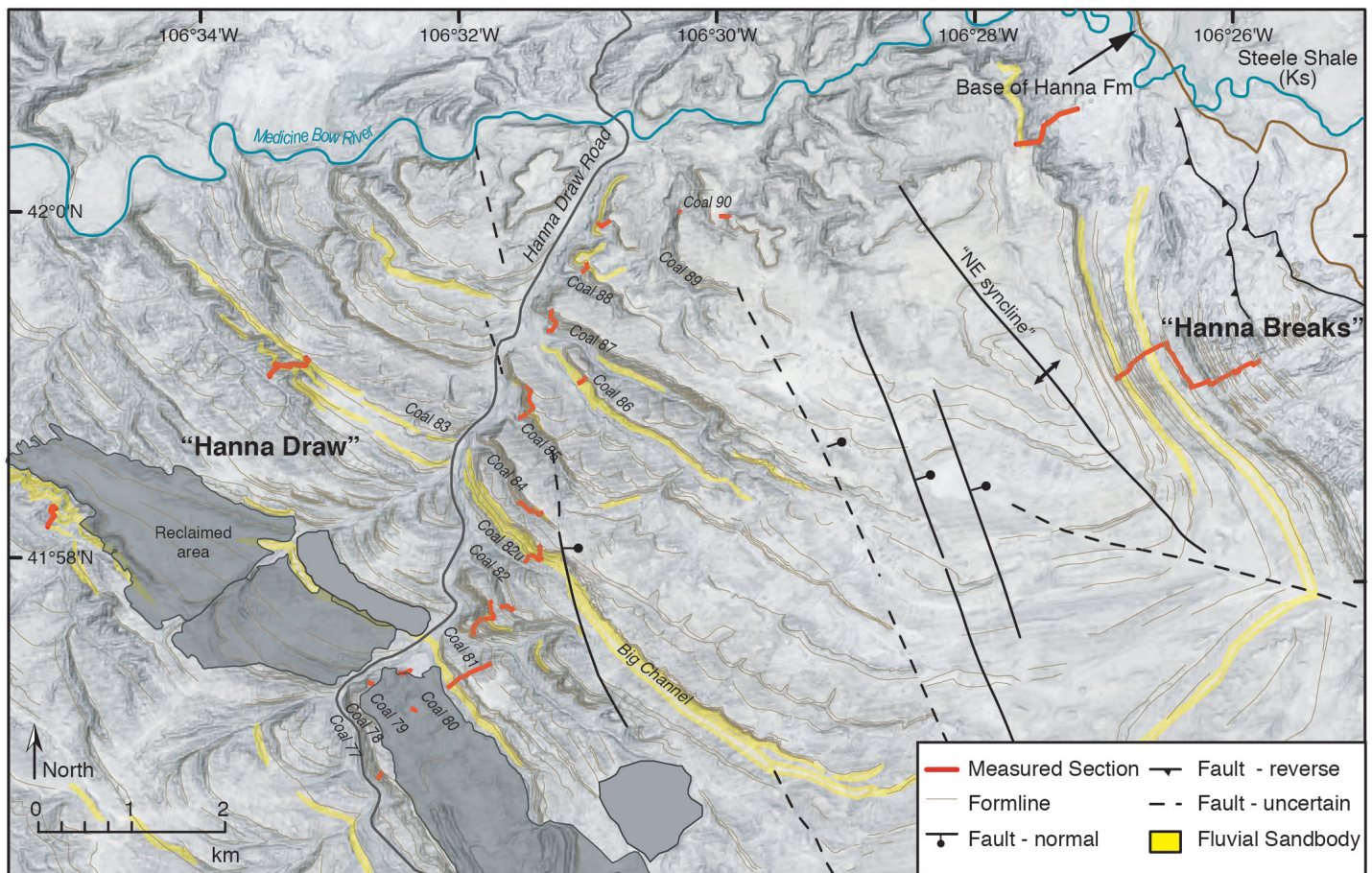


Figure 2. Location of the Hanna Draw and “The Breaks” sections within the Hanna Basin, modified from Dechesne et al. (in review). Large, laterally extensive fluvial sandstones are highlighted in Yellow, and the “Big Channel” sandstone occurs within the PETM interval. Section lines of Dechesne et al. (in review) are in red.

geographic coverage it is difficult to evaluate spatial gradients in response, and test fundamental climate hypotheses. This project expands this existing database to the Hanna Basin of south-central Wyoming, with the aim of evaluating spatial gradients in alluvial and biologic response to the PETM.

Broadly speaking, the terrestrial response to elevated carbon dioxide levels is expected to be variable to due topographic complexity and shifting atmospheric circulation patterns under different latitudinal thermal gradients. As such it is critical to develop additional continental locations where the temperature, hydrologic, and biologic changes are constrained. The Hanna Basin record is a particularly important complement to the record already collected in the Bighorn Basin because stratigraphic data suggest a difference in water availability between the two basins. Both the PETM interval and the entire early Eocene sequence preserved in the Willwood

Formation in the Bighorn Basin contain abundant red beds, indicative of well-drained soils and seasonal precipitation (Kraus and Riggins, 2007; Kraus et al., 2015). The Bighorn Basin records the consequences of an overall drier basin experiencing an abrupt global warming event. In contrast, the Hanna Basin sedimentary sequence remains drab-colored and coal-rich from bottom to top, suggesting that wet, swampy conditions prevailed through the PETM and early Eocene (Dechesne et al., in review). It records the consequences of a more humid basin experiencing an abrupt global warming event. Thus, comparisons of the Hanna and Bighorn basins will allow us to disentangle the roles of temperature and water availability in driving vegetation change and the fluvial response in a dominantly humid setting. This water availability difference is likely due to the location of the Hanna Basin, farther to the east and potentially more proximal to moisture sources as compared to the Bighorn Basin (Sewall & Sloan,

2006). The Laramide Orogeny created a complex topography within the Western Interior that strongly influenced water vapor transport paths (Sewall & Sloan, 2006). In general, however, circulation models suggest the easternmost Laramide basins were wetter as moisture from the paleo-Gulf of Mexico moved north and westward. This resulted in semi-arid and dry conditions in the western and northernmost Laramide basins (Sewall & Sloan, 2006).

GEOLOGIC SETTING

The Hanna Basin of south-central Wyoming is a Laramide style basin bounded by the Rawlins uplift to the west, Sweetwater Arch in the north, the Simpson Ridge anticline in the east, and the Medicine Bow and Sierra Madre Mountains in the south (regional basin/mts figure). It is exceptional among the Laramide basins because of its high subsidence rate, extremely thick Cretaceous to Eocene sedimentary strata, and extensive coal deposits (Dobbin et al., 1929; Roberts and Kirschbaum, 1995; Wroblewski, 2003). The Paleocene-Eocene boundary is preserved in the Hanna Formation, which is over 2000 meters thick at the center of the basin (WOGCC, 2016; Gill et al., 1970; Wroblewski, 2003) and consists of conglomerates, sandstones, siltstones, carbonaceous shales, and coals. These deposits are interpreted as low gradient fluvial to paludal and lacustrine (Dobbin et al., 1929; Wroblewski, 2003; Lillegraven et al., 2004). The student projects targeted a specific set of extensive outcrops along the Hanna Draw Road and in “The Breaks” (Figure 2), which have been the focus of new geologic and paleontologic work by PI Currano, stratigrapher Marieke Dechesne of the USGS, and paleobotanist Regan Dunn of the Field Museum. The majority of research focuses on a 250-meter thick stratigraphic interval with pollen biostratigraphic constraints and initial bulk $\delta^{13}\text{C}$ values that indicate the PETM is preserved.

PROJECT GOALS

Our team included six undergraduate researchers, two faculty members (Currano and Foreman), and two scientific collaborators (Dechesne and Dunn). The major projects goals include: (1) constraining the location of the PETM in the Hanna Basin using carbon



Figure 3. Members of the Keck Wyoming crew in the uppermost portion of the trench through the PETM in the Hanna Draw section. From bottom left, Xavier Nogueira, Christine Shonnard, Jake Polsak, Anthony Semeraro, Marieke Dechesne, Ellen Currano, Keifer Nace, and James Chisholm. Photograph by Brady Foreman.

isotope analyses; (2) characterizing and quantifying changes in fluvial and overbank deposition spanning the PETM; and (3) identifying and interpreting changes in vegetation cover spanning the PETM. The project goals were achieved by a combination of intensive field work and targeted lab work that focuses on stratigraphic section measuring, lithofacies analysis, a new highly-refined bulk organic carbon isotope stratigraphy, and application of new plant cuticle proxies for vegetation cover.

RESEARCH PROJECTS

The methodologies employed in this study combine foundational approaches to stratigraphy, sedimentology, and isotope geochemistry and new, cutting edge proxies for vegetation cover using the preserved leaf cuticles of ancient plants. All students were trained to measure and correlate stratigraphic sections, describe lithofacies, and prepare samples for bulk organic $\delta^{13}\text{C}$ analyses. As a team, we trenched

(Figure 3), measured, and described a stratigraphic section through the Paleocene-Eocene Thermal Maximum at Hanna Draw. In the lab, we worked together to prepare samples for geochemical analyses. Students then learned additional techniques related to their specific projects.

James Chisholm (CSU San Bernardino) analyzed all the carbon isotope data collected by the Keck Wyoming Project. His project identified where the PETM carbon isotope excursion (CIE) occurred within the Hanna Draw and The Breaks stratigraphic sections, compared the magnitude and duration of the CIE between our two sections, and assessed the causes of background “noise” related to baseline environmental conditions.

Xavier Nogueira (Temple University) and **Anthony Semeraro** (Western Washington University) examined fluvial systems during the late Paleocene, PETM, and Eocene. Nogueira collected samples from twenty-five sandstone bodies and performed point counts of minerals from thin sections. He tested whether compositional differences among samples were due to time, depositional environment, or flow direction and hypothesized about sediment sources. Semeraro measured paleoflow directions in modern and ancient channel systems to investigate fluctuations in stream flow during the PETM. He chose three modern meandering rivers and three modern braided systems, measured over 1000 flow directions from each, and calculated dispersion values (i.e. the variability in flow direction) for each river, showing that meandering rivers have more variability in flow direction than braided rivers. Last, he calculated dispersion values for channel systems in the late Paleocene, PETM, and early Eocene of the Hanna, Bighorn, and Piceance Creek. The Hanna flow direction measurements are his own.

Keifer Nace (Whitman College) and **Jake Polsak** (Western Washington University) documented vegetation structure using our new leaf area index (LAI = foliage area in m^2 / ground area in m^2) proxy (Dunn et al. 2018). This proxy utilizes the morphology of leaf epidermal cells, preserved as imprints on cuticles, to reconstruct canopy openness (Dunn et al. 2018). Dunn has already constructed a record of LAI across the PETM interval in both the

Hanna Draw sections documenting changes in LAI at the PETM, but context was needed to determine whether the change observed during the PETM was significant. In particular, large sheet sandstones occur during the PETM, making it unclear whether climatic or lithologic changes were responsible for the decrease in LAI observed during the PETM. Nace measured sections before and after the PETM that included large sandstone units and reconstructed LAI throughout each section. She then compared her results with the Dunn’s PETM record. Polsak assessed temporal and spatial variability in LAI within the early Eocene by measuring four contemporaneous sections and reconstructing LAI at high temporal and spatial resolution in each section. He then examined variability in LAI across time, space, and lithology.

Christine Shonnard (Beloit College) compared cyclic overbank deposition within the Hanna Formation of south-central Wyoming and Willwood Formation of northwest Wyoming. Both formations include repetitive packages of fine-grained deposits and sandstones, although the composition of the fine-grained deposits varies between formations, likely driven by drainage within the basin. The Hanna Formation contains organic-rich silts and shales, whereas the Willwood Formation is dominated by redbeds. Shonnard described lithological changes at high resolution in two sections in The Breaks, performed geochemical analyses, and reconstructed paleoclimate. She compared her sedimentary cycles with those from the Willwood Formation.

ACKNOWLEDGEMENTS

This material is based upon work supported by the Keck Geology Consortium and the National Science Foundation under Grant No. 1659322, as well as NSF grant EAR 145031 to Ellen Currano. We gratefully acknowledge our longtime Hanna Basin collaborators, Regan Dunn and Marieke Dechesne, for sharing their time and expertise with the Keck students. We thank the Palm family and Q Creek Ranch for land access and Mark Clementz for use of his lab.

REFERENCES

Bataille, C.P., Watford, D., Ruegg, S., Lowe, A.,

- Bowen, G.J. 2016. Chemostratigraphic age model for the Tornillo Group: A possible link between fluvial stratigraphy and climate. *Palaeogeography, Palaeoclimatology, Palaeoecology* 457: 277-289.
- Bowen, G.J., Bowen, B.B. 2008. Mechanisms of PETM global change constrained by a new record from central Utah. *Geology* 36: 379-382.
- Clechenko, E.R., Kelly, D.C., Harrington, G.J., Stiles, C.A. 2008. Terrestrial records of a regional weathering profile at the Paleocene-Eocene boundary in the Williston Basin of North Dakota. *GSA Bulletin* 119: 428-442.
- Dechesne, M., Currano, E.D., Dunn, R.E., Higgins, P., Hartman, J., Chamberlain, K. in review. Climatic and tectonic responses of the fluvial to paludal strata of the Hanna Formation around the Paleocene-Eocene Boundary, Hanna Basin, Wyoming.
- Dobbin, C.E., Bowen, C.F., Hoots, H.W. 1929. Geology and coal and oil resources of the Hanna and Carbons basins, Carbon County, Wyoming. *U.S. Geological Survey Bulletin* 804: 88.
- Dunn, R.E., Currano, E.D., Dechesne, M., & Foreman, B.Z. (2018). Forest canopy response to greenhouse warming at the Paleocene-Eocene Thermal Maximum. *GSA Annual Meeting*, Indianapolis.
- Foreman, B.Z., Heller, P.L., Clementz, M.T. 2012. Fluvial response to abrupt global warming at the Palaeocene/Eocene boundary. *Nature* 491: 92-95.
- Koch, P.L., Zachos, J.C., Gingerich, P.D. 1992. Correlation between isotope records in marine and continental carbon reservoirs near the Palaeocene/Eocene boundary. *Nature* 358: 319-322.
- Kraus, M.J., Riggins, S., 2007. Transient drying during the Paleocene–Eocene Thermal Maximum (PETM): analysis of paleosols in the Bighorn Basin, Wyoming. *Palaeogeography, Palaeoclimatology, Palaeoecology* 245: 444-461.
- Kraus, M.J., Woody, D.T., Smith, J.J., Dukic, V., 2015. Alluvial response to the Paleocene-Eocene Thermal Maximum climatic event, Polecat Bench, Wyoming (U.S.A.). *Palaeogeography, Palaeoclimatology, Palaeoecology* 435: 177-192.
- Lillegraven, J. A., Snoke, A. W., McKenna, M. C. 2004. Tectonic and paleogeographic implications of late Laramide geologic history in the northeastern corner of Wyoming’s Hanna Basin. *Rocky Mountain Geology* 39: 7-64.
- Gill, J. R., Merewether, E. A., and Cobban, W. A., 1970, Stratigraphy and nomenclature of some Upper Cretaceous and lower Tertiary rocks in south-central Wyoming. *U.S. Geological Survey Professional Paper* 667, 53 p.
- Roberts, L.N.R., and Kirschbaum, M.A., 1995, Paleogeography of the Late Cretaceous of the Western Interior of middle North America—Coal distribution and sediment accumulation. *U.S. Geological Survey Professional Paper* 1561, 155 p.
- Sewall, J.O., Sloan, L.C. 2006. Come a little bit closer: A high-resolution climate study of the early Paleogene Laramide foreland. *Geology* 34: 81-84.
- WOGCC , Wyoming Oil and Gas Conservation Commission well log database: <http://wogcc.wyo.gov/> (July 2016).
- Wing, S.L., Currano, E.D., 2013. Plant response to a global greenhouse event 56 million years ago. *American Journal of Botany* 100: 1234–1254.
- Wroblewski, A. F.-J., 2003, The role of the Hanna Basin in revised paleogeographic reconstructions of the Western Interior Sea during the Cretaceous–Tertiary transition, in Horn, M. S., ed., *Wyoming Geological Association Guidebook, 2002 Field Conference “Wyoming Basins”* and 2003 Field Conference, p. 17–40.
- Zachos, J.C., Pagani, M., Sloan, L., Thomas, E., Billups, K., 2001. Trends, rhythms, and aberrations in global climate 65 Ma to present. *Science* 292: 686–693.

EVALUATION OF BULK ORGANIC CARBON ISOTOPE RECORDS FROM EARLY PALEOGENE STRATA IN THE HANNA BASIN (WYOMING, U.S.A.) SPANNING THE PALEOCENE-EOCENE THERMAL MAXIMUM

JAMES CHISHOLM, Department of Geological Sciences, California State University, San Bernardino
Research Advisor: Joan E. Fryxell

INTRODUCTION

The early Paleogene was dominated by a global greenhouse climatic state punctuated by abrupt, transient warming events known as hyperthermals (McInerney and Wing, 2011). These hyperthermals were each less than ~200,000 years long and were associated with perturbations in the global carbon cycle (McInerney and Wing, 2011). The perturbations are manifested as negative excursions in stable carbon isotope records from proxies hosted in both marine and nonmarine strata (McInerney and Wing, 2011). The Paleocene-Eocene Thermal Maximum (PETM) was the largest of these events and occurred approximately 56 million years ago (McInerney and Wing, 2011). Although identified at many locations within marine strata, there exist only a few locations in nonmarine strata where the climatic event has been identified (McInerney and Wing, 2011). This study sought to extend the geographic range of these localities by developing a bulk organic carbon isotope record from early Paleogene strata in the Hanna Basin of south-central Wyoming.

Bulk organic $\delta^{13}\text{C}$ values capture an average value of organic matter, mostly plant debris, preserved in sedimentary rock (Benner et al., 1987; Wynn et al., 2006; Wynn, 2007). These carbon isotope values are useful for tracking changes in the isotopic composition of atmospheric CO_2 as well as a range of ecophysiological conditions experienced by plants. This includes water stress, photosynthetic pathway, and plant type (Farquhar et al., 1980, 1989; Arens et al., 2000; Jahren et al., 2008; Diefendorf et

al., 2010; Kohn, 2010). Additionally, post-mortem alteration of bulk organic $\delta^{13}\text{C}$ values can occur due to mixing with refractory, allochthonous carbon and various diagenetic modifications as the organic matter experiences higher pressures and temperatures at depth (Benner et al., 1987; Wynn et al., 2006; Wynn, 2007; Baczynski et al., 2013; 2016). Thus, bulk organic $\delta^{13}\text{C}$ records tend to be “noisy” relative to other carbon isotope records such as n-alkanes, marine carbonates, and pedogenic carbonates (McInerney and Wing, 2011). However, bulk organic $\delta^{13}\text{C}$ values have successfully identified the PETM in nonmarine strata in previous studies (Magioncalda et al., 2008; Foreman et al., 2012; Baczynski et al., 2013, 2016), and bulk organic $\delta^{13}\text{C}$ proxies are particularly useful when thick accumulations of nonmarine strata (in excess of 100 meters) must be assessed to identify the ~200 kyr PETM interval.

The PETM has been linked with the massive release of isotopically light, exogenic carbon into the atmosphere and oceans (McInerney and Wing, 2011). However, the source of this isotopically light carbon is still uncertain. Various researchers have proposed volcanic emissions, meteorite impacts, mantle degassing, extreme forest fires, widespread permafrost oxidation, and the release of methane clathrates (McInerney and Wing, 2011). The release of methane clathrates is currently the most favored hypothesis, but it is difficult to rectify this carbon source with the magnitude of shallowing of the carbonate compensation depth in the ocean and the observed warming (McInerney and Wing, 2011). Constraining the true magnitude of the isotopic excursion and carbon source or sources

is critical in determining the climate's sensitivity to fluctuations in $p\text{CO}_2$ (McInerney and Wing 2011). Having additional data from multiple geographic areas will yield a more accurate understanding of the carbon cycle perturbation and allows us to evaluate how local environmental conditions before, during, or after the PETM may have changed. The Western Interior of the United States is a particularly good location to undertake such a project as a series of intermontane basins preserve early Paleogene strata deposited during the Laramide Orogeny. The PETM has been identified in three of these basins, and in two of these three the PETM is identified in bulk organic $\delta^{13}\text{C}$ values as well as other proxies (Magioncalda et al., 2004; Foreman et al., 2012; Baczynski et al., 2013; 2016).

GEOLOGIC BACKGROUND

This study focuses on a bulk organic carbon isotope record derived from the early Paleogene Hanna Formation in the Hanna Basin of south-central Wyoming (Fig. 1). The Hanna Basin is a Laramide structural basin formed during the Laramide Orogeny

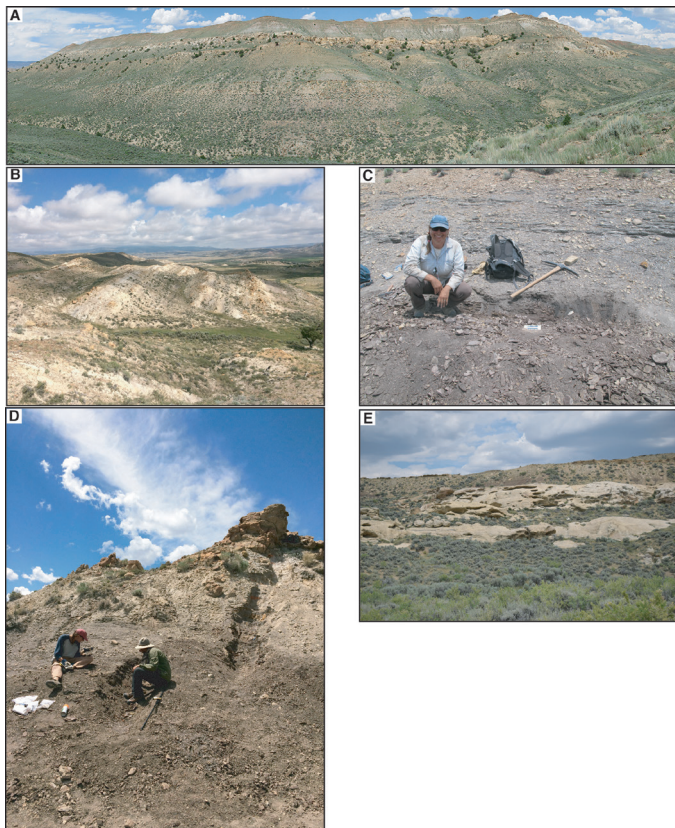


Figure 1. Field photographs of two stratigraphic sections, A) Hanna Draw and B) Hanna Breaks, C) overbank coal unit, D) overbank depositional cycle, and E) fluvial sandbody.

in the Late Cretaceous through early Paleogene (Dickinson et al., 1988). The basin is surrounded by various basement involved uplifts including the Rawlins Uplift to the west, the Medicine Bow Mountains to the south, and the Seminoe-Shirley-Freezout Hills mountains to the north. The Hanna Basin is anomalous in the thickness of accumulated strata amongst Laramide basins, preserving in excess of 12,000 meters of Cambrian through Miocene strata (Wroblewski, 2002). The early Paleogene Hanna Formation is approximately 3500 meters of this total. The Hanna Formation spans deposition from approximately 62 Ma to at least 54 Ma based on scattered mammal fossils, palynology, and U-Pb detrital zircon geochronologic maximum depositional ages (Wroblewski, 2003 and references therein; Dechesne et al., in review). The depositional environments within the Hanna Formation are diverse, and include fluvial, lacustrine, palustrine, and swamp lithofacies associations (Lillegraven and Snoko, 1996; Secord, 1998; Wroblewski, 2002; Dechesne et al., in review). Within the stratigraphic interval of focus in this study thick, laterally continuous fluvial sandbodies are present as well as a variety of organic-rich overbank facies above Coal 82 of Dobbin et al. (1929). The large fluvial sandbody (“Big Channel” in Fig. 1) was traced laterally by Dechesne et al. (in review) to the Hanna Breaks area, where our second stratigraphic section is located.

METHODS

Two stratigraphic sections were measured, one near the basin center called Hanna Draw and one towards the northeast margin called Hanna Breaks (Fig. 1). Sections were measured using standard Jacob's staff and Brunton compass methods and corrected for local strike and dip of the strata (originally measured by Dechesne et al., in review). The Hanna Draw section was a total of 285 meters thick, and the Hanna Breaks section was a total of 488 meters thick. The sections were trenched using hand tools to expose fresh sedimentary rock for standard lithofacies descriptions (e.g., grain size, sorting, bed contacts, sedimentary structures). Fist-sized samples of rock were obtained from trenched sections, wrapped in aluminum foil, and labeled with their stratigraphic height for carbon isotope analyses. In total 403 samples were obtained

from the Hanna Draw section representing an average spacing of every 0.7 meters. In the Hanna Breaks section, a total of 222 samples were obtained for an average spacing of 2.2 meters. However, in each section the stratigraphic spacing of samples varies due to outcrop limitations and an increase in sampling density in proximity to the Paleocene-Eocene boundary.

Samples were prepared for isotopic analysis by grinding each sample using a mortar and pestle into a fine powder. This is followed by removing any carbonate phases in the samples (diagenetic or cements) whose $\delta^{13}\text{C}$ values can greatly differ from organic $\delta^{13}\text{C}$ values. Approximately 1 gram of powder was loaded into labeled vials and subjected to an acid treatment. Initially, 30 mL of 0.5M HCl was added, the sample sealed and mixed using a vortex mixer. The sample was allowed to react for 12 hours, prior to centrifuging and decanting of reacted acid. This step was repeated a second time, and each sample reacted for a total of 24 hours. Finally, the sample was rinsed four times using deionized water using the same mix, centrifuging, and decanting process. After the rinsing steps the samples were dried in a freeze-dryer under a vacuum. The dry samples were then weighed (between 0.27 and 50.00 mg depending on expected %C content) in tin capsules. This overall preparation method is similar that applied by Magioncalda et al. (2004) and Baczynski et al. (2013; 2016). The Total Organic Carbon composition and the isotopic values were analyzed at UC Davis Stable Isotope Facility using an elemental analyzer (Elementar Vario EL Cube) interfaced with a continuous flow isotope ratio mass spectrometer (PDZ Europa 20-20), and precision/accuracy assessed using internal standards ($\pm 0.2\text{‰}$). All data are reported in standard delta-notation relative to VPDB. Replicates of samples in the Hanna Draw section ($n = 50$) display $\delta^{13}\text{C}$ values within $0.40\text{‰} \pm 0.6$ (1σ) of one another on average and a median offset of 0.2‰ . Replicates of unknown samples in Hanna Breaks section ($n = 75$) display $\delta^{13}\text{C}$ values within $0.3\text{‰} \pm 0.2$ (1σ) with median offsets of 0.2‰ .

RESULTS

Figures 2 and 3 show the up-section variability in

carbon isotope stratigraphy. $\delta^{13}\text{C}$ values have an average of $-27.3\text{‰} \pm 1.5\text{‰}$ (1σ) in the Hanna Draw section and an average of $-26.8\text{‰} \pm 1.1\text{‰}$ in the Hanna Breaks section. Both sections show a large spread in $\delta^{13}\text{C}$ values, with Hanna Draw ranging from -31.8‰ to -21.4‰ (10.4‰ range) and Hanna Breaks from -29.8‰ to -20.1‰ (9.8‰ range). Most lithologies display variations in $\delta^{13}\text{C}$ values, of less than 1.5‰ standard deviation in each stratigraphic section. However, the sandstones at Hanna Draw have an unusually high standard deviation of 2.55‰ . When $\delta^{13}\text{C}$ values and %C are plotted against one another for each section there does not seem to be a correlation between them, as indicated by very low R^2

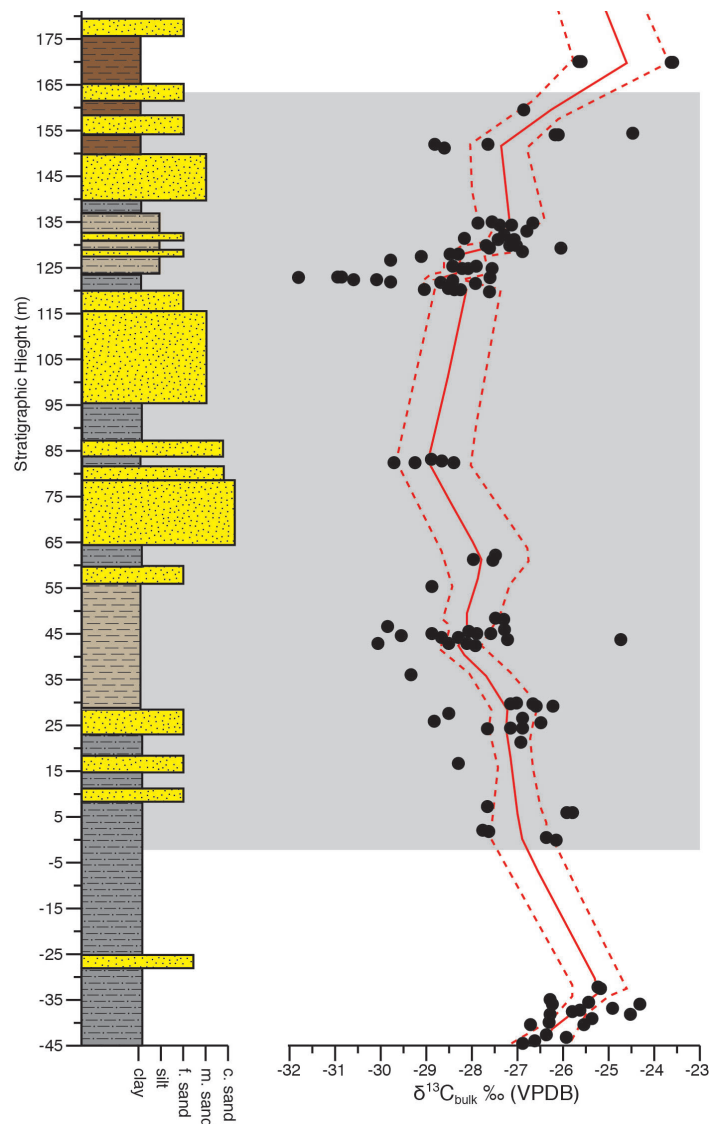


Fig. 2. Carbon isotope record through the Hanna Draw stratigraphic section. Red line is a LOESS smoothing average and dashed red line a 95% confidence interval. Grey zone demarks PETM interval.

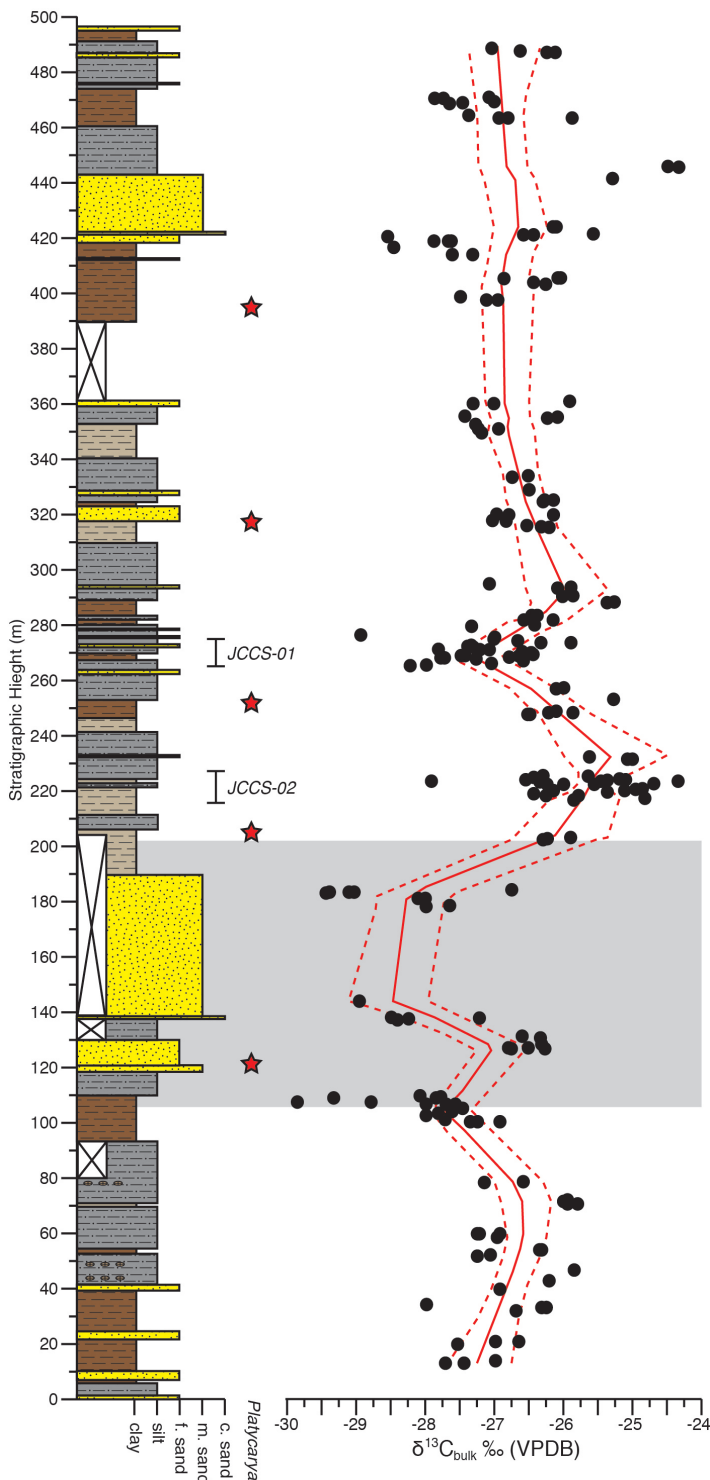


Fig. 3. Carbon isotope record through the Hanna Breaks stratigraphic section. Red line is a LOESS smoothing average and dashed red line a 95% confidence interval. Grey zone demarks PETM interval.

values of 0.11 and 0.008 for each stratigraphic section respectively (Fig. 4).

In each of the stratigraphic sections there is a high amount of variability in $\delta^{13}\text{C}$ values (Figs. 2 & 3), but

also structure to the carbon isotope records up-section. In the Hanna Draw area $\delta^{13}\text{C}$ values from the -40 to 0 m stratigraphic range from -24.3‰ to -26.8‰. Then the $\delta^{13}\text{C}$ value begin to decrease in the following 60 m to a lowest value of -30.1‰ at 42.75 m. This is then followed up by a large fluvial sand body. At the 120-meter level, $\delta^{13}\text{C}$ values starts to increase again up to the 180-meter level where the highest value of $\delta^{13}\text{C}$ is -21.42‰ is achieved at 159.75 m.

In the Hanna Breaks section between 0 and 100 meters $\delta^{13}\text{C}$ values range from -25.8‰ to -28.0‰. Over the next ten meters, carbon isotope values decrease, with the lowest value in the section (-29.8‰) occurring at 107.6 meters. This decrease is approximately five meters below the first major sandstone unit, after which carbon isotope values remain low, although variable (the most positive value in the section, -20.1‰ also occurs at 126.4 m), until the 183.92-meter level when $\delta^{13}\text{C}$ values increase again. Above 200 m, carbon isotope values become higher, with most values ranging from -24.3‰ to -28.0‰, but typically isotopically higher than those stratigraphically associated with the large fluvial sandbody.

The amount of organic carbon (%C) has an average of $5.7\% \pm 12.7\%$ in Hanna Draw and $2.9\% \pm 4.7\%$ in Hanna Breaks. Hanna Draw shows both greater variation and amount of %C. The major control on %C appears to be lithology. Coals and shales contain higher amounts of %C. Whereas the rest of Hanna Draw lithologies display significantly less %C in comparison, sandstones contain the least amount of %C. In the Hanna Breaks section %C shows a similar pattern. All %C have a relatively low standard

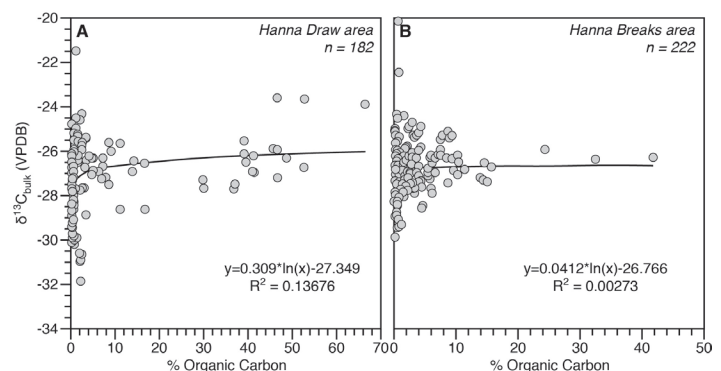


Fig. 4. Relationship between carbon isotope value and percent carbon at Hanna Draw (A) and Hanna Breaks (B).

deviation in comparison to the Hanna Draw and only shale has large $\delta^{13}\text{C}$ values. Sandstone continues to have the lowest values of $\delta^{13}\text{C}$.

DISCUSSION & CONCLUSIONS

$\delta^{13}\text{C}$ Variability

$\delta^{13}\text{C}$ can be influenced by several factors that could lead to variability in the data. Photosynthetic pathways (i.e., C3 versus C4) can affect $\delta^{13}\text{C}$ values by 14‰ causing data to overlap (O’Leary, 1988). However, only C3 photosynthesis plants were dominant in the Paleocene with C4 dominantly appearing in the Miocene (Cerling et al., 1993). This is further supported by $\delta^{13}\text{C}$ values only being in the ranges of expected C3 photosynthesis of -33‰ to -24‰ (O’Leary, 1988). Water stress and plant functional type (e.g., angiosperm versus gymnosperm) can also influence $\delta^{13}\text{C}$ values (Diefendorf et al., 2010; Kohn, 2010). Greater water stress leads to higher $\delta^{13}\text{C}$ values in plants and gymnosperms tend to exhibit lower $\delta^{13}\text{C}$ values than evergreen angiosperms (Diefendorf et al., 2010; Kohn, 2010). The only major change in precipitation/hydrologic change and vegetation overturn currently known in the Laramide region during the latest Paleocene is associated with the PETM itself (Wing et al., 2005). Both factors would be expected to produce a protracted increase in $\delta^{13}\text{C}$ values. This is not observed in the data. Instead greater than 1‰ of variability is observed over short stratigraphic intervals, sometimes even within a single bed or replicate samples. This suggests that something other than widespread hydrologic and vegetation changes are controlling $\delta^{13}\text{C}$ values. Preservation and diagenesis of plant matter present in our samples could also be the source of this $\delta^{13}\text{C}$ variation. By comparing the $\delta^{13}\text{C}$ and $\delta^{15}\text{N}$ and determining their relationship we can see if $\delta^{15}\text{N}$ is contributing to the change in $\delta^{13}\text{C}$. As diagenetic alteration occurs and increases a logarithmic relationship wherein decreases in $\delta^{15}\text{N}$ and higher $\delta^{13}\text{C}$ values should develop (Benner et al., 1987; Wing et al., 2005; Wynn et al., 2006; Wynn, 2007). Figure 4 illustrates the relationship between the two data sets, showing no strong relationship between $\delta^{13}\text{C}$ and $\delta^{15}\text{N}$. Thus, most of the small-scale variability in $\delta^{13}\text{C}$ values appears to be stochastic in character.

Identification of PETM

The PETM is an abrupt global warming event, less than 200 kyrs, and is preserved in marine records in a few stratigraphic meters (McInerney and Wing, 2011). In nonmarine strata its stratigraphic thickness can reach to over 40 meters (Magioncalda et al., 2004; Foreman et al., 2012). The greater thickness in nonmarine strata is likely related to higher overall sedimentation and subsidence rates. However, identifying the PETM is still nontrivial and requires additional chronostratigraphic constraints in addition to the aforementioned negative carbon isotope excursion. These commonly include magnetostratigraphic constraints, radiometric dates, and biostratigraphic constraints such as mammal and pollen fossils. Recently, colleagues have constrained the base of the Eocene within the Hanna Formation using the presence of *Platycarya*, an early Eocene indicator pollen taxa (Dechesne et al., in review). The first appearance of this Eocene indicator essentially co-occurs with the negative carbon isotope excursion observed in both our stratigraphic sections (Fig. 2 & 3). This strongly suggests this is the PETM, and it is bolstered by maximum depositional ages of ~ 54 Ma from U-Pb ages from detrital zircons stratigraphic higher in the column (Dechesne et al., in review).

The magnitude of the excursion is between $\sim 2\text{‰}$ to 4‰ in the Hanna Draw and Hanna Breaks sections. This compares well with the typical size of the PETM excursion magnitude from a variety of nonmarine bulk organic $\delta^{13}\text{C}$ values, which range from 2.2‰ to 4.6‰ (McInerney & Wing, 2011). The size of the excursion in the Hanna Formation is roughly the same as it is in the Bighorn Basin (Magioncalda et al., 2004) and Piceance Creek Basin (Foreman et al., 2012) to the north and south of the Hanna Basin. Interestingly, these two basins are dominated by red-bed paleosol development and well-drained conditions on the floodplain. These depositional environments are the opposite of those observed in the Hanna Formation, which indicate poorly drained, wet floodplains. The size of the magnitude is approximately the same in all three basins, but the baseline, absolute $\delta^{13}\text{C}$ values are lower in the Hanna Formation by 1-2‰. This offset is likely due to reduced water stress within the Hanna Formation as compared to the other basins (Kohn,

2010).

ACKNOWLEDGEMENTS

This material is based upon work supported by the Keck Geology Consortium and the National Science Foundation under Grant No. 1659322, as well as NSF grant EAR 145031 to Ellen Currano. I would also like to thank my fellow Keck researchers for assistance in the field, Christine Shonnard, Jake Polsak, Keifer Nace, Anthony Semararo, and Xavier Nogueira, project directors Ellen Currano and Brady Foreman, scientific collaborators Marieke Dechesne and Regan Dunn, and my campus advisor Joan Fryxell.

REFERENCES

- Baczynski, A.A., McInerney, F.A., Wing, S.L., Kraus, M.J., Bloch, J.I., Boyer, D.M., Secord, R., Morse, P.E., Fricke, H.C. 2013. Chemostratigraphic implications of spatial variation in the Paleocene-Eocene Thermal Maximum carbon isotope excursion, SE Bighorn Basin, Wyoming. *Geochemistry, Geophysics, Geosystems*, 14: 4133-4152.
- Baczynski, A.A., McInerney, F.A., Wing, S.L., Kraus, M.J., Morse, P.E., Bloch, J.I., Chung, A.H., Freeman, K.H. 2016. Distortion of carbon isotope excursion in bulk soil organic matter during the Paleocene-Eocene thermal maximum. *GSA Bulletin* 128: 1352-1366.
- Benner, R., Fogel, M.L., Sprague, E.K., Hodson, R.E. 1987. Depletion of ^{13}C in lignin and its implications for stable isotope studies. *Nature* 327, 708-710.
- Cerling, W.T., Quade Y.J. 1993. Global ecological change in the late Miocene: expansion of C4 ecosystems *Nature* 361: 344-345.
- Dechesne, M., Currano, E.D., Dunn, R.E., Higgins, P., Hartman, J.H., Chamberlain, K.R., Holm-Denoma, C.S. in review, *Geosphere*. Depositional patterns of the fluvial to paludal strata of the Hanna Formation across the Paleocene-Eocene boundary, Hanna Basin, Wyoming.
- Diefendorf, A.F., Mueller, K.E., Wing, S.L., Koch, P.L., Freeman, K.H. 2010. Global patterns in leaf ^{13}C discrimination and implications for studies of past and future climate. *PNAS* 107: 5738-5743.
- Dobbin, C. E., Bowen, C. F., Hoots, H. W. 1929. Geology and coal and oil resources of the Hanna and Carbons basins, Carbon County, Wyoming. *U.S. Geological Survey Bulletin* 804: 88 p.
- Foreman B., Clementz M.T., Heller P.L. 2012. Evaluation of paleoclimatic conditions east and west of the southern Canadian Cordillera in the mid-late Paleocene using bulk organic $\delta^{13}\text{C}$ records. *Palaeogeography, Palaeoclimatology, Palaeoecology* 376: 103-113.
- Jahren, A.H., Arens, N.C., Harbeson, S.A., 2008. Prediction of atmospheric $\delta^{13}\text{C}\text{O}_2$ using fossil plant tissues. *Reviews of Geophysics* 46, RG1002.
- Koch, P. 1998. Isotopic reconstruction of past continental environments. *Annual Reviews of Earth and Planetary Sciences* 26: 573-613.
- Kohn, M.J., 2010. Carbon isotope compositions of terrestrial C3 plants as indicators of (paleo) ecology and (paleo)climate. *PNAS* 107: 19691-19695.
- Lillegraven, J.A., Snoke, A.W. 1996. A new look at the Laramide orogeny in the Seminoe and Shirley mountains, Freezeout Hills, and Hanna Basin, south-central Wyoming. *Wyoming State Geological Survey Public Information Circular* no. 36, 52 p.
- Magioncalda, R., Dupuis, C., Smith, T., Steurbaut, E., Gingerich, P., 2004. Paleocene–Eocene carbon isotope excursion in organic carbon and pedogenic carbonate: direct comparison in a continental stratigraphic section. *Geology* 32: 553-556.
- McInerney, F., Wing, S. 2011. The Paleocene-Eocene thermal maximum: a perturbation of carbon cycle, climate, and biosphere with implications

for the future. *Annual Reviews of Earth and Planetary Sciences* 39: 489-516.

Midwood, A.J., Boutton, T.W., 1998, Soil carbonate decomposition by acid has little effect on $\delta^{13}\text{C}$ of organic matter. *Soil Biology and Biochemistry* 30(10/11): 1301-1307.

O'Leary, M.H., 1988. Carbon isotopes in photosynthesis. *BioScience* 38: 328-336.

Secord, R. 1998. Paleocene mammalian biostratigraphy of the Carbon Basin, southeastern Wyoming, and age constraints on local phases of tectonism. *Rocky Mountain Geology* 33: 119-154.

Wynn, J.G. 2007. Carbon isotope fractionation during decomposition of organic matter in soils and paleosols: implications for paleoecological interpretation of paleosols. *Palaeogeography, Palaeoclimatology, Palaeoecology* 251: 437-448.

Wynn, J.G., Bird, M.I., Wong, V.N.L. 2005. Rayleigh distillation and the depth profile of $^{13}\text{C}/^{12}\text{C}$ ratios of soil organic carbon from soils of disparate texture in Iron Range National Park, Far North Queensland, Australia. *Geochimica et Cosmochimica Acta* 69: 1961-1973.

Wynn, J.G., Harden, J.W., Fries, T.L. 2006. Stable carbon isotope depth profiles and soil organic carbon dynamics in the lower Mississippi Basin. *Geoderma* 131: 89-109.

Wing, S.L., Harrington, G.J., Smith, F.A., Bloch, J.I., Boyer, D.M., Freeman, K.H. 2005. Transient floral change and rapid global warming at the Paleocene-Eocene boundary. *Science* 310(5750): 993-996.

Wroblewski, A. 2002. The Role of the Hanna Basin in Revised Paleogeographic Reconstructions of the Western Interior Sea During the Cretaceous-Tertiary Transition. Wyoming Geological Association Guidebook. 2002 Field Conference, p. 17-40.

VEGETATION STRUCTURE AND LITHOLOGY RESPONSE TO THE PALEOCENE-EOCENE THERMAL MAXIMUM IN THE HANNA BASIN, WYOMING

KEIFER NACE, Whitman College
Research Advisor: Pat Spencer

INTRODUCTION

The Paleocene-Eocene Thermal Maximum (PETM), a rapid global warming event ~56 million years ago caused by a large release of isotopically-light carbon into earth's atmosphere and oceans, provides geologic parallels to anthropogenic climate change. Thousands of petagrams of carbon were released in less than 20ka, causing a global negative carbon isotopic excursion (CIE), ocean acidification, a 5-8° C increase in global temperatures, and at least a doubling of atmospheric CO₂ levels (McInerney & Wing, 2011). In midlatitude continental interiors, increased temperatures led to lower mean annual rainfall, causing more seasonally dry conditions and increased water stress (Kraus et al., 2015). PETM sandstones in both the Bighorn and Piceance Creek Basin record changes in fluvial systems, likely caused by changes in sediment flux, increased variability of precipitation, reductions in vegetation cover, or some combination of these (Foreman et al., 2012; Foreman, 2014). Few extinctions occurred during the PETM, but terrestrial and marine organisms experienced major shifts in geographic ranges, changes in food sources, and rapid evolution (McInerney & Wing, 2011). The best record of plant responses to PETM environmental change to date comes from the Bighorn Basin in northwestern Wyoming. Wing et al. (2005) demonstrated a decrease in leaf size, reflecting an increase in water stress. Taxonomic analyses showed a distinct difference in flora composition during the PETM versus directly before or after (Wing & Currano, 2013). Conifers and a combination of deciduous and evergreen broad-leaved families were the primary pre- and post-PETM megaflores; PETM megaflores lack conifers but were

abundant in the dry-tolerant Fabaceae family (Wing et al. 2005; Wing & Currano, 2013; Smith et al. 2007). During the CIE recovery, many typical Paleocene plants returned, implying that the plant populations were able to migrate to refugia during the Thermal Maximum (Wing & Currano, 2013).

Paleobotanic and sedimentologic studies have documented taxonomic turnover as well as hypothesized that vegetation cover decreased during the PETM. Here, we use Leaf Area Index [LAI = foliage area (m²) / ground area (m²)] to quantitatively reconstruct, for the first time, vegetation structure before, during, and after the PETM. Vegetation structure, the three-dimensional architecture of a plant community, is crucial to ecosystems, impacting fluvial systems, soil temperature and moisture, erosion, plant and animal compositions, and the hydrologic and carbon cycles (Dunn, et al., 2015). Modern LAI values range from 0 (open canopy) to 6 (dense canopy) (Dunn et al., 2015). Reconstructed LAI (rLAI) modeling is based on the sun's impact on the leaf epidermis. In shaded environments, epidermal cells are larger, more elliptical, and have more undulatory cell walls than cells exposed to the sun. Since vegetation structure is directly related to light, larger, more elliptical, and more undulatory cells are likely to be associated with a dense canopy rather than with an open forest. A relationship between the morphology of leaf epidermal cells and LAI was first established using phytoliths (Dunn et al. 2015), and later expanded to use fossil cuticle, which is preserved in depositional environments that do not preserve phytoliths (Dunn et al., personal communication). A modern calibration set of Costa Rican soils collected from a wide range of LAI conditions was used to

establish these relationships (Dunn et al. 2015).

GEOLOGIC SETTING

The Hanna Basin, located in south-central Wyoming, is a Laramide basin with a high sedimentation rate, preserving a thick sequence of Cretaceous to Eocene sedimentary strata (Gill et al., 1970). The Hanna Formation, made up of alternating drape coal beds, bodies of carbonaceous shale and mudstone, and sand bodies, contains the Paleocene-Eocene boundary. The basin serves as an important record of the vegetation and fluvial systems in a generally humid environment, compared to the well-studied, seasonally dry Bighorn Basin. Since the Hanna Basin was at midlatitude, in the continental interior, it is possible that it endured similar effects of the PETM as the Bighorn Basin and in the Piceance Creek Basin, including a warmer, seasonally dryer climate with increased monsoonal precipitation. We hypothesize that the Hanna Basin will show a less dense vegetation structure (lower LAI value) during the PETM than before and after, due to a drier climate and increased water stress on plants.

METHODS

Bed by bed descriptions of grain size, grain shape, sedimentary structures, color, clay content, and organic matter were recorded. Sections and bed thicknesses were measured using a Jacob's staff. During the PETM, there is a significant lithological change from predominantly fine-grained sediments to laterally extensive, multistory sandstone beds (Dechesne et al., in review). Therefore, in order to isolate the effects of lithological and PETM climate changes on vegetation structure, sections were chosen before and after the PETM that include large sandstone beds. The pre-PETM section includes a large, laterally extensive sheet sand, and the post-PETM section includes both a smaller, lenticular channel and a large, laterally extensive sheet sand.

Samples of fine-grained, organic-rich rocks were collected from the three sections for LAI analysis. Four samples were analyzed from the pre-PETM section, and ten samples were analyzed from the post-PETM section. Nineteen samples, 16 of which occur within the negative carbon isotope excursion, were

collected and analyzed for the PETM section between 2016-2018 (Dunn et al., 2018). To isolate leaf cuticles from the matrix, fragments of the collected rock samples were sent to Global Geolabs for palynological processing. Leaf cuticles were examined through a Leica compound light microscope and photos of the cuticles were taken with a Vernier camera at 40x magnification. The photographed cuticles were traced using a Wacom tablet and morphometric measurements were made using ImageJ. Seventy-five photos were taken and about 300 epidermal cells were traced and measured for each sample. LAI was quantified using Dunn et al.'s (2018) cuticle calibration dataset and the following relationship includes aspect ratio ($AR = \text{major} / \text{minor axis}$) and undulation index ($UI = \text{epidermal cell circumference} / \text{circumference of the circle with the same area as the cell}$)

$$rLAI = 4.05(\text{mean UI}) + 15.32(\text{mean AR}) - 25.38$$

Eq. 1

Fresh, organic-rich rock samples, exposed through trenching, were collected for carbon isotope analyses. Six samples were taken from the pre-PETM, 155 samples from the PETM, and 32 samples from the post-PETM sections. The preparation process for bulk organic carbon isotope ($\delta^{13}\text{C}$) measurements included powdering samples using a mortar and pestle, treating samples in two HCl baths to dissolve all carbonates, and weighing dry samples into tin capsules, as in Aziz et al. (2008) and Baczynski et al. (2013; 2016). The total organic carbon (TOC) and the carbon isotopic values were measured at UC Davis Stable Isotope Facility using an elemental analyzer (Elementar Vario EL Cube) interfaced to a continuous flow isotope ratio mass spectrometer (PDZ Europa 20-20). Precision/accuracy was assessed using internal standards and all data were reported in standard delta-notation relative to VPDB.

RESULTS

Fig. 1 presents stratigraphically related lithology, rLAI, and $\delta^{13}\text{C}$ values before the PETM. The first 38 meters of section preserve interbedded meandering sandstone channel sequences, shales, and mudstones. At 38 meters in the section, a large, 47-meter-thick

Pre-PETM Lithology, rLAI, and $\delta^{13}C$

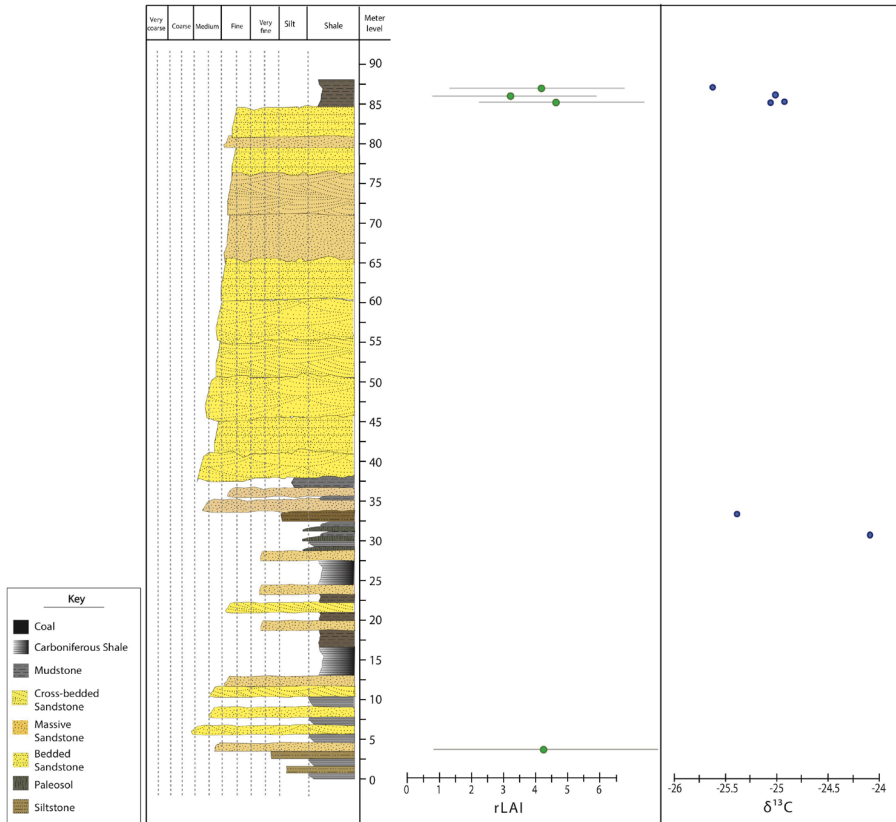


Figure 1. Pre-PETM lithology, rLAI, and $\delta^{13}C$ values.

PETM Lithology, rLAI, and $\delta^{13}C$

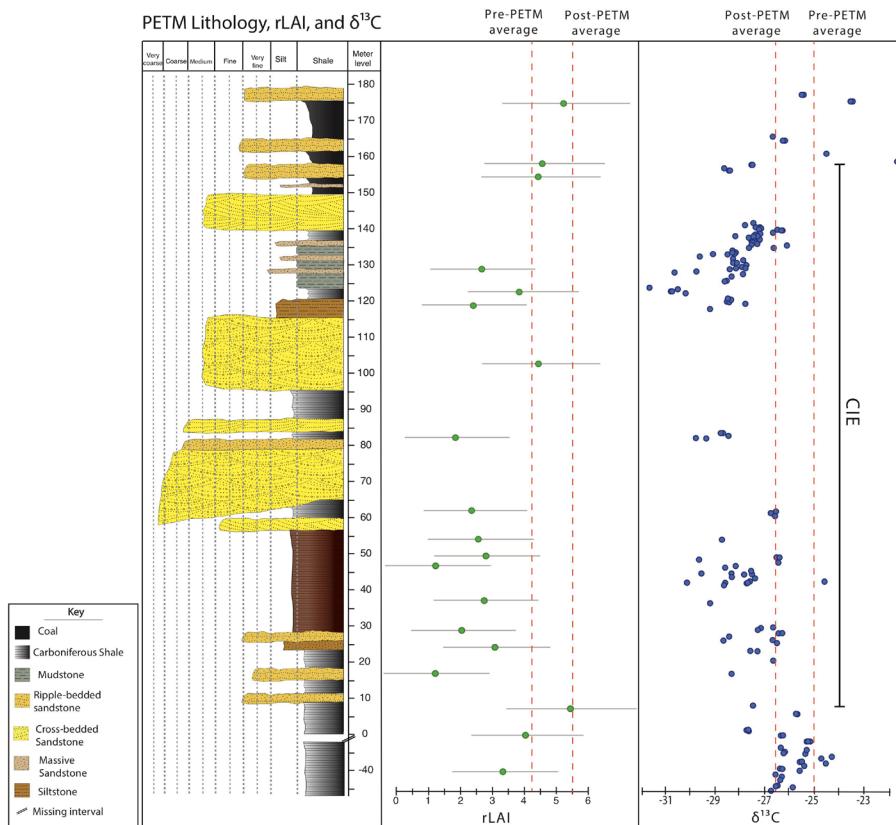


Figure 2. PETM lithology, rLAI, and $\delta^{13}C$ values. Pre- and Post-PETM rLAI and $\delta^{13}C$ averaged values are indicated by the red dotted lines, and the CIE is marked by the black line.

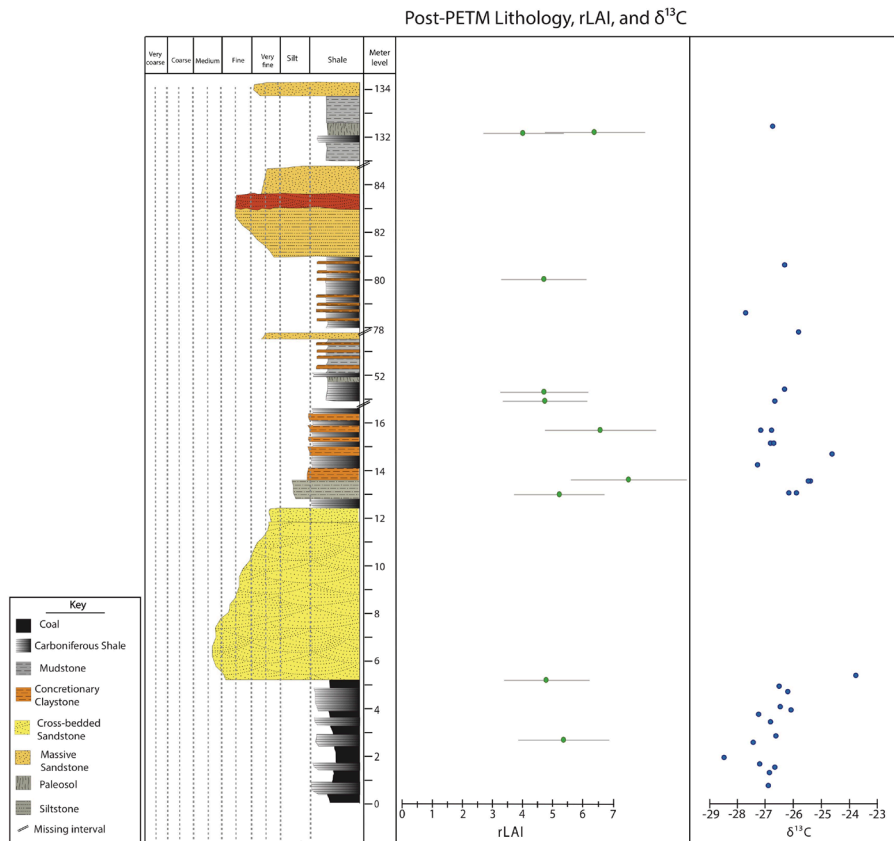


Figure 3. Post-PETM lithology, rLAI, and $\delta^{13}\text{C}$ values

bedded sheet sandstone is present, followed by mudstone to the top of the section. rLAI values ranged from 3.9 to 4.6, with an average value of 4.2 ± 2.0 . $\delta^{13}\text{C}$ values averaged -25.03‰ with a narrow range from -25.60‰ to -24.18‰ (1.42‰ range). TOC also displayed a narrow range from 7.4% to 11.4% (4% range) with a mean value of 9.39%.

Lithology, rLAI, and $\delta^{13}\text{C}$ values from the PETM section are presented in Figure 2. The first 60 meters of this section is primarily carbonaceous shale. At 10 meters, $\delta^{13}\text{C}$ decreases marking the onset of the CIE, and the lowest rLAI value (1.2) occurs at 16.5 meters. In the middle of the CIE, at 65 meters, a 17-meter-thick coarse-grained, braided channel sequence is deposited, followed by interbedded shale and sand deposits (Semeraro et al., 2019). A second, 21-meter-thick braided channel is present at 96 meters, and 23 meters of fine-grain deposits of siltstone, shale, and mudstone come after. At 140 meters, a third coarse-grained braided channel accumulated over 11 meters. Fine-grained sands interbedded with coal complete the section at 178 meters, with the CIE terminating at 157 meters. During the CIE, the mean rLAI value was 3.0 ± 1.9 , with a range from 1.2 to 4.6. Bulk organic

carbon isotope values during the CIE displayed a range from -31.83‰ to -24.76‰ (7.07‰ range) with an average of -28.08‰ . TOC show a large range from 0.11% to 36.74% (36.36% range) with a mean value of 1.04%.

The base of the post-PETM section is dominated by interbedded coals and carbonaceous shales (Fig. 3). At meter five in the section, a seven-meter-thick lenticular sand channel coarsens upwards and is bounded by a carbonaceous shale and concretionary claystone sequence. The missing interval break in the stratigraphic section between 16.6 meters and 51.1 meters is dominated by a similar shale and claystone sequence. Between 51.1 and 54 meters, the lithology is dominated by a mudstone and concretionary claystone sequence and is capped by a small, very fine-grained sandstone bed. After the sandstone, within the missing interval and through to 81 meters in the section, the lithology consists of the shale and concretionary claystone sequence. The last shale bed grades into a siltstone and then to a cross-bedded sandstone at 85 meters. Between 85 and 130 meters, a 45-meter-thick sheet sandstone is present, followed by mudstone dominated lithology. Post-PETM, rLAI values range

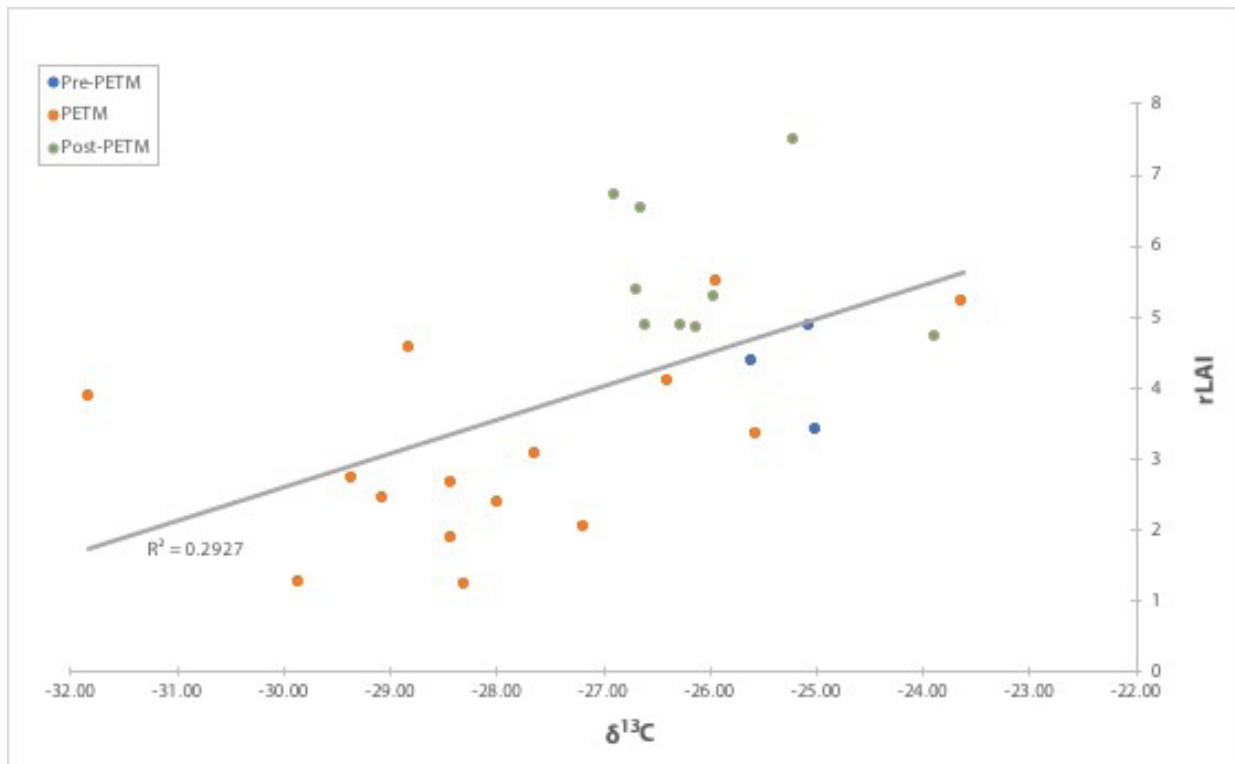


Figure 4. Correlation of rLAI and $\delta^{13}C$ values

from 4.1 to 7.5 with a mean value of 5.5 ± 2.0 . $\delta^{13}C$ values average to be -26.7‰ , and ranged from -28.56‰ to -23.89‰ (4.67‰ range). TOC values demonstrate a wide range from 0.51% to 66.24% (65.73% range) with a mean value of 16.07%.

Figure 4 illustrates the correlation between rLAI and $\delta^{13}C$, showing that the more negative $\delta^{13}C$ values relate to lower rLAI values; however, this relationship is weak ($R^2=0.29$). No relationship is present between TOC and rLAI.

DISCUSSION

Prior to the PETM, our section demonstrates a meandering fluvial system, with floodplain deposits of shales and mudstones interbedded with thin sandstone splays. The 47-meter-thick sandstone within the section represents a meandering point bar lateral accretion and is followed by flood plain deposits. Meandering rivers systems require bank strength, often stabilized by vegetation (Braudrick et al., 2009; Schumm, 1985), and rLAI values of 3.9 to 4.6 provide evidence for vegetated bank stabilization. Our post-PETM section preserves a swampy, densely forested environment, as indicated by abundant

coals and carbonaceous shales and the highest rLAI values in our dataset. Swamp facies are occasionally interrupted by sand deposits. The post-PETM section transitions back to a meandering system as indicated by the 45-meter-thick, laterally extensive sandstone with fine floodplain deposits. The meandering channel sequences pre- and post- do not cause a decrease in rLAI within the PETM, but the elevated values combined with the meandering channels indicate stable, vegetated banks prior to and after the recovery of the PETM.

The PETM caused significant changes to vegetation structure and fluvial systems within the Hanna Basin. During the CIE, rLAI values decreased (average rLAI = 3.0), indicating a more open canopy environment in contrast to before (4.2) and after (5.5). Importantly, the decrease in rLAI occurs before the first laterally extensive channel, suggesting that the reduction in rLAI was a result of climate change rather than a change of fluvial systems. Other PETM sites within continental interiors show a decrease in mean annual precipitation (Kraus et al., 2015) or increased monsoonal precipitation (Forman et al. 2012), both of which can significantly affect vegetation. During periods with higher temperatures, seasonal changes

in precipitation led to water stress, changes in phenology, and decreased biomass. The effects of extreme precipitation in mesic sites led to a decrease in soil water content and above-ground primary productivity of plants (Zeppel et al., 2014). The shift to a potentially braided channel system after rLAI decreases may be the result of bank destabilization due to the decrease in vegetation. In addition, braided systems require high discharge and sediment loads (Tucker & Slingerland, 1997). An increase in seasonally extreme precipitation events could account for higher discharge rates, whereas increased erosion from destabilized banks could explain increase sediment loads.

Correlation testing revealed rLAI and $\delta^{13}\text{C}$ to be weakly related. Diefendorf et al. (2010) found that Δleaf (the offset between $\delta^{13}\text{C}_{\text{atm}}$ and $\delta^{13}\text{C}_{\text{leaf}}$) values in C3 plants decrease with reduction of water availability and with increased water-efficiency use. Furthermore, a decrease in Δleaf values would indicate an increase in $\delta^{13}\text{C}$ values, which differs from our findings. Our results indicate a decrease in $\delta^{13}\text{C}$ values with a decrease in water availability. This difference in results indicates that chance may play a role in the negative carbon isotope excursion during the PETM as opposed to a positive isotope excursion. In addition, the correlation between rLAI and $\delta^{13}\text{C}$ could be driven by the radical taxonomical change from a mixed angiosperm/conifer flora to an angiosperm dominated flora during the PETM (Smith et al., 2007).

CONCLUSION

In this study we evaluated the interaction of climate and fluvial system changes on vegetation structure. During the PETM, vegetation became less dense due to warmer, more seasonally dry conditions with periods of extreme precipitation. Reductions in vegetation potentially caused a shift from meandering to braided fluvial systems. Post-PETM, a swampy, densely forested environment is preserved, and eventually transitions back to a meandering fluvial system, similar to the pre-PETM environment. This reconstruction of climatic effects on vegetation and fluvial systems adds to studies conducted within midlatitude continental interiors, such as in the Bighorn Basin and Piceance Creek Basin. Further

megafloora paleobotany research could add to the larger picture of vegetation and climate within the Hanna Basin. Understanding vegetation structure response to the PETM illustrates a portrait of possible modern vegetation reactions to anthropogenic climate change.

ACKNOWLEDGEMENTS

This material is based upon the work supported by the Keck Geology Consortium and the National Science Foundation Grant No. 1659322, as well as NSF grant EAR 145031 to Ellen Currano. Thank you to the project directors, Ellen Currano and Brady Foreman, for your continuous support throughout the project, and also thank you, Regan Dunn and Marieke Dechesne for sharing your expertise. My love for the field and curiosity to learn the stories of ancient landscapes has been ignited by your guidance and encouragement. I would also like to thank Pat Spencer and the Whitman College Geology department for your assistance as well as the ASWC Travel and Student Development Fund for sponsoring my flight to GSA regional meeting. Finally, thank you to James Chisholm, Xavier Nogueira, Anthony Semeraro, Christine Shonnard, and especially Jake Polsak for your great company while digging trenches, tracing cuticles, and cooking field meals.

REFERENCES

- Aziz HA, Hilgen FJ, van Luijk GM, Sluijs A, Kraus MJ, et al. (2008). Astronomical climate control on paleosol stacking patterns in the upper Paleocene-lower Eocene Willwood Formation, Bighorn Basin, Wyoming. *Geology*, vol. 36, pp. 531–34.
- Baczynski, A.A., McInerney, F.A, Wing, S.L., Kraus, M.J., Bloch, J.I., Boyer, D.M., Secord, R., Morse, P.E., & Fricke, H.C. (2013). Chemostratigraphic implications of spatial variation in the Paleocene-Eocene Thermal Maximum carbon isotope excursion, SE Bighorn Basin, Wyoming. *Geochemistry, Geophysics, Geosystems*, vol. 14, pp. 4133-4152. doi: <https://doi.org/10.1002/ggge.20265>
- Baczynski, A.A., McInerney, F.A, Wing, S.L., Kraus,

- M.J., Morse, P.E., Bloch, J.I., Chung, A.H., & Freeman, K.H. (2016). Distortion of carbon isotope excursion in bulk soil organic matter during the Paleocene-Eocene thermal maximum. *GSA Bulletin*, vol. 128, pp. 1352–1366. doi: <https://doi.org/10.1130/B31389.1>
- Braudrick, C. A., W. E. Dietrich, G. T. Leverich, and L. S. Sklar (2009), Experimental evidence for the conditions necessary to sustain meandering in coarse bedded rivers, *National Academy of Sciences*, vol. 106, no. 40, pp. 16936-16941. <https://www.jstor.org/stable/40485114>
- Dechesne, M., Currano, E.D., Dunn, R.E., Higgins, P., Hartman, J. H., Chamberlain, K.R., & Holm-Denoma, C.S. (In review). Depositional patterns of the fluvial to paludal strata of the Hanna Formation across the Paleocene – Eocene boundary, Hanna Basin, Wyoming. *Geosphere*.
- Diefendorf AF, Mueller KE, Wing SL, Koch PL, Freeman KH. (2010). Global patterns in leaf ^{13}C discrimination and implications for studies of past and future climate. *Proc. Natl. Acad. Sci. USA*, vol. 107, pp. 5738–43.
- Dunn, R.E., Currano, E.D., Dechesne, M., & Foreman, B.Z. (2018). Forest canopy response to greenhouse warming at the Paleocene-Eocene Thermal Maximum. *GSA Annual Meeting*, Indianapolis.
- Dunn, R.E., Strömberg C.A.E., Madden, R.H., Kohn, M.J., Carlini, A.A. (2015). Linked canopy, climate, and faunal change in the Cenozoic of Patagonia. *Science*, vol. 347, no. 6219, pp. 258-261.
- Foreman, B.Z. (2014). Climate-driven generation of a fluvial sheet sand body at the Paleocene–Eocene boundary in north-west Wyoming (USA). *Basin Research*, vol. 26, pp. 25–241. doi: [10.1111/bre.12027](https://doi.org/10.1111/bre.12027).
- Foreman, B.Z., Heller, P.L., & Clementz, M.T. (2012). Fluvial response to abrupt global warming at the Paleocene/Eocene boundary. *Nature*, vol. 491, pp. 92-95.
- Gill, J.R., Merewether, E. A. & Cobban, W. A. (1970). Stratigraphy and Nomenclature of Some Upper Cretaceous and Lower Tertiary Rocks in South-Central Wyoming. *USGS Report*. doi: [10.3133/pp667](https://doi.org/10.3133/pp667)
- Kraus, M.J., Woody D.T., Smith J.J., Dukic, V. (2015). Alluvial response to the Paleocene–Eocene Thermal Maximum climatic event, Polecat Bench, Wyoming (U.S.A.). *Palaeogeography, Palaeoclimatology, Palaeoecology*, vol. 435, pp. 177-192.
- McInerney, F.A. & Wing, S.L. (2011). The Paleocene-Eocene thermal maximum: a perturbation of carbon cycle, climate, and biosphere with implications for the future. *Annu. Rev. Earth Planet. Sci.*, vol. 39, pp. 489–516.
- Schumm, S.A. (1985). Patterns of alluvial rivers. *Annu. Rev. Earth Planet Sci.*, vol. 13, pp. 5-27.
- Semeraro, A., Currano, E.D., Foreman, B.Z. (2019). Paleocurrent variability in meandering and braided river systems: modern calibrations and stratigraphic case studies spanning the Paleocene-Eocene Thermal Maximum. *Proceedings of the Keck Geology Consortium*, v. 32.
- Smith, F.A., Wing, S.L. & Freeman, K.H. (2007). Magnitude of the carbon isotope excursion at the Paleocene-Eocene Thermal Maximum: the role of plant community change. *Earth Planet. Sci. Lett.*, vol. 262, pp. 50–65.
- Tucker, G.E. & Slingerlan, R. (1997). Drainage basin responses to climate change. *Water Resources Research*, vol. 33, pp. 2031-2047.
- Wing, S.L. & Currano, E.D. (2013). Plant Response to Global Greenhouse Event 56 Million Years Ago. *American Journal of Botany*, 100 (7), 1-21. doi: [10.3732/ajb.1200554](https://doi.org/10.3732/ajb.1200554)
- Wing SL, Harrington GJ, Smith FA, Bloch JI, Boyer DM, Freeman KH. 2005. Transient floral change and rapid global warming at the Paleocene-Eocene boundary. *Science*, vol. 310, pp. 993–96.

Zeppel, M.J.B, Wilks, J.V., & Lewis, J.D. (2014).
Impacts of extreme precipitation and
seasonal changes in precipitation on plants.
Biogeosciences, vol. 11, pp. 3083–3093.

PROVENANCE OF FLUVIAL AND DELTAIC SANDSTONES ACROSS THE PALEOCENE-EOCENE BOUNDARY, HANNA BASIN, WYOMING

XAVIER ROJAS NOGUEIRA, Temple University
Research Advisor: Jesse Thornburg

INTRODUCTION

South-central Wyoming's Hanna Basin contains many sandstone bodies deposited during to Paleocene through Eocene across the basin separated by periods finer grained lacustrine, overbank, and coal swamp deposition. These sandstone bodies were deposited primarily in fluvial and deltaic environments and contain sediment eroded of the surrounding upland regions (Wroblewski, 2002; Dechesne et al., in review). This study characterizes the relative mineralogical proportions of 25 Hanna Basin sandstone samples in order to improve interpretations of Hanna Basin paleo-drainage and possible climatic forcing during the Paleocene-Eocene Thermal Maximum, a major global warming event that occurred 56 Ma. Paleo-flow measurements were taken for the fluvial sandstone bodies to add context to the grain mineralogy data and more accurately associate sediment with potential upland sources.

BACKGROUND

The Hanna Basin

The Hanna Basin is a sedimentary basin in south central Wyoming (Fig. 1). It was formed during the Laramide Orogeny, which segmented the Sevier foreland basin of the United States into a series of intramontane basins during the latest Cretaceous into the Paleogene (Dickinson et al., 1988). Basement-involved uplifts caused the flexural subsidence of the adjacent crust and generated accommodation space that was then filled by sediment eroded off the evolving mountain ranges (Dickinson et al., 1988; Weil et al., 2016). This history of unroofing

and uplift is recorded in provenance changes within alluvial strata in the adjacent sedimentary basins. The Hanna Basin preserves over 12,500 meters of Cambrian through Miocene sedimentary strata including anomalously thick Paleocene and Eocene strata of the Hanna Formation that reaches 3500 meters (Wroblewski, 2002). The age of the Hanna Formation is constrained by scattered mammal fossils, palynology, and U-Pb detrital zircon geochronologic maximum depositional ages and is likely between 62 Ma at the base and slightly younger than 54 Ma at the top (Wroblewski, 2002 and references therein; Dechesne et al., in review). Strata varies across the

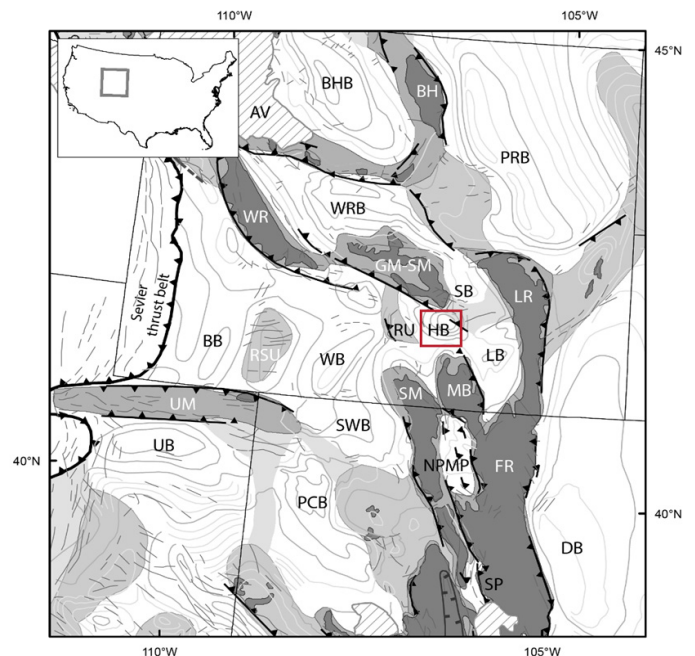


Figure 1. A regional geologic map showing the Hanna Basin relative to the surrounding upland areas and basins (Dechesne et al., in review). Important abbreviations include Hanna Basin (HB), Medicine Bow Mountains (MB), Sierra Madre Mountains (SM), Rock Springs Uplift (RSU), Granite Mountains-Seminole Mountains (GM-SM), and Laramie Basin (LB).

basin predominantly including, but not limited to, swampy coal beds, lacustrine siltstones, carbon rich overbank deposition, and fluvial and deltaic sandstone bodies (Lillegraven and Snoke, 1996; Secord, 1998; Wroblewski, 2002; Dechesne et al., in review). The sandstone bodies are commonly tabular or lenticular in form, and relatively resistant to weathering causing outcrops to protrude from the otherwise weathered fine-grained deposits.

The Paleocene-Eocene Thermal Maximum

The Paleocene-Eocene Thermal Maximum (PETM) was a geologically abrupt perturbation of the global carbon cycle and climate system that occurred 56 million years ago (McInerney & Wing, 2011). Average annual temperatures were raised by 5-8° for about 200 kyrs, a phenomenon that extensively affected the biosphere as well as atmospheric and oceanic circulation (McInerney & Wing, 2011). The PETM is associated with a release of isotopically light carbon into the atmosphere and oceans and expressed as a significant negative carbon isotope excursion in both marine and nonmarine proxies, and has been investigated as a possible analog for modern anthropogenic climate change (McInerney, & Wing, 2011). There are relatively few nonmarine stratigraphic sections wherein the PETM has been identified, but, where it has been identified there appear to be distinct fluvial responses. Specifically, researchers have observed an increase in fluvial channel-density, the size of fluvial sandbodies, river flow depths and widths, as well as an increase in the grain size of sediment transported by rivers during the PETM (Foreman et al., 2012; Foreman, 2014; Schmitz and Pujalte, 2007). Foreman et al. (2012) and Foreman and Rasmussen (2016) were able to constrain the provenance of sediment within the Piceance Creek Basin of northwest Colorado to isolate a climatic influence of river deposition, as well as characterize basin-scale paleodrainage conditions. This study represents a first step towards such an endeavor within the Hanna Basin of south-central Wyoming.

METHODS

In order to observe possible changes in provenance as recorded in sandstone mineralogy, we obtained 25

sandstone samples from sandbodies from over 1000 meters of stratigraphic section in the basin. These include samples from the basal fluvial sandbody through minor sandbodies overlying “Camp Channel”, which is associated with Coal 86 and Coal 87 of Dobbin et al. (1929). Samples were selected to capture different ages and depositional environments within the basin. In the field, sample selection favored medium to coarse grained sandstones with little to no diagenetic features, each sample location was recorded with GPS. Samples were taken from the sand bodies representing Paleocene deposition (n=11), Eocene deposition (n=10), and four were taken from a multi-tiered sand body within a stratigraphic interval representing PETM deposition (Dechesne et al., in review). In addition, we included seventeen samples from large fluvial depositional environments, four deltaic samples, one marginal lacustrine channel sample, and three from a channelized deltaic environment. Thin sections were made from the sandstone samples, and we applied the Gazzi-

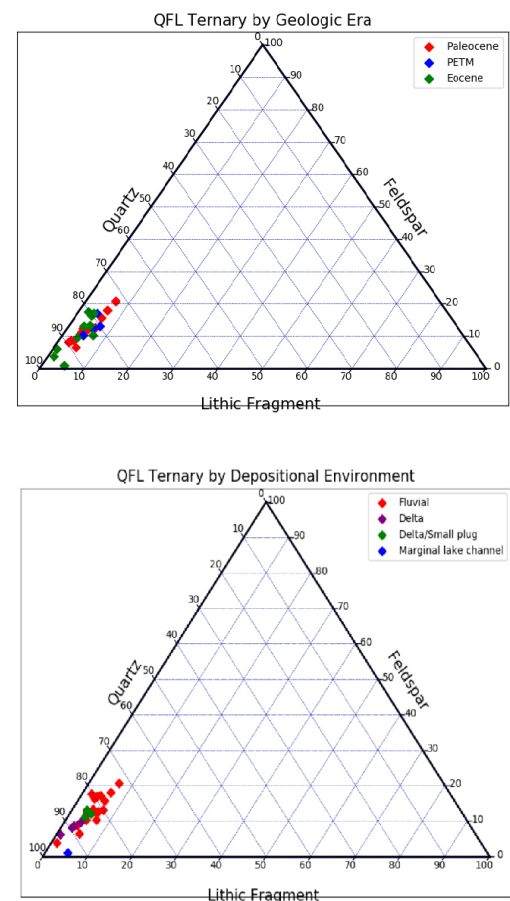


Figure 2. QFL Ternary plots showing the mineralogical proportions of the point counted sandstone samples sorted by age, depositional environment, and average paleo-flow direction.

Dickinson method point counting 400 minerals per slide documenting the relative abundance of mono- and poly-crystalline quartz, plagioclase, potassium feldspar, and lithic fragments (igneous, sedimentary, and metamorphic) as well as minor accessory minerals such as micas and minor amphiboles. The minerals were then grouped in accordance with the methodology applied by Dickinson (1970), with sedimentary, igneous, and metamorphic rock clasts categorized as lithics, poly- and mono-crystalline quartz clasts classified as Quartz and Plagioclase and Potassium Feldspar classified as Feldspar to plot each sample sorted by age and depositional environment into QFL ternary plots.

To supplement the mineralogical data, 284 paleo-flow measurements were taken from the fluvial deposited sandstone bodies by recording the strike and dip of unaltered trough cross bedding. The paleo-flow measurements for each horizontally continuous sand body were digitally averaged into a single azimuth, vector value.

RESULTS

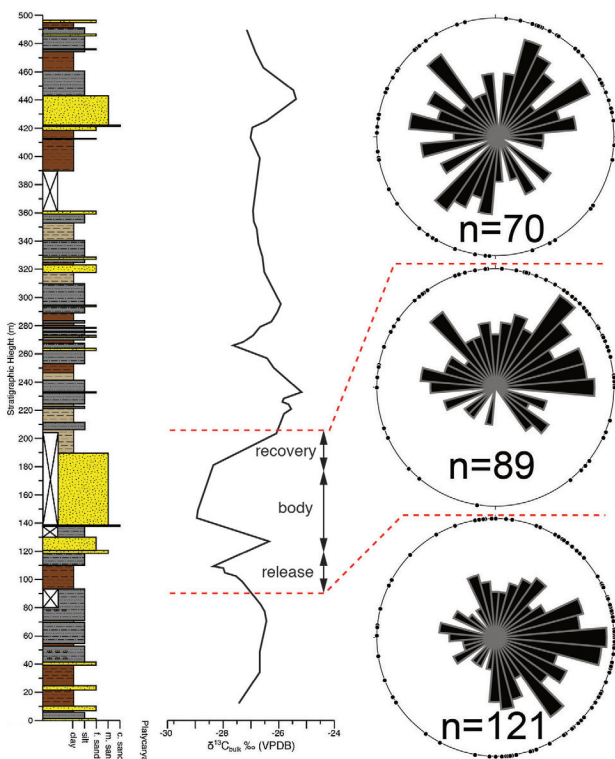


Figure 3. Paleocurrent rose diagrams spanning the Paleocene-Eocene Thermal Maximum and accompanying stratigraphic section and carbon isotope record.

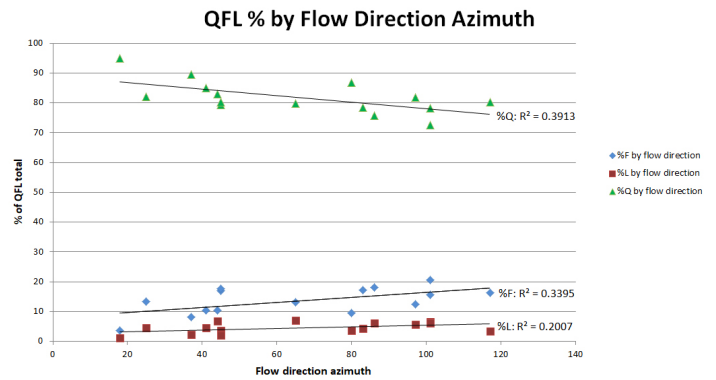


Figure 4. Linear regression of fluvially deposited sandstone samples' QFL proportions explained by the sand body average paleo-flow direction.

The descriptive statistics of the QFL proportion varied somewhat by age (Fig. 2; Table 1), but two tailed t-tests conducted comparing the means of Quartz, Feldspar, and Lithic percentages between the geologic eras (Paleocene, PETM, and Eocene) were unable to reject the null hypothesis that the compositions were drawn from the same underlying population at the 0.05 confidence level. Fluvial sandbodies tend to be richer in feldspars than deltaic deposits and marginal lacustrine sandstones (Fig. 2). Rose diagrams of paleocurrent directions (Fig. 3) show a range of directions with river flowing dominantly to the east in the Paleocene, to the north-northeast during the PETM, and to the northeast during the early Eocene (Fig. 3). However, the early Eocene directions are particularly variable and there are components of flow to the northwest and southwest (Fig. 3). For fluvial sandbodies that had both a thin section sample and paleocurrent measurements we were able to calculate a linear regression with the fluvial samples' QFL proportions plotted against the associated average flow direction azimuth (Fig. 4) produced R^2 values of 0.39, 0.34 and, 0.24 for Quartz, Feldspar, and Lithic proportions respectively with the Feldspar proportion slightly rising with increased flow azimuth (more towards the South-East) at the expense of the Quartz proportion.

DISCUSSION

The QFL ternary diagrams, t-tests, and linear regressions allow the point counted mineralogy data to be interpreted basins larger geologic context. Depositional environment appears to be one factor

affecting mineralogy with large fluvial deposits containing higher proportions of Feldspar clasts compared to deltaic, lacustrine, and small channel plug deposit. This finding is somewhat intuitive and could represent Feldspar's lower hardness affecting its transport durability causing distal deposits to be relatively poor in countable Feldspar clasts. The t-tests found no significant difference in the QFL proportions between deposits from the Paleocene, PETM, and Eocene, which supports rejecting the hypothesis that PETM related climatic forcing significantly changed the Hanna Basin drainage and sediment sourcing. This is a similar result to that observed in the Piceance Creek Basin of northwest Colorado spanning the PETM (Foreman et al., 2012; Foreman and Rasmussen, 2016). This implies that the proposed fluvial response of greater channel mobility and "flushing" of fine-grained sediment downstream did not cause any new source lithologies to be exposed in the hinterlands of these basins. Indeed any increases in erosion were not associated with unroofing sequences and may be related to greater reworking or transport of transiently stored sediment in alluvial systems versus greater erosion in hinterland. However, this hypothesis requires further testing.

Calculating linear regression for the QFL proportions (dependent variable) as controlled by average paleo-flow azimuth of the fluvial sandstone body sampled (independent variable) indicates that average paleo-flow azimuth may have some effect on the proportion of Feldspar and Quartz where fluvial deposits that flowed more to the southeast contain a higher Feldspar proportion than deposits with paleo-flows towards the northeast. This relationship between paleo-flow and mineralogy could be driven by the lithology differences between the active uplifts surrounding the Hanna Basin during the Paleocene-Eocene transition (Hajek et al., 2012; Wroblewski, 2002). The calc-alkaline pluton of the Seminoe Mountains to the northeast could be the source of the more Feldspar rich sediment associated with the fluvial sand bodies with more southeast directed paleo-flows. The higher potentially higher Quartz proportions in the northeastern flowing fluvial deposits could have been sourced from the Medicine Bow or Sierra Madre mountains, which are to the south and southwest of the Hanna Basin respectively (Figure 1). Both uplifted

regions contain exposed Proterozoic and Paleozoic granitic plutons as well as quartzite units that could supply the more Quartz rich sands.

ACKNOWLEDGEMENTS

This material is based upon work supported by the Keck Geology Consortium and the National Science Foundation under Grant No. 1659322. Special thanks to Brady Foreman, Ellen Currano, Jesse Thornburg, Regan Dunn, and Marieke Dechesne for the expertise and help along the way. I would also like to acknowledge my partner Anthony Semeraro for keeping me company during long days in the fields as well as the work and support of my peers Christine Shonnard, Jake Polsak, Keifer Nace, and James Chisholm.

REFERENCES

- Dechesne, M., E.D. Currano, E. D., Dunn, R.E., Higgins, P., Hartman, J.H., Chamberlain, K.R., and Holm-Denoma, C.S., In review, Depositional patterns of the fluvial to paludal strata of the Hanna Formation across the Paleocene – Eocene boundary, Hanna Basin, Wyoming.
- Dickinson, R.W. (1970). Interpreting detrital modes of greywacke and arkose, *Journal of Sedimentary Petrology*, 40(2), 695-707.
- Dickinson, R.W., Klute, A.M., Hayes, J.M., Janecke, U.S., Lundin, R.E., et al. (1988). Paleogeographic and paleotectonic setting of Laramide sedimentary basins in the central Rocky Mountain region, *Geological Society of America Bulletin*, 100, 1023-1039.
- Dobbin, C. E., Bowen, C. F., Hoots, H. W. 1929. Geology and coal and oil resources of the Hanna and Carbons basins, Carbon County, Wyoming. U.S. Geological Survey Bulletin 804: 88 p.
- Foreman, Z.B. (2014). Climate-driven generation of a fluvial sheet sand body at the Paleocene–Eocene boundary in north-west Wyoming (USA), *Basin Research*, 26, 225-241.

- Foreman, B.Z., Rasmussen, D.M. (2016) Provenance signals in the Piceance Creek Basin: Unroofing of the Sawatch Range and extent of the early Paleogene California river system (Colorado, U.S.A.) *Journal of Sedimentary Research* 86: 1345-1358.
- Foreman B., Clementz M.T., Heller P.L. 2012. Evaluation of paleoclimatic conditions east and west of the southern Canadian Cordillera in the mid-late Paleocene using bulk organic $\delta^{13}\text{C}$ records. *Palaeogeography, Palaeoclimatology, Palaeoecology* 376: 103-113.
- Hajek, E. A., P.L. Heller, and E.L. Schur. (2012). Field test of autogenic control on alluvial stratigraphy (Ferris Formation, Upper Cretaceous–Paleogene, Wyoming), *GSA Bulletin*, 124(11/12), 1898–1912.
- Lillegraven, J.A., Snoke, A.W. 1996. A new look at the Laramide orogeny in the Seminoe and Shirley mountains, Freezeout Hills, and Hanna Basin, south-central Wyoming. Wyoming State Geological Survey Public Information Circular no. 36, 52 p.
- McInerney, F. A. & Wing, S. L. (2011). The Paleocene-Eocene Thermal Maximum: a perturbation of carbon cycle, climate, and biosphere with implications for the future. *Annu. Rev. Earth Planet. Sci.*, 39, 489–516
- Murphy, B. H., Farley, K. A., Zachos, J. C. (2010). An extraterrestrial ^3He -based timescale for the Paleocene-Eocene Thermal Maximum (PETM) from Walvis Ridge, IODP Site 1266. *Geochim. Cosmochim. Acta*, 74, 5098–5108.
- Schmitz, B., Pujalte, V. 2007. Abrupt increase in seasonal extreme precipitation at the Paleocene–Eocene boundary. *Geology* 35: 215-218.
- Secord, R. 1998. Paleocene mammalian biostratigraphy of the Carbon Basin, southeastern Wyoming, and age constraints on local phases of tectonism. *Rocky Mountain Geology* 33: 119-154.
- Weil, A. B., A. Yonkee, Schultz, M. (2016). Tectonic evolution of a Laramide transverse structural zone: Sweetwater Arch, south central Wyoming, *Tectonics*, 35, 1090–1120.
- Wroblewski, A. (2002). The Role of the Hanna Basin in Revised Paleogeographic Reconstructions of the Western Interior Sea During the Cretaceous-Tertiary Transition, Wyoming Geological Association Guidebook - 2002 Field Conference, Laramie, WY.

VARIABILITY IN VEGETATION DENSITY ACROSS LATERALLY COEVAL STRATIGRAPHIC SECTIONS WITHIN THE HANNA BASIN, WYOMING, USA

JAKE POLSAK, Western Washington University
Research Advisor: Brady Z. Foreman

INTRODUCTION

Vegetation structure influences many important variables of ecosystems such as hydrological and carbon cycles, erosion, animal migration patterns, and plant diversity. However, ancient vegetation structure has been exceptionally difficult to quantify. Recent development of a new proxy based on the morphology of leaf epidermal cells, imprinted upon fossilized plant cuticles, offers a unique opportunity to reconstruct past landscapes. Previous work by Dunn et al. (2015) developed a model to quantify ancient vegetation density or Leaf Area Index (LAI = foliage area in m^2 / ground area in m^2) using first phytoliths and later fossilized cuticle. This model measures the area, undulation of the perimeter, and aspect ratio (major axis length / minor axis length) of leaf epidermal cells to determine whether samples represent shade- or sun-dominated environments. The relationship between cell morphology and LAI is derived from studies of modern systems that indicate that the degree of sunlight exposure during leaf growth influences epidermal cell shape. Leaves that grow in direct sunlight tend to develop more rounded cells with less undulatory cell walls; whereas leaves that developed in a shade dominated environment tend to be more elliptical in shape with more undulated cell walls.

The goal of this project is to document temporal and spatial variability in reconstructed LAI (rLAI) from four contemporaneous stratigraphic sections. How do reconstructed rLAI values vary vertically within and between adjacent sedimentary beds? How do rLAI values vary laterally across a landscape? Can changes in rLAI be correlated with one another and linked to depositional environments?

GEOLOGIC SETTING

The field research for this project was conducted in the Hanna Basin located in Carbon County, Wyoming, within the Western Interior of the United States. This basin formed during the Laramide orogeny and is bounded by the Rawlins uplift to the south and the Shirley Mountains and Freezeout Hills to the north. The basin has recently been discovered to contain the Paleocene-Eocene Thermal Maximum (PETM), an abrupt global warming event 56 million years ago caused by the release of thousands of petagrams of carbon into the atmosphere (McInerney and Wing, 2011), and is an ideal study area to examine how vegetation structure differs before, during and after the PETM. This project is specifically located within the early Eocene ‘Super Swamp’ section at Hanna Draw (Figure 1), about 150 m above the PETM. The name ‘Super Swamp’ was assigned to this section because, at approximately 100 meters thick, it is the thickest package of coals and carbonaceous shales in the upper Hanna Formation. Discrete, lens-shaped sandstone channel deposits occur within ‘Super Swamp,’ and this study examines at high resolution 10-20 meter sections spanning a channel deposit.

METHODOLOGY

My partner and I measured four laterally coeval stratigraphic sections within the ‘Super Swamp’ section using a Jacob’s staff. Each stratigraphic section was described bed by bed, and lithologies were examined to determine which samples would produce sufficient cuticle remains with imprints of ancient leaf epidermal cells for LAI analysis. Of these

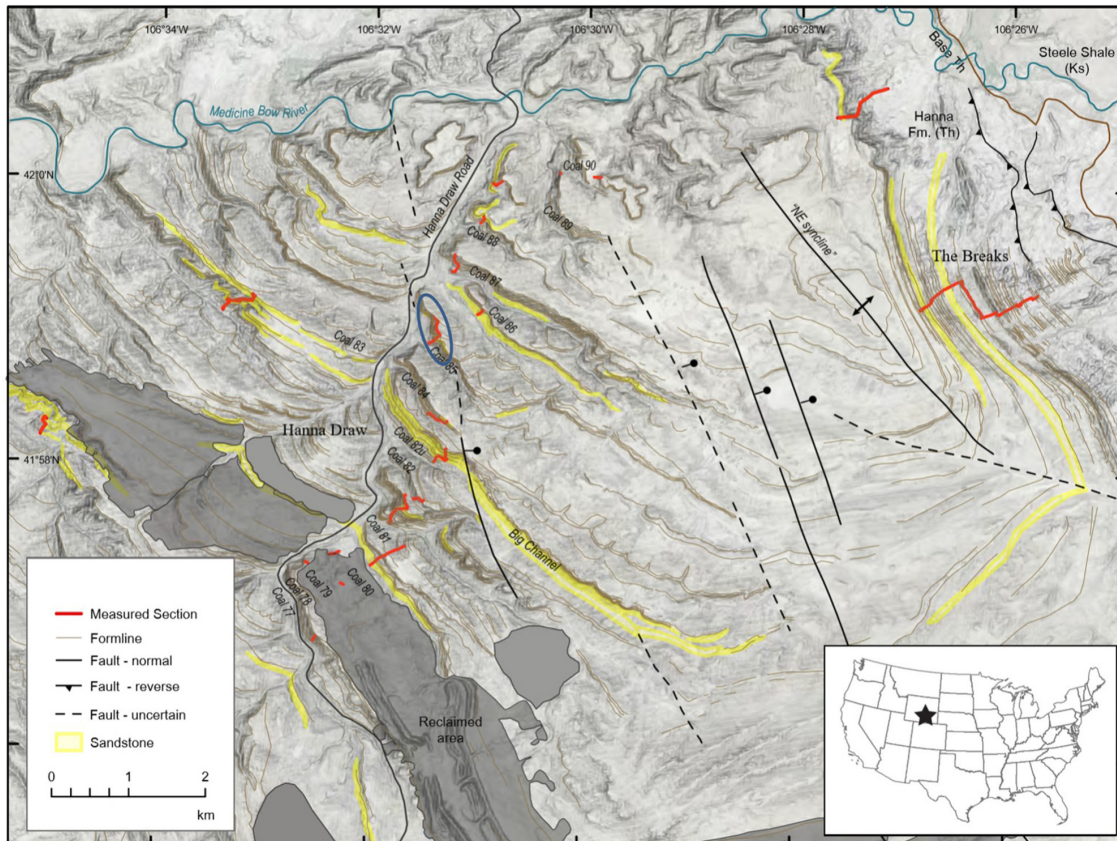


Figure 1: This map of the Hanna Basin in south-central, WY, shows the geologic features within the basin in addition to the location of my research, indicated by the blue ellipses.

beds, the most lucrative samples were derived from shales exhibiting high clay content, laminations, and moderate to high organics. From these beds, 18 rock samples were collected for LAI analysis. Samples were processed by Global Geolabs using standard palynological procedures, and all organic matter (including cuticle fragments) were mounted on microscope slides.

Leaf epidermal cells were examined using a Zeiss microscope under a 40x objective. Approximately fifty to seventy-five photographs were taken for each slide of cuticle fragments with leaf epidermal cells preserved (Figure 2). Photographs were then uploaded into ImageJ, where the area, undulation, and roundness of each cell could be measured. For each photograph, roughly seven to ten cells were traced on an HP Spectre laptop touchpad and measurements were placed into an excel file. The data were then analyzed in R using code written by Dr. Reagan Dunn. LAI values for each sample were calculated using the following relationship:

$$rLAI = 4.05 (\text{mean UI}) + 15.32 (\text{mean AR}) - 25.38$$

where rLAI is reconstructed LAI, UI is undulation index, and AR is aspect ratio. rLAI values were compared within a section and between the four sections.

RESULTS

Raven Stratigraphic Column

The first stratigraphic section measured, Raven, indicated on the far left of Figure 3, sets the tone for the entire lateral succession. The basal 0.3 meters of the section are anthracite coal. This bed has a gradational contact with the unit above, a carbonaceous shale that is 0.4 meters thick. This pattern of anthracite coal transitioning into carbonaceous shale and vice versa continues until a sandstone unit that begins at 5.1 meters and extends to 12.5 meters (7.5 meters thick). LAI samples were taken from two carbonaceous shale beneath the sandstone at approximately 2.7 meters and 5.1 meters and yielded reconstructed values of 5.37 and 4.71. Above the sandstone is first a clay rich shale and

then a slightly harder, more resistant layer following it; LAI samples were taken from both of these beds (Units 20 at 13 meters had an rLAI of 5.26 & Unit 21 at 13.5 meters had an rLAI of 7.47). We then see an alternation of carbonaceous shale and claystone beds to the top of the section at 16.6 meters. Our fifth and final LAI reconstruction, from a carbonaceous shale bed at 15.7 meters, was 6.7.

Rattlesnake Stratigraphic Column

The Rattlesnake column is 220 meters to the southeast of the Raven column and exhibits a similar pattern beginning with anthracite coal at the base of the section and gradationally transitioning to carbonaceous shale. This continues until the appearance of a siltstone bed at approximately 3.55 meters, followed by a thin (0.1 meter thick) sandstone bed 3.65 meters above the base of the column. This sequence is repeated once and followed by another carbonaceous shale. The succeeding bed at 4.1 meters is composed of very fine grained sandstone with small root fossils; the rLAI value for this bed was 1.3. This bed is followed by a coarser grained sandstone, a carbonaceous shale bed, and then another very fine grained sandstone which again contained traces of root fossils and yielded an rLAI of 2.29. Above this are a paleosol, a 4.3 meter thick sandstone unit, and then alternating carbonaceous shales and siltstones. Unit 28, an organic rich, laminated, carbaceous shale, had an rLAI of 2.71. Continuing upsection, we then

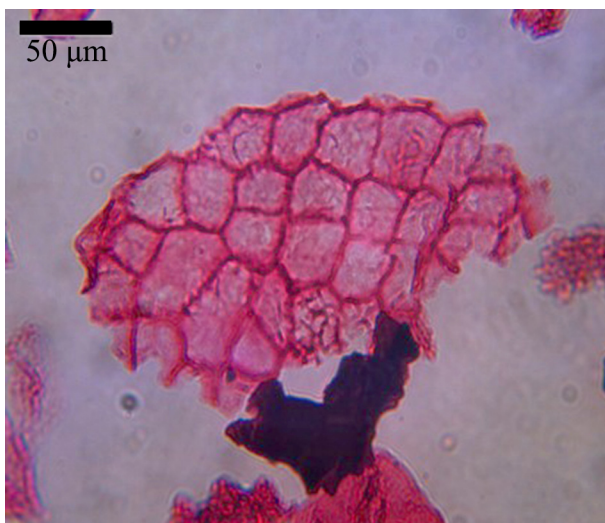


Figure 2: This photograph is an example of a fossilized cuticle fragment whose cell walls were traced and measured. This sample comes from unit 12 of the Rattlesnake stratigraphic column.

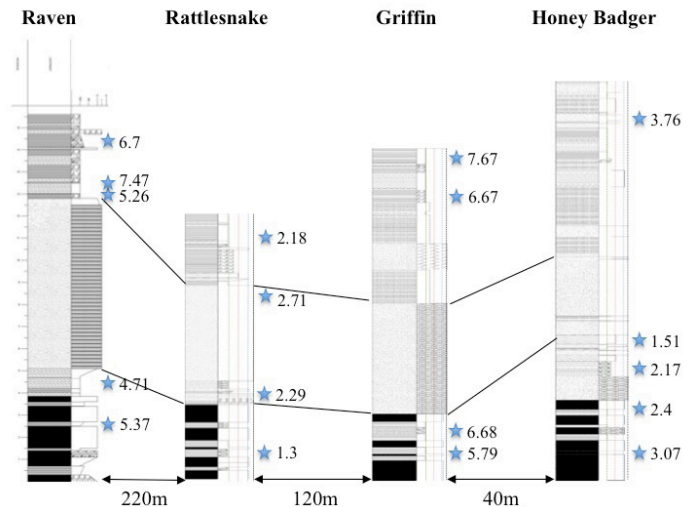


Figure 3: This figure displays the four laterally coeval columns across the 'Super Swamp' section within the Hanna Basin. The LAI values on each column are indicated with a star next to the bed from which they were sampled.

have two claystone beds that encapsulate a shale with charcoal interbeds. At the very top of the section in Unit 32 is a 0.4 meter thick clay and organic rich shale that had an rLAI of 2.18.

Griffin Stratigraphic Column

Similar to the previous sections, the lowermost 2.4 meters of the Griffin stratigraphic column are alternating coal and carbonaceous shales; a carbonaceous shale bed at 1.5 meters in the section had an rLAI of 5.79. A paleosol occurs at 2.4 meters, followed by a return to alternating coal and carbonaceous shale. The bed after the paleosol, a carbonaceous shale at 2.65 meters, was examined for LAI to compare with the bed below the paleosol; its rLAI is 6.68. A 5 meter thick sandstone bed with a sharp contact with the underlying coal bed is overlain by mudstone. After the mudstone bed is a 1.2 meter thick sandstone bed with trough crossbedding, followed by claystone, another mudstone, and another carbaceous shale at 13.1 meters that had an rLAI of 6.67. This bed grades into a sequence of alternating claystones and shales, which repeats until the top of the column, ~15 meters, which consists of shale interbedded with concretionary claystone (rLAI = 7.67).

Honey Badger Stratigraphic Column

Our most lithologically diverse column begins like the previous three, with anthracite coal at its base. However, its next bed consists of a laminated coal that was interbedded with carbonaceous shale that had an rLAI of 3.07. Above this, as in previous sections, alternating anthracite coal and shale layers occur until a 1-meter thick sandstone at 4.4 meters. The coal bed beneath the sandstone channel had an rLAI of 2.4. Above the sandstone is claystone, followed by a laminated siltstone with high organics and *Metasequoia* fossils; rLAI of this unit was 2.17. Continuing upsection is another sandstone bed followed by siltstone, clay rich shale, silty sandstone (rLAI = 1.51), and shale respectively. Successively, we then find alternating sandstone and mudstone layers for about 8 meters, until 13.9 meters from the base of the section. At this point, we find small carbonaceous shale beds among larger claystone beds followed by a 0.2 meter-thick sandstone bed. Above the sandstone lies our last LAI reconstruction for this section, a value of 3.76 from a carbonaceous shale with high organics and clay content. The remaining beds consist of silty sandstone, paleosol, mudstone, claystone, another silty sandstone, and at the top of the column, at 16.85 meters, a weak paleosol.

General Trends Among the Section

The results demonstrate higher rLAI values in both the Raven and Griffin stratigraphic sections, ranging from 4 to 7 rLAI, while the Rattlesnake and Honey Badger stratigraphic columns indicate a much more open canopy coverage, ranging from 1-3 rLAI values (Figure 3). These quantitative values are visually represented in Figure 4 by photos of differing grades of canopy coverage. Although the rLAI values differ significantly within and among sections, they do display some consistencies and patterns that are worth noting. Laterally, the stratigraphic columns alternate magnitudes of rLAI values from higher order values to lower order values and repeat in a left to right sequence. The lower rLAI values coincide with smaller sandbodies in the Rattlesnake and Honey Badger sections, while the higher rLAI values in the Raven and Griffin sections occur in proximity to larger sand bodies. In addition to rLAI values alternating laterally, there were also changes in rLAI values

vertically within the stratigraphic columns. In both the Honey Badger and Raven stratigraphic sections, samples immediately above the sandstone plug from a migrating river display increased rLAI values. This can be seen especially in the Honey Badger section where rLAI values increase in units twelve and thirty-two. In both cases these values spike and then return to lower, more consistent levels.

INTERPRETATIONS

Our data allow us to paint a picture of oscillating canopy coverage throughout the stratigraphic columns and observe how the vegetation changed throughout geologic time as a migrating river crosses through this area. Despite the differing LAI magnitudes among the sections horizontally there are consistencies that suggest some patterns are present. The jump in rLAI values within the Honey Badger and Raven stratigraphic sections indicate an increase in canopy coverage after the sandstone plug, implying that the migrating river represented by the coeval sandbodies has a direct effect on vegetation densities in this area. This could be due to a saturation of the soil promoting plant growth and increasing vegetation. However, while it does have a short-term impact of the vegetation in these sections the rLAIs do decrease further upsection. This suggests that although a local impact such as a migrating river could provide minor alterations to the LAI values, they will ultimately return to the what the overarching climate supports. This can be seen especially in the Honey Badger section, where rLAI values increase in units 12 and 32, which are both located after sandstone layers.

To address the different magnitudes of the rLAI values among the sections, although analytical error is a possibility, the size of the sandstone beds vary among sections, which could also affect vegetation structure. The smaller and more sporadic sandbodies in the Rattlesnake and Honey Badger sections indicate that rivers avulsed and migrated more readily and thus impacted these sections over a shorter amount of time generating a more open canopy in these stratigraphic columns.

ACKNOWLEDGEMENTS

This material is based upon the work supported by the Keck Geology Consortium and the National Science Foundation Grant No. 1659322, as well as NSF grant EAR 145031 to Ellen Currano. The protocol for analyses was developed using funding from the Negaunee Foundation, the Field Museum of Natural History, a National Geographic Explorers Grant, NSF DDIG (DEB-1110354), NSF EAR 0819910, and GSA and with assistance from Melanie Conner, Delta Burchi, and Ana Soble. I thank my Keck Geology Consortium researchers Keifer Nace, Christine Shonnard, Xavier Nogueira, Anthony Semeraro, and James Chisholm for their assistance with this project, as well as Regan Dunn and Marieke Dechesne for their mentorship.

REFERENCES

- Dunn, R.E., Currano, E.D., Dechesne, M., & Foreman, B.Z. (2018). Forest canopy response to greenhouse warming at the Paleocene-Eocene Thermal Maximum. GSA Annual Meeting, Indianapolis.
- Dunn, R.E., Strömberg C.A.E., Madden, R.H., Kohn, M.J., Carlini, A.A. (2015). Linked canopy, climate, and faunal change in the Cenozoic of Patagonia. *Science*, vol. 347, no. 6219, pp. 258-261.
- Holdridge, L.R. (1967). *Life Zone Ecology*. Tropical Science Center, San Jose, Costa Rica, 206 p.
- McInernery, F.A. & Wing, S.L. (2011). The Paleocene-Eocene thermal maximum: a perturbation of carbon cycle, climate, and biosphere with implications for the future. *Annu. Rev. Earth Planet. Sci.*, vol. 39, pp. 489–516.

PALEOCURRENT VARIABILITY IN MEANDERING AND BRAIDED RIVER SYSTEMS: MODERN CALIBRATION AND STRATIGRAPHIC CASE STUDIES SPANNING THE PALEOCENE-EOCENE THERMAL MAXIMUM

ANTHONY SEMERARO, Western Washington University
Research Advisor: Brady Z. Foreman

INTRODUCTION

Small width-to-depth ratios and sinuous single-thread channels characterize meandering river morphologies. Large width-to-depth ratios and relatively straight, multi-threaded channels characterize braided river morphologies. Meandering rivers typically form on shallow alluvial slopes with denser vegetation and fine-grained floodplains, which stabilizes the banks and allows the generation of sinuosity. Braided rivers generally form with wide shallow channels and high bedload transport in locations with low bank cohesion and variable discharge. The lack of bank cohesion, possibly from a lack of vegetation and clay content, destabilizes riverbanks, increasing the erosion of the banks, and preventing the formation of a large sinuous channel. Instead numerous smaller channels with migrating bars form throughout the river that subdivide the flow. Both river morphologies are common on modern day Earth, and are commonly identified in ancient stratigraphic sequences (Miall, 1985; Nichols, 2009). Criteria for distinguishing between these morphologies focus on grain size, in-channel lithofacies, channel morphology, fluvial sandbody geometry, and overbank lithofacies associations (Miall, 1985; Nichols, 2009). Here, I evaluate another proposed indicator that may be useful in determining paleo-channel morphodynamics. Both major river morphologies flow in a mean vector direction (i.e., down the steepest slope towards base level), but the individual channel flow measurements of a meandering river hypothetically should vary more greatly than braided rivers, simply as a consequence of

the greater sinuosity exhibited by meandering rivers.

This is a particularly important problem in terms of Earth surface dynamics and the interpretation of sediment transport on other planetary surfaces. For example, there was no deep-rooted terrestrial vegetation present until the evolution of vascular plants with deep root systems in the late Devonian (Gibling and Davies, 2012). This change in terrestrial vegetation contributed to the evolution of fluvial system morphology (Gibling et al., 2013). During this shift, coal beds and other vegetation markers began to appear in the rock record. River deposits shifted from those indicative of mainly wide, sheet-like braided morphology to more isolated, lenticular geometries with well-developed point bar deposits (Davies, 2010). Researchers suggest that riverbanks with just 18-20% roots by volume are approximately 20,000 times more stable than banks lacking vegetation root structures, which lead to the change (Davies, 2010). Moreover, these changes are also captured by small-scale, simplified flume experiments (Tal and Paola, 2007).

This research focuses on the main factors that differentiate meandering and braided rivers by creating a modern dataset to assess the morphologies of paleoriver data from which it is difficult to recover the planform morphology. Using Google Earth, a modern database of 6 rivers (3 meandering, 3 braided) was created to find the dispersion values (a measurement of variability) of channel directions of meandering and braided rivers. This study assesses if meandering and braided river morphologies can be found from

paleocurrent data reliably and how many paleocurrent measurements need be taken in order to obtain reliable results. Furthermore, we apply our modern data sets to new and compiled paleocurrent measurements spanning the Paleocene-Eocene Thermal Maximum (PETM), an abrupt global warming event 56 million years ago, that corresponds to substantial changes in fluvial deposition in the Western Interior of the United States (Foreman et al., 2012; Foreman, 2014; Dechesne et al., in review).

GEOLOGIC SETTING

We focus on six modern river systems, identified below, that display end-member planform morphologies of meandering and braided configurations. Our stratigraphic data set is derived from three Laramide structural basins in the Western Interior of the United States. The new and compiled paleocurrent data are derived from the Piceance Creek Basin in northwest Colorado (Foreman et al., 2012), the Bighorn Basin in northwest Wyoming (Foreman, 2014), and the Hanna Basin of south-central Wyoming (Dechesne et al., in review; this study). All three basins within this study formed during the Laramide Orogeny between the Late Cretaceous and Paleogene, as thin-skinned deformation of the Sevier Orogeny gave way to thick-skinned deformation (Dickinson et al., 1988; Dickinson, 2004; Fig. 1). The region of North America wherein all three basins lay was part of a shallow interior sea until the uplift of the Laramide ranges (Wroblewski, 2003; Dickinson, 2004). The Laramide Orogeny caused basement-involved uplift of several ranges around each of the three basins of interest, which provided detritus to the adjacent basins. The paleocurrent records are derived from the fluvial units within these basins, and the paleocurrent measurements are divided into pre-, during, and post-PETM stratigraphic bins.

The PETM was a global warming event that occurred approximately 56 Ma and lasted for approximately 200 kyrs with a global temperature rise between 5° and 8°C (McInerney and Wing, 2011). This climate change event was caused by a massive influx of approximately 4000 petagrams of carbon into the atmosphere potentially from a variety of sources (McInerney and Wing, 2011). The rapid increase in

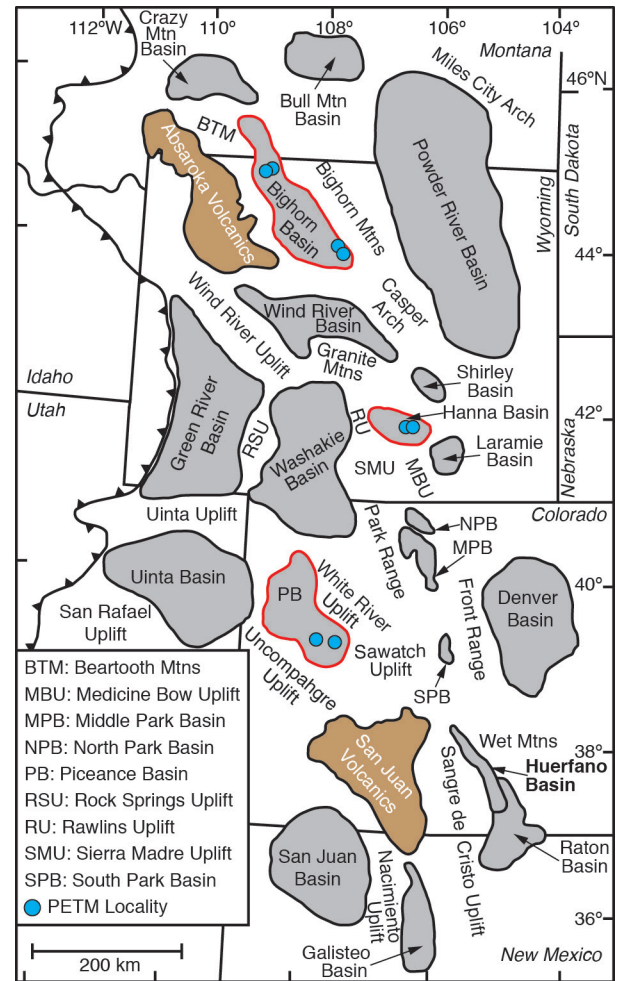


Figure 1. Map of the Western Interior of North America showing locations of Laramide basins that contain the PETM and paleocurrent measurements used in this study outlined in red.

temperature likely caused many terrestrial changes in vegetation, precipitation, and atmospheric circulation (McInerney and Wing, 2011; Carmichael et al., 2017). Rapid changes in temperature and precipitation regimes likely altered vegetation structure from denser, deciduous forests into sparser drier vegetation regimes dominated by legumes (Wing et al., 2005). After the PETM, vegetation quickly shifted back to near its pre-event condition. Additionally, there is evidence for decreases in mean annual precipitation and potentially increased discharge and sediment flux in Laramide basins (Wing et al., 2005; Kraus and Riggins, 2007; Foreman et al. 2012; Foreman, 2014). Fluvial stratigraphic responses include the deposition of thick, laterally continuous sandbodies, putatively related to changes in river morphodynamics during the PETM and potentially a transient shift in river planform morphology (Fig. 2).

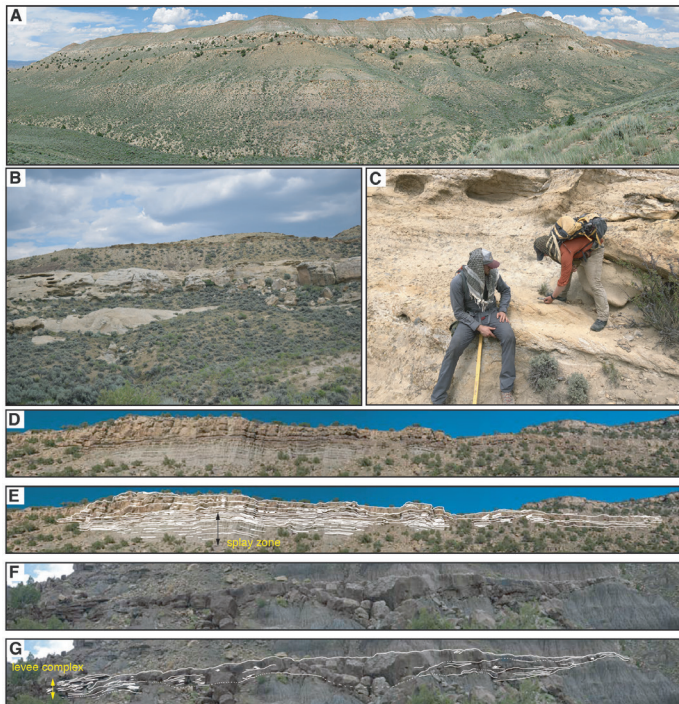


Figure 2. (A) Outcrop photo-mosaic of the Hanna Formation at one of the carbon isotope stratigraphic sections. Note the large fluvial sandbody, which is within the PETM. (B) Example of fluvial sandbody within the Eocene portion of the study area. (C) Photograph of large-scale cross-bedding being measured for paleocurrent. (D&E) outcrop image of a fluvial sandbody in the Molina Member of the Wasatch Formation (northwest Colorado) interpreted as the result of a braided river system, and (E&F) outcrop image of a fluvial sandbody in the Atwell Gulch Member of the Wasatch Formation (northwest Colorado) interpreted as the result of a meandering river system.

METHODOLOGY

Modern Data

Google Earth was utilized to measure 1000 synthetic current measurements for 6 rivers (3 meandering, 3 braided) that were analyzed through directional statistics to calculate their dispersion values. The sections of each river that appeared the least affected by anthropogenic forces (dams, channels, canals, levees, etc.) were chosen. To calculate the dispersion value, first the polar coordinate directions are converted to Cartesian coordinates, the average x and y coordinates are then squared, summed together, and the square root is taken to obtain the dispersion value. The higher the dispersion value, the more confined the spread of the data, whereas the lower the value, the more equally spread the data is. The original current measurements are plotted on rose diagrams to visually analyze the differences in river morphology

as well as to find the mean vector of the data. To find how many current measurements are needed to get a reliable estimate of dispersion values, the original 1000 measurements were subsampled down to 5 measurements by randomly selecting n measurements from the original 1000 using Monte Carlo methods to calculate the dispersion value 500 times to get an average dispersion value for each sample size (Figure 3). 95% confidence intervals are calculated for each sample size and are negligible until fewer than 25 measurements.

Stratigraphic Data

Paleocurrent data was measured from sedimentary structures in the sandbody outcrops including trough cross bedding, planar cross bedding, and climbing ripples in all three basins (DeCelles and Langf, 1983; Fig. 2). Paleocurrent measurements for Hanna Basin were taken directly for this study. Data from the Bighorn and Piceance basins were collected by Foreman (2014) and Foreman et al. (2012), respectively. Using these features in the outcrops, the flow directions were measured using a brunton compass (Figure 1c). In each basin, the outcrops were grouped into pre-PETM, PETM, and post-PETM to analyze how river morphology changed throughout the PETM. Bighorn Basin has 397 total paleocurrent measurements (95 pre-PETM, 139 PETM, 163 post-PETM), Piceance Creek Basin has 209 total measurements (74 pre-PETM, 59 PETM, 76 post-PETM), and Hanna Basin has 280 measurements (121 pre-PETM, 89 PETM, 70 post-PETM). The measurements for each group were subsampled from 75 down to 5 measurements and the dispersion value was analyzed for them with the same directional statistics and Monte Carlo method as the modern datasets. The dispersion value remains constant above 40-50 current measurements of a river. Ancient datasets with fewer than 75 measurements were extrapolated to 75 measurements based upon the constant dispersion value at >50 measurements.

RESULTS

Modern Data

Modern river systems identified as meandering and braided show a clear separation between dispersion

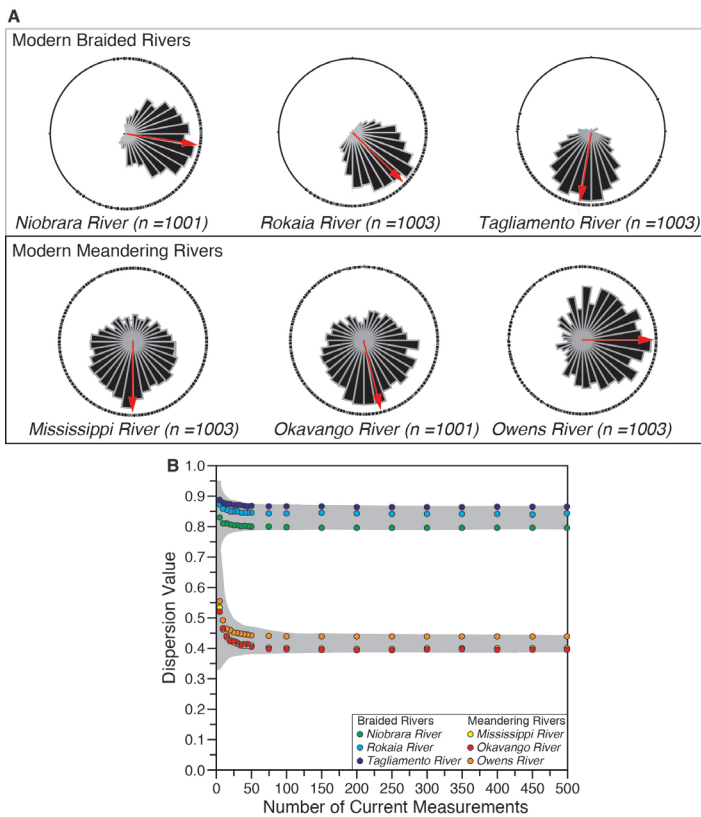


Figure 3. (A) Example of rose diagrams for modern meandering and braided river systems (n equal to the total number of measurements and the red arrow denotes the vector mean), and (B) dispersion values of current measurements at decreasing sample size (grey zone includes the values between the individual rivers analyzed and a 95% confidence interval for each dispersion estimate determined by subsampling routine). Note only ~25 current measurements are needed to distinguish meandering from braided dispersion values.

values for all paleocurrent measurements above $n = 25$. Dispersion values for braided rivers ranged from 0.78 to 0.89 and values for meandering ranged from 0.39 to 0.55 (Figure 3). Braided rivers displayed a lack of measurements on their rose diagrams opposite of the mean vector, indicating that a majority of channels flow towards the mean vector direction downstream. In contrast meandering rivers display 360° of paleoflow directions (Figure 3). The formation of many smaller channels in braided rivers increased the number of measurements over a similar distance, whereas meandering rivers with one channel can only provide a few measurements over a similar reach. Braided rivers in general have a majority of their current directions flowing close (<90 degrees) to the main vector direction whereas meandering rivers contain current measurements that flow variably (up to and >90 degrees) in the opposite direction of the

mean vector with flow directions encompassing every bracket angle on the rose diagram. The sinuosity of the meandering rivers yields greater spread in their paleoflow directions and a decreased dispersion value.

Stratigraphic Data

Paleo-river systems from each basin experienced similar shifts in dispersion values in relation to the PETM (Fig. 4 & 5). Specifically, each basin displays an increase at the PETM, and then a decrease after the event. The range of dispersion values for each basin and time interval is conservatively estimated by the following methods. The first number in each range for each dataset is the dispersion value for $n > 50$ measurements. The higher number in the range is the highest dispersion value each dataset reaches; this is for 5 measurements and the 95% confidence interval is too great to distinguish between river morphologies. The Bighorn Basin started with a range of 0.47 to 0.55, with an increase to 0.75 to 0.79 during the PETM, with a decrease down to 0.56 to 0.66. The Hanna Basin experienced a very minor increase in dispersion value within the range 0.58 to 0.74. After the PETM, the dispersion value for the Hanna Basin decreased greatly to a range of 0.20 to 0.50. The Piceance Creek Basin started with values from the Atwell Gulch Member between 0.66 to 0.73, increased to 0.74 to 0.78 within the Molina Member, and then dropped to 0.55 to 0.64 for the Shire Member (Figure 4,5). A majority of the data sets plot between the modern database braided and meandering values with one set from Hanna Basin plotting below the meandering database.

DISCUSSION AND CONCLUSIONS

Our modern datasets suggest that river systems with different planform morphologies will produce different paleocurrent patterns. Braided rivers have wide and shallow channels with numerous bars within the channels whereas meandering rivers consist of one sinuous deep channel with lateral migration and deposition. Braided morphologies generally tend to flow in one direction with all channels within the river flowing towards the mean vector direction of the river. Meandering morphologies with their sinuous channels can flow in almost any direction relative to the mean

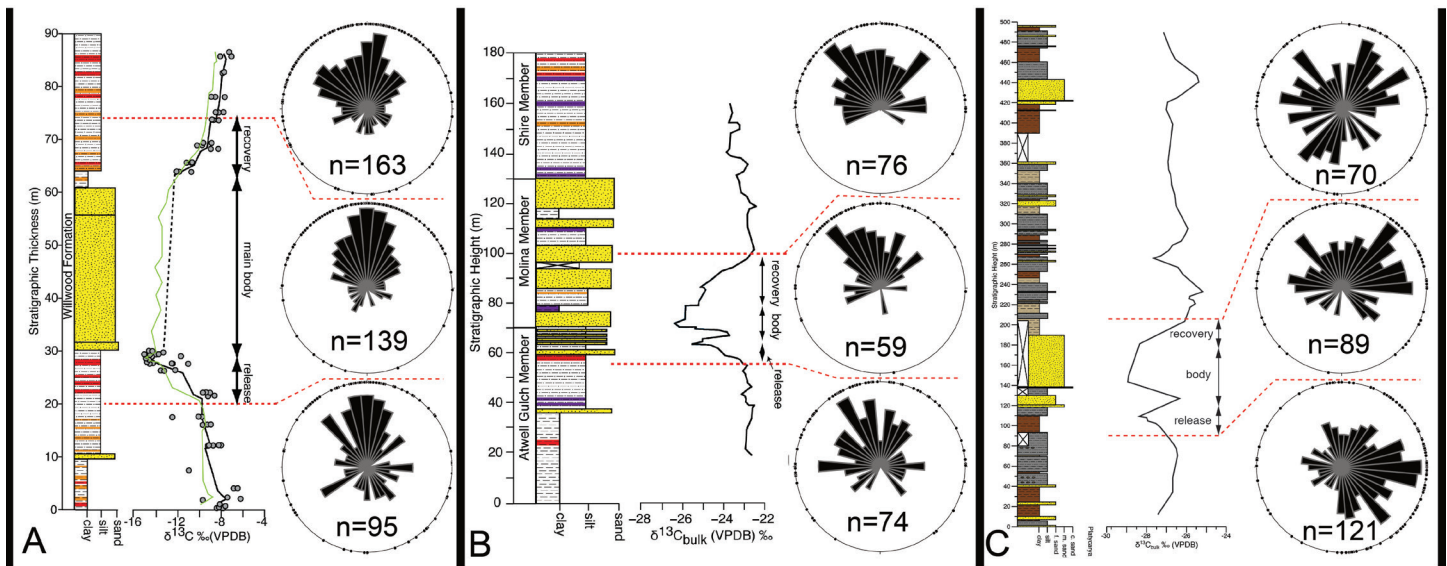


Figure 4. Stratigraphic sections and carbon isotope stratigraphies in (A) Bighorn Basin, (B) Piceance Basin, (C) Hanna Basin. Each of the basins studied herein showing up-section changes in paleodrainage before (bottom), during (middle), and after the PETM (top). Data from Bowen et al. (2001), Foreman et al. (2012), Foreman (2014), Chisholm (2019), and this study.

vector direction of the river. The modern data suggest that using this difference in flow directions and enough measurements (i.e., $n > 25$), the morphology of an ancient river can be found using directional statistics, as meandering rivers will have a greater spread of flow directions (lower dispersion value) and braided rivers will have a more narrow spread (higher dispersion value). Additional rivers should be included in future work to evaluate if the distinction between meandering and braided rivers holds. Moreover, the sinuosity of the river systems should be calculated to explicitly tie the dispersion of current measurements with channel morphology. The observation that the ancient data sets largely fall in between modern dispersion values could have a number of causes. First, the modern data set may not have captured the full range of meandering and braided dispersion values exhibited by modern river systems. Second, the ancient datasets pool multiple river channel deposits over relatively large stratigraphic intervals together, which means different channel morphologies might have been artificially mixed, yielding intermediate dispersion values. Lastly, this might be due to time-averaging of paleocurrent directions within the stratigraphic datasets. Each fluvial sandbody represents the net depositional evolution of a river channel while it inhabited a particular position on the floodplain, potentially representing several hundreds to thousands of years. In contrast, the modern datasets are a snapshot of river

morphology.

Paleocurrent measurements from the Bighorn Basin fall within the meandering river dispersion values for pre-PETM measurements, and then change to a braided river dispersion value during the PETM, and a trend returning towards meandering planforms again after the end of the PETM. The paleocurrent measurements from the Piceance Creek Basin and Hanna Basin do not directly fit within either braided rivers or meandering rivers dispersion values, as they may be transitioning from one morphology to the other and have a mixed morphology. In the Hanna Basin, the change in river planform is almost negligible from before the PETM to the PETM event meaning that there was only a slight shift in morphology in the Hanna Basin until a sharp decrease in dispersion value after the PETM. In the Piceance Creek Basin, there are large changes in dispersion value for pre-PETM, PETM, and post-PETM, but for each series of measurements, the dispersion values do not match either modern morphology. Transition periods when climatic forcings are changing could result in the slow transition from one planform to another in a fluvial system, rendering each individual sand body analyzed with a different planform that prevents the data from representing one definite planform and instead a mix of planforms that do not line up with either meandering and or braided morphology.

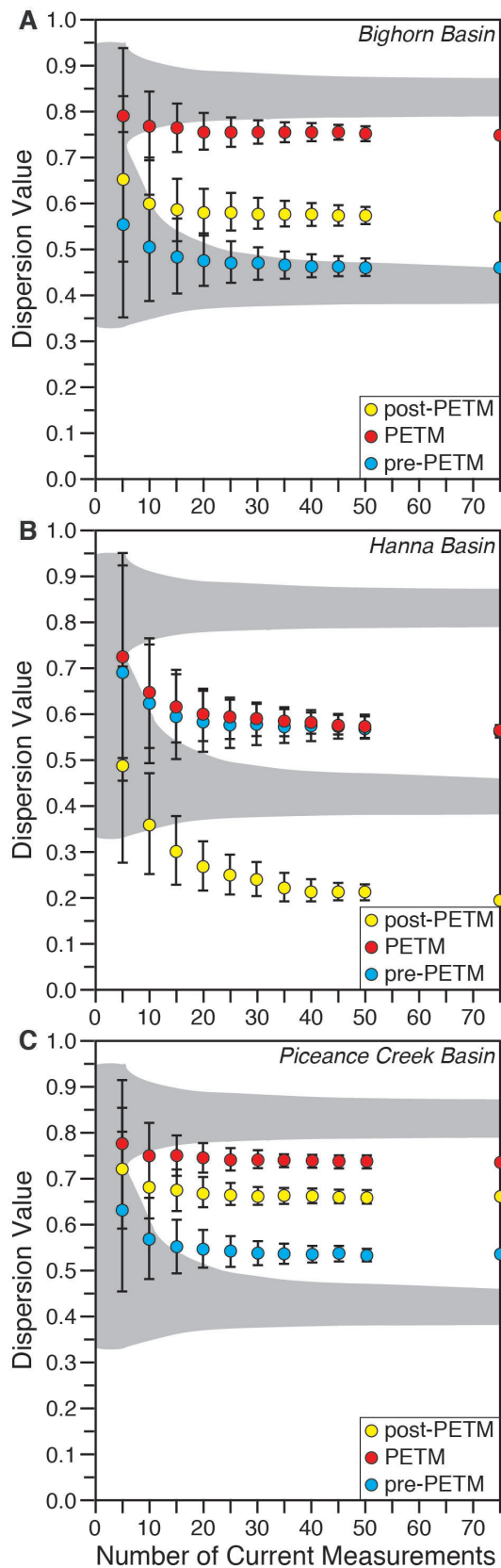


Figure 5. Plot of dispersion values of the Early Paleogene paleocurrent measurements for (A) Bighorn Basin, (B) Hanna Basin, and (C) Piceance Creek Basin. Grey zone is the meandering and braided dispersion value fields defined by modern river analyses.

The ancient river systems that did not fit into either definite morphology could have a mixed morphology such as an island-braided morphology or have a different morphology than modern rivers due to the lack of anthropogenic changes such as deforestation and levee/dam construction (Gibling and Davies, 2012). As precipitation, vegetation, and numerous other factors affect the requirements to fully transition a river from one planform to another (Bertoldi et al., 2009), if only one or two factors change, then the river could adopt a mixed planform forcing the dispersion value to not match a well-defined modern morphology. Previous studies have suggested that rivers became more braided and mobile during the PETM in a number of alluvial basins (Schmitz & Pujalte, 2007; Foreman et al., 2012; Foreman 2014; Dechense et al., in review) and more efficient transport of sediment. Both factors could have reduced sinuosity and altered dispersion values. These changes in river morphodynamics appear to be related to an increase in the seasonality of precipitation and reduction in vegetation density in the floodplains (Wing et al., 2005; Kraus and Riggins, 2007; Foreman et al., 2012; Foreman, 2014; Carmichael et al., 2017). However, the paleocurrent analysis presented herein suggests it may not be a clear-cut case of a transition from purely meandering river systems to braided river systems and back again.

ACKNOWLEDGEMENTS

This material is based upon work supported by the Keck Geology Consortium and the National Science Foundation under Grant No. 1659322, as well as NSF grant EAR 145031 to Ellen Currano. I would like to show my appreciation for guidance through this project from Brady Foreman and Ellen Currano as well as Marieke Dechesne and Regan Dunn. Additional thanks to my Keck student collaborators Xavier Noguiera, Christine Shonnard, Keifer Nace, Jake Polsak, and James Chisholm.

REFERENCES

Bertoldi, W., Zanoni, L., Tubino, M. 2009. Planform Dynamics of Braided Streams. *Earth Surface Processes and Landforms* 34(4): 547-557.

- Carmichael, M., J., Inglis, G.N., Badger, M.P.S., Naafs, B.D.A., Behrooz, L., Rimmelzwaal, S., Monteiro, F.M., Rohrssen, M., Farnsworth, A., Buss, H.L., Dickson, A.J., Valdes, P.J., Lunt, D.J., Pancost, R.D. 2017. Hydrological and associated biogeochemical consequences of rapid global warming during the Paleocene-Eocene Thermal Maximum. *Global and Planetary Change* 157: 114-138.
- Corenblit, D., Tabacchi, E., Steiger, J., Gurnell, A.M. 2007. Reciprocal Interactions and Adjustments between Fluvial Landforms and Vegetation Dynamics in River Corridors: A Review of Complementary Approaches. *Earth-Science Reviews* 84(1-2): 56-86.
- Davies, N. S., Gibling, M. R. 2010. Cambrian to Devonian Evolution of Alluvial Systems: The Sedimentological Impact of the Earliest Land Plants. *Earth-Science Reviews* 98(3-4): 171-200.
- DeCelles, P.G., Langf, R.P. 1983. Two New Methods of Paleocurrent Determination from Trough Cross-Stratification. *Journal of Sedimentary Research* 53: 629-642.
- Dechesne, M., Currano, E.D., Dunn, R.E., Higgins, P., Hartman, J.H., Chamberlain, K.R., Holm-Denoma, C.S. in review, *Geosphere*. Depositional patterns of the fluvial to paludal strata of the Hanna Formation across the Paleocene-Eocene boundary, Hanna Basin, Wyoming.
- Foreman, B. Z. 2014. Climate-Driven Generation of a Fluvial Sheet Sand Body at the Paleocene-Eocene Boundary in North-West Wyoming (USA). *Basin Research* 26(2): 225-241.
- Foreman, B. Z., Heller, P.L., Clementz, M.T. 2012. Fluvial Response to Abrupt Global Warming at the Palaeocene/Eocene Boundary. *Nature* 491: 92-95.
- Gibling, M.R., Davies, N.S., Falcon-Lang, H.J., Bashforth, A.R., DiMichele, W.A., Rygel, M.C., Ielpi, A. 2014. Palaeozoic Co-Evolution of Rivers and Vegetation: a Synthesis of Current Knowledge. *Proceedings of the Geologists' Association* 125(5-6): 524-533.
- Hajek, E. A., Heller, P.L., Schur, E.L. 2012. Field Test of Autogenic Control on Alluvial Stratigraphy (Ferris Formation, Upper Cretaceous-Paleogene, Wyoming). *Geological Society of America Bulletin* 124(11-12): 1898-1912.
- Kraus, M.J., Riggins, S. 2007. Transient drying during the Paleocene-Eocene Thermal Maximum (PETM): Analysis of paleosols in the Bighorn Basin, Wyoming. *Palaeogeography, Palaeoclimatology, Palaeoecology* 245(3-4): 444-461.
- Kraus, M.J., Woody, D.T., Smith, J.J., Dukic, V. 2015. Alluvial Response to the Paleocene–Eocene Thermal Maximum Climatic Event, Polecat Bench, Wyoming (U.S.A.). *Palaeogeography, Palaeoclimatology, Palaeoecology* 435: 177-192.
- McInerney, F.A., Wing, S.L. 2011. The Paleocene-Eocene Thermal Maximum: A Perturbation of Carbon Cycle, Climate, and Biosphere with Implications for the Future. *Annual Review of Earth and Planetary Sciences* 39(1): 489-516.
- Miall, A.D. 1985. Architectural-Element Analysis: A new method of facies analysis applied to fluvial deposits. *Earth Science Reviews* 22: 261-308.
- Nichols, G. 2009. *Sedimentology and Stratigraphy*, 2nd Edition: West Sussex, United Kingdom, Wiley-Blackwell, 432 p.
- Schmitz, B., Pujalte, V. 2007. Abrupt increase in seasonal extreme precipitation at the Paleocene–Eocene boundary. *Geology* 35: 215-218.
- Tal, M., Paola, C. 2007. Dynamic single-thread channels maintained by the interaction of flow and vegetation. *Geology* 35: 347-350.
- Wing, S. L., Currano, E.D. 2013. Plant Response to a Global Greenhouse Event 56 Million Years Ago. *American Journal of Botany* 100(7): 1234-1254.
- Wing, S.L., Harrington, G.J., Smith, F.A., Bloch, J.I., Boyer, D.M., Freeman, K.H. 2005. Transient

floral change and rapid global warming at the Paleocene-Eocene boundary. *Science* 310(5750): 993-996.

Wroblewski, A. 2002. The Role of the Hanna Basin in Revised Paleogeographic Reconstructions of the Western Interior Sea During the Cretaceous-Tertiary Transition. Wyoming Geological Association Guidebook. 2002 Field Conference, p. 17-40.

EARLY PALEOGENE OVERBANK DEPOSITIONAL PATTERNS IN THE HANNA BASIN AND COMPARISON WITH COEVAL STRATA IN THE BIGHORN BASIN (WYOMING, U.S.A.)

CHRISTINE SHONNARD, Beloit College
Research Advisor: Jay Zambito

INTRODUCTION

During the Laramide Orogeny a series of intermontane basins developed in the Rocky Mountain region, the strata of which record the local uplift and paleoclimate history (Dickinson et al., 1988; Aziz et al., 2008; Abels et al., 2013, 2016). This study focuses on two of these basins; the well studied Bighorn Basin in northwestern Wyoming and the relatively under-studied Hanna Basin of south-central Wyoming. Both contain distinctive patterns of early Paleogene alluvial deposition including fluvial sandbodies and a variety of floodplain lithofacies (Aziz et al., 2008; Abels et al., 2013, 2016; Kraus and Gwinn, 1997; Wroblewski 2002; Dechesne et al., in review). The well-studied Willwood Formation of the Bighorn Basin contains weakly developed red-bed paleosols stacked between sandy fluvial avulsion deposits (Abels et al., 2013; Fig. 1). Similarly, the Hanna Formation of the Hanna Basin is notable for its repetitive patterns of sand-rich units interbedded with finer organic-rich shales, siltstones, and carbonaceous strata (Dechesne et al., in review; Fig. 1). This project will analyze depositional cycles in the Hanna Formation, and compare these to those of the Bighorn Basin in order to reveal any common depositional patterns and hypothesize on their potential controls. While separating allogenic and autogenic controls of cyclical sedimentation patterns in fluvial settings is a difficult task (Abels et al., 2013), comparing patterns in these two basins could illuminate whether there were local, regional, or even global climatic controls on basin deposition during this time.

BACKGROUND

Sedimentary depositional cycles are not unique to the Hanna Basin—in the well-studied Paleocene-Eocene deposits of the Bighorn Basin alternating deposits of paleosols, formed on a river floodplain during times of river stability, and fluvial avulsion deposits, deposited when the river searches for a new channel bed, have been identified in the Willwood Formation (Kraus and Gwinn, 1997) (Fig. 1). The cause of this river stability and instability is debated—it has been attributed to being autogenic floodplain development cycles in which stable floodplain deposits are preserved as mature paleosols and avulsion periods are preserved as immature paleosols interbedded with sheet sandstones (Clyde and Christensen, 2003). Such autogenic causes of floodplain-avulsion cycles can be difficult to separate from allogenic causes, such as tectonic or climatic changes which drive changes in river morphology through uplift or changes in precipitation (Hajek et al., 2012; Abels et al., 2013; Foreman, 2014).

A number of previous studies have analyzed the stratigraphy, color spectra, inorganic carbon isotopic values from soil carbonate nodules, and geochemistry of the depositional cycles in the Willwood Formation (Aziz et al., 2008; and Abels et al., 2013, 2016). These studies suggested that the duration of the depositional cycles were linked to Milankovitch cyclicity. For example, Abels et al. (2013) concluded that avulsion cycles are basically an autogenic process triggered by flooding, whose periodicity is affected by precession-scale astronomical climate cycles. The repetitive patterns in overbank deposition and

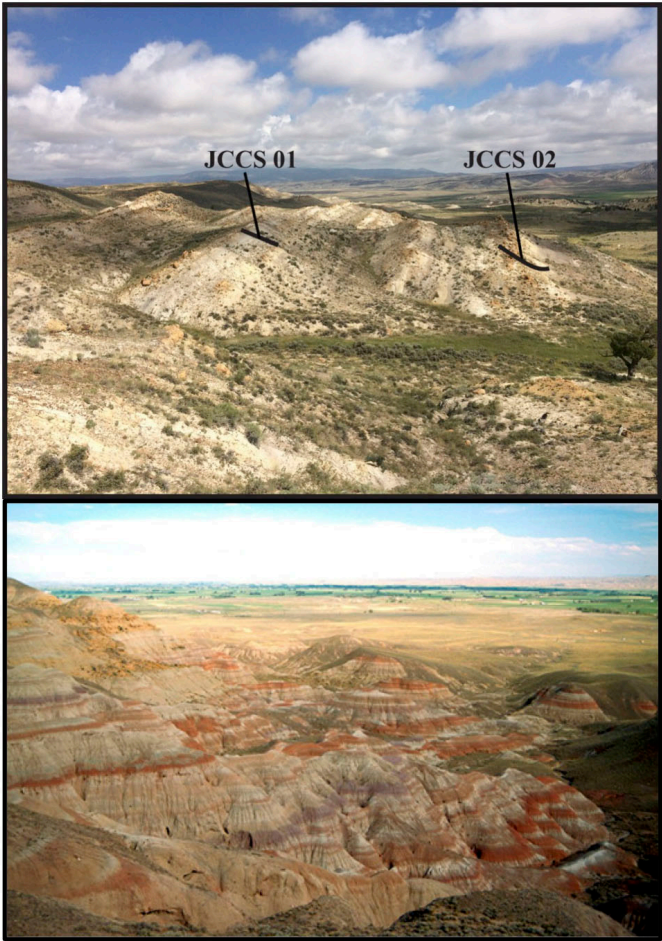


Figure 1. Top: Section Overview of the Leg 17 area of the Hanna Basin, showing the locations of the two stratigraphic sections JCCS-01 and JCCS-02 and the characteristic cyclical deposition of Leg-17. Picture facing towards the south-east (photo by Dr. Jay Zambito). Bottom: Overview of Polecat Bench, including the Willwood Formation, Bighorn Basin (photo by Dr. Will Clyde).

floodplain lithofacies in the Hanna Basin are an ideal setting for evaluating and testing this hypothesis in a different basin.

Geologic Setting

The study area is part of the Leg 17 section of the Hanna Formation in the Hanna Basin, of Wyoming (Fig. 1). The original Leg 17 section was first measured by Lillegraven (1994), and an updated section, including isotopes and paleobotanical analyses was completed by Dechesne et al. (in review). The Hanna Formation is Paleocene-Eocene in age (roughly 59-54 million years old) (Wroblewski, 2002; Dechesne et al., in review). The Leg 17 section has characteristic cycles of lacustrine, paludal, and fluvial depositional environments, bounded by ledge-

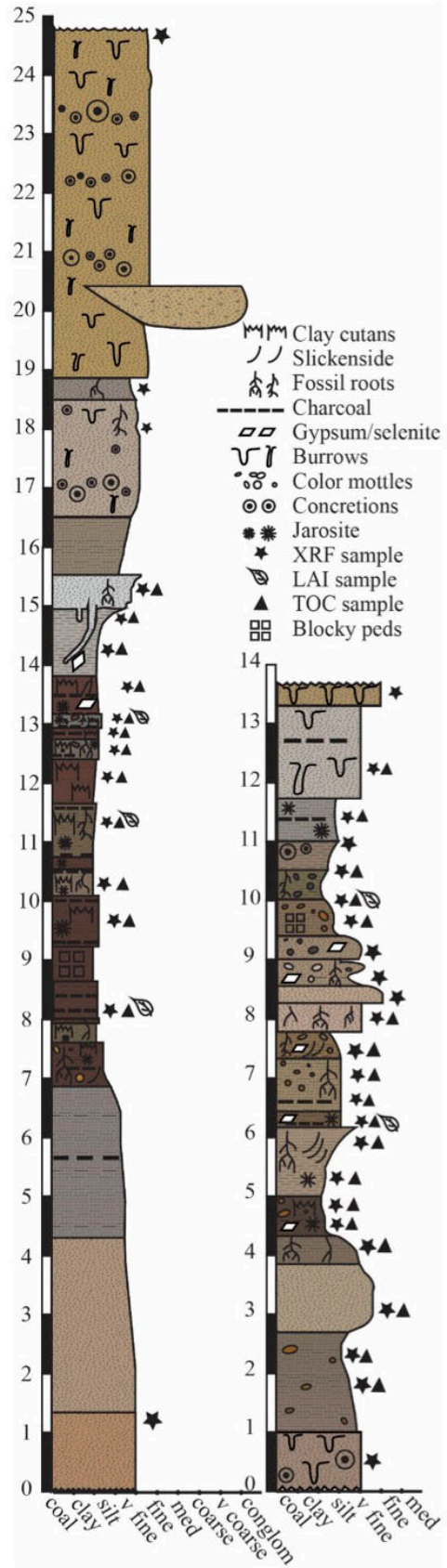


Figure 2. Stratigraphic sections of JCCS-01(right) and 02(left), showing unit thicknesses, changes in lithology, and features.

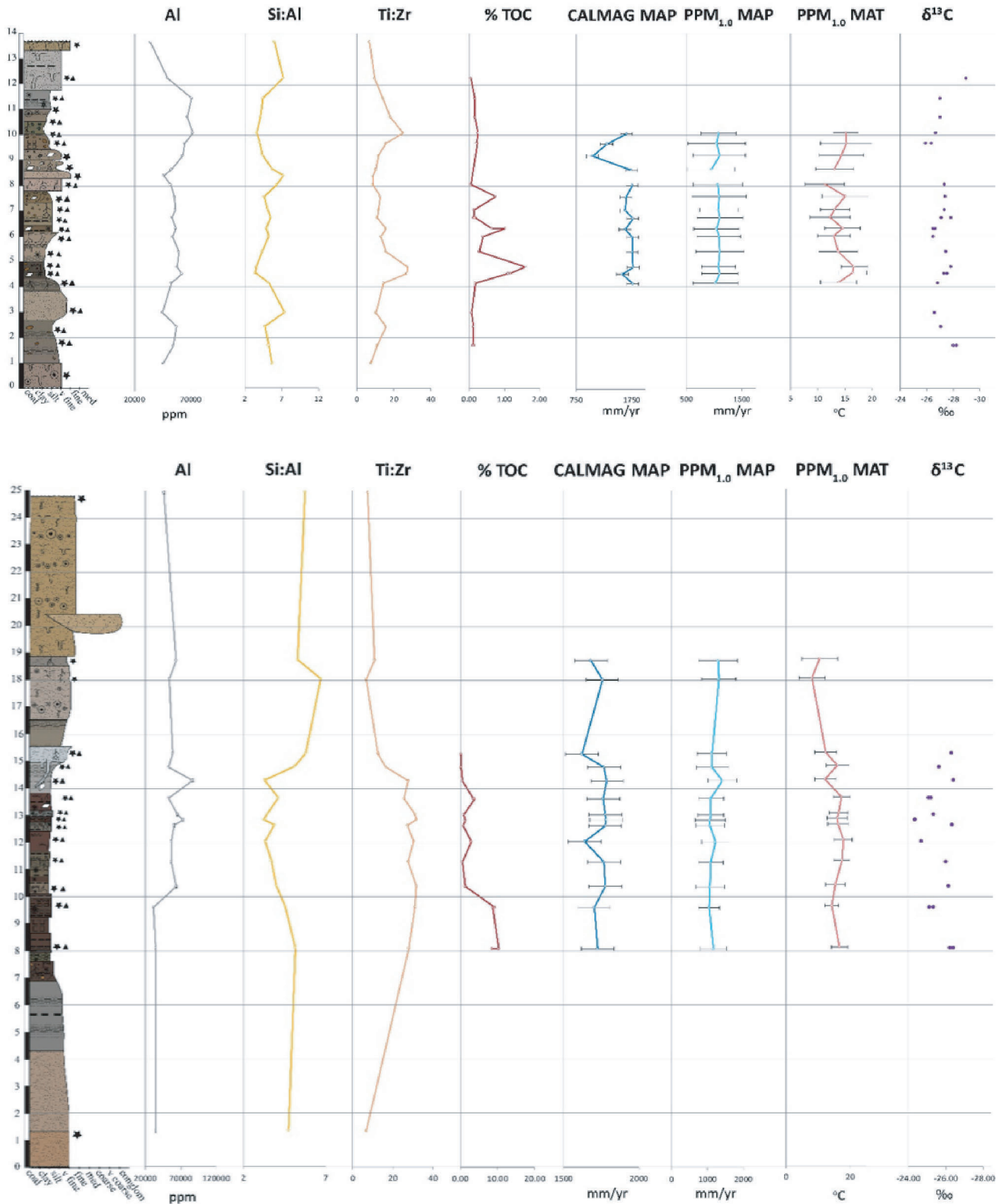


Figure 3. The changes in lithology of sections JCCS-01 and -02 plotted with changes in Al, Si:Al, Ti:Zr, %TOC, CALMAG MAP, PPM1.0 MAP, PPM1.0 MAT, δ¹³C plotted against stratigraphic level.

forming sandstone units (Fig. 2). This project focuses on two cycles within the Leg 17 section, designated as JCCS-01 and JCCS-02. The sections are located within the earliest Eocene portion of the Hanna Formation, post-dating the PETM as indicated by the presence of *Platycarya* pollen (Dechesne et al. in review).

METHODS

Lithological

Two depositional cycles in the Leg 17 section were deemed relatively representative of the formation by visually approximating their height and lateral consistency (Fig. 1). These cycles, JCCS-01 and JCCS-02, are defined as starting with a ledge forming sandstone unit, proceeding up through interbedded siltstones, carbonaceous shales, and claystones and are capped by an upper ledge-forming sandstone (Fig. 2). The sections were trenched, measured at a high resolution (centimeter-scale), and sampled for total organic carbon, stable carbon isotopes, and geochemical analyses about every 0.5 m. A total of 30 carbon isotope samples were collected, 18 at section JCCS-01, and 12 at section JCCS-02 (Figs. 2 and 3).

Geochemical

Samples analyzed for both total organic carbon (TOC) and organic stable carbon isotope ratio ($\delta^{13}\text{C}$) were prepared by powdering a small piece of each sample, dissolving carbonate material through a series of reactions with 0.5N HCl, and rinsing. Small amounts (1-40 mg) of each sample were packaged into tin capsules. This process is similar to that of Baczynski et al. (2013; 2016). The TOC and isotopic composition were analyzed at UC Davis Stable Isotope Facility using an elemental analyzer (Elemental Vario EL Cube) interfaced to a continuous flow isotope ratio mass spectrometer (PDZ Europa 20-20); precision/accuracy was assessed using internal standards. All data is reported in standard delta-notation relative to the Vienna Pee Dee Belemnite.

Portable x-ray fluorescence (pXRF) analysis was performed at Beloit College Department of Geology to determine the elemental composition of the samples collected in JCCS-01 (24 samples) and JCCS-02 (16

samples) using a Thermo Fisher Scientific Niton XL3t GOLDD+ Handheld XRF Analyzer (Fig. 3). The rock samples were homogenized with a mortar and pestle prior to pXRF analysis. The elemental compositions of each sample were standardized using calibration factors developed with eight standards, including those of NIST and the USGS (Rowe et al. 2012).

Elemental data collected using pXRF was used for a variety of environmental proxies. The relative concentrations of Al (as a proxy for clay), Ti:Zr (for sand:clay-sized particles), and Si:Al (for silica) were graphed in relation to their stratigraphic position (Zambito et al., 2017). Additionally, geochemical analysis of bulk oxide ratios in paleosol units can be used to reconstruct ancient climate patterns (Abel et al., 2016). Multiple methods exist, including the CALMAG weathering index developed to reconstruct mean annual precipitation (MAP) for vertisols (clay-rich soils whose dominant features are caused by shrink-swell processes) (Nordt and Driese, 2010). For the CALMAG method, $\text{MAP (mm)} = 22.69 \times \text{CALMAG} - 435.8$, and $\text{CALMAG} = \text{Al}_2\text{O}_3 / (\text{Al}_2\text{O}_3 + \text{CaO} + \text{MgO}) \times 100$, where each oxide is a weight percent. Because some soils in the stratigraphic section contain slickensides and high clay content (Fig. 2), the CALMAG method may be appropriate.

Alternately, the paleosol paleoclimate model (PPM1.0) was developed using paleosols from a wide range of depositional environments and is suitable for ancient climate reconstructions because the model is not dependent on characteristics that would be lost over time (Stinchcomb et al., 2016). This method uses nonlinear spline and a partial least squares regression to reconstruct mean annual temperature (MAT) and MAP using geochemical oxide ratios of paleosols. PPM1.0 is calculated using Al_2O_3 , CaO, MgO, Fe_2O_3 , MnO, P_2O_5 , SiO_2 , ZrO_2 , K_2O , and Na_2O . Because Na is not detected by the pXRF, proxy Na_2O values found in the supplementary material of Stinchcomb et al. (2016) were selected for each unit based on soil order and land cover.

RESULTS

Lithological

The stratigraphy of section JCCS-01 (13.68 m thick)

Table 1. R² values of $\delta^{13}\text{C}$ plotted against to total organic carbon (TOC), CALMAG Mean Annual Precipitation (MAP), PPM_{1.0} MAP, and PPM_{1.0} Mean Annual Temperature (MAT); and of PPM_{1.0} MAP plotted against PPM_{1.0} Mean Annual Temperature, CALMAG MAP, and CALMAG MAP using only paleosols (paleosols containing slickensides or clay cutans).

Section	r ² value						
	$\delta^{13}\text{C}$				PPM _{1.0} MAP		
	TOC (%)	CALMAG MAP	PPM _{1.0} MAP	PPM _{1.0} MAT	PPM _{1.0} MAT	CALMAG MAP	CALMAG MAP vertisols only
JCCS-01	4x10 ⁻⁷	0.1783	0.4099	2x10 ⁻⁵	0.0293	0.0173	0.2186
JCCS-02	0.0004	0.0041	0.0949	0.1159	0.4041	0.0092	0.5361

shows the progression from an orange, heavily bioturbated bottom ledge-forming sandstone into a mottled sandy siltstone layer, another sandstone, six mudstones exhibiting mottling, ancient rootlets, gypsum or selenite crystals, slickensides, and jarosite. Next comes another sandstone layer, a series of four mudstones exhibiting ancient roots, mottling, gypsum, and blocky ped structures, a siltstone with concretions, a sandy siltstone with a charcoal layer and jarosite, a tan bioturbated sandstone, and finally, a second weathered-orange, heavily bioturbated ledge-forming sandstone, which had a similar properties to the lowest sandstone (Fig. 2).

JCCS-02 (24.93 m thick) starts with an orange-grey, massive, ledge-forming sandstone with carbonate cement, a fine-grained light grey sandstone fining into a grey sandy siltstone with charcoal. The next 13 units, spanning 6.9 m, alternate between chocolate brown, fissile, charcoal-rich silty claystones and medium grey blocky claystones, both containing clay cutans, slickensides, fossil roots, mottles, coalified wood, and jarosite. Generally, the chocolate-brown fissile units contained more coalified wood and the blocky grey units contained more ancient rootlets and blocky ped structures. The overlying unit is a coarsening upward grey mudstone, which contains fossil tree roots that penetrate down into underlying layers. The fossil tree roots also contain hematitic liesegang banding and gypsum crystals. Next, a medium grey coarsening upward friable sandy siltstone is overlain by a light yellow-grey very fine grained sandstone containing burrows, a layer of hematite concretions and a liesegang banding which grades into a medium yellow-grey very fine-grained sandstone. The final unit is a thick orange-grey, sandstone heavily bioturbated

by burrows 2.5 to 5 cm in diameter and ~20 cm in length. The unit contains concretionary cement in places. Laterally, this unit transitions to a channel-form containing clasts 1 to 5 cm in diameter including those of the Jurassic-aged Mowry Shale and dark metamorphic/igneous clasts.

Geochemical

Concentrations of elements of interest (Al, Si, Ti, and Zr) collected using pXRF appear to correlate with inferred mineralogic variations and observed grain size in the lithostratigraphic sections (Fig. 3). For example, in both sections, Al and Ti show the same trends and correlate with clay content. Si and Si:Al (an estimate of “clayeyness”; Sheldon and Tabor, 2009) have the same patterns in both sections, indicating that the Si concentrations are dominated by sand-sized silica quartz rather than silicon in clay minerals. Zr increases in sand-rich and Si-rich units whereas Ti and Al increase within the clay-rich units. Potentially Ti is reflecting a greater proportion of fine-grained rutile in these lithofacies.

The $\delta^{13}\text{C}$ values range between about -24‰ and -28‰ and show minor, structured fluctuations up-section, which are especially well-developed in JCCS-01 (Fig. 3). The lowest $\delta^{13}\text{C}$ values roughly occur with the higher % TOC levels and finer-grained lithofacies. However, the covariation does not appear significant when larger data sets are considered (see Chisholm contribution to this volume).

Climate Estimates

The PPM_{1.0} MAT reconstruction from individual beds

yielded a mean value of $14.14^{\circ}\text{C} \pm 3.4$ (the average of the uncertainties in each individual measurement) and a range of 5.4°C in JCCS-01. The mean PPM1.0 MAT for JCCS-02 is $14.74^{\circ}\text{C} \pm 3.3$ with a range of 9.2°C (Fig. 3). The mean PPM1.0 MAP reconstruction in JCCS-01 is 106.92 ± 41.6 cm/yr and the range is 15.6 cm/yr. In JCCS-02, the mean PPM1.0 MAP is 115.91 ± 40.5 cm/yr, and the range is 36.2 cm/yr (Fig. 3). In JCCS-01, the mean of the CALMAG MAP reconstruction is 163.24 ± 10.8 cm/yr and the range is 73.1 cm/yr. In JCCS-02, the mean CALMAG MAP is 170.49 ± 10.8 cm/yr, and the range is 16.5 cm/yr (Fig. 3). There appears to be weak to no correlation with lithology for each climatic parameter in either section.

Overall the pairwise paleo-precipitation reconstructions, CALMAG and PPM1.0 MAP, are uncorrelated, but when only considering units exhibiting slickensides or clay cutans (paleosols more like vertisols), the relationship is slightly strengthened ($R^2=0.2186$ in JCCS-01 and 0.5361 in JCCS-02) (Table 1). The paleo-precipitation reconstructions are uncorrelated with $\delta^{13}\text{C}$ values (for $\delta^{13}\text{C}$ vs. CALMAG MAP, $R^2=0.1783$ in JCCS-01 and $R^2=0.0041$ in JCCS-

02; for $\delta^{13}\text{C}$ vs. PPM1.0 MAP, $R^2=0.4099$ in JCCS-01 and $R^2=0.0949$ in JCCS-02) (Table 1). There is no meaningful correlation between the PPM1.0 MAT reconstruction and $\delta^{13}\text{C}$ ($R^2=2 \times 10^{-5}$ in JCCS-01 and $R^2=0.1159$ in JCCS-02), nor between the PPM1.0 MAT and PPM1.0 MAP values ($R^2=0.0293$ in JCCS-01 and $R^2=0.4041$ in JCCS-02) (Table 1).

DISCUSSION & CONCLUSIONS

The lithologic and geochemical datasets suggest a structured pattern to overbank deposition; stratigraphic zones marked by bioturbated, orange, tabular sandbodies are overlain by fine-grained units with varying degrees of soil development and organic matter preservation. Two such depositional “cycles”, one ~ 5 meters thick and a second ~ 4 meters thick, are observed in JCCS-01. Section JCCS-02 documents one definitive cycle of ~ 15 meters thick, and a second potential cycle ~ 4 m thick. The overall depositional environment is interpreted as palustrine with varying degrees of siliciclastic input and standing water. Sandstones display characteristics similar to those of marginal lacustrine environments and crevasse splays may record conduits for sediment and water to the more distal floodplains. Siltstones and claystones with evidence of bioturbation by roots and high organic content are likely more distal portions of the floodplain, and the lithofacies that display the greatest amounts of coal and fissility more distal portions subject to standing water and anoxic marsh-like conditions. Other cycles in the complete Leg 17 stratigraphic section show thickness variation of similar scale, and an average thickness of about 10 meters. Up-section variability in these channels could be caused by shrinking and expanding of overbank palustrine environments due to relative changes in water and/or sediment supply related to overall climatic conditions in the basin or more stochastic components of the sediment transport system. Additionally, they may mark periods of avulsion (recorded by sandstones) and relative stability of the main fluvial channels in the basin (recorded by coal-rich, fine-grained units).

Comparing our results with lithologic variations in the well-studied Bighorn Basin can help evaluate these processes as well as assess a climatic driver in

Table 2. A comparison of MAP and MAT values from the Hanna and Bighorn Basins collected through geochemical and paleo-botanical methods (leaf area analysis = LAA, and leaf margin analysis = LMA).

Basin	Location	MAP (cm/yr)	Method	MAT ($^{\circ}\text{C}$)	Method	Estimated m level to L17
Hanna Basin	Eocene D ^a	108 +46.9, -32.7	LAA	21.9 \pm 3.8	LMA	180
	Eocene E ^b	132 +56.9, -39.7	LAA	19.1 \pm 3.7	LMA	376
	JCCS-01	163.24 \pm 10.8	CALMAG	14.14 \pm 3.4 ^c	MAT PPM1.0	270
		106.92 \pm 41.6 ^c	PPM1.0			
	JCCS-02	170.49 \pm 10.8	CALMAG	14.74 \pm 3.3 ^c	MAT PPM1.0	220
115.91 \pm 40.5 ^c		PPM1.0				
Bighorn Basin	Elk Creek Section ⁱ			16.4 \pm 2.7 ^d	LMA	N/A
	400-ky after the PETM			18.2 \pm 2.3 ^h	LMA	
	PETM	Lower flora: 80 +114, -56 and 41 ^h	LAA	20.1 \pm 2.8 ^c	LMA	
		Upper flora: 144 +206, -100 and 132 ^h	LAA	26 ^e	Apatite Oxygen isotope composition	
		123+ 177, -86 ^h	LAA	19.8 \pm 3.1 ^h	LMA	
Latest Paleocene	173 +75, -52 ^f	LAA	16.4 \pm 2.9 ^d	LMA		

^a Site D location is just after the PETM, 40 m below JCCS-02. (Azevedo Schmidt, 2018).

^b Site E is about 100 m above JCCS-01. (Azevedo Schmidt, 2018).

^c The upper and lower limit values for PPM1.0 were calculating by taking the average of the differences between the high and low estimates and the best estimate.

^d Wing et al., 2000

^e Wing et al., 2006

^f Diefendorf et al., 2015

^g Fricke et al., 2004

^h Wing et al., 2005

ⁱ 112 m above the base of the PETM

light of the geochemical-based estimates provided in the Hanna Basin. Previous studies in the Willwood Formation recognized two scales of overbank cycle thicknesses, ~8 meters and ~3 meters thick (Aziz et al., 2008; Abels et al., 2013). As noted previously these cycles are defined by two packages of overbank deposition: heterolithic, sand-dominated units indicative of crevasse splays and variably red-mottled paleosols in siltstones and claystones (Abels et al., 2013). The crevasse splay and soil units are clearly associated with multiple fluvial sandstone channels (Kraus and Middleton, 1987; Foreman, 2014). Overall the observed cycles in the Willwood Formation (ranging from 4.5 to ~10 m thick) appear to be comparable to or slightly thinner than the Hanna cycles (ranging from ~4 to ~15 m thick) (Abels et al., 2013). The major difference appears to be the difference between poorly-drained, palustrine overbank conditions (Hanna Formation) and well-drained, strongly pedogenically-modified overbank conditions (Willwood Formation). This could be due to differences in the rate of sediment supply relative to subsidence in each basin or the overall climate in each.

Table 2 shows a summary of major proxy-based paleoclimate estimates from each basin. The estimates reflect different proxy approaches to estimating MAT and MAP. Early Eocene paleofloral (Azevedo Schmidt, 2018) and geochemical estimates (this study) document largely overlapping MAP estimates with a large degree of variability, but geochemical proxy records appear to under-predict MAT relative to paleofloral records (Table 2). Estimates of MAT between the basins appear insufficient to establish major differences in climate between the two. Early Eocene and Late Paleocene estimates in the Bighorn Basin are similar to those estimated by the PPM1.0 method in the Hanna Basin, but paleofloral records in the Hanna Basin suggest a warmer overall climate during the Eocene that experienced MAT more similar to PETM conditions in the Bighorn Basin (Table 2). At the present time it is unclear which is more representative. Note that PPM1.0 does not take the effects of diagenesis into consideration and the units being studied have undergone diagenesis. Based on these datasets we suggest that potentially abnormally rapid subsidence rates in the Hanna Basin (Hajek

et al., 2012) may have been responsible for poor floodplain drainage rather than the dominant climate, which has been proposed for some unusually rapidly subsiding areas in the Sevier foreland basin of Utah (Roberts, 2007).

Our datasets offer an initial test of the Abels et al. (2013) and Aziz et al. (2008) hypotheses that the observed avulsion cycles in overbank deposition in the Willwood Formation were related to precessional-scale variability and represent an example of Milankovitch-forcing on alluvial systems. The MAP estimates generated in this study, which show no significant up-section structure from dry to wet (or vice versa) associated with the lithologic cycles, indicate that depositional cycles are unrelated to hydrologic cycle variations driven by Milankovitch parameters. Moreover, the higher sedimentation rates in the Hanna Formation (due to greater subsidence) imply that, although the cycle thickness are mostly similar to the thicknesses in the Willwood Formation, it is likely that the Hanna Basin cycles represent a shorter duration of geologic time (i.e., shorter than the 20 kyr precession timescale). Additionally, the $\delta^{13}\text{C}$ values show no variability up-section correlated with MAT or MAP suggesting meso-scale climate did not play a significant role in cycle deposition. Therefore, this study suggests that the overbank cycles in the Hanna Basin described here are largely driven by autogenic processes, which have been shown to create cyclical stratigraphy in model systems (Jerolmack and Paola, 2007; Sheets et al., 2007; Hajek et al., 2010). Additional outcrop and geochemical analyses will be needed to test this hypothesis with larger datasets.

ACKNOWLEDGEMENTS

This material is based upon work supported by the Keck Geology Consortium and the National Science Foundation under Grant No. 1659322 as well as NSF grant EAR 145031 to Ellen Currano. I would like to thank all of those involved in the Keck 2018-19 research project: advisors and mentors Ellen Currano, Brady Foreman, Marieke Dechesne, Regan Dunn, and Jay Zambito, as well as student colleagues James Chisholm, Jake Polsak, Xavier Nogueira, Keifer Nace, and Anthony Semeraro.

REFERENCES

- Abels, H. A., Kraus, M. J., and Gingerich, P. D., 2013, Precession-scale cyclicity in the fluvial lower Eocene Willwood Formation of the Bighorn Basin, Wyoming (USA): *Sedimentology*, v. 60, p. 1467-1483, doi: 10.1111/sed.12039.
- Abels, H. A., Lauretano, van Yperen, A. E., Hopman, T., Zachos, J. C., Lourens, L. J., Gingerich, P. D., and Bowen, G. J., 2016, Environmental impact and magnitude of paleosol carbonate carbon isotope excursions marking five early Eocene hyperthermals in the Bighorn Basin, Wyoming: *Climate of the Past*, v. 12, p. 1151-1163, doi: 10.5194/cp-12-1151-2016.
- Azevedo Schmidt, L. E., 2018. The effects of depositional environment on plant and insect herbivore communities across the Paleocene-Eocene Boundary, Hanna Basin WY. MS Thesis. University of Wyoming, Laramie, WY.
- Aziz, H. A., Hilgen, F. J., van Lujik, G., M., Sluijs, A., Kraus, M. J., Pares, J. M., and Gingerich, P. D., 2008, Astronomical climate control on paleosol stacking patterns in the upper Paleocene-lower Eocene Willwood Formation, Bighorn Basin, Wyoming: *Geology*, v. 36, no. 7, p. 531-534; doi: 10.1130/G24734A.1.
- Bush, R. T., Wallace, J., Currano, E. D., Jacobs, B. F., McInerney, F., A., Dunn, R. E., and Tabor, N. J., 2017, Cell anatomy and leaf $\delta^{13}\text{C}$ as proxies for shading and canopy structure in a Miocene forest from Ethiopia: *Palaeogeography, Palaeoclimatology, Palaeoecology*, v. 485, p. 593-604, doi: 10.1016/j.palaeo.2017.07.015.
- Clyde, W. C., and Christensen, K. E., 2003, Testing the relationship between pedofacies and avulsion using Markov analysis: *American Journal of Science*, v. 303:1, p. 60-71, doi: 10.2475/ajs.303.1.60.
- Currano, E. D., Wilf, P., Wing, S. L., Labandeira, C. C., Lovelock, E. C., and Royer, D. L., 2008, Sharply increased insect herbivory during the Paleocene-Eocene Thermal Maximum: *National Academy of Sciences*, 105(6), p. 1960-4, p. 547-67, doi: 10.1073/pnas.0708646105.
- Currano, E. D., Labandeira, C. C., and Wilf, P., 2010, Fossil insect folivory tracks paleotemperature for six million years: *Ecological Society of America*, v. 80 (4), doi: 10.1890/09-2138.1.
- Dechesne, M., E.D. Currano, E. D., Dunn, R.E., Higgins, P., Hartman, J.H., Chamberlain, K.R., and Holm-Denoma, C.S., In review, Depositional patterns of the fluvial to paludal strata of the Hanna Formation across the Paleocene – Eocene boundary, Hanna Basin, Wyoming.
- Dickinson, W. R., Klute, M. A., Hayes, M. J., Janecke, S. U., Lundin, E. R., McKittrick, M. A., and Olivares, M. D., 1988, Paleogeographic and paleotectonic setting of Laramide sedimentary basins in the central Rocky Mountain region: *Geologic Society of America Bulletin*, v. 100, p. 1023-1039.
- Diefendorf, A. F., Freeman, K. H., Wing, S. W., Currano, E. D., Mueller, K. E., 2015, Paleogene plants fractionated carbon isotopes similar to modern plants: *Earth and Planetary Science Letters*, v. 429, p. 33-44.
- Dunn, R. E., Currano, E. D., Dechesne, M., Foreman, B. Z., 2018, Forest canopy response to greenhouse warming at the Paleocene-Eocene Thermal Maximum: Abstract 213-8 presented at Fall Meeting, Geological Society of America, Indianapolis, Indiana, 3-7 November.
- Dunn, R. E., Stromber, C. A., Madden, R. H., Kohn, M. J., and Carlini, A. A., 2015, Linked canopy, climate, and faunal change in the Cenozoic of Patagonia: *Science* v. 347: 6219, p. 258-261, doi: 10.1126/science.1260947.
- Foreman, B. Z., 2014, Climate-driven generation of a fluvial sheet sand body at the Paleocene-Eocene boundary in north-west Wyoming (USA): *Basin Research*, v. 26, p. 225-241, doi: 10.1111/bre.12027.
- Fricke, H. C., and Wing, S. L., 2004, Oxygen isotope

- and paleobotanical estimates of temperature and $\delta^{18}\text{O}$ -latitude gradients over North America during the early Eocene: *American Journal of Science*, v. 304, p. 612-635, doi: 10.2475/ajs.304.7.612.
- Hajek, E. A., Heller, P. L., and Schur, E. L., 2012, Field test of autogenic control on alluvial stratigraphy (Ferris Formation, Upper Cretaceous-Paleogene, Wyoming): *GSA Bulletin*, v. 124, no. 11/12, p. 1898-1912, doi: 10.1130/B30526.1.
- Hajek, E.A., Heller, P.L., and Sheets, B.A., 2010, Significance of channel-belt clustering in alluvial basins: *Geology*, v. 38, no. 6, p. 535-538, doi:10.1130/G30783.1.
- James Cook University, 2018, Advanced Analytical Centre: Element-to-stoichiometric oxide conversion factors: <https://www.jcu.edu.au/advanced-analytical-centre/services-and-resources/resources-and-extras/element-to-stoichiometric-oxide-conversion-factors> (accessed January 2019).
- Jerolmack, D.J., and Paola, C., 2007, Complexity in a cellular model of river avulsion: *Geomorphology*, v. 91, no. 3-4, p. 259-270, doi:10.1016/j.geomorph.2007.04.022.
- Sheets, B.A., Paola, C., and Kelberer, J.M., 2007, Creation and preservation of channel-form sand bodies in an experimental alluvial system, in Nichols, G.J., Williams, E., and Paola, C., eds., *Sedimentary Processes, Environments and Basins: International Association of Sedimentologists Special Publication 38*, p. 555-567.
- Jones, J. A., Creed, I. F., Hatcher, K. L., Warren, R. J., Adams, M. B., Benson, M. H., Boose, E., Brown, W. A., Campbell, J. L., Covich, A., Clow, D. W., Dahm, C. N., Elder, K., Ford, C. R., Grimm, N. B., Henshaw, D. L., Larson, K. L., Miles, E. S., Miles, K. M., Sebestyen, S. D., Spargo, A. T., Stone, A. B., Vose, J. M., and Williams, M. W., 2012, Ecosystem Processes and Human Influences Regulate Streamflow Response to Climate Change at Long-Term Ecological Research Sites: *BioScience*, v. 62, no. 4, p. 390-404, doi: 10.1525/bio.2012.62.4.10.
- Karageorgis, A. P., Kaberi, H., Price, N. B., Muir, G. K., Pates, J. M., and Lykousis, V., 2005, Chemical composition of short sediment cores from Thermaikos Gulf (eastern Mediterranean); sediment accumulation rates, trawling and winnowing effects: *Continental Shelf Research*, v. 25:19, p. 2456-2475, doi: 10.1016/j.csr.2005.08.006.
- Keck Geology Consortium, 2017, Assessing vegetation and fluvial responses to the PETM: <https://keckgeology.org/2017/12/wyoming2018/> (accessed December, 2018).
- Kowalski, B., Dilcher, D., 2003, Warmer paleotemperatures for terrestrial ecosystems: *Proceedings of the National Academy of Sciences of the USA*, v. 100 (10), p. 167-170, doi: 10.1073/pnas.232693599.
- Kraus, M. J., and Riggins, S., 2006, Transient drying during the Paleocene-Eocene Thermal Maximum (PETM): Analysis of paleosols in the bighorn basin, Wyoming: *Palaeogeography, Palaeoclimatology, Palaeoecology*, v. 245, p. 444-461, doi:10.1016/j.palaeo.2006.09.011.
- Kraus, M. J., 1999, Paleosols in clastic sedimentary rocks: their geologic applications: *Earth-Science Reviews*, v. 47, p. 41-70.
- Kraus, M.J., and Middleton, L.T., 1987, Contrasting architecture of two alluvial suites in different structural settings. In: *Recent Developments in Fluvial Sedimentology* (Ed. by F.G. Ethridge) *Soc. Econ. Paleo. Mineral. Spec. Pub.*, v. 30, p. 253-262.
- Kraus, M. J., and Gwinn, B. M., 1997, Facies and facies architecture of Paleogene floodplain deposits, Willwood Formation, Bighorn Basin, Wyoming, USA: *Sedimentary Geology*, v. 114, p. 33-54.
- Kraus, M. J., McInerney, F. A., Wing, S. L.,

- Secord, R., Baczynski, A. A., and Bloch, J. I., 2012, Paleohydrologic response to continental warming during the Paleocene–Eocene Thermal Maximum, Bighorn Basin, Wyoming: *Palaeogeography, Palaeoclimatology, Palaeoecology*, v. 370, p. 196-208.
- Lillegraven, J. A., 1994, Age of upper reaches of Hanna Formation, northern Hanna Basin, south-central Wyoming: *Berliner geowissenschaftliche Abhandlungen, Reihe E (Paläobiologie)*, Band 13 (B. Krebs-Festschrift), p. 203–219.
- McInerney, F. A., and Wing, S. L., 2011, The Paleocene-Eocene Thermal Maximum: A perturbation of carbon cycle, climate, and biosphere with implications for the future: *Annual Review Earth Planetary Sciences*, v. 39, p. 489-516.
- NOAA National Centers for Environmental information, Climate at a Glance: Statewide Time Series, published February 2019, retrieved on February 28, 2019 from: <https://www.ncdc.noaa.gov/cag/>.
- Nordt, L. C., and Driese, S. D., 2010, New weathering index improves paleorainfall estimates from Vertisols: *Geology*, v. 38:5, p. 407-10, doi: 10.1130/G30689.1.
- Roberts, E.M., 2007, Facies architecture and depositional environments of the Upper Cretaceous Kaiparowits Formation, southern Utah: *Sedimentary Geology* v, 197, p. 207-233.
- Rowe, H., Hughes, N., Robinson, K., 2012, The quantification and application of handheld energy-dispersive x-ray fluorescence (ED-XRF) in mudrock chemostratigraphy and geochemistry: *Chemical Geology* 324-325, p. 122-131, doi: 10.1016/j.chemgeo.2011.12.023.
- Sheldon, N.D., and Tabor, N.J., 2009, Quantitative paleoenvironmental and paleoclimatic reconstruction using paleosols: *Earth-Science Reviews*, v. 95, p. 1-52.
- Stinchcomb, G.E., Nordt., L. C., Driese, S. G., Lukens, W. E., Williamson, F. C., and Tubbs, J. E., 2016, A data-driven spline model designed to predict paleoclimate using paleosol geochemistry: *American Journal of Science*, v. 316, p. 746-777, doi: 10.2475/08.2016.02.
- Wilf, P., Wing, S. L., Greenwood, D. R. & Greenwood, C. L., 1998, Using fossil leaves as paleoprecipitation indicators. An Eocene example: *Geology*, v. 26, p. 203–206.
- Wing, S. L., Lovelock, E. C., and Currano, E. D., 2006, Climatic and floral change during the PETM in the Bighorn Basin, Wyoming, USA. *Climate & Biota of the Early Paleogene*. Bilbao, Spain.
- Wing, S. L., Harrington, G. J., Smith, F. A., Bloch, J. I., Boyer, D. M., and Freeman, K. H., 2005, Transient Floral Change and Rapid Global Warming at the Paleocene-Eocene Boundary: *Science* v. 320, p. 993-996, doi: 10.1126/science.1116913.
- Wing, S. L., Bao, H., and Koch, P. L., 2000, An early Eocene cool period? Evidence for continental cooling during the warmest part of the Cenozoic. Pp. 197-237. In B. T. Huber, K. G. MacLeod, and S. L. Wing, eds. *Warm climates in earth history*. Oxford U P, Cambridge).
- Wing, S. L., Lovelock, E. C., and Currano, E. D., 2006, Climatic and floral change during the PETM in the Bighorn Basin, Wyoming, USA: *Climate & Biota of the Early Paleogene*. Bilbao, Spain.
- Wolfe, J. A., 1979, Temperature parameters of humid to mesic forests of Eastern Asia and relation to forests of other regions of the Northern Hemisphere and Australasia: *United States Geological Survey Professional Paper*, 1106: 1–37.
- Wroblewski, A. 2002. The Role of the Hanna Basin in Revised Paleogeographic Reconstructions of the Western Interior Sea During the Cretaceous-Tertiary Transition. *Wyoming Geological Association Guidebook*. 2002 Field Conference,

p. 17-40.

Zambito, J., McLaughlin, P., and Bremmer, S., 2017, Elemental chemostratigraphy of the Cottage Grove Hole MP-18 core: Implications for litho- and hydrostratigraphy in Wisconsin: Wisconsin Geological and Natural History Survey Open-File Report 2017-03, p. 1-7.